APPLIED COMPUTATIONAL ELECTROMAGNETICS SOCIETY JOURNAL

February 2020
Vol. 35 No. 2
ISSN 1054-4887

The ACES Journal is abstracted in INSPEC, in Engineering Index, DTIC, Science Citation Index Expanded, the Research Alert, and to Current Contents/Engineering, Computing & Technology.

The illustrations on the front cover have been obtained from the research groups at the Department of Electrical Engineering, The University of Mississippi.

FEBRUARY 2020 REVIEWERS: REGULAR PAPERS

Stamatios Amanatiadis
Burak Aricioglu
Manuel Arrebola
Ercument Arvas
Ankan Bhattacharya
Jerdvisanop Chakarothai
Guan-Yu Chen
Kejian Chen
Ozlem Coskun
Xunwang Dang
Danesh Daroui
Alistair Duffy
Atef Elsherbeni
Ian Flintoft
Alfredo Gomes Neto
Nan Hu
Taha Imeci
Tianqi Jiao
Sebastien Lallechere
Yingsong Li
Paulo Mendes
Branislav Notaros
Giuseppe Pelosi
Anthony Pendurthy
Zhen Peng
Jalil Rashed-Mohassel
Vince Rodriguez
Nitin Saluja
Yan Shi
Hamidreza Siampour
Meriah Sidi Mohammed
Manuel Sierra Castañer
Koushick V.
Xing-Chang Wei
Wei-Chung Weng
Binbin Yang
Karam Younus

THE APPLIED COMPUTATIONAL ELECTROMAGNETICS SOCIETY JOURNAL

Vol. 35 No. 2 February 2020

TABLE OF CONTENTS – REGULAR PAPERS

Comparative Study on Indoor Path Loss Models at 28 GHz, 60 GHz, and 73.5 GHz Frequency Bands

Huthaifa A. Obeidat [1], Ali A. Abdullah [2], Mahmood F. Mosleh [3], Atta Ullah [2], Omar A. Obeidat [4], and Raed A. Abd-Alhameed [2]

[1] Department of Communications and Electronics Engineering
Jerash University, Jerash, Jordan
h.obeidat@jpu.edu.jo

[2] School of Electrical Engineering and Computer Science
University of Bradford, Bradford, BD7 1DP, UK
(a.a.abdUllah1, a.Ullah5, r.a.a.abd)@bradford.ac.uk

[3] College of Electrical and Electronic Engineering Techniques
Middle Technical University, Baghdad, Iraq
drmahfa@yahoo.com

[4] College of Engineering, Wayne State University
Detroit, Michigan, MI 48202, USA
omar.obeidat@wayne.edu

Abstract ─ In this paper, a comparative study between different indoor path loss prediction models is conducted. The investigated models include averaged wall loss model (AWM), single slope model (SSM), linear attenuation model (LM), two slope model (TSM), partitioned model (PM), and Motley-Keenan model (MKM). The models were tested in a simulated environment of the 3rd floor of Chesham building, the University of Bradford, a different set of frequencies were used including 28 GHz, 60 GHz, and 73.5 GHz, TSM shows the best performance, both AWM and MKM tend to have a similar performance at millimetre-frequencies, both models' prediction for corridor and LOS regions are pessimistic while TSM, SSM, and LM have better estimations in these regions.

Index Terms ─ Indoor path loss models, millimetre-wave frequencies, Motley Keenan model, ray tracing, received signal strength, single slope model, two slope model.

I. INTRODUCTION

The astonishing growth of wireless applications in our daily life urges the radio engineer designers to have optimum algorithms to have best radio wave coverage; those applications cover a variety of services including communication services, medical, industrial, and public transport usage [1]. The IEEE 802.11 WLAN became the principal WLAN technology due to its low cost, ease of disposition and flexible mobility [2]. The unlicensed available spectrum makes the use of WLAN attractive within indoor environments for different applications especially for millimetre wave band [3]. However, deploying WLAN routers requires knowledge of the propagation channel; therefore, having an accurate indoor channel modelling becomes critical [1]. Currently, massive research is being conducted to utilize millimetre wave frequencies in 5G systems [4-5], this utilization includes 28 GHz [4], 60 GHz [5], and 73 GHz [4].

The wireless channel in indoor environments is more complicated compared to outdoor environments. Multipath fading affects wireless systems performance; as a result, the wireless device and the router have to match in order to suppress multipath manifestations which demands awareness of the detailed propagation channel [6].

Many efforts have been done in order to characterise the channel's parameters; radio coverage designers use path loss prediction models to distribute the access points within the facility such that they provide the best coverage [7].

The indoor channel $h(t)$ is a time-space varying, which can be expressed mathematically based on Saleh Valenzuela model as [8]:

$$h(t,\theta) = \sum_{l=0}^{\infty}\sum_{k=0}^{\infty}\beta_{kl}e^{j\varphi_{kl}}\delta\begin{pmatrix} t \\ -T_l \\ -\tau_{kl}\end{pmatrix}\delta\begin{pmatrix} \theta \\ -\Theta_l \\ -\omega_{kl}\end{pmatrix}, \quad (1)$$

Submitted On: June 29, 2019
Accepted On: December 15, 2019

where β_{kl} is the multipath gain, φ is the phase associated with the l^{th} cluster and k^{th} ray, l is the number of clusters, k is the number of arrival rays within the l^{th} cluster, T_l is the arrival time of the l^{th} cluster, τ_{kl} is the arrival time of the k^{th} ray within the l^{th} cluster, and ω_{kl} is the arrival angle of the k^{th} ray of the l^{th} cluster [9].

In the case of small bandwidths, multipath components fall within the bins on the delay axis which follow either Rayleigh or Rician distributions [9]; however, when using Ultra Wide-Band (UWB) systems the number of components falling within the delay bins is less; therefore, the Central Limit Theorem is no longer valid. In such a case, the 802.15.3a standard model is adopted to consider these effects [9]. Indoor systems can be considered as pico-cell arrangements, a single pico-cell arrangement together with a general MIMO scheme is proposed in [10]. The MIMO system shows the potential to improve system performance.

MIMO antennas are widely used in 5G systems to increase data rate [11], one of the major concerns regarding designing a MIMO antenna is the mutual coupling, several research papers tackled this problem and obtained a lower mutual coupling [12]. Improvements on the IEEE 802.11n indoor channel were made by [13] where more realistic channel representation for MIMO systems using uniform circular array antenna at either the transmitter or the receiver was established and studied. In their work, the spatial and temporal clustered channel model developed involving treating the reflected rays as clusters. In [14] capacity investigations on hybrid uniform linear and circular arrays were conducted, it was concluded that using multi-cluster based approach gives more accurate results compared to single cluster case which leads to better optimum design of antenna.

Mutual coupling reduction has been studied extensively in the literature using meta-material [15, 16], periodic multi-layered EM bandgap structures [17], and orthogonal structure [18].

The small-scale effect is undesired and has to be removed; there are two methods to remove small scale effect, the first method takes the power sum of all multipath rays, known as "*power sum prediction, (PS)*" [29]:

$$\langle P_{PS} \rangle = \sum_M P_M, \tag{2}$$

where $\langle P_{PS} \rangle$, M, and P_M are the averaged power using the PS method, number of multipath rays and power of each individual ray respectively.

The second method takes the average of the squared sum of all-electric fields (amplitudes and phases): this is known as "*vector sum prediction (VS)*" [29]:

$$\langle P_{VS} \rangle = \left| \sum_M \sqrt{P_M}\, e^{-j\varphi_M} \right|^2, \tag{3}$$

where $\langle P_{VS} \rangle$ is the averaged power using the VS method and φ_M is the Mth ray phase in radians.

Wireless InSite supports both methods, it is up to the user to select the operating method from the settings. Practically, it's difficult to use the PS averaging method, especially at higher frequencies therefore, VS averaging method is used instead.

In [30] a comprehensive study on estimating local mean signal strength in indoor environments using VS averaging method was conducted using a different number of samples, different arrangement sizes and different arrangement configurations. In this paper, different indoor path loss prediction parameters are investigated for different sets of frequencies. The organisation of this paper is as follows: Section II presents the methodology adopted in the conducted study and describes the simulation setup and the procedure followed to evaluate each model. Section III investigates the collected results; a comparative study between the investigated models is conducted, and finally, conclusions and recommendations are presented.

II. PROBLEM DEFINITION AND METHODOLOGY

The main target of this paper is to understand, the performance of some popular indoor path loss models at millimetre wave frequencies. Many indoor path loss models have been studied in literature, some models consider free-space loss along with losses due to walls and floors like Motley Keenan Model (MKM) [19], averaged wall loss model (AWM) [7], ITU-R P.1238 model [20], COST231 indoor model [21], and enhanced COST231 [22]. Another set of models use free space propagation model with different values for the path loss exponents (PLE) like single slope model (SSM) [23], two slope model (TSM) [24], and partitioned model (PM) [25].

Some models consider the effect of free space propagation in addition to attenuation factors which depend on the nature of the tested environment and the operating frequency like linear attenuation model (LM) [26].

Since simulations are conducted for a single floor, propagation through floors will not be investigated since COST231 model will turn into Motley-Keenan model. Similarly, the ITU-R P.1238 model will be reduced to a single slope model. The examined models include Motley-Keenan model, single slope model, two slope model, linear attenuation model, averaged wall loss model and partitioned model. The multi-floor propagation environment will be discussed in another paper.

A. Single Slope Model (SSM)

The received power at any distance is given by [23]:

$$P_r(dB) = P_0(dB) - 10n \log_{10}(d), \tag{4}$$

where P_0 is the reference power measured at a 1 m from the transmitter, n is the path loss exponent and d is the distance from transmitter (Goldsmith, 2005).

B. Two Slope Model (TSM)

In [24] two-path loss exponents were used to have a better fitting for the signal strength variation, the first PLE n_1 is applied for the "*near transmitter propagation*" where no obstruction in the 1st Fresnel zone, while the second PLE n_2 is applied for the "*breakpoint propagation*" when furniture and other obstacles fall in the 1st Fresnel zone and PLE is larger than free-space path loss,

$$P_r = P_0 - 10\begin{cases} n_1 \log_{10}(d) & d < d_{bp} \\ n_1 \log_{10}(d_{bp}) + n_2 \log_{10}\left(\frac{d}{d_{bp}}\right) & d > d_{bp} \end{cases}, \quad (5)$$

where d_{bp} is the breakpoint distance.

C. Linear Attenuation Model (LAM)

Instead of using the path loss exponent, a loss factor a was proposed to be added to the free space loss [26],

$$P_r(dB) = P_0(dB) - 20\log_{10}(d) - a \cdot d, \quad (6)$$

where d represents distance in metre.

D. Partitioned Model (PM)

Predetermined values of n are used depending on the transmitter-receiver separation [25]:

$$P_r = P_0 - \begin{cases} 20\log_{10} d, & 1m < d \le 10m \\ 20 + 30\log_{10}\frac{d}{10}, & 10m < d \le 20m \\ 29 + 60\log_{10}\frac{d}{20}, & 20m < d \le 40m \\ 47 + 120\log_{10}\frac{d}{40}, & d > 40m \end{cases}. \quad (7)$$

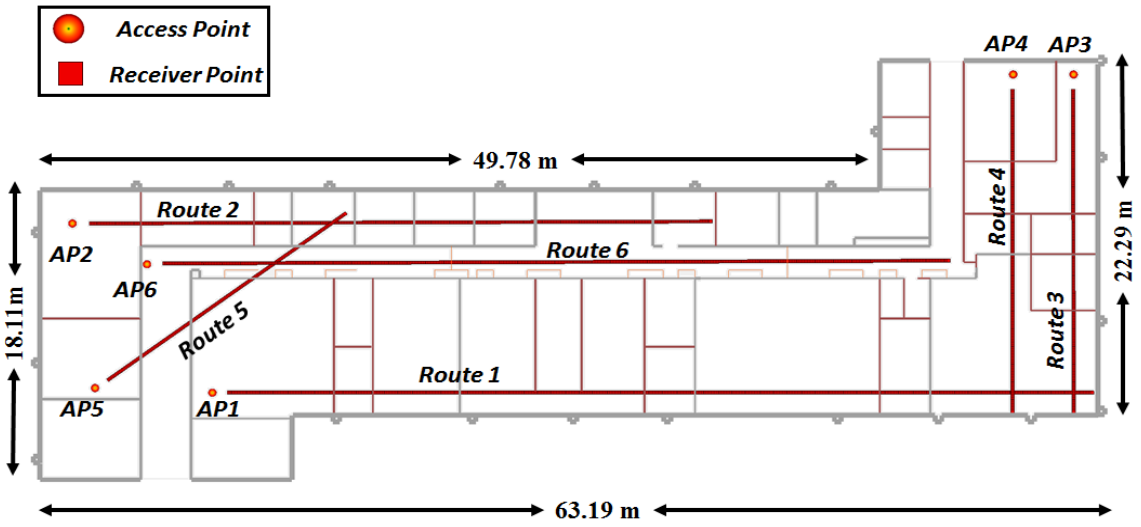

Fig. 1. Simulated experiment in the 3rd floor Chesham building, University of Bradford.

E. Motley-Keenan Model (MKM)

In Motley-Keenan Model, losses are estimated by considering the free space propagation loss in addition to the effect of walls and floors [19],

$$L = L_{FS} + L_C + \sum_{i=1}^{I} N_{wi} L_{wi} + \sum_{j=1}^{J} N_{fj} L_{fj}, \quad (8)$$

where L_{FS}, L_C, N_w, N_f, L_w, L_f, i, and j are the free space loss, a constant term (loss at a reference distance d_0 = 1 m), number of walls, number of floors, wall loss factor, floor loss factor, type of wall and type of floor respectively.

F. Average Wall Model (AWM)

This model is similar to MKM; however, due to multipath and waveguiding effects, losses from walls are considered as correction factors, in other words, wall losses W_{AML} can be positive or negative whatever makes the best fit for the measurements, the received signal strength after the L[th] wall is given by [7]:

$$P_r(d) = P_0 - 20\log_{10}(d) - W_{AWM} \cdot L. \quad (9)$$

Upon applying the above equations, there is a set of unknown parameters to be estimated, these parameters include PLE for SSM (i.e., n), PLE for TSM (i.e., n_1, n_2), attenuation factor (AF) for LM (i.e., a), wall losses for MKM (L_{wi}), and averaged wall losses for AWM (W_{AWM}). The estimation of these parameters is explained in the next section.

III. SIMULATION SETUP

Figure 1 shows the examined scenarios in the simulated environment; these routes are chosen in a representative way for the indoor environments, route 1 and 4 represent propagation in lab offices, which have both concrete and drywalls. Route 2 represents propagation in lecturers' offices which mainly have concrete walls, route 3 represents propagation in lab offices with drywalls only. Route 5 represents

propagation in the environment with concrete walls only while route 6 represents propagation in corridors. MIMO antenna systems are widely integrated into the mm-wave applications, therefore in our simulation a 16×16 MIMO circularly polarised antenna system was used with a λ/2 spacing between elements. Access points transmit power is 20 dBm, receiver sensitivity was set to -120 dBm.

In this paper, simulations were conducted using Wireless InSite ray-tracing software for high-frequency ranges namely, 28 GHz, 60 GHz, and 73.5 GHz, their corresponding bandwidths are 0.8 GHz [4], 2.15 GHz [27], and 2 GHz [28] respectively. The Wireless InSite scenarios settings are presented in Table 1.

Table 1: Wireless InSite settings for the investigated scenarios

Property	Setting
Number of reflections	6
Number of transmissions	4
Number of diffractions	1
Number of reflections before the first diffraction	3
Number of reflections after the last diffraction	3
Number of reflections between diffractions	1
Number of transmissions before the first diffraction	2
Number of transmissions after the last diffraction	2
Number of transmissions between diffractions	1
Ray tracing method	SBR
Propagation model	Full 3D

As shown in Fig. 2, the simulation environment considers concrete walls, drywall, glass, wooden doors and tables, metal cabinets and indoor foliage which makes the environment more representative. The model also considered the effect of the interaction between building materials and operating frequencies as shown in Table 2 according to the ITU-R P.2040 recommendations [31]. The purpose of this study is to evaluate the behaviour of each model with high frequencies, these frequencies are proposed for use in the 5G systems. Simulations took place in a simulated environment of B3-wing, Chesham Building, University of Bradford.

In Wireless InSite, received signal strength (RSS) data were collected over routes shown in Fig. 1, since path loss models are used to predict the signal strength along a route, we took samples from the simulated data and then models' parameters were generated using a Matlab routine such that they make the best fit to the samples. After that, those parameters are passed to a Matlab routine to predict the RSS for each model for the investigated routes. Root means Square Error (RMSE) between the Wireless InSite data and the generated path loss models data is used as a performance metric, the smaller the RMSE, the better the model.

Table 2: Material properties with frequency

Frequency (GHz)		28	60	75.3
Concrete	ε_r	5.31	5.31	5.31
	σ	0.48	0.90	1.06
Glass	ε_r	6.27	6.27	6.27
	σ	0.23	0.57	0.72
Wood	ε_r	1.99	1.99	1.99
	σ	0.17	0.38	0.47
Drywall	ε_r	2.94	2.94	2.94
	σ	0.12	0.21	0.24

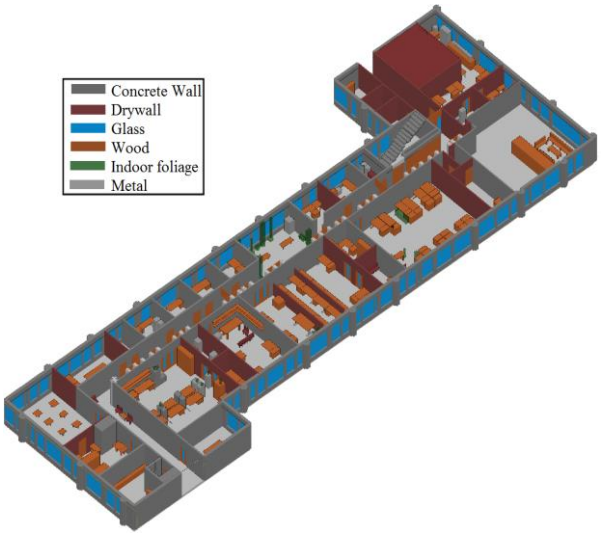

Fig. 2. 3D view of the simulated environment for B3-wing, Chesham Building, University of Bradford.

IV. RESULTS AND DISCUSSIONS

Figure 3 shows propagation through the corridor at (a) 28 and (b) 73.5 GHz. As seen in the figure, there is a remarkable path loss difference between the two frequencies; at 73.5 GHz most of the RSS values fall down -100 dBm after 20 m, while at 28 GHz, all RSS readings are above -90 dBm for the entire route. Since the operating frequencies are at millimetre wave, walls tend to act as reflectors. In the following discussion, we refer to each simulation run through one of these propagation cases as a scenario.

Propagation through drywalls (Route #3 in Fig. 1) at 60 GHz is presented in Fig. 4. At low frequencies waves penetrate drywalls with small losses; as frequency increases, drywall losses will increase as its electrical properties will change. The RMSE for AWM, SSM, LM, PM, MKM and TSM models in dB are 8.61, 15.6, 13.6, 19.14, 9.1, and 10.12 respectively. Wall losses-based

prediction models (MKM and AWM) show good performance while SSM, and PM which use PLEs have poor performance, the same observation was recorded with LM which uses AF. TSM, on the other hand, shows better performance as it uses two PLEs instead of one.

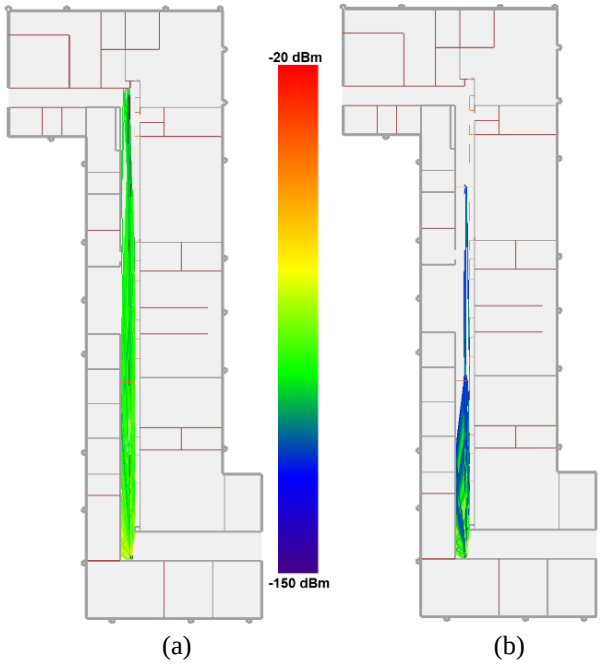

Fig. 3. Propagation paths through a corridor at: (a) 28 GHz, and (b) 73.5 GHz.

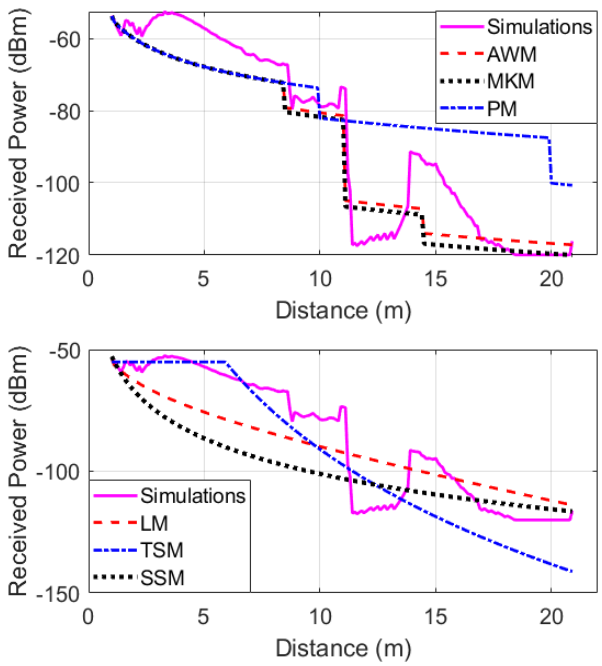

Fig. 4. Propagation through Drywalls at 60 GHz.

Propagation through concrete walls (Route #5 in Fig. 1) at 73.5 GHz is presented in Fig. 5. The average signal loss for a wave propagates through the concrete wall is in the range of (20 - 30) dBm. Unlike wall losses-based model, PLE-based models and LM were unable to represent the sharp changes in RSS level, PM underestimates the losses through concrete walls; since it uses fixed values for PLEs. The RMSE for AWM, SSM, LM, PM, MKM and TSM models in dB are 8.56, 10.44, 17.6, 28, 10.43, and 12.1 respectively.

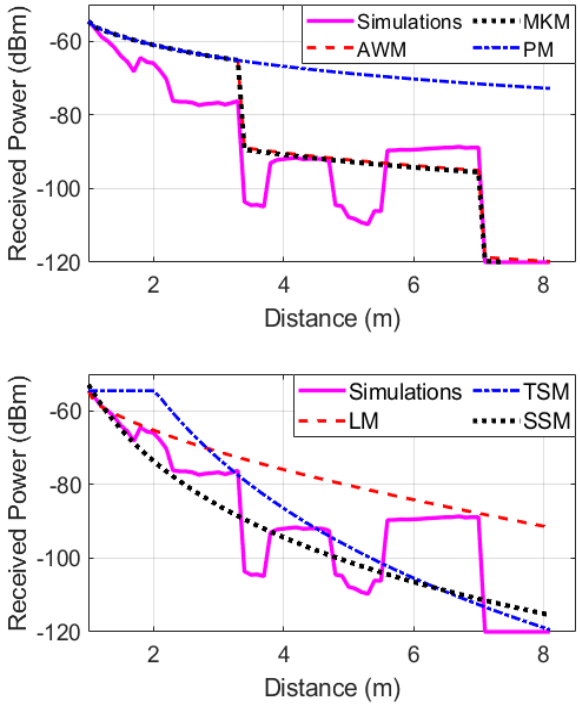

Fig. 5. Propagation through concrete walls at 73.5 GHz.

Figure 6 shows propagation through the corridor in the simulated environment (Route #6 in Fig. 1) at 28 GHz; propagation paths are shown in Fig. 3 (a). The RMSE of the AWM, SSM, LM, PM, MKM and TSM models in dB are 10.05, 4.03, 3.87, 18.04, 10.05, and 2.98 respectively. Waveguiding effect has a great impact on the propagation through corridors, therefore models that have parameters that only counts for losses (like AWM, MKM, and PM) will be insufficient to predict the signal behaviour. On the other hand, models that use the PLEs and AF tend to have better performance as they can predict the signal strength more accurately. TSM model shows the best performance, where (n_1, n_2) found to be 1.56 and 3.41 respectively. LM shows the second-best performance, where $a = 0.3$ adjusts the path loss values to consider the effect of waveguiding propagation. SSM shows third-best performance where γ is found to be 2.88 which can be regarded to the effect of waveguiding.

In this particular scenario, both AWM and MKM performances are not accurate as the models use the simple Friis formula (γ=2) due to the absence of walls. However, propagation in the indoor environment including corridors does not generally follow Friis formula. PM shows the worst result as it does not consider the waveguiding effect.

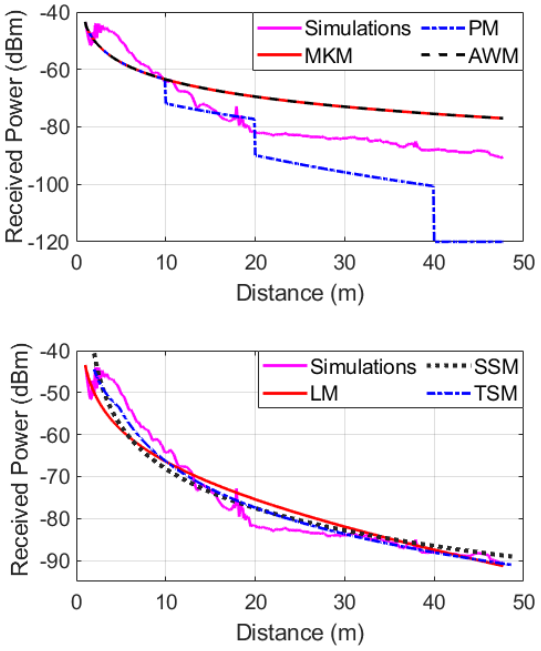

Fig. 6. RSS through the corridor at 28 GHz.

It's observed for high frequencies, that AWM does not provide a significant improvement over MKM; this may be regarded as the fact that AWM uses a similar concept of MKM. However, losses due to walls may be positive (i.e., add gain rather than loss). This may be possible for UHF or WLAN frequencies. At higher frequencies like millimetre wave frequencies, wall penetration losses become higher and it's unlikely to have a stronger signal level even if the wall is thin or made from a material that has very low conductivity. Table 3 shows how wall losses for AWM and MKM are close. As a result, the behaviour is almost the same as seen in Fig. 7, therefore, there is no great distinction between the two models at high frequencies. Metrics comparison for the investigated frequencies are presented in Tables 4, 5, and 6 which show similar performance for the two models.

Table 3: Estimated wall losses for AWM and MKM in dB

Frequency (GHz)	Concrete		Drywall	
	MKM	AWM	MKM	AWM
28	27	27	7	6.82
60	24	23.5	8	8.02
73.5	24	23.5	9	9.23

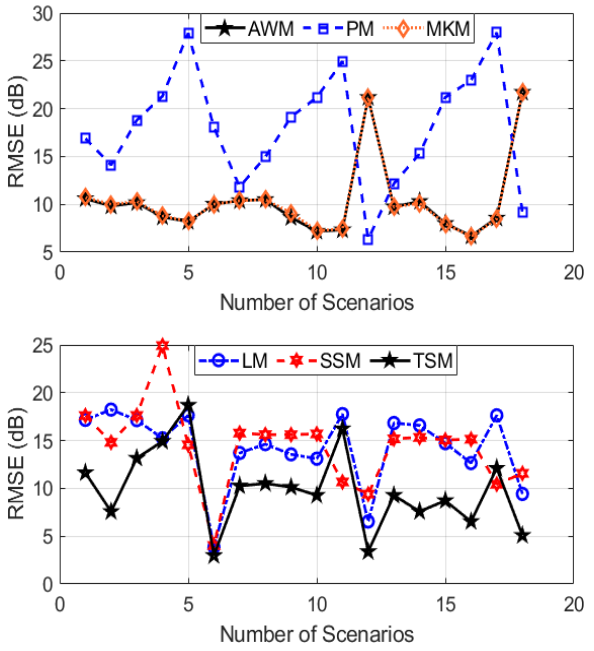

Fig. 7. Performance comparison between all investigated models.

The PM shows poor results as the mean RMSE for all scenarios and frequencies exceeds 20 dB; this is because the model has fixed PLEs which do not necessarily fit any geometry at any frequency. The result is consistent with the metrics presented in Tables 4, 5, and 6 where the PM has the worst performance statistics.

Using two PLEs gives the TSM more flexibility and advantage over SSM as seen in Fig. 7 where TSM outperforms SSM for more than 83% of the tested scenarios. This also is confirmed by metrics statistics. In some scenarios, the dataset used for generating PLEs for TSM may not be adequate, therefore, SSM may have similar or better performance as shown in the figure.

Both LM and SSM have similar performance as shown in Fig. 7, this demonstrates the similarity between α and γ. LM has better results at 28 GHz and at 60 GHz since the performance is more stable as depicted in Tables 4 and 6. At 60 GHz, SSM outperforms the LM and shows more stable performance as shown in Table 5.

Table 4: Metrics statistics for examined models at 28 GHz (in dB)

	Max. RMSE	Min. RMSE	STD	Average RMSE
AWM	10.60	8.2	0.93	9.58
SSM	24.93	4.03	6.79	15.60
LM	18.24	3.87	5.49	14.88
PM	27.90	14.11	4.74	19.51
MKM	10.72	8.20	0.96	9.67
TSM	18.70	3.01	5.55	11.50

Table 5: Metrics statistics for examined models at 60 GHz (in dB)

	Max. RMSE	Min. RMSE	STD	Average RMSE
AWM	21.18	7.18	5.25	10.86
SSM	15.78	9.40	2.94	13.80
LM	17.77	6.54	3.68	13.22
PM	24.97	6.34	6.75	16.40
MKM	21.18	7.28	5.19	10.97
TSM	16.23	3.39	4.08	9.97

Table 6: Metrics statistics for examined models at 73.5 GHz (in dB)

	Max. RMSE	Min. RMSE	STD	Average RMSE
AWM	21.71	6.67	5.48	10.83
SSM	15.31	10.44	2.19	13.79
LM	17.64	9.42	3.13	14.64
PM	27.95	9.17	7.12	18.12
MKM	21.71	6.62	5.51	10.77
TSM	12.11	5.09	2.43	8.22

The averaged estimated values for PLEs and AF parameters are presented in Table 7. As seen in the table, α, γ, and n_2 tend to increase linearly as frequency increases from 60 to 73.5. These increments point to losses increments as frequency increases. Since propagation at 28 GHz covers a larger range, it is expected to have larger values for the investigated metrics. In corridors, γ found to be 2.87, 4.03, and 4.1506 at 28, 60, and 73.5 GHz respectively. While α tends to be 0.3, 0.9, and 1.2 for the same set of frequencies.

Table 7: Averaged estimated parameters for LM, SSM and TSM

Frequency (GHz)	α (dB/m)	γ	n_1	n_2
28	2.38	5.18	0.58	25.88
60	1.62	5	0.4	16.3
73.5	2.34	5.03	1.19	24.52

In Table 8 performance comparison between all models at all frequencies and scenarios is presented, TSM shows the best performance as it has lowest RMSE for 44.44% for all tested scenarios, PM shows the worst performance for all examined frequencies. The descending order of the Models' performance is TSM then AWM/MKM, LM, SSM, and PM.

The propagation area is larger at 28 GHz; therefore, the signal can reach further distances and more walls are included, in this case, both MKM and AWM will have better performance compared to the TSM which will have difficulty to represent this large area with only two PLE's.

Table 8: Overall performance for all models at all frequencies (dB)

Model	Min. RMSE	Max. RMSE	STD	Average RMSE
AWM	6.67	21.71	4.19	10.42
SSM	4.03	24.93	4.27	14.39
LM	3.87	18.24	4.03	14.24
PM	6.34	27.95	6.05	18.00
MKM	6.62	21.71	4.17	10.46
TSM	3.01	18.70	4.19	9.89

V. CONCLUSIONS

A comparative study between different indoor path loss prediction models has been presented, based on models generated using Matlab and compared to Wireless InSite ray-tracing software simulations. It was found that MKM and AWM have similar performance for high frequencies. Also, it was found that both models show good performance for path loss predictions through walls while their predictions for LOS propagation regions and corridors are pessimistic; on the other hand, models based on path loss exponents and attenuation factors show good performance at these regions and have poor performance for path loss predictions through walls. TSM tends to have the best performance while AWM/MKM show the best performance. LM and SSM have close performance and their corresponding parameters tend to increase as frequency increases. For all frequencies, PM had the worst results as it uses fixed values for path loss exponents.

ACKNOWLEDGMENT

This work is partially supported by innovation programme under grant agreement H2020-MSCA-ITN-2016 SECRET-722424 and the financial support from the UK Engineering and Physical Sciences Research Council (EPSRC) under grant EP/E022936/1.

REFERENCES

[1] H. Liu, H. Darabi, P. Banerjee, and J. Liu, "Survey of wireless indoor positioning techniques and systems," *IEEE Transactions on Systems, Man, and Cybernetics, Part C (Applications and Reviews)*, vol. 37, pp. 1067-1080, 2007.

[2] T. A. Levanen, J. Pirskanen, T. Koskela, J. Talvitie, and M. Valkama, "Radio interface evolution towards 5G and enhanced local area communications," *IEEE Access*, vol. 2, pp. 1005-1029, 2014.

[3] N. Moraitis and P. Constantinou, "Indoor channel measurements and characterization at 60 GHz for wireless local area network applications," *IEEE Transactions on Antennas and Propagation*, vol. 52, pp. 3180-3189, 2004.

[4] G. R. Maccartney, T. S. Rappaport, S. Sun, and S. Deng, "Indoor office wideband millimeter-wave

propagation measurements and channel models at 28 and 73 GHz for ultra-dense 5G wireless networks," *IEEE Access*, vol. 3, pp. 2388-2424, 2015.

[5] W. W. S. Methley, S. Walker, and J. Parker, "5G candidate band study, study on the suitability of potential candidate frequency bands above 6GHz for future 5G mobile broadband systems," Mar. 2015.

[6] H. Hashemi, "The indoor radio propagation channel," *Proceedings of the IEEE*, vol. 81, pp. 943-968, 1993.

[7] J. Lloret, J. J. López, C. Turró, and S. Flores, "A fast design model for indoor radio coverage in the 2.4 GHz wireless LAN," in *Wireless Communication Systems, 2004, 1st International Symposium on*, Mauritius, Mauritius, pp. 408-412, 2004.

[8] Q. H. Spencer, B. D. Jeffs, M. A. Jensen, and A. L. Swindlehurst, "Modeling the statistical time and angle of arrival characteristics of an indoor multipath channel," *IEEE Journal on Selected Areas in Communications*, vol. 18, pp. 347-360, 2000.

[9] A. F. Molisch, J. R. Foerster, and M. Pendergrass, "Channel models for ultrawideband personal area networks," *IEEE wireless communications*, vol. 10, pp. 14-21, 2003.

[10] P. Vieira, M. Queluz, and A. Rodrigues, "HSDPA capacity enhancement using MIMO in a pico-cell environment," in *IEEE/ACES International Conference on Wireless Communications and Applied Computational Electromagnetics, 2005*, pp. 630-633, 2005.

[11] E. A. Juanda, T. Hariyadi, A. A. Reguna, and A. B. Pantjawati, "Omnidirectional MIMO antenna with collinear array for LTE applications," *Pertanika Journal of Science & Technology*, vol. 26, 2018.

[12] Q. D. Nguyen, T. T. Le, D. T. Le, X. N. Tran, and Y. Yamada, "A compact MIMO ultra-wide band antenna with low mutual coupling," *Applied Computational Electromagnetics Society Journal*, vol. 31, 2016.

[13] M. Mangoud and Z. Mahdi, "Realistic Spatio-temporal channel model for broadband MIMO WLAN systems employing uniform circular antenna arrays," *ACES Journal-Applied Computational Electromagnetics Society*, vol. 26, p. 394, 2011.

[14] M. A. Mangoud, "Capacity investigations of MIMO systems in correlated rician fading channel using statistical multi-clustered modelling," in *2008 8th International Conference on ITS Telecommunications*, pp. 352-356, 2008.

[15] K. Yu, Y. Li, and X. Liu, "Mutual coupling reduction of a MIMO antenna array using 3-D novel meta-material structures," *Applied Computational Electromagnetics Society Journal*, vol. 33, pp. 758-763, 2018.

[16] S. Luo, Y. Li, Y. Xia, and L. Zhang, "A low mutual coupling antenna array with gain enhancement using metamaterial loading and neutralization line structure," *Applied Computational Electromagnetics Society Journal*, vol. 34, 2019.

[17] T. Jiang, T. Jiao, and Y. Li, "A low mutual coupling MIMO antenna using periodic multi-layered electromagnetic band gap structures," *Applied Computational Electromagnetics Society Journal*, vol. 33, 2018.

[18] A. Foudazi, M. T. Ghasr, and K. M. Donnell, "Mutual coupling in aperture-coupled patch antennas fed by orthogonal SIW line," in *2016 IEEE International Symposium on Antennas and Propagation (APSURSI)*, pp. 1587-1588, 2016.

[19] J. Keenan and A. Motley, "Radio coverage in buildings," *British telecom technology Journal*, vol. 8, pp. 19-24, 1990.

[20] I. T. U. ITU, "Propagation data and prediction methods for the planning of indoor radio-communication systems and radio local area networks in the frequency range 900 MHz to 100 GHz," in *Recommendation ITU-R P.1238-7*, ed. Geneva: ITU, 2012.

[21] G. F. Pedersen, *COST 231-Digital mobile radio towards future generation systems*: European Commission, 1999.

[22] C. Serôdio, L. Coutinho, L. Reigoto, J. Matias, A. Correia, and P. Mestre, "A lightweight indoor localization model based on motley-keenan and cost," in *Proceedings of The World Congress on Engineering 2012, WCE 2012*, London, U.K., pp. 1323-1328, 2012.

[23] M. Lott and I. Forkel, "A multi-wall-and-floor model for indoor radio propagation," in *Vehicular Technology Conference, 2001, VTC 2001 Spring, IEEE VTS 53rd*, Rhodes, Greece, Greece, pp. 464-468, 2001.

[24] C. B. Andrade and R. P. F. Hoefel, "IEEE 802.11 WLANs: A comparison on indoor coverage models," in *Electrical and Computer Engineering (CCECE), 2010 23rd Canadian Conference on*, Calgary, AB, Canada, pp. 1-6, 2010.

[25] N. A. Alsindi, B. Alavi, and K. Pahlavan, "Measurement and modeling of ultrawideband TOA-based ranging in indoor multipath environments," *IEEE Transactions on Vehicular Technology*, vol. 58, pp. 1046-1058, 2009.

[26] R. Davies, A. Simpson, and J. Mcgreehan, "Propagation measurements at 1.7 GHz for microcellular urban communications," *Electronics letters*, vol. 26, pp. 1053-1055, 1990.

[27] A. Technologies, "Wireless LAN at 60 GHz - IEEE

80211ad-explained-agilent-white-paper," 03/ 09/ 2017, 2017.
[28] N. Instruments, (2016, 25/10/2016), *mmWave: The Battle of the Bands*. Available: http://www.ni.com/white-paper/53096/en/, 2016.
[29] R. A. Valenzuela, O. Landron, and D. Jacobs, "Estimating local mean signal strength of indoor multipath propagation," *IEEE transactions on vehicular technology*, vol. 46, pp. 203-212, 1997.
[30] H. Obeidat, A. AlAbdullah, N. Ali, R. Asif, O. Obeidat, M. Bin-Melha, *et al.*, "Local average signal strength estimation for indoor multipath propagation," *IEEE Access*, 2019.
[31] I. T. U. ITU, "Effects of building materials and structures on radiowave propagation above about 100 MHz," in *Recommendation ITU-R P.2040-1*, ed. Geneva: Electronic Publication, 2015.

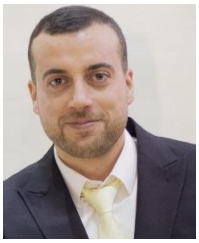

Huthaifa Obeidat is Assistant Professor at Communication and Electronics Department at Jerash University in Jordan, he received the Ph.D. in Electrical Engineering from the University of Bradford, UK, in 2018, he was awarded M.Sc. degree in Personal Mobile and Satellite Communication from the same University in 2013. His research interests include Radiowave Propagation, millimetre wave propagation, e-health applications, Antenna, and Location-Based Services. Obeidat has been a member of the Jordanian Engineering Association since 2011.

Ali Alabdullah received the B.S. and M.S. degrees in Electrical and Electronics Engineering from the University of Technology, Baghdad, Iraq, in 1994 and 1999, respectively. He is currently pursuing the Ph.D. degree in Electrical Engineering with the Faculty of Engineering and Informatics, University of Bradford, Bradford, UK. He was an Instructor and Assistant Lecturer with the University of Technology, Baghdad, Iraq, from 1994 to 2003. From 2006 to 2014, he was an Assistant Lecturer with the Department of Communication Engineering, College of Electronics, University of Nineveh, Mosul, Iraq. His general research interests mainly lie in emerging technologies for 5G Wireless/Mobile Communication System including Adaptive Beamforming Algorithms for wireless networks, Muti-User Massive MIMO, New Modulation and Waveform schemes, Heterogeneous Network, and mmWave Channel Models.

Mahmood Mosleh works at the Department of Computer Engineering Techniques, College of Electrical and Electronic Engineering Techniques, Baghdad, Iraq. Mahmood does research in Communication Engineering. Their current project is 'Combination of LMS and RLS Adaptive Equalizer for Selective Fading Channel.' The next project is in the field of Wireless Sensor Networks, design and implementation. He was awarded a degree of the professorship in the field of Communications Engineering after publishing several researches in such field.

Atta Ullah received his B.Sc. and M.Sc. degrees in Electronics Engineering from University of Peshawar, Pakistan in 1999 and 2002 respectively and after this, he received M.Sc. in Communication Engineering from the University of York, the UK in 2008. He has worked as Electronics Design Engineer in Creative Electronics in Pakistan and worked as Lecturer at University of Hail, Saudi Arabia. Now he is currently working toward his Ph.D. degree within the Radio Frequency and sensor design research group. His research interests include Simulation, design and implementation of front-end antenna systems for millimetre wave communications.

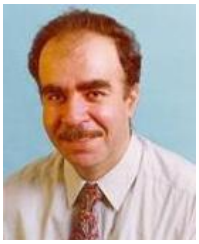

Raed Abd-Alhameed (M'02SM'13) is currently a Professor of Electromagnetic and Radiofrequency Engineering with the University of Bradford, U.K. He is also the Leader of Radiofrequency, Propagation, Sensor Design, and Signal Processing; in addition to leading the Communications Research Group for years within the School of Engineering and Informatics, University of Bradford. He has long years' research experience in the areas of radio frequency, signal processing, propagations, antennas, and electromagnetic computational techniques. He has published over 600 academic journal and conference papers; in addition, he has co-authored four books and several book chapters. He is a principal investigator for several funded applications to EPSRCs and the leader of several successful knowledge Transfer Programmes, such as with Arris (previously known as Pace plc), Yorkshire Water plc, Harvard Engineering plc, IETG Ltd., Seven Technologies Group, Emkay Ltd., and TwoWorld Ltd. He was a recipient of the Business Innovation Award for his successful KTP with Pace and Datong companies on the design and implementation of

MIMO sensor systems and antenna array design for service localizations. He is the chair of several successful workshops on energy-efficient and reconfigurable transceivers: Approach toward Energy Conservation and CO2 Reduction that addresses the biggest challenges for the future wireless systems. He has been a Guest Editor of IET Science, Measurements and Technology Journal since 2009. His interest in computational methods and optimizations, wireless and mobile communications, sensor design, EMC, beam steering antennas, energy-efficient PAs, and RF predistorter design applications. He is a fellow of the Institution of Engineering and Technology and a fellow of the Higher Education Academy and a Chartered Engineer.

Omar Obeidat received his B.Sc. degree in Electrical Engineering from Jordan University of Science and Technology 2006, in 2009 he was awarded M.Sc. degree in Wireless Communication Engineering from Al-Yarmouk University. He is a Ph.D. Candidate at Wayne State University. His research interests include Non-destructive evaluation, thermal imaging, and indoor localization services.

Near-Field Scattering of Typical Targets Illuminated by Vortex Electromagnetic Waves

Hai-tao Chen [1], Ze-qi Zhang [1], and Jie Yu [2]

[1] Department of Antenna Research
Wuhan Maritime Communication Research Institute, Wuhan, 430079, China
hbcht@163.com, zhangzq0812@163.com

[2]Department of Science and Technology
Wuhan Maritime Communication Research Institute, Wuhan, 430079, China
43704378@qq.com

Abstract ─ Based on the full-wave electromagnetic simulation and the principle of near-field diagnostics, the near-field scattering characteristics of typical scatterers illuminated by vortex electromagnetic waves are studied. It's shown from the simulation data that the ability of identification of scatterer characteristics by vortex electromagnetic wave is higher. In addition to the amplitude and phase patterns, the orbital angular momentum (OAM) modal spectrum patterns of the scattering field also carry the information of the geometric shape and material characteristics. The application of OAM modal spectrum patterns will help to improve the ability of information acquisition and target detection of electromagnetic wave.

Index Terms─ Near-field scattering, OAM modal spectrum, vortex electromagnetic wave.

I. INTRODUCTION

Electromagnetic theory shows that electromagnetic (EM) wave can carry not only linear momentum, but also angular momentum. Angular momentum can be divided into spin angular momentum (SAM) and orbital angular momentum (OAM). SAM corresponds to the polarization of EM wave, and OAM depends on the phase structure of EM wave front, which describes the transverse vortex modes of helical beam. Vortex EM wave is a kind of wave with non-zero mode OAM. There is $\exp(jl\varphi)$ phase factor in the field expression of the vortex EM wave, in which φ is the azimuth angle around the propagation direction, and l is the OAM mode number, also known as the topological charge. Theoretically, there are infinite OAM modes for the vortex EM wave. These OAM modes are orthogonal and completeness, constituting an infinite dimension linear space, which is called as OAM modal spectrum domain. Using OAM modal spectrum characteristics to enhance the information transmission, acquisition and target detection has become a very attractive research direction in the field of microwave communication, radar detection and target recognition [1-3].

Scattering characteristics of vortex EM waves are of great scientific significance in both information transmission and information acquisition. For information transmission, due to the influence of space environment, complex effects such as dispersion loss, reflection, refraction, fading and multipath will occur during the propagation of vortex EM wave, which leads to the distortion of vortices and the coupling between OAM modes. The interaction between the vortex EM wave and various obstacles in the propagation process can be attributed to the scattering effect. For information acquisition, the study of electromagnetic scattering characteristics is the basis of radar detection and recognition.

Because of the potential of vortex EM waves in radar imaging, recently some research groups have published research work on radar imaging technology based on the OAM characteristics, trying to improve the resolution of radar imaging [4-6]. In present research of radar imaging technology based on vortex EM wave, the targets are always simplified as the combination of ideal scattering points, ignoring the phase gradient of the incident wave illuminating on the target. Recent advances have shown that the response of complex targets and ideal scattering points to vortex EM wave is quite different, which is reflected not only in the spatial pattern of scattering field, but also in the OAM modal spectral domain. Zhang et al. published an experimental study on RCS diversity effects of vortex EM wave irradiation on complex targets [7]. The results show that for simple targets, such as metal spheres, the same RCS fluctuation characteristics can be obtained under different modes of vortex EM wave irradiation, but for a slightly complex target such as bi-metallic sphere combination, even if the incident angle is the same, different modes of vortex

Submitted On: October 22, 2019
Accepted On: December 28, 2019

EM wave can also obtain different RCS. Tang et al. published the results of scattering characteristics of chaff clouds on vortex EM wave [8]. The results show that for a single small dipole, the scattering is not different from that of the plane wave, but for a cloud composed of a large number of dipoles, the scattered wave has a unique distribution in the OAM modal spectrum domain.

The OAM modal characteristics of vortex EM wave mainly exist in the near field region. With the increase of propagation distance, the OAM modal characteristics will gradually degenerate. Therefore, it is more practical to study the near-field scattering of the vortex EM wave, which may play an important role in target detection and recognition.

Based on the commercial EM simulation software FEKO and the principle of near-field diagnostics, the near-field scattering characteristics of typical scatterers illuminated by vortex EM wave are studied in this paper. The full-wave simulation near-field diagnostics are adopted to extract the scattered near-field in Section II, in which the OAM modal analysis is also presented. Some simulation results are shown in Section III, and Section IV is the conclusion.

II. EXTRACTION OF SCATTERED NEAR-FIELD AND OAM MODAL ANALYSIS

Nayeri, Elsherbeni and Yang proposed a near-field diagnostic method based on full-wave electromagnetic simulation software FEKO for reflect-array antenna analysis [9]. Based on this method, the scattered near-field of target illuminated by vortex EM wave is extracted. The process is as follows:

a) Establish the model of the vortex EM wave transmitting antenna in FEKO. In this paper, the circular phased dipole array is used as the transmitting antenna. The radiation field of the transmitting antenna on the scattering field sampling plane is simulated and recorded as the incident field $\mathbf{E}_{\mathrm{i}}$.

b) Establish the model of the transmitting antenna and scatterer in FEKO. The field intensity on the scattering field sampling plane is simulated and recorded as the total field $\mathbf{E}_{\mathrm{t}}$.

c) Read the incident field and total field data by a Matlab code, and subtract the incident field from the total field, then get the scattering field $\mathbf{E}_{\mathrm{s}}$:

$$\vec{E}_s = \vec{E}_t - \vec{E}_i \,. \tag{1}$$

The phase gradient method has been proposed to detection the OAM mode, in which the signal phases received by two antennas are compared [10]. However, the scattered near-field by complex object illuminated by OAM wave has disorderly phase distribution. The calculated OAM mode spectrum will be depended on the position of the receiving antennas. In order to achieve a comprehensive spectrum analysis of the scattered near field, an aperture integral approach is proposed in this paper based on the orthogonality of the OAM mode. Assuming an imaginary receiving antenna with aperture S is set to receive the scattering field, the received OAM modal spectrum can be calculated as the following formula:

$$P(l) = \frac{1}{A_s}\int_S E_s(x,y)e^{-jl\varphi}dxdy \,, \tag{2}$$

where l is the OAM mode number, S is the receiving antenna aperture, defined as a circular area of radius [0, R] and angle [0, 2π], A_s is area of the receiving aperture. φ is the phase angle of the complex number $x+jy$. The scattering field data obtained by FEKO software is sampled on rectangular grid, so the OAM modal spectrum can be expressed as a summation form:

$$P(l) = \frac{1}{N_s}\sum_{(m,n)\in S} E_s(m,n)e^{-jl\varphi_{mn}} \,, \tag{3}$$

where N_{S} is the number of sampling points falling into the receiving aperture range.

A slotted conductor plate which had been simulated and measured in Ref. [11] is used in this paper as an illustration to check the near-field diagnostic process based on FEKO simulation.

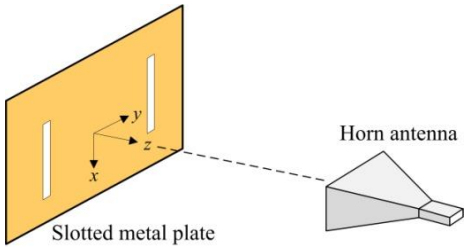

Fig. 1. Illustration example for determining the surface scattered magnetic field on a slotted metal plate illuminated by a horn antenna.

The checking illustration is shown in Fig. 1, in which a metal plate containing two slots is illuminated by a horn antenna. According to Ref. [11], the size of the plate is 30.5cm×30.5cm×0.31cm, and the two slots are 20cm×3.8cm and located symmetrically about the plate center with a distance 11.1cm. The distance between the slotted plate and the horn antenna is 107cm. The incident electromagnetic wave is x-polarization and the frequency is 2GHz.

The near-field diagnostics process is used to extract the scattering magnetic field on a sampling plane which is at the distance 1.27cm from the slotted plate. In order to compare it with the measured data, the "back-propagation approach" [11] is adopted to transform the magnetic field on the sampling plane to on the slotted plate. The normalized scattered magnetic field is shown in Fig. 2, which is in good agreement with the measured data presented in Ref. [11].

In order to check the OAM spectrum analysis method, the spectrum of a vortex EM wave with noninteger OAM state is examined by the aperture integral approach and the Fourier series method [10, 12] respectively. The mode number of the incident wave is set to 0.5. The radius of the receiving aperture is $2\lambda_0$ and the sample spacing is $0.1\lambda_0$. The spectrum patterns of the two methods are accordant, as shown in Fig. 3.

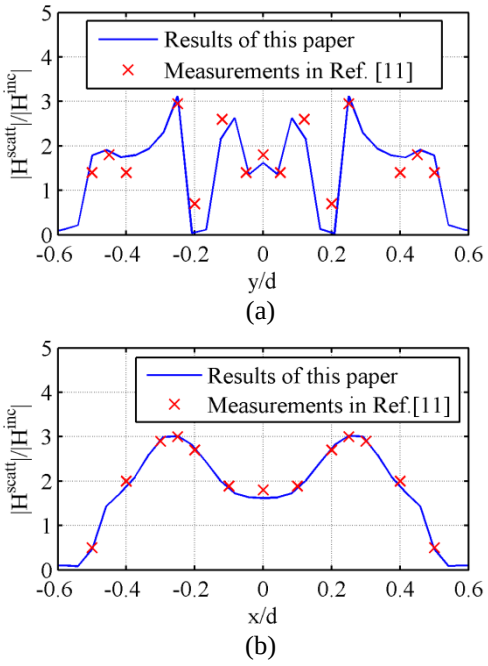

Fig. 2. Normalized scattered magnetic field on the slotted plate. Incident electric field is parallel to the slots. (a) Cross section of the magnetic field in the *y*-direction, and (b) *x*-direction are shown.

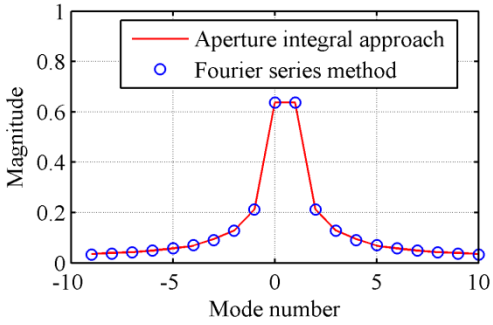

Fig. 3. OAM spectrum of the vortex EM wave with OAM mode l=0.5.

III. SIMULATION EXAMPLES

A. Scattering of PEC plates

The circular four-element phased array is used as the vortex EM wave transmitting antenna. The radius of the array is $1\lambda_0$ and the radiated electric field is *x*-polarized. As shown in Fig. 4, a $10\lambda_0 \times 10\lambda_0$ rectangular PEC plate is symmetrically placed on the propagation axis of the transmitting beam, $30\lambda_0$ away from the transmitting array. Based on the simulation results of FEKO software, the scattering field is extracted by using the near-field diagnostics method. The scattering field sampling plane is $10\lambda_0$ away from the plate. Figure 5 shows the amplitude and phase pattern of the *x*-polarization scattering field and the OAM modal spectrum. When calculating the OAM modal spectrum, the receiving aperture is a circle with radius of $1\lambda_0$. Figure 5 (a) shows the magnitude of the scattering field, from which the edge of the plate can be roughly seen. The phase pattern shows that the scattering field of the conducting plate is still a vortex EM wave with first order OAM. Figure 5 (c) shows the mode spectrum of the scattering field, which confirms that the first order mode is still dominant.

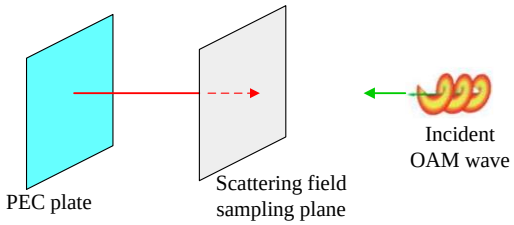

Fig. 4. Scattering of the OAM waves by a PEC plate.

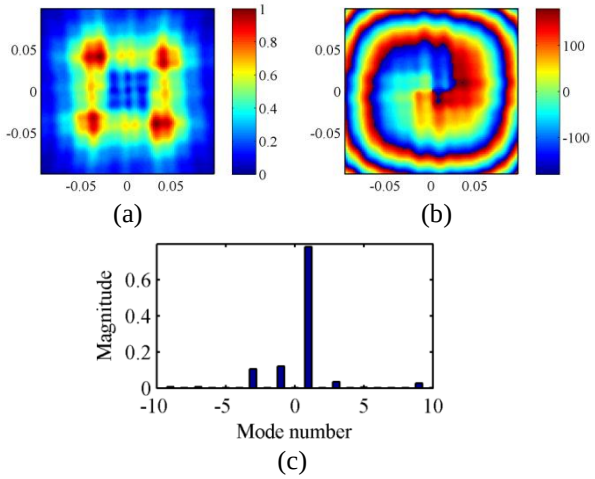

Fig. 5. Backscattering field of the PEC plate illuminated by the OAM wave with l=1. (a) Amplitude, (b) phase, (c) modal spectrum. The plate is placed symmetrically perpendicular to the axis of the OAM wave, $30\lambda_0$ from the transmitting antenna array, $10\lambda_0$ from the scattering field sampling plane.

If the transmitting antenna is fed in-phase, the OAM modulus of the transmitting beam is turn to zero. Figure 6 shows the amplitude, phase and mode spectrum patterns

of the scattering field. Compared with Fig. 5, it can be seen that the vortex EM wave with OAM mode number l=1 has better identification ability for the edges and corners of the plate. Note that the mode spectrum magnitude in Fig. 5 (c) is much smaller than that in Fig. 6 (c). It can be attributed to the amplitude nulls in the beam direction for OAM wave.

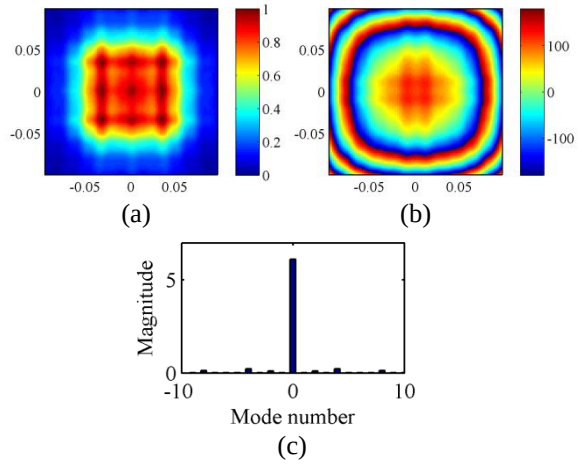

Fig. 6. Backscattering field of the PEC plate illuminated by the OAM wave with l=0. (a) Amplitude, (b) phase, and (c) modal spectrum. The plate is placed symmetrically perpendicular to the axis of the OAM wave, $30\lambda_0$ from the transmitting antenna array, $10\lambda_0$ from the scattering field sampling plane.

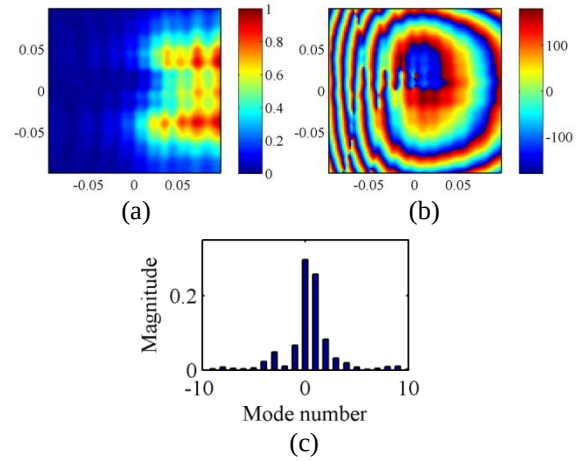

Fig. 7. Backscattering field of the PEC plate illuminated by the OAM wave with l=1. (a) Amplitude, (b) phase, and (c) modal spectrum. The plate is placed perpendicular to the axis of the OAM wave and deviates from the axis by $5\lambda_0$, $30\lambda_0$ from the transmitting antenna array, $10\lambda_0$ from the scattering field sampling plane.

It can be seen from Fig. 5 that the scattering field of the PEC plate arranged axially symmetrically along the vortex EM wave propagating axis maintains the OAM mode spectrum of the incident wave well. Now the plate is shifted $5\lambda_0$ perpendicular to the axis of the OAM wave. Then the vortex EM wave illuminating on the plate will no longer have a complete phase gradient distribution. It can be predicted that the scattering field will no longer have a simple first-order OAM mode. The simulation data shown in Fig. 7 verifies it. It can be seen that besides the first-order OAM, the 0-order OAM component in the scattering field is also stronger.

B. Scattering of cones

The scattering of OAM waves by a conducting cone is investigated, as shown in Fig. 8. The diameter of the conical surface is $10\lambda_0$ and the height is also $10\lambda_0$. The conical axis coincides with the propagation axis of the vortex EM wave. The top of the cone points to the transmitting antenna at a distance of $30\lambda_0$. The sampling plane of the scattering field is $10\lambda_0$ from the top of the cone.

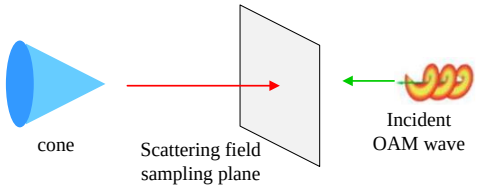

Fig. 8. Scattering of the OAM waves by a cone.

Similarly, a four-element circular phased array is used as the vortex EM wave transmitting antenna. The amplitude and phase patterns of the scattering field on the sampling plane are shown in Fig. 9. From the phase pattern, it can be seen that in a small area around the center, the scattering field still has good first-order OAM characteristics, but in other areas, the spiral phase distribution has not been seen. Figure 10 shows the OAM modal spectrum obtained from different receiving apertures. It can be seen that when the receiving aperture exceeds the radius of the bottom of the cone, the high-order OAM mode will increase significantly.

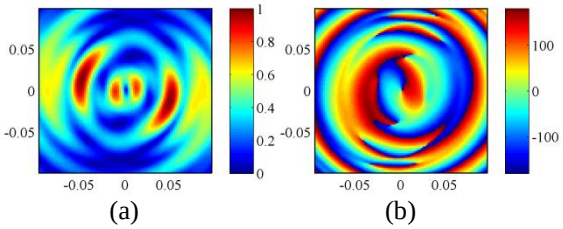

Fig. 9. Backscattering field of PEC cone illuminated by the OAM wave with l=1. (a) Amplitude and (b) phase.

Replaced the PEC cone by a dielectric cone with same size and the dielectric constant is ε_r=4.0. Figure 11 shows the scattering field on the sampling plane when the incident wave is first-order OAM and 0-order OAM,

respectively. The receiving aperture is a circle with radius of $2\lambda_0$. It can be found that the vortex EM wave has higher recognition ability for conical vertices. Besides the amplitude and phase, the OAM modal spectrum pattern also reflects the characteristic information of scatterers. Compared with the PEC conical scattering, the bottom edge diffraction effect of the dielectric cone is obviously weakened, and the parasitic OAM mode l=-1 is enhanced.

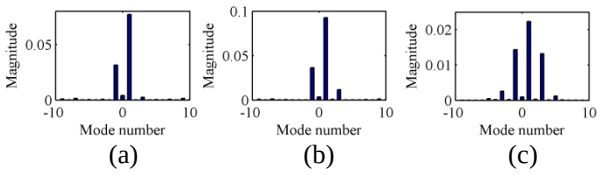

Fig. 10. OAM modal spectrum patterns of the scattering field of the PEC cone illuminated by OAM wave with l=1. Receiving aperture radius: (a) $R=\lambda_0$; (b) $R=2\lambda_0$; (c) $R=5\lambda_0$.

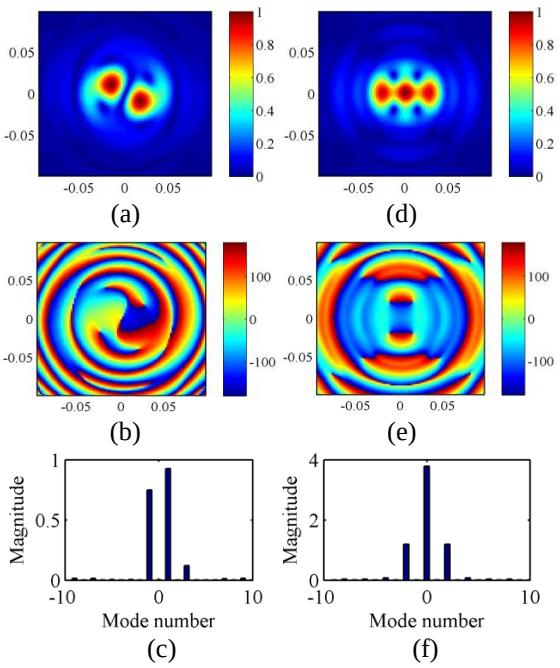

Fig. 11. Scattering field of the dielectric cone illuminated by OAM wave. (a) Amplitude, (b) phase, and (c) modal spectrum for the incident wave with OAM mode l=1. (d) Amplitude, (e) phase, and (f) modal spectrum for the incident wave with OAM mode l=0.

C. Scattering of two metal spheres

A case of scattering of vortex EM wave from multi-targets is investigated. As shown in Fig. 12, two metal spheres with radius $2.5\lambda_0$ and distance $10\lambda_0$ are symmetrically placed on the propagation axis of the transmitting beam, $30\lambda_0$ away from the transmitting array. The spheres are illuminated by a twelve-element circular phased array. The radius of the array is $1.5\lambda_0$. The OAM mode of the transmitting is set to 0, 1, 2 and 3 respectively. The amplitude, phase and OAM modal spectrum pattern of the scattering field are shown in Fig. 13, in which the receiving aperture is a circle with radius of $5\lambda_0$. The sampling plane of the scattering field is $10\lambda_0$ away from the center of the spheres.

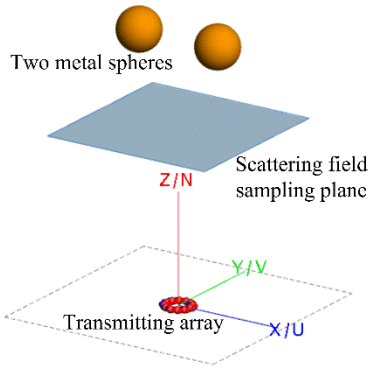

Fig. 12. Two metal spheres illuminated by OAM circular phased array.

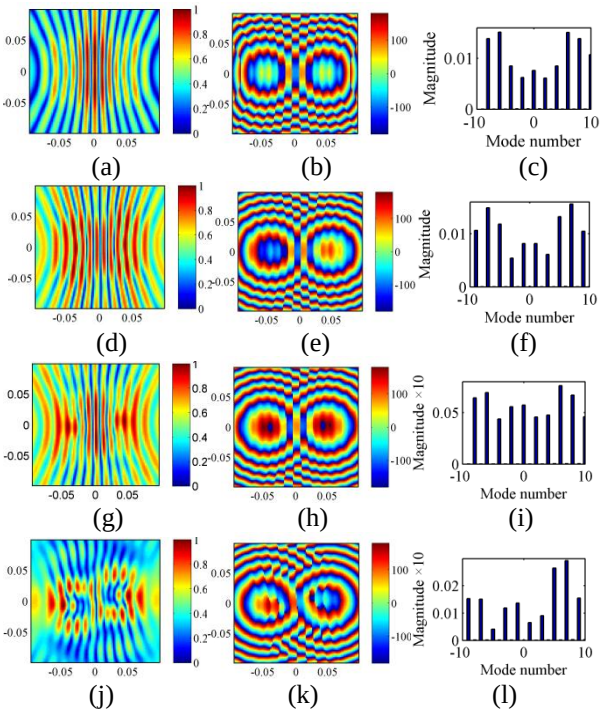

Fig. 13. Near scattering field by two spheres illuminated by OAM wave with different mode. (a) Amplitude, (b) phase, and (c) modal spectrum for the incident wave with OAM mode l=0. (d) Amplitude, (e) phase, and (f) modal spectrum for the incident wave with OAM mode l=1. (g) Amplitude, (h) phase, and (i) modal spectrum for the incident wave with OAM mode l=2. (j) Amplitude, (k) phase, and (l) modal spectrum for the incident wave with OAM mode l=3.

The interference fringes can be clearly observed from the simulated results. It is caused by the interference of two metal spheres scattering field. The position of two metal spheres can be clearly judged from the phase pattern of the scattering field. Since the target no longer has axisymmetric properties, there are many higher order modes in the OAM spectral domain of the scattering field. It can be found that when the mode of incident wave OAM is l=0 and l=2, the mode spectrum of scattering field OAM is similar, which can be explained as the incident wave of mode l=0 and l=2 has the same phase on the centers of the two spheres.

IV. CONCLUSION

It is demonstrated that the scattering field of different targets illuminated by OAM wave does not only show the spatial distribution of amplitude and phase, but also exhibit unique distribution characteristics in the OAM modal spectrum domain. Through the interaction between the vortex EM wave and the target, more target information can be obtained from the echo signal, which provides a new technical way for target detection and recognition.

REFERENCES

[1] L. Allen, M. W. Beijersbergen, R. J. C. Spreeuw, and J. P. Woerdman. "Orbital angular momentum of light and the transformation of laguerre-gaussian laser modes," *Phys. Rev. A*, 45, 8185, 1992.

[2] B. Thide, et al., "Utilization of photon orbital angular momentum in the low-frequency radio domain," *Phys. Rev. Lett*., 99, 087701, 2007.

[3] F. Tamburini, et al., "Encoding many channels on the same frequency through radio vorticity: First experimental test," *New J. Phys*., 14, 033001, 2012.

[4] K. Liu, Y. Cheng, Z. Yang, H. Wang, Y. Qin, and X. Li, "Orbital-angularmomentum-based electro-magnetic vortex imaging," *IEEE Antennas Wireless Propag. Lett*., vol. 14, pp. 711-714, 2015.

[5] B. Tang, K.-Y. Guo, J.-P. Wang, et al., "Orbital-angular-momentum-based imaging radar," *IEEE Antennas and Wireless Propagation Letters*, vol. 16, pp. 2975-2978, 2017.

[6] X. Bu, Z. Zhang, L. Chen, et al., "Implementation of vortex electromagnetic waves high-resolution synthetic aperture radar imaging," *IEEE Antennas And Wireless Propagation Letters*, vol. 17, no. 5, pp. 764-767, 2018.

[7] C. Zhang, D. Chen, and X. Jiang, "RCS diversity of electromagnetic wave carrying orbital angular momentum," *Scientific Reports*, 7: 15412 doi:10. 1038/s41598-017-15250-7, 2017.

[8] B. Tang, J. Bai, and X.-Q. Sheng, "Orbital angular momentum carray wave scattering by the chaff clouds," *IET Radar, Sonar and Navigation*, vol. 12, no. 6, pp. 649-653, 2018.

[9] P. Nayeri, A. Z. Elsherbeni, and F. Yang, "Design, full-wave analysis, and near-field diagnostics of reflectarray antennas," *ACES Journal*, vol. 28, no. 4, pp. 284-292, Apr. 2013.

[10] K. Liu, H. Liu, Y. Qin, et al., "Generation of OAM beams using phased array in the microwave band," *IEEE Trans. Antennas Propagat*., vol. 64, no. 9, pp. 3850-3857.

[11] P. H. Harms, J. G. Maloney, M. P. Kesler, E. J. Kuster, and G. S. Smith, "A system for unobtrusive measurement of surface currents," *IEEE Trans. Antennas Propagat*., vol. 49, pp. 174-184, Feb. 2001.

[12] F. Tamburini, E. Mari, B. Thidé, C. Barbieri, and F. Romanato, "Experimental verification of photon angular momentum and vorticity with radio techniques," *Appl. Phys. Lett*., vol. 99, no. 20, p. 204102, 2011.

A New Method for Stranded Cable Crosstalk Estimation Based on BAS-BP Neural Network Algorithm Combined with FDTD Method

Q. Q. Liu, Y. Zhao, C. Huang, W. Yan, and J. M. Zhou

Department of Electrical and Automation Engineering
Nanjing Normal University, Nanjing, 210046, China
1376684687@qq.com, zhaoyang2@njnu.edu.cn, 1547796467@qq.com, 61197@njnu.edu.cn, 386439740@qq.com

Abstract ─ In this paper, based on the research of back propagation (BP) neural network algorithm optimized by the beetle antennae search (BAS) algorithm, a new method for predicting stranded cable crosstalk is proposed. Firstly, the stranded wire model and the equivalent multiconductor transmission lines model are both established. Then, the extraction network of the stranded wire electromagnetic parameter matrix is constructed by using the BAS-BP neural network algorithm. Finally, the network is combined with the finite difference time domain (FDTD) method to solve the near end crosstalk (NEXT) and far end crosstalk (FEXT) of a specific three-core stranded model. The new method has good agreement with the crosstalk results obtained by the electromagnetic field numerical method. The validity of the new method is verified.

Index Terms ─ Back propagation (BP) neural network algorithm, Beetle antennae search (BAS) algorithm, Finite difference time domain (FDTD) method, Multiconductor transmission lines (MTL), Stranded cable crosstalk.

I. INTRODUCTION

In the 1960s, scholars began to study the internal crosstalk of twisted pair [1]. Some scholars also studied the electromagnetic characteristics of the stranded wire in the field coupling [2-3], but the research on the internal crosstalk of multi-core stranded wire is still less. The stranded wire is realized by the equal-angle rotation of the twisted single-wire winding bobbin and the uniform forward movement of the stranded wire, which has strong anti-interference ability [4]. It is suitable for high working frequency.

Generally, the stranded wire crosstalk can be analyzed by referring to the research method of the non-uniform transmission line [5-6]. In the cascade idea proposed by Professor C. R. Paul, the cascading uniform transmission line is equivalent to a non-uniform transmission line and the per unit length (p.u.l.) RLCG electromagnetic parameter matrix can describe the transmission equation of each uniform transmission line [7-10]. The FDTD algorithm has good advantage in solving the crosstalk of non-uniform transmission lines, which is based on the cascaded transmission line theory (TLT) [11]. The most critical step in solving crosstalk by using FDTD algorithm is to extract the RLCG parameters of the transmission line. In [12], the domain decomposition method (DDM) is used to calculate the capacitance and inductance matrix of an arbitrary cross-section multiconductor transmission line (MTL). In [13], the integral equation (IE) method is used to extract the resistance parameters of random rough surface wires. In [14], the finite element method (FEM) is used to solve the problem of electromagnetic parameter extraction. In [15], the parameter matrix of the random unit length of a circular conductor is analyzed by using the polynomial chaotic coefficient. However, there is no good way to extract the electromagnetic parameters of multi-core strands.

In fact, the electromagnetic parameter matrix of the strand changes as the stranded cable changes along the extension axis. Also, the strand wire can be viewed as a multiconductor transmission line with a continuously rotating cross section at the angle of the extension axis. In order to visualize the influence of this continuous variation on the RLCG electromagnetic parameter matrix of the stranded wire, BP neural network with strong nonlinear mapping ability was introduced in our previous research to extract the RLCG electromagnetic parameter matrix at any position of the strand [16-18]. However, from a mathematical point of view, the conventional BP neural network is a local search method, which solves a complex nonlinear problem. In addition, BP neural network is very sensitive to initial network weights, and initialize network with different weights, which tend to converge to different local minimums. It is the reason why scholars get different results each time they training [19-20]. Aiming at the defect of BP neural network, this paper finally proposes an algorithm model of the BAS algorithm optimization BP neural network (BPNN). The BAS algorithm searches by the individual beetle, which has higher precision and efficiency [21]. Finally, in the solution analysis part of the crosstalk, this paper combines the stranded wire electromagnetic

Submitted On: October 17, 2019
Accepted On: December 15, 2019

parameter matrix extraction network with the FDTD algorithm to estimate the NEXT and FEXT of a specific three-core stranded wire.

Based on the BAS-BP algorithm, this paper proposes a new approach for the electromagnetic parameter extraction of the stranded wire. Then using the FDTD algorithm to calculate the NEXT and FEXT of the stranded wire. Section II defines the model of the stranded wire and the sample extraction model of the stranded electromagnetic parameters. Section III deals with the specific implementation flow of the BAS-BP neural network algorithm combined with the FDTD method. Section IV provides the analysis of a specific three-core stranded wire model by using the BAS-BP algorithm combined with the FDTD method and the verification of the crosstalk simulation. Section V summarizes this paper.

II. STRANDED WIRE MODELING

A. Establishment of the stranded wire model

For the convenience of research, only the stranded wire with the same cross-sectional shape is considered. In this paper, the stranded wire is modeled on the basis of a single spiral [22]. Figure 1 is the single spiral model. (1) and (2) are mathematical formulas for the single spiral:

$$\begin{cases} x = R_1 \sin(\alpha l) \\ y = R_1 \cos(\alpha l) \\ z = \alpha p l / 2\pi \end{cases}, \tag{1}$$

$$\alpha = \sqrt{(R_1^2) + (p / 2\pi)^2}\,. \tag{2}$$

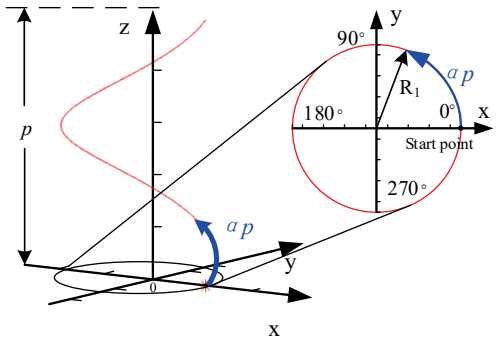

Fig. 1. Single spiral model.

Where R_1 is the radius of rotation, α is the twist factor, p is the pitch, αp is the angle of rotation, and l is the line length. In fact, the n-core strand is composed of n single wires, but the starting positions of different single wires are different. In this paper, any cross section that is consistent with the initial cross-sectional shape of the n-core strand is defined as the transposition of the n-core strand, and the adjacent transpositions are phase-shifted by $2\pi/n$. The position of the transposition corresponds to the position of the stranded line is kp/n, and the corresponding degree of radial rotation is $2k\pi/n$, where k=1, 2...n. Taking the three-core stranded wire as an example, the degree of rotation of the cross section of the transposition is $2\pi/3$, $4\pi/3$, 2π, as shown in Fig. 2.

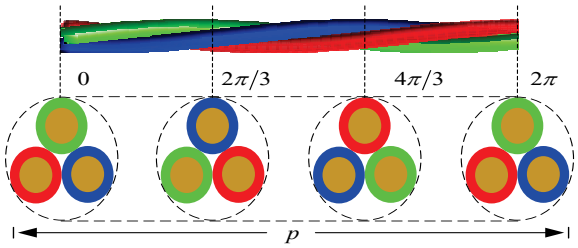

Fig. 2. Three-core stranded wire model.

B. RLCG parameter sample matrix extraction model

Stranded wires in engineering application typically contain separate insulating layers, which may also contain shielding layers. The finite element method (FEM) is able to accurately and quickly solve the p.u.l. RLCG parameter matrix of a uniform transmission line of arbitrary cross section. AnsysQ3D is a circuit parasitic parameter extraction software based on the FEM algorithm, but it cannot directly extract the RLCG parameter matrix at any position of the strand.

From the cross-section, the cross-sectional shape of the strand at any position is the same. There is only a change in the relative position between the strand and the ground. From the axial extension point of view, the stranded wire can be regarded as a multiconductor transmission line which is formed by cascading an infinite number of infinitely small cross section conductors which are continuously rotated in the axial direction. Therefore, the relative position between the strand and the ground can be converted into a corresponding rotation angle, that is, one pitch of the strand corresponds to a 360° rotation angle, and the phase difference between the adjacent two pitches is 360°. So the corresponding angle of the distance from the pitch initial end at d is $\frac{d}{p} * 2\pi$.

Any position of the stranded wire corresponds to its own RLCG parameter matrix and the corresponding rotation angle. For the unique property of the stranded wire, the p.u.l. RLCG parameter matrix of the multi-core uniform transmission line with different rotation angles can be extracted by the above simulation software. Then the sample parameter matrix required for the BAS-BP neural network and its corresponding angle matrix as the network input can be obtained.

Equation (3) is the electromagnetic parameter matrix of the n-conductor transmission line:

$$X = \begin{bmatrix} x_{11} & x_{12} & ... & x_{1n} \\ x_{21} & x_{22} & ... & x_{2n} \\ .. & .. & ... & .. \\ x_{n1} & x_{n2} & ... & x_{nn} \end{bmatrix}. \quad (3)$$

Where X represents the RLCG parameter matrix and x represents the specific value of the electromagnetic parameter. When the loss is not considered, the RLCG electromagnetic parameter matrix of the transmission line is a symmetric matrix, $x_{ji} = x_{ij}$. Therefore, it is only necessary to take the main diagonal element number and the upper triangular element of the matrix as the research object, as shown in the formula (4), (5):

$$\dot{R} = [r_{11}, r_{12}, r_{22}, ..., r_{nn}], \dot{L} = [l_{11}, l_{12}, l_{22}, ..., l_{nn}], \quad (4)$$

$$\dot{C} = [c_{11}, c_{12}, c_{22}, ..., c_{nn}], \dot{G} = [g_{11}, g_{12}, g_{22}, ..., g_{nn}]. \quad (5)$$

Replace $\dot{R}$, $\dot{L}$, $\dot{C}$ and $\dot{G}$ with the column vector y:

$$y = \left[\dot{R}, \dot{L}, \dot{C}, \dot{G}\right]^T = [y_1, y_2, ..., y_m]^T. \quad (6)$$

Where y represents the value of the sample element of the RLCG parameter matrix, the total number of elements in y is m, $m = 2n(1+n)$, n is the number of core. Figure 3 shows the RLCG parameter data processing procedure.

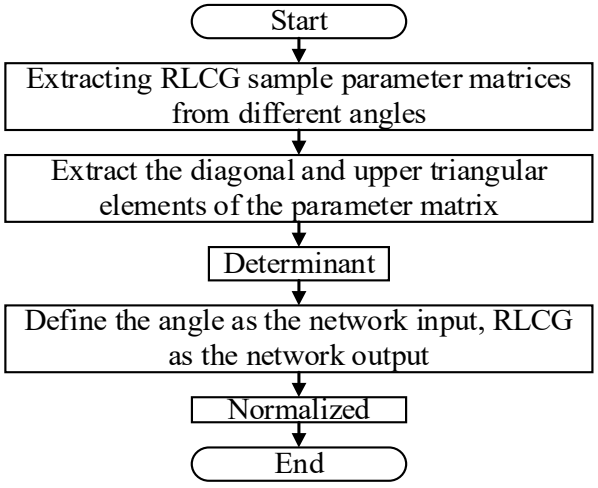

Fig. 3. Data pre-processing flow chart.

III. BAS-BP ALGORITHM COMBINED WITH FDTD ALGORITHM PREDICTING CROSSTALK

A. BP neural network algorithm

The BP network is mainly composed of signal forward propagation and error back propagation. Forward propagation is the process, by which the signal is input by the input layer and processed by the output layer after being processed by the hidden layer neurons. If the error between the predicted value and the true value does not meet the accuracy requirements set by the network, it will turn to the back propagation phase of the error. Error backpropagation is to pass the obtained error back to the input layer through the hidden layer. In this process, the error is distributed to each neuron and the weight and threshold are adjusted along the direction, in which the error function decreases the fastest. This process continues to cycle until the error in the training network output meets the accuracy requirements or the number of iterations is reached.

By analyzing the number of input and output elements, a small and medium-sized BP neural network with only one hidden layer is selected.

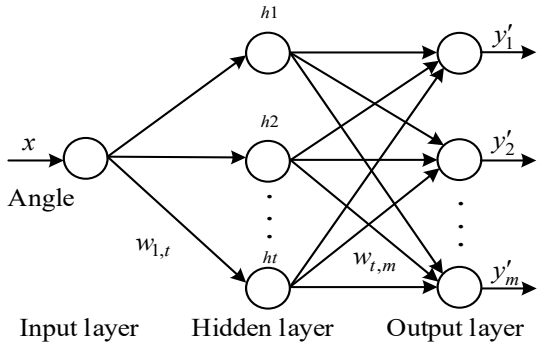

Fig. 4. Topological structure of the BP neural network.

Figure 4 is a single hidden layer BP neural network topology. The stranded wire rotation angle is the input of the network, and the RLCG parameter column vector is the network output. $w_{1,t}$ is the weight of the hidden layer from the input layer to the t-th layer, $w_{t,m}$ is the weight of the t-th layer hidden layer to the m-th layer output layer, t is the number of hidden layer neurons, and t is an empirical range value. It is affected by the number of input elements n and the number of output elements m:

$$t = 0.5(m+n) + a, (a = 1, 2, ..., 10). \quad (7)$$

B. BAS algorithm

The BAS global search algorithm [21] is a meta-heuristic algorithm for multi-objective function optimization based on the principle of the beetle foraging proposed in 2017. When the beetle is foraging, it always distinguishes the direction according to the strength of the food smell. The beetle has two long antennae. If the right side of the antenna receives stronger odor than the left side, the beetle will fly to the right, otherwise it will fly to the left. According to this simple principle, the beetle can effectively find food. Similar to genetic algorithms, particle swarm optimization, etc., the BAS algorithm can automatically implement the optimization process without knowing the specific form of the function and the gradient information. However, compared with the swarm

intelligence optimization algorithm, the BAS algorithm only needs one beetle, the computational complexity is greatly reduced, and its core code is only four lines, which is easy to implement. For low-dimensional optimization functions, it has a very high convergence speed and convergence quality.

The algorithm flow is as following [20]:

(1) Establish and normalize the random vector of the beetle facing:

$$\vec{b} = \frac{rands(k,1)}{\| rands(k,1) \|}. \tag{8}$$

Where *rands*() is a random function, *k* represents the spatial dimension.

(2) Calculate the coordinates of the space position of the beetle:

$$\begin{cases} x_{rt} = x^t + d_0 * \vec{b} / 2 \\ x_{lt} = x^t - d_0 * \vec{b} / 2 \end{cases}, (t = 0,1,2,...,n). \tag{9}$$

Where x_{rt} indicates the position coordinates of the right-handed beard on the *t*-th iteration; x_{lt} indicates the position coordinate of the left-handed beard on the *t*-th iteration; x^t represents the centroid coordinate of the beetle at the *t*-th iteration; d_0 represents the distance between the left and right beard.

(3) According to the fitness function, it is confirmed that the odor intensity, that is the intensity of $f(x_l)$ and $f(x_r)$, $f()$ is the fitness function.

(4) Update the position of the beetle:

$$x^{t+1} = x^t - \sigma^t * \vec{b} * sign(f(x_{rt}) - f(x_{lt})). \tag{10}$$

Where σ^t represents the step factor at the *t*-th iteration; *sign*() is a symbolic function.

C. BAS-BP neural network combined with FDTD algorithm predicting crosstalk

The FDTD algorithm is a numerical method that uses cascaded ideas to solve the crosstalk of non-uniform transmission lines. According to the cascading idea, the strand can be decomposed into a series of uniform transmission lines of a finite number of tiny units. If assuming that the RLCG parameter matrix of each unit is a fixed value, the entire transmission line equation will be solved by iteratively solving the transmission line equation of each unit.

Figure 5 is the equivalent circuit model of the p.u.l. multiconductor transmission lines. Where *dz* represents an infinitesimal length transmission line. r_i and r_j are the p.u.l. resistors that make up the resistance matrix R. l_{ii} and l_{ij} are the p.u.l. self-inductance and mutual inductance that constitute the inductance matrix L. c_{ii} and c_{ij} are the p.u.l. self-capacitance and mutual capacitance that constitute the capacitance matrix C. g_{ii} and g_{ij} are the p.u.l. self-directed and transconducted that form the conductance matrix G.

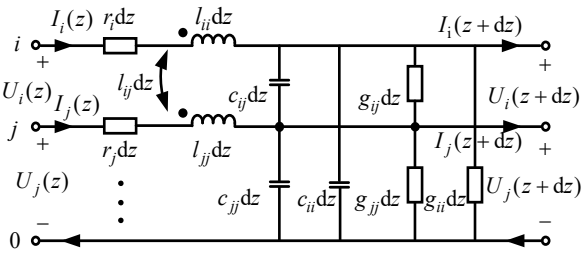

Fig. 5. The per unit length equivalent circuit for MTLs.

According to the TLT [24], the uniform multiconductor transmission line equation is:

$$\frac{\partial U}{\partial z} = -RI - L\frac{\partial I}{\partial t}, \tag{11}$$

$$\frac{\partial I}{\partial z} = -GV - C\frac{\partial V}{\partial t}. \tag{12}$$

Where *U*, *I* represent the voltage and current of the transmission line, respectively and they are a function of space *z* and time *t*. Therefore, the establishment of the multiconductor transmission line equation largely depends on the acquisition of the p.u.l. RLCG parameter matrix. In other words, the most important step in solving the stranded wire crosstalk by using the FDTD algorithm is to obtain a high-precision RLCG parameter matrix.

From a mathematical point of view, there is a highly nonlinear mapping relationship *F* between the RLCG parameters and the rotation angle (from the initial port position) in the strand model:

$$X = F(angle). \tag{13}$$

This kind of functional relationship is difficult to express with common functions, but BP neural network can describe this mapping effectively and conveniently [16]. At the same time, many existing researches show that using the optimization algorithm to optimize the BP neural network initial weights, then training the network can greatly improve the network performance. It can greatly avoid the problem that random initialization causes the network falling into local optimum. Similar to the genetic algorithm, particle swarm algorithm and other intelligent optimization algorithms, it can better solve the poor accuracy of the BP neural network. However, the above optimization algorithm occupies more computer memory, and the main program runs longer [19]. Considering the accuracy and calculation time, this paper uses the BAS global search algorithm to find the optimal initial weights and thresholds of the BP neural network, and applies it to the constructed network to construct the final training network [21]. The model constructed by this method can well overcome the problems of poor stability of the BPNN and prevent it falling into local optimum. The modeling steps are as following:

(1) Create a random vector to be oriented by the

beetle and define the spatial dimension *k*. The model structure is $1-M-N$. 1 is the number of neurons in the input layer (angle), *M* is the number of neurons in the hidden layer and the number of neurons in the output layer is *N*. Then the spatial dimension for searching is *k*, $k=1*M+M*N+M+N$.

(2) Setting of the step factor σ. The step factor is used to control the regional search ability of the beetle. The initial step size should be as large as possible to cover the current search area and not fall into the local minimum. This paper adopts the linear decreasing weight strategy to ensure the fine search:

$$\sigma^{t+1}=\sigma^{t}*eta, t=(1,2,...,n)\cdot \tag{14}$$

Where *eta* takes the number close to 1 between [0,1], and takes 0.8 in this paper.

(3) Determine the fitness function. The root mean square error (MSE) of the test data is used as a fitness evaluation function to advance the search for spatial regions. The function is:

$$fitness=MSE=\frac{1}{N}\sum_{i=1}^{N}(t_{sim}(i)-y_i)^2\cdot \tag{15}$$

Where *N* is the number of samples for the training set; $t_{sim}(i)$ is the output value for the model of the *i*-th sample; y_i is the actual value of the *i*-th sample. Therefore, the position where the fitness function value is the smallest when the algorithm iterates to stop is the optimal solution for the problem.

(4) Initialize the beetle position. The initial parameter takes the random number between [-0.5, 0.5] as the initial solution set of the BAS algorithm, which is the initial position of the beetle, and saves it in *bestX*.

(5) Evaluation. The fitness function value at the initial position is calculated from the fitness function (15) and stored in *bestY*.

(6) Update the position of the beetle. According to the formula (9), the position coordinates of the left and right beards are updated.

(7) Updating of the solution. According to the position of the left and right whiskers in the algorithm of the beetle, the right and left fitness function values are respectively obtained. Comparing the intensity and updating the position of the beetle according to equation (10), that is, adjust the weights and thresholds of the BP neural network. Then calculating the fitness function value at the current position. If the fitness function value at this time is better than *bestY*, it should update *bestY*, *bestX*.

(8) Iterative stop control. Determining whether the fitness function value reaches the set precision (taken as 0.000005) or iterates to the maximum number (100 generations). If the condition is met, it goes to step (9). Otherwise, it returns to step (6) to continue iteration.

(9) Optimal solution generation. When the algorithm stops iterating, the solution in the *bestX* is the optimal solution of the training, that is the optimal initial weights and thresholds of the BP neural network. The above optimal solution is brought into the BP neural network for secondary training and learning. Finally, the stranded wire RLCG parameter matrix extraction model is formed.

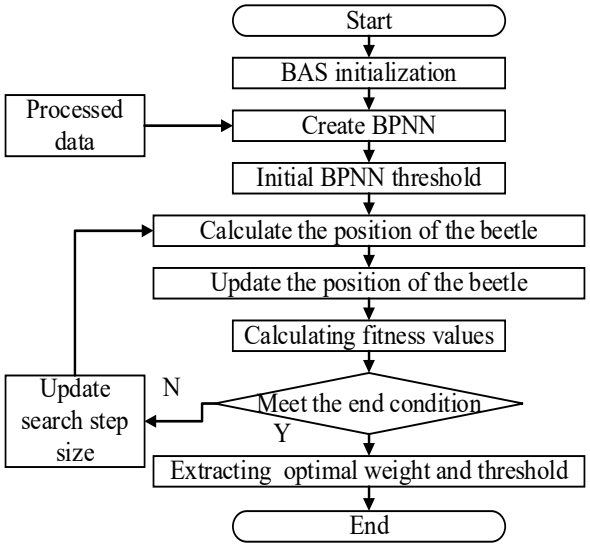

Fig. 6. The BAS algorithm optimized BP neural network flow chart.

By combining the RLCG parameter matrix extraction network at any position of the strand and the FDTD algorithm, the crosstalk of the strand can be predicted. Based on the above discussion, the specific flow chart of BAS-BP neural network model combined with FDTD algorithm for predicting crosstalk is given. Fig. 6 shows a flow chart for the BAS algorithm to optimize the initial weights and thresholds of the BP neural network. Figure 7 shows a flow chart for the BAS-BP neural network RLCG parameter extraction model combined with the FDTD algorithm to predict the stranded crosstalk.

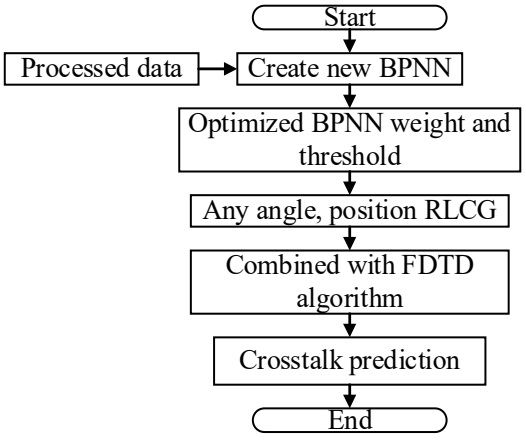

Fig. 7. The BAS-BP algorithm combines the FDTD method predicting crosstalk flow chart.

In this experiment, the BP neural network model adopts single input and single hidden layer setting. According to the empirical formula of hidden layer neurons (7), the value range of hidden layer neurons is [7,17]. In order to improve prediction accuracy, comparing the MSE values under the number of neurons in each hidden layer in turn, and select the optimal t value, that is, the number of neurons in the hidden layer is 12. Therefore, for the three-core stranded wire, the BP neural network structure is set to 1-12-12, and the dimension of the search space of the beetle search algorithm is 180. Since there are no effective guiding theories and methods for setting the step factor in the BAS algorithm, the trial and error method is used here to determine the initial step size $\delta^0 = sqrt(k)$, and the number of iterations n = 100.

IV. VERIFICATION AND ANALYSIS

A. Verification test of the BAS-BP algorithm

In order to facilitate the research, this paper uses three-core stranded wire as an example to verify and analyze the proposed method. The wire radius in the wire harness is 0.89 mm. The insulating material of the wire is a PVC material having a relative dielectric constant of 2.7. The wire thickness is 0.8 mm. The wire length is 1000mm. The wire to ground distance is 8mm. Connecting 50Ω resistors at both ends of the wire. The details are shown in Table 1. The specific distribution pattern to the ground is shown in Fig. 8.

Table 1: Three-core twisted cable

Parameters	Values
Number of cores	3
Single wire radius	0.89 mm
Single wire conductivity	58000000 S/m
Single wire insulation thickness	0.8 mm
Insulation layer relative permittivity	2.7
Pitch	1000 mm
Height	4mm

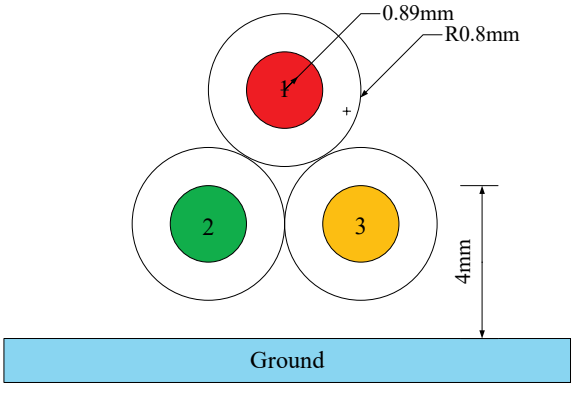

Fig. 8. Three-core stranded wire cross-section distribution pattern.

Taking the cross-section shape of Fig. 8 as the reference section (corresponding to the rotation degree of 0°), the p.u.l. RLCG parameter matrix is extracted by AnsysQ3D simulation software. Due to the axial symmetry of the three-core stranded wire, the RLCG parameter matrix in different transpositions can be transformed into each other through row-column transformation. Therefore, it is only necessary to extract the stranded RLCG parameter matrix within 1/3 of the pitch shown in Fig. 1 to obtain the RLCG parameter matrix of the entire pitch. Starting from 0° and ending at 117°, the R, L, C, G parameter matrix samples were taken from the three-core multi-stranded wire in 1/3 pitch at equal intervals of 3°to get a total of forty samples. The initial parameter matrix is as following (RLCG parameter matrix at 0°):

$$R=\begin{bmatrix}0.365,0.016,0.037\\0.016,0.305,0.009\\0.037,0.009,0.336\end{bmatrix}\Omega, \tag{16}$$

$$L=\begin{bmatrix}585.44,314.15,314.15\\314.15,529.95,287.82\\314.15,287.82,529.95\end{bmatrix}\times10^{-9}H, \tag{17}$$

$$C=\begin{bmatrix}62.011,-27.019,-27.026\\-27.019,65.049,-25.750\\-27.026,-25.750,65.068\end{bmatrix}\times10^{-12}F, \tag{18}$$

$$G=\begin{bmatrix}0.875,-0.435,-0.435\\-0.435,0.893,-0.434\\-0.435,-0.434,0.893\end{bmatrix}\times10^{-3}S. \tag{19}$$

In general, the effect of the R and G parameters is ignored because the transmission line resistance is much smaller than its termination resistance. Therefore, the BAS-BP neural network only trains and tests the L and C parameter matrices of the three-core stranded wire. This experiment sets the training error accuracy of the neural network to $E_{\min} = 10^{-6}$. The BAS-BP neural network algorithm flow of Fig. 5 was used in combination with the MATLAB2018 software platform for training and testing. The samples were randomly arranged using a random function. The first 30 sets of data were used as training data and the last ten sets of data were used as test samples. The training errors of the first 30 groups are shown in Fig. 9. The pre-set accuracy requirements are achieved around 55 generations. Figure 10 is the optimal fitness curve for the BAS-BP model, which tends to be stable after 55 generations of iteration. The corresponding ten groups of samples correspond to angles of 3°, 9°, 51°, 69°, 114°, 36°, 24°, 57°, 27°, and 33°, respectively. Figure 11 is a test error distribution diagram. The maximum error of the test does not exceed 0.008 and the mean value of the test error is only 0.0013, which shows good prediction accuracy. The formula for calculating

the test error using equation (6) is as following:

$$E_{test} = \frac{y' - y}{y}. \tag{20}$$

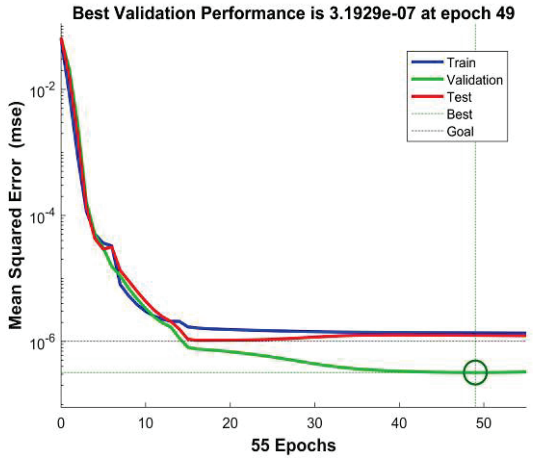

Fig. 9. The iteration number and mean square error of BAS-BP neural network training.

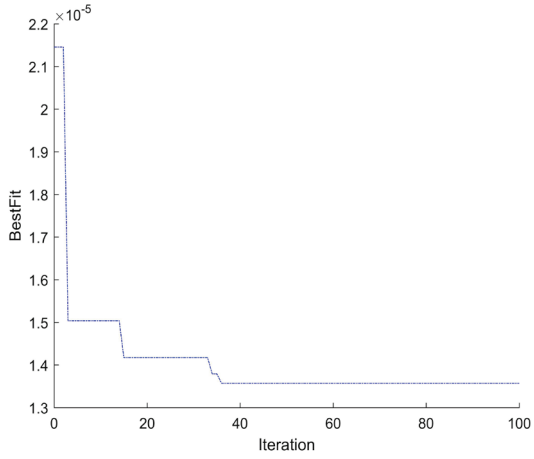

Fig. 10. The BAS-BP neural network algorithm fitness curve.

In this paper, the relative error evaluation index is selected to evaluate the performance of the model. The calculation formula is as following:

$$E_i = \frac{\left| y_i' - y_i \right|}{y_i}, (i = 1, 2, ..., n) \cdot \tag{21}$$

Where E_i is the relative error, $y_i'(i = 1, 2, ..., n)$ is the predicted value of the i-th sample, $y_i(i = 1, 2, ..., n)$ is the true value of the i-th sample; n is the number of samples. The smaller the relative error is, the better the model performance.

In order to test whether the BAS-BP prediction model is superior to other intelligent optimization algorithm models in RLCG electromagnetic parameter extraction, this paper chooses the GA-BP neural network model and the BAS-BP model to compare prediction accuracy from relative error mean and iterative process. The performance of the model is described by the CPU running time. The results are shown in Table 2.

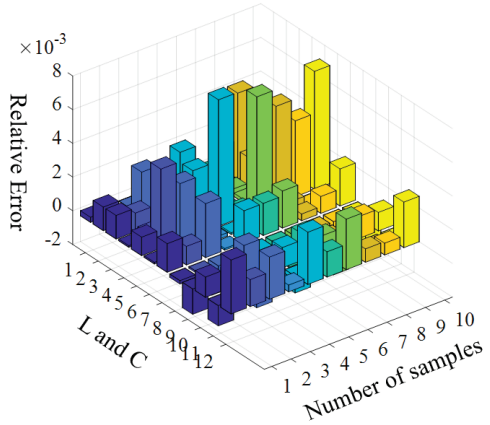

Fig. 11. Test sample error histogram.

Table 2: Comparison of different model effects

	Relative Error Mean		CPU Time/s
Model	Test L	Test C	Train
BPNN	0.0808	0.0026	0.7174
BAS-BPNN	0.0016	0.0011	39.0157
GA-BPNN	0.0023	0.0011	208.3355

It can be seen from Table 2 that the BP, the BAS-BP and the GA-BP algorithms can fit the capacitance matrix, but the accuracy of the latter two is higher than that of the BP algorithm. As to the fitting effect on the inductance matrix can be seen, the BAS-BP algorithm is optimal in extraction accuracy and the relative error mean is only 0.0016. In general, the accuracy of the BAS-BP algorithm and the GA-BP algorithm representing the optimization algorithm are not much different, but from the CPU running time, the BAS-BP is only about one-fifth of the GA-BP. Therefore, from the perspective of overall prediction accuracy and convergence speed, the BAS-BP algorithm works best, reflecting that the BAS-BP algorithm has good applicability and effectiveness in RLCG parameter extraction.

B. Crosstalk analysis

The schematic diagram of the crosstalk test of the triple-stranded wire is shown in Fig. 12. The termination is 50Ω load, ie Zi=50Ω (where i = 1, 2, 3, 4, 5, 6), the line length is 1 meter, and the wire 1 is the power line.

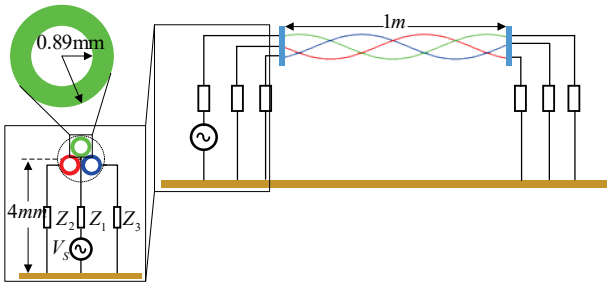

Fig. 12. Three-core stranded crosstalk experimental schematic diagram.

The stranded line RLCG parameter matrix extraction network based on the BAS-BP algorithm is combined with FDTD algorithm to predict the strand crosstalk. The crosstalk results solved by using the full wave simulation method of the CST Cable Studio® commercial software (the electromagnetic field numerical method based on the Huygens wave propagation model) were used as reference standards. The full wave algorithm is an approximate exact solution [24]. According to the parameters in Table 1, the crosstalk of the three-core stranded wire is solved by two methods in the frequency band 100KHz - 1GHz. This paper ignores the small influence of different frequencies on the electromagnetic parameters of the strand [23] and uses 500MHz as the reference value.

Figure 13 and Fig. 14 are the NEXTs of lines 2 and 3, respectively. Because of the structural characteristics of the triple-core stranded wires, the 2nd and 3rd wires have similar crosstalk characteristics. The NEXTs of lines 2 and 3 solved by the new method are both -59.17 dB at 100KHz, which are 0.68dB different from the crosstalk result of the full wave simulation, and then grow steadily in the middle and low frequency bands. At high frequencies, the NEXTs of lines 2 and 3 fluctuate around -17 dB. However, line 2 is in good agreement with the results of full wave simulation. Similarly, the FEXT results for the three-stranded strands solved by the two methods are shown in Fig. 15 and Fig. 16. The FEXTs solved by the new method are -63.30 dB at 100kHZ, which are 1dB different from the result of the full wave simulation solution, and then grow steadily in the middle and low frequency bands. At high frequencies, they fluctuate around -15 dB, and the crosstalk solved by the new method shows slight differences with full wave simulation.

By analyzing the results of the crosstalk solution, the NEXT and FEXT solved by the new method show a good agreement and consistency with the full wave simulation results, especially in the middle and low frequency bands. In the high frequency range, the new method and the full-wave simulation result do not have a slight displacement in the frequency band, but there are some discrepancies in the value, which may be caused by the following problems. First, the space segmentation of the FDTD algorithm in this paper is 150 segments, which may not achieve the actual twisting effect. In theory, as the number of segments increases, the accuracy of the new method will also increase. Second, the BAS-BP neural network constructing the stranded wire RLCG parameter extraction model still has slight deviations, and this effect will be multiplied at high frequencies. Third, for the convenience of research, this paper ignores the small influence of R, G parameters and the influence of frequency on RLCG. Fourth, the full wave simulation will affect the accuracy of the crosstalk solution because of the setting of parameters, the selection of the number of sample points, and the setting of the simulation task. It cannot perfectly reproduce the true crosstalk of the three-core stranded wire. So there is a slight impact on the consistency of two curves. However, in general, the crosstalk predicted by the BAS-BP algorithm combined with the FDTD method has extremely high precision (coincidence) at low frequencies, and at high frequencies, it is consistent with the simulation results in the trend of crosstalk.

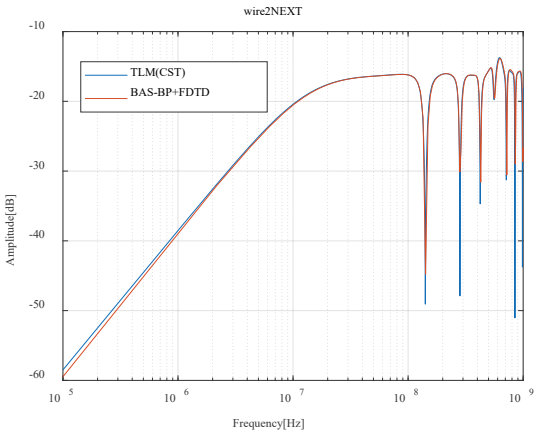

Fig. 13. Conductor No. 2 NEXT.

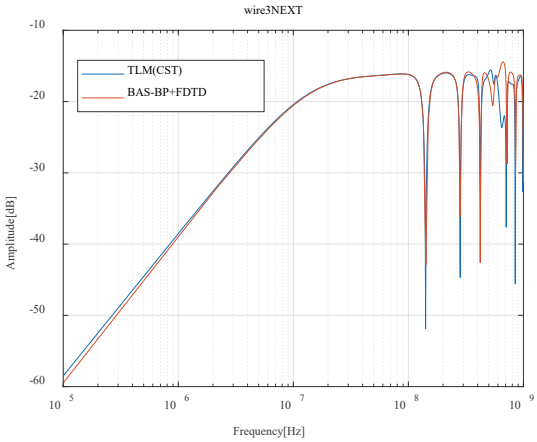

Fig. 14. Conductor No. 3 NEXT.

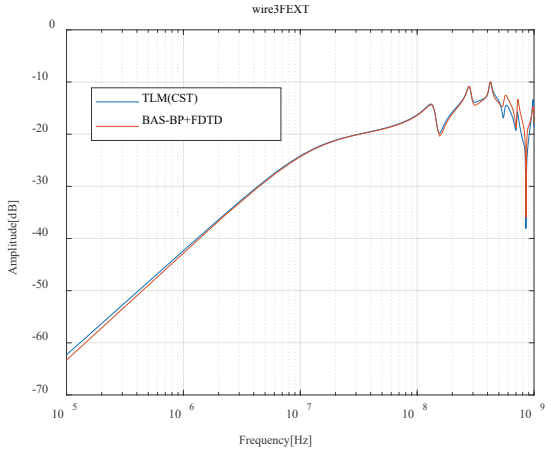

Fig. 15. Conductor No. 2 FEXT.

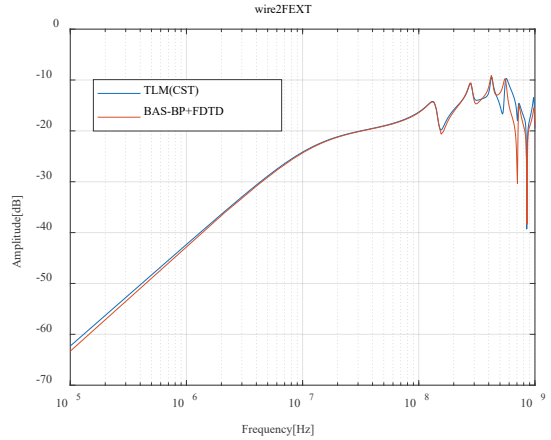

Fig. 16. Conductor No. 3 FEXT.

V. CONCLUSION

This paper proposes a new method based on the BAS-BP algorithm combined with the FDTD algorithm to predict the strand crosstalk. Through studying a specific three-core stranded wire and referring to the full wave simulation results, the applicability and high efficiency of the proposed method in the stranded wire crosstalk prediction are verified. The verification results show that, first, the RLCG parameter matrix extraction network has higher precision. The test results show that the relative error is less than 0.008 and the average relative error is only 0.0013. Second, the optimization effect of the BAS algorithm on the BP neural network is significantly better than swarm optimization algorithm. Third, in the 100KHz and 1GHz bands, the new method calculates the NEXT and FEXT of the stranded wire with high accuracy, especially in the middle and low frequency bands. Finally, the method proposed in this paper has strong vitality and creativity. There are still many places worth studying in the combination of adaptive beetle swarm algorithm and windward differential algorithm.

ACKNOWLEDGMENT

The paper is supported by National Natural Science Foundation of China (51475246), National Natural Science Foundation of Jiangsu Province (BK20161019), Aviation Science Foundation (20172552017).

REFERENCES

[1] J. R. Moser and R. F. Spencer, “Predicting the magnetic fields from a twisted-pair cable,” *IEEE Transactions on Electromagnetic Compatibility*, vol. 10, no. 3, pp. 324-329, Sept. 1968.

[2] A. Y. Alksne, “Magnetic fields near twisted wires,” *IEEE Transactions on Space Electronics and Telemetry*, vol. 10, no. 4, pp. 154-158, Dec. 1964.

[3] S. A. Pignari and G. Spadacini, “Plane-wave coupling to a twisted-wire pair above ground,” *IEEE Transactions on Electromagnetic Compatibility*, vol. 53, no. 2, pp. 508-523, May 2011.

[4] G. Flavia, “Immunity to conducted noise of data transmission along DC power lines involving twisted-wire pairs above ground,” *IEEE Transactions on Electromagnetic Compatibility*, vol. 55, no. 1, pp. 195-207, Feb. 2013.

[5] S. Grivet-Talocia, “Adaptive transient solution of non-uniform multiconductor transmission lines using wavelets,” *IEEE Transactions on Antennas and Propagation*, vol. 48, no. 10, pp. 1563-1573, Oct. 2000.

[6] P. Manfredi, D. De Zutter, and D. V. Ginste, “Analysis of non-uniform transmission lines with an iterative and adaptive perturbation technique,” *IEEE Transactions on Electromagnetic Compatibility*, vol. 58, no. 3, pp. 859-867, June 2016.

[7] G. Spadacini and S. A. Pignari, “Numerical assessment of radiated susceptibility of twisted-wire pairs with random non-uniform twisting,” *IEEE Transactions on Electromagnetic Compatibility*, vol. 55, no. 5, pp. 956-964, Oct. 2013.

[8] C. Jullien, P. Besnier, M. Dunand, et al., “Advanced modeling of crosstalk between an unshielded twisted pair cable and an unshielded wire above a ground plane,” *IEEE Transactions on Electromagnetic Compatibility*, vol. 55, no. 1, pp. 183-194, Feb. 2013.

[9] A. Shoory, M. Rubinstein, A. Rubinstein, et al., “Simulated next and fext in twisted wire pair bundles,” in *Proc. EMC Europe Symp.*, York, UK, pp. 266-271, Sept. 2011.

[10] M. Tang and J. Mao, “A precise time-step integration method for transient analysis of lossy non-uniform transmission lines,” *IEEE Trans-*

actions on Electromagnetic Compatibility, vol. 50, no. 1, pp. 166-174, Feb. 2018.

[11] S. Dai, A. Z. Elsherbeni, and C. E. Smith, "Non-uniform FDTD formulation for the analysis and reduction of crosstalk on coupled microstrip lines," *Journal of Electromagnetic Waves and Applications*, vol. 10, no. 12, pp. 1663-1682, June 1996.

[12] S. J. Liu, "An efficient algorithm for the parameter extraction of multiconductor transmission lines in multilayer dielectric media," *IEEE Antennas and Propagation Society International Symposium*, July 2005.

[13] Q. Chen and N. Wong, "A stochastic integral equation method for resistance extraction of conductors with random rough surfaces," in *Proc. IEEE. Int. Symp. on Intelligent Signal Processing and Communications*, Tottori, Japan, pp. 411-414, Dec. 2006.

[14] G. Plaza, F. Mesa, and M. Horno, "Quick computation of (C), (L), (G), and (R) matrices of multiconductor and multilayered transmission systems," *IEEE Transactions on Microwave Theory and Techniques*, vol. 43, no. 7, pp. 1623-1626, July 1995.

[15] P. Manfredi and F. G. Canavero, "Numerical calculation of polynomial chaos coefficients for stochastic per - unit - length parameters of circular conductors," *IEEE Trans. on Magnet*., vol. 50, no. 3, pp. 74-82, Mar. 2014.

[16] T. Rashid, *Make Your Own Neural Network.* Charleston, USA: Create Space Independent Publishing Platform, 2016.

[17] M. Hassoun, *Fundamentals of Artificial Neural Networks*. Cambridge, USA: Bradford Book, 2003.

[18] C. Yang, et al., "Analysis on RLCG parameter matrix extraction for multi-core twisted cable based on back propagation neural network algorithm," *IEEE Access*, vol. 2, no. 1, pp. 16-19, Aug. 2019.

[19] H. L. Yang, H. C. Lin, and S. Huang, "Forecasting exchange rate using EMD and BPNN optimized by particle swarm optimization," *International Conference on Data Mining and Intelligent Information Technology Applications*, Oct. 2011.

[20] T. T. Wang and Q. Liu, "Prediction of storm surge disaster loss based on BAS-BP model," *Marine Environmental Science*, vol. 37, no. 3, pp. 457-463, 2018 (in Chinese).

[21] X. Jiang and S. Li, "Beetle antennae search without parameter tuning (BAS-WPT) for multi-objective optimization," Nov. 2017.

[22] C. D. Taylor and J. P. Castillo, "On the response of a terminated twisted - wire cable excited by a plane-wave electromagnetic field," *IEEE Trans-actions on Electromagnetic Compatibility*, vol. 2, no. 1, pp. 16-19, Feb. 1980.

[23] C. R. Paul, *Analysis of Multiconductor Trans-mission Lines.* 2nd ed., New York, USA: Wiley, 1994.

[24] CST Microwave Studio, ver. 2008, Computer Simulation Technology, Framingham, MA, 2008.

Frequency Splitting Based on Spoof Surface Plasmon Polaritons Coplanar Waveguide

Jun Wang [1], Yanhui Liu [3], Lei Zhao [2,*], Zhang-Cheng Hao [1,4,*], Lei Qiao [5], Yongjin Zhou [6], and Yingsong Li [7]

[1] State Key Lab of Millimeter-Waves, School of Information Science and Engineering
Southeast University, Nanjing, Jiangsu 211189, China

[2] School of Information and Control Engineering
China University of Mining and Technology, Xuzhou, 221116, China

[3] AVIC Beijing Changcheng Aeronautical Measurement and Control Technology Research Institute
Beijing, 101111, China

[4] Purple Mountain Laboratories, Nanjing, 100022, China

[5] Beijing Institute of Control Engineering, Beijing, 100190, China

[6] Key Laboratory of Specialty Fiber Optics and Optical Access Networks
School of Communication and information Engineering, Shanghai University, Shanghai 200444, China

[7] College of Information and Communication Engineering
Harbin Engineering University, Harbin, 150001, China
*leizhao@jsnu.edu.cn, zchao@seu.edu.cn

Abstract ─ In this paper, a novel frequency splitter is proposed based on the spoof surface plasmon polaritons (SSPPs) coplanar waveguide (CPW). The proposed frequency splitter uses the semi-circular holes etched on the both sides of the middle line of the CPW to realize mode conversion and frequency splitting. The operating principles of the proposed frequency splitter have been analyzed by the dispersion curves, electric field distributions, and equivalent circuit. Moreover, the splitting frequency of the splitter can be easily controlled by changing the corresponding parameters. Furthermore, full-wave simulation along with the measured results are given to describe the performance of the proposed frequency splitter. The highly consistent between simulated and measured results validates the design conception, which means that the proposed design is of importance to develop surface-wave integrated circuits.

Index Terms ─ Coplanar waveguide, frequency splitter, spoof surface plasmon polaritons.

I. INTRODUCTION

Spoof surface plasmon polaritons (SSPPs) have been widely used to design various microwave SSPP-based antennas [1-4], low-pass or band-pass filters [5-11], and power dividers [12-22]. According to its specific performance of confining fields, various SSPP structures were proposed (such as flaring grounds, gradient corrugation slits, lumped elements, and hole array) to design miniaturized devices.

Power divider is a key component in microwave communication systems, which can be used to separate the power of the input signal into two output channels with equal or unequal power levels. Conventional SSPP-based power dividers were designed based on the coplanar waveguide (CPW) etched with periodic gradient grooves [12-14], SSPP metal grating splitters with finite thickness [15-18], and some other structures [19-22]. However, most of the power dividers based on the periodic gradient grooves were anti-symmetrical designs, which were adverse to transmission efficiency improvement. Moreover, some SSPP metal grating splitters with finite thickness have also been proposed in [15-18]. The designs divide the signal into two or more different directions. Nevertheless, the fabrication cost was expensive. Additionally, a design based on the lumped element was proposed in [20] and it was not a planar design, which was not benefit for integration. Hence, [21] proposed a high efficiency and planar splitting structure, which was based on the CPW with

Submitted On: November 2, 2019
Accepted On: December 28, 2019

hole arrays etched on its stripline. Nevertheless, all of the above proposed designs were wave splitter, which separate the power of the input signal into two output channels with equal levels and less of them can be used to design a frequency splitter. In [23], a planar frequency splitter experimentally based on SSPPs of planar composite periodic gratings was proposed. However, this design is not conduct to size miniaturization. Therefore, designing a compact planar low cost SSPP-based frequency splitter with high efficiency and good isolation is technically very challenging. Recently, [24] proposed a SSPP waveguide filter based on the CPW etched with semi-hole arrays to achieve the SSPP performance and maybe a good candidate for designing the desired SSPP-based devices.

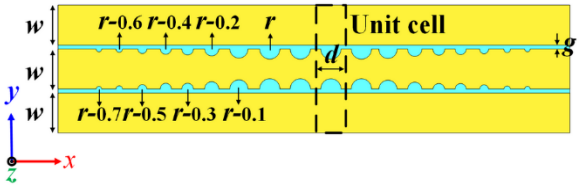

(a)

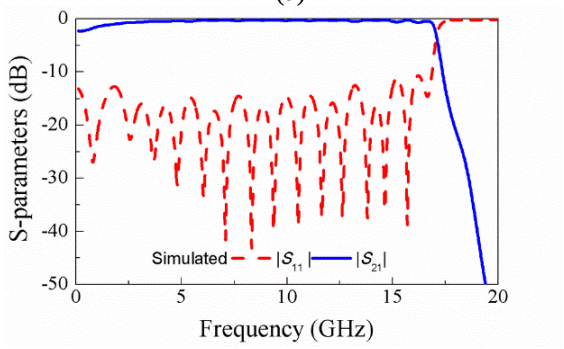

(b)

Fig. 1. (a) Configuration of the semi-hole arrays SSPP waveguide, and (b) simulated S-parameters of the semi-hole arrays SSPP waveguide.

In this paper, a frequency splitter based on the semi-hole arrays SSPP-based structure is proposed. The frequency splitter is designed by using the semi-hole arrays etched on the CPW stripline as input signal and splitting the input wave into two output channels with the different cut-off frequencies, which can be controlled by changing the length of unit cell. The operating principle of the proposed frequency splitter is analyzed using dispersion relationships, electric field distributions, and equivalent circuit. Meanwhile, fabricated prototypes are measured and verified our simulated results. The proposed frequency splitter has the following advantages: 1) the transmission efficiency is high; 2) the isolation of the two outputs is good; 3) the cut-off frequency can be easily controlled by changing the corresponding parameters; 4) the design is compact and the fabrication cost is low.

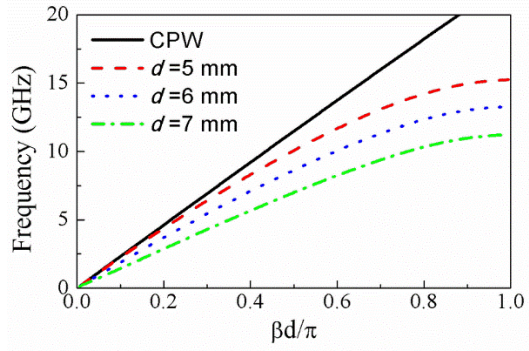

(a)

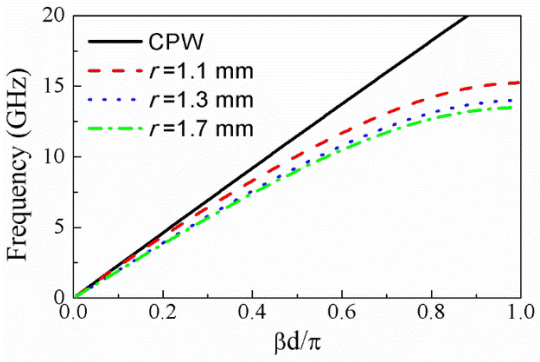

(b)

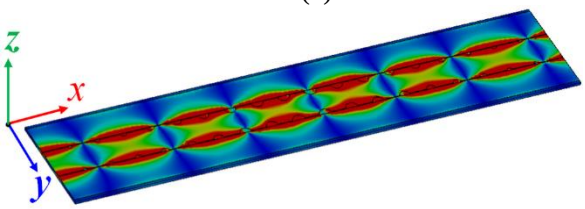

(c)

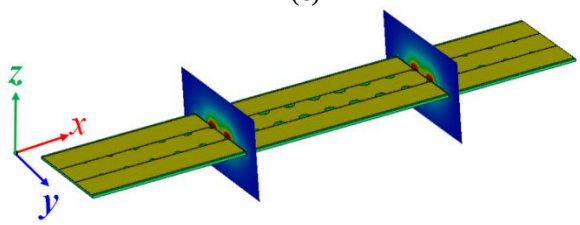

(d)

Fig. 2. (a) Dispersion curves with different unit cell length when r = 1.1 mm, (b) dispersion curves with different hole radii when d = 5 mm, (c) electric field distribution on the x–y plane at 8 GHz when d = 5 mm, and (d) magnitudes of energy flows on cross sections at 8 GHz when d = 5 mm.

II. DESIGN CONSIDERATIONS

A. Semi-hole arrays SSPP waveguide

The configuration of the semi-hole arrays SSPP waveguide is sketched in Fig. 1 (a), which is a 50-Ω CPW line etched with periodic semi-hole arrays on the both sides of the middle line. The design is printed on the F4B substrate with a thickness of 0.5 mm, a relative permittivity of 2.65, and a loss tangent of 0.0015. The width and gap of CPW are denoted as w and g, respectively. The unit cell is shown in the dashed frame, its length is marked as d. The detailed designed parameters values are w = 6 mm, g = 0.1 mm, d = 5 mm, and r = 1.1 mm. The simulated $|S_{11}|$ and $|S_{21}|$ of the semi-hole arrays SSPP waveguide are plotted in Fig. 1 (b), it is clear that the design has a cut-off frequency at 16 GHz and the transmission efficiency is very high, which means that the design has transformed quasi-TEM wave to SSPPs (TM) wave.

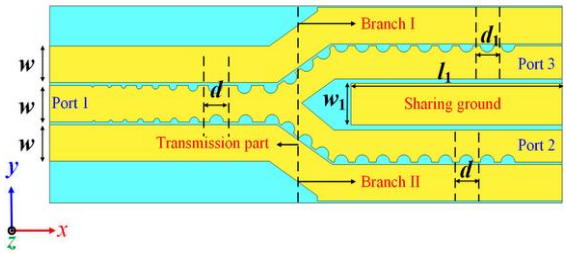

(a)

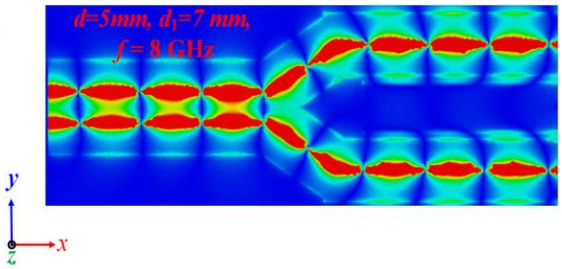

(b)

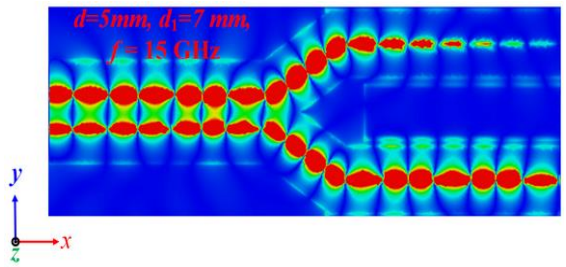

(c)

Fig. 3. (a) Structure of the proposed frequency splitter, (b) the simulated electric field distribution on the *x-y* plane when d=d_1=5 mm at 15 GHz, and (c) the simulated electric field distribution on the *x-y* plane when d=5 mm, d_1=7 mm at 15 GHz.

In order to further illustrate the design can transform the quasi-TEM wave to SSPPs (TM) wave efficiently, Figs. 2 (a) and (b) present the simulated dispersion curves of the semi-hole arrays SSPP waveguide with different unit cell lengths and hole radii, respectively. It can be clearly seen that the cut-off frequency decreases as the d and r increase. Figures 2 (c) and (d) give the simulated electric field distribution on the *x-y* plane and the magnitudes of energy flows on cross-sections at 8 GHz when d = 5 mm. From these two figures, we can observe that the EM energy is highly localized within a small region around the slot lines of CPW. Hence, the design can support the SSPPs wave propagates on its surface and the dispersion characteristics can be used to control its cut-off frequency.

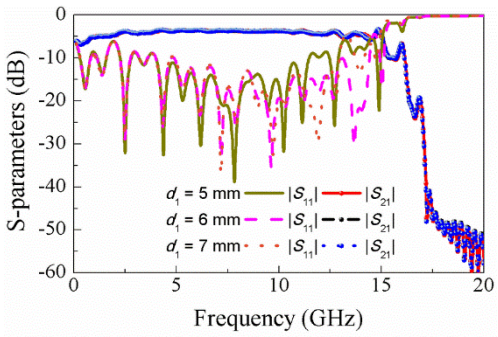

(a)

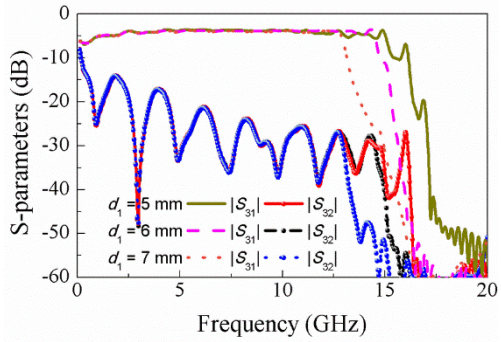

(b)

Fig. 4. Simulated (a) $|S_{11}|$, $|S_{21}|$, and (b) $|S_{31}|$, and $|S_{32}|$ with different d_1 values.

B. The proposed frequency splitter

From the above analysis, we know that the semi-hole arrays SSPP waveguide can support the SSPP mode and have a high transmission efficiency. In order to design a frequency splitter, we split the structure as two branches, as shown in Fig. 3 (a). The transmission part has the same parameter values as the semi-hole arrays SSPP waveguide. The opening angle of the two branches is 60°. The performance of the proposed frequency splitter can be controlled by changing the unit cell length of the branch I (denoted as d_1). From the dispersion curves in Fig. 2 (a),

we known that the cut-off frequency are decreases as the unit cell length raises, which means that the cut-off frequency of branch I can be controlled by changing d_1. Figures 3 (b) and (c) give the simulated electric field distributions on the *x*-*y* plane at 8 GHz and 15 GHz when d=5 mm and d_1=7 mm, respectively. It can be seen that the branch I and II have the same energy flow from transmission part to port 2 and 3 at 8 GHz when d=5 mm and d_1=7 mm. However, when the frequency is increases to 15 GHz, the energy cannot propagate from branch I to port 3, because the cut-off frequency of the design is below 15 GHz in this case (as shown in Fig. 2 (a)). Nevertheless, the energy can propagate from branch II to port 2, which means that the proposed design can split the signal as two channels with different cut-off frequency.

To obtain the performance of the proposed frequency splitter, the parametric studies are analyzed using commercial software CST. The S-parameters with different d_1 values are presented in Fig. (4). The highest $|S_{21}|$ and $|S_{31}|$ is up to -3.6 dB. From Fig. 4 (a), it is clear that the $|S_{21}|$ almost has no change with the d_1 changes. Moreover, it can be seen in Fig. 4 (b) that the cut-off frequency of $|S_{31}|$ is decrease with d_1 increase and the transmission efficiency below the cut-off frequency is still high. Furthermore, the isolation between port 2 and 3 is all below -15 dB within the operating frequency band. Based on the above analysis, we know that the proposed frequency splitter can divide the input SSPP waves into two branches with different cut-off frequency and can achieve a good performance.

C. Equivalent circuit of the proposed frequency splitter

To further physically explain the frequency splitter behavior, a simplified *LC* equivalent circuit (neglecting *R* as its value will be negligibly small in case of metals) of the proposed frequency splitter is proposed in Fig. 5. In the equivalent circuit, each conducting line in the design can be modeled as an inductance while any pair of parallel conducting edges is represented by some capacitance values. The values of L_1 and C_1 of CPW feeding part can be derived from [25] and [26] and can be expressed as:

$$L_1 = Z_0 \frac{\sqrt{\varepsilon_{re}}}{c_0}\ , \tag{1}$$

$$C_1 = \frac{L_1}{{Z_0}^2}\ , \tag{2}$$

where Z_0 is the characteristic impedance of the CPW feeding part, ε_{re} is the effective dielectric constant, and c_0 is the velocity of light in frees pace.

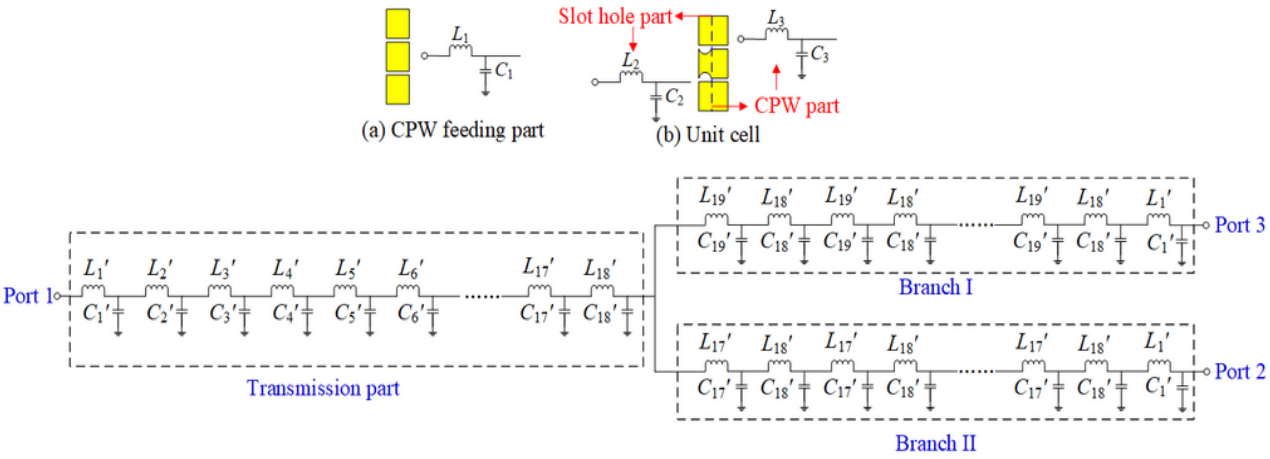

Fig. 5. Simplified equivalent circuits of: (a) CPW feeding part, (b) unit cell, and (c) the whole structure.

In Figs. 5 (a) and (b), the detailed equivalent circuit segmentations of the CPW feeding part and unit cell are presented. The unit cell can be divided as slot hole part and CPW part. If we regard the semi-hole as a uniform rectangular slot, then the slot hole part still can be equivalent as a CPW part. Therefore, based on the above equivalent circuits, a simplified equivalent circuit model for the whole system is synthesized, as shown in Fig. 5 (c), which utilizes the equivalent circuits of the CPW feeding part and unit cell. Additionally, all the odd marks of the *LC* represent the CPW part and the even marks of the *LC* represent the slot hole part. When the unit cell length (d_1) of branch I increases or decreases, the corresponding circuit values of slot hole part of unit cell remains the same and the CPW part changes (as shown in Fig. 5 (b)), which means that the corresponding equivalent circuits of branch I just need to adjust the parameters of L_{19}' and C_{19}' as the unit cell changes. This schematic can be used to understand the performance of the system in circuital terms, and as a useful tool for future designs. According to formulas (1)-(2) and using the advanced design system (ADS) software to optimize the values, the values of the equivalent circuit (when d=d_1=5 mm, the corresponding equivalent circuit

parameters L_{17}'= L_{19}' and C_{17}'= C_{19}') are empirically calculated as: L_1' = 0.379 nH, L_2' = 0.821 nH, L_3' = 0.33 nH, L_4' = 0.893 nH, L_5' = 0.314 nH, L_6' = 0.839 nH, L_7' = 0.298 nH, L_8' = 0.89 nH, L_9' = 0.282 nH, L_{10}' = 0.806 nH, L_{11}' = 0.266 nH, L_{12}' = 0.558 nH, L_{13}' = 0.25 nH, L_{14}' = 0.408 nH, L_{15}' = 0.233 nH, L_{16}' = 0.409 nH, L_{17}' = 0.225 nH, L_{18}' = 0.204nH, L_{19}' = 0.225 nH, C_1' = 0.237 pF, C_2' = 0.196 pF, C_3' = 0.2 pF, C_4' = 0.272 pF, C_5' = 0.196 pF, C_6' = 0.286 pF, C_7' = 0.186 pF, C_8' = 0.221 pF, C_9' = 0.176 pF, C_{10}' = 0.19 pF, C_{11}' = 0.166 pF, C_{12}' = 0.205 pF, C_{13}' = 0.156 pF, C_{14}' = 0.204 pF, C_{15}' = 0.146 pF, C_{16}' = 0.343 pF, C_{17}' = 0.141 pF, C_{18}' = 0.0147 pF, and C_{19}' = 0.141pF.

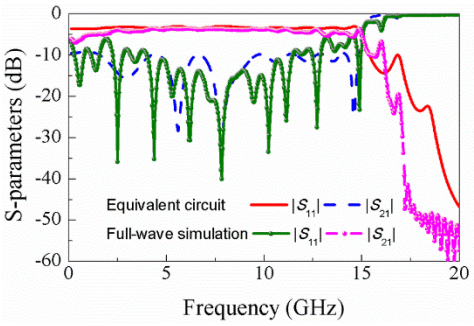

Fig. 6. Simulated S-parameters of the proposed frequency splitter and equivalent circuit model.

The full-wave simulation results are demonstrated together with the scattering parameters of the corresponding simplified equivalent circuit model, as shown in Fig. 6 (a). The results of the full-wave simulation and equivalent circuit (when d=d_1=5 mm, the corresponding equivalent circuit parameters L_{17}'= L_{19}' and C_{17}'= C_{19}') are given and we can see that the simulation results of the equivalent circuit model present the similar trend with the full-wave simulation results, which validate the proposed design exhibits the expected behavior. Moreover, Fig. 6 (b) shows the simulated equivalent circuit results when we change the L_{19}' and C_{19}' values, it is clear that the cut-off frequency of branch I decreases as L_{19}' and C_{19}' increase, which has a good agreement with the physic model (increasing the unit cell length, the cut-off frequency will decrease).

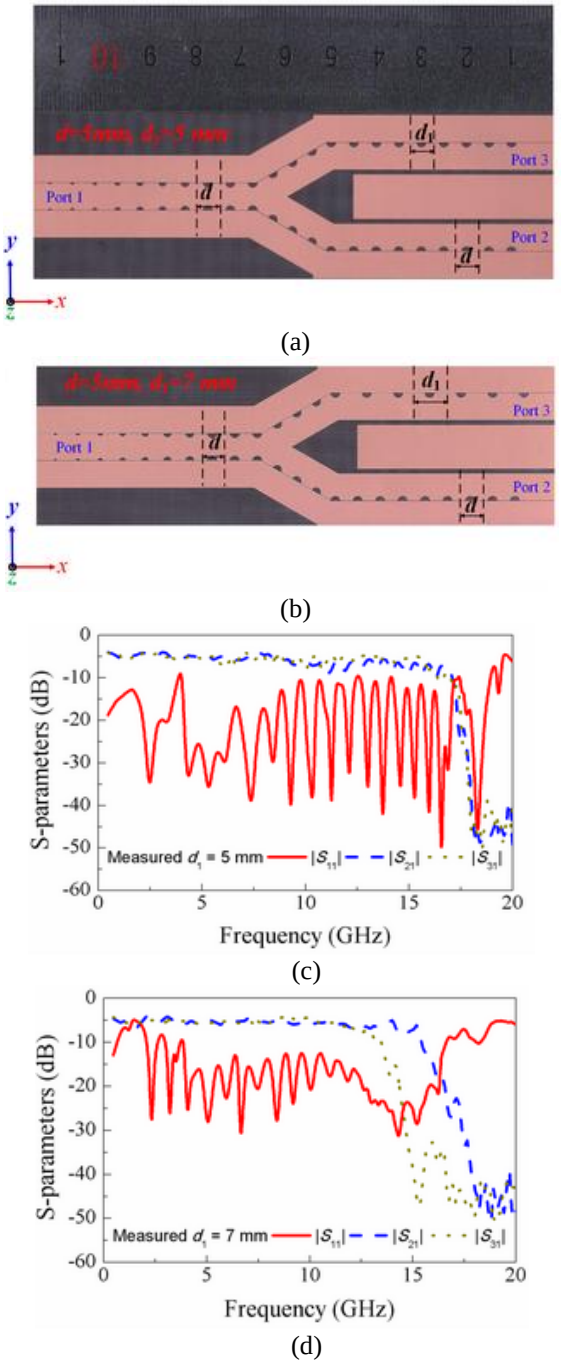

Fig. 7. Photograph of the fabricated frequency splitter when: (a) d_1=5 mm, (b) d_1=7 mm, measured S-parameters of the proposed frequency splitter when (c) d_1=5 mm, and (d) d_1=7 mm.

III. EXPERIMENTAL VERIFICATION

The actual prototypes of the proposed frequency splitter are fabricated on the F4B substrate and measured to characterize its simulated performance, as shown in Fig. 7. The prototypes are fabricated using the standard printed circuit board technologies. The thickness of the

fabricated substrate is 0.5 mm, ε_r = 2.65, loss tangent tan δ = 0.0015, and the thickness of metallic strips is 0.035 mm, which can be regarded as a perfect electrical conductor. Figures 7 (c) and (d) show the measured results of the proposed frequency splitter when d_1=5 mm and d_1=7 mm, respectively. It is clear that the measured results are highly consistent with the simulated ones. As shown in Fig. 7 (c), the port 2 and 3 have the same cut-off frequency when d=d_1=5 mm. However, the cut-off frequency of port 3 shift to lower frequency when d_1 increases to 7 mm, shown in Fig. 7 (d). Moreover, the differences between the measured and simulated results at some frequencies and the frequencies have slight difference with the simulated results, which are maybe caused by the SMA soldering and measurement tolerances. As expected, the fabricated prototype can realize a good frequency splitting characteristic and can find potential applications in surface-wave integrated circuits at the microwave frequency band.

IV. CONCLUSION

A frequency splitting SSPP based on the CPW is proposed at microwave frequencies. The frequency splitter is first investigated based on the special semi-hole arrays SSPP waveguide, which is designed by separating the transmission part as two branches. The proposed frequency splitter is investigated by using the dispersion curves and electric field distributions. Prototypes of the proposed frequency splitter with different d_1 have been fabricated and measured to verify the design conception, the measured results agree well with the simulated ones, which show that the proposed design can split the SSPPs with high transmission efficiency, low loss, good isolation, and low cost. The proposed frequency splitting SSPPs features some advantages, which is helpful to design future SSPP devices and find some other applications in microwave frequency band.

ACKNOWLEDGMENT

This work was supported in part by the National Natural Science Foundation of China under Grant 61771226 and 61372057, in part by the Natural Science Foundation of the Jiangsu Higher Education Institutions of China under Grant 18KJA110001, in part by the Natural Science Foundation of the Xuzhou of China under Grant KC18003, in part by the Scientific Research Foundation of Graduate School of Southeast University under Grant YBPY1954, and Open Project of State Key Laboratory of Millimeter Waves under Grant K202031.

REFERENCES

[1] D. Tian, R. Xu, G. T. Peng, J. X. Li, Z. Xu, A. X. Zhang, and Y. X. Ren, "Low-profile high-efficiency bidirectional endfire antenna based on spoof surface plasmon polaritons," *IEEE Antennas Wireless Propag. Lett.*, vol. 17, no. 5, pp. 837-840, May 2018.

[2] Y. J. Han, Y. F. Li, H. Ma, J. F. Wang, D. Y. Feng, S. B. Qu, and J. Q. Zhang, "Multibeam antennas based on spoof surface plasmon polaritons mode coupling," *IEEE Trans. Antennas Propag*., vol. 65, no. 3, pp. 1187-1192, Mar. 2017.

[3] Z. C. Hao, J. X. Zhang, and L. Zhao, "A compact leaky-wave antenna using a planar spoof surface plasmon polariton structure," *International Journal of RF and Microwave Computer-Aided Engineering*, e21617, 1-7, 2019.

[4] A. Kianinejad, Z. N. Chen, L. Zhang, W. Liu, and C. W. Qiu, "Spoof plasmon-based slow-wave excitation of dielectric resonator antennas," *IEEE Trans. Antennas Propag*., vol. 64, no. 6, pp. 2094-2099, Jun. 2016.

[5] Y. J. Guo, K. D. Xu, Y. H. Liu, and X. H. Tang, "Novel surface plasmon polariton waveguides with enhanced field confinement for microwave-frequency ultra-wideband bandpass filters," *IEEE Access*, vol. 6, pp. 10249-10256, Mar. 2018.

[6] L. Zhao, X. Zhang, J. Wang, W. H. Yu, J. D. Li, H. Su, and X. P. Shen, "A novel broadband band-pass filter based on spoof surface plasmon polaritons," *Sci. Rep.*, vol. 6, no. 36069, Oct. 2016.

[7] J. Wang, L. Zhao, Z. C. Hao, and T. J. Cui, "An ultra-thin coplanar waveguide filter based on the spoof surface plasmon polaritons," *Appl. Phys. Lett.*, vol. 113, no. 7. p. 071101, Aug. 2018.

[8] Y. J. Zhou, and B. J. Yang, "Planar spoof plasmonic ultra-wideband filter based on low-loss and compact terahertz waveguide corrugated with dumbbell grooves," *Appl. Opt.*, vol. 54, no. 14, pp. 4529-4533, May 2015.

[9] H. F. Ma, X. P. Shen, Q. Cheng, W. X. Jiang, and T. J. Cui, "Broadband and high-efficiency conversion from guided waves to spoof surface plasmon polaritons," *Laser Photon. Rev*., vol. 8, no. 1, pp. 146-151, Jan. 2014.

[10] J. Wang, L. Zhao, and Z. C. Hao, "A band-pass filter based on the spoof surface plasmon polaritons and CPW-Based coupling structure," *IEEE Access*, vol. 7, pp. 35089-35096, Apr. 2019.

[11] L. L. Liu, Z. Li, C. Q. Gu, P. P. Ning, B. Z. Xu, Z. Y. Niu, and Y. J. Zhao, "Multi-channel composite spoof surface plasmon polaritons propagating along periodically corrugated metallic thin films," *J. Appl. Phys.*, vol. 116, no. 1, p. 013501, July 2014.

[12] X. Gao, L. Zhou, X. Y. Yu, W. P. Cao, H. O. Li, H. F. Ma, and T. J. Cui, "Ultra-wideband surface plasmonic Y-splitter," *Opt. Express*, vol. 23, no. 18, pp. 23270-23277, Aug. 2015.

[13] S. Y. Zhou, J. Y. Lin, S. W. Wong, F. Deng, L. Zhu, Y. Yang, Y. J. He, and Z. H. Tu, "Spoof surface plasmon polaritons power divider with

large isolation," *Sci. Rep.*, vol. 8, no. 5947, Apr. 2018.
[14] Y. L. Wu, M. X. Li, G. Y. Yan, L. Deng, Y. A. Liu, and Z. Ghassemlooy, "Single-conductor co-planar quasi-symmetry unequal power divider based on spoof surface plasmon polaritons of bow-tie cells," *AIP advances*, vol. 6, pp. 105110, Oct. 2016.
[15] Y. J. Zhou, Q. Jiang, and T. J. Cui, "Bidirectional surface wave splitters excited by a cylindrical wire," *Opt. Express*, vol. 19, no. 6, pp. 5260-5267, Mar. 2011.
[16] J. Shibayama, J. Yamauchi, and H. Nakano, "Metal disc-type splitter with radially placed gratings for terahertz surface waves," *Electron. Lett.*, vol. 51, no. 4, pp. 352-353, Feb. 2015.
[17] Y. J. Zhou and T. J. Cui, "Multidirectional surface-wave splitters," *Appl. Phys. Lett.*, vol. 98, no. 22, pp. 221901, May 2011.
[18] Y. L. Wu, Z. Zhuang, L. Deng, and Y. A. Liu, "Three-dimensional multiway power dividers based on transformation optics," *Sci. Rep.*, vol. 6, no. 24495, Apr. 2016.
[19] J. Wang, Z.-C. Hao, and L. Zhao, "A wideband frequency beam scanning antenna based on the spoof surface plasmon polaritons," *IEEE International Symposium on Antennas and Propagation and USNC-URSI Radio Science Meeting*, pp. 141-142, 2019.
[20] S. Passinger, A. Seidel, C. Ohrt, C. Reinhardt, A. Stepanov, R. Kiyan, and B. N. Chichkov, "Novel efficient design of Y-splitter for surface plasmon polariton applications," *Opt. Express*, vol. 16, no. 19, pp. 14369-14379, Sep. 2008.
[21] J. Wang, L. Zhao, Z. C. Hao, X. P. Shen, and T. J. Cui, "Splitting spoof surface plasmon polaritons to different directions with high efficiency in ultra-wideband frequencies," *Opt. Lett*, vol. 44, no. 13, pp. 3374-3377, July 2019.
[22] B. G. Xiao, S. Kong, J. Chen, and M. Y. Gu, "A microwave power divider based on spoof surface plasmon polaritons," *Opt. Quant. Electron.*, vol. 48, pp. 179, Feb. 2016.
[23] X. Gao, J. H. Shi, X. P. Shen, H. F. Ma, W. X. Jiang, L. M. Li, and T. J. Cui, "Ultrathin dual-band surface plasmonic polariton waveguide and frequency splitter in microwave frequencies," *Appl. Phys. Lett.*, vol. 102, no. 15, pp. 151912, Apr. 2013.
[24] L. Zhao, S. Liu, J. Wang, X. P. Shen, and T. J. Cui, "A band-stop filter based on spoof surface plasmon polaritons," *Electron. Lett.*, vol. 55, no. 10, pp. 607-609, May 2019.
[25] R. K. Mongia, I. J. Bahl, P. Bhartia, and J. Hong, *RF and Microwave Coupled-Line Circuits*, 2nd ed. Artech house, Boston, 1999.
[26] J. Sor, Y. X. Qian, and T. Itoh, "Miniature low-loss CPW periodic structures for filter applications," *IEEE Trans. Microw. Theory Techn.*, vol. 49, no. 12, pp. 2336-2341, Dec. 2001.

Jun Wang was born in Jiangsu, China. He received the B.S. and M.S. degrees from Jiangsu Normal University, Xuzhou, China, in 2013 and 2017, respectively. He is currently pursuing the Ph.D. degree with Southeast University, Nanjing, China. His research interests include the design of RF/microwave antennas and components.

Yanhui Liu was born in Hebei, China. She received the M.S degrees in the application of Information Systems from China University of Geosciences (Beijing) in 2014. Since 2014, she works at AVIC Beijing Changcheng Aeronautical Measurement & Control Technology Research Institute. Her current research interests include automated test systems and related standards.

Lei Zhao (M'09–SM'18) received the B.S. degree in Mathematics from Jiangsu Normal University, China, 1997, the M.S. degree in Computational Mathematics, and the Ph.D. degree in Electromagnetic Fields and Microwave Technology from Southeast University, Nanjing, China, in 2004 and 2007, respectively.

He joined the China University of Mining and Technology, Xuzhou, China, in 2019, where he is currently the Full Professor. From Sept. 2009 to Dec. 2018, he worked in Jiangsu Normal University, Xuzhou, China. From Aug. 2007 to Aug. 2009, he worked in Department of Electronic Engineering, The Chinese University of Hong Kong as a Research Associate. From Feb. 2011 to Apr. 2011, he worked in Department of Electrical and Computer Engineering, National University of Singapore as a Research Fellow. From Sep. 2016 to Sep. 2017, he worked in Department of Electrical and Computer Engineering, University of Illinois at Urbana-Champaign, USA as a visiting scholar. He has authored and coauthored over 60 referred journal and conference papers. His current research interests include spoof surface plasmon polaritons theory and its applications, antennas design and its applications, computational

electromagnetics, and electromagnetic radiation to human's body.

Zhao serves as an Associate Editor for IEEE Access, an Associate Editor-in-Chief for ACES Journal and a reviewer for multiple journals and conferences including the IEEE Trans. on Microwave Theory and Techniques, IEEE Trans. Antennas and Propagation, IEEE Access, IEEE Antennas and Wireless Propagation Letters, ACES Journal, and other primary electromagnetics and microwave related journals.

Zhang-Cheng Hao (M'08-SM'15) received the B.S. degree in Microwave Engineering from XiDian University, Xi'an, China, in 1997, and the M.S. degree and Ph.D. degree in Radio Engineering from Southeast University, Nanjing, China, in 2002 and 2006, respectively. In 2006, he was a Postdoctoral Researcher with the Laboratory of Electronics and Systems for Telecommunications, École Nationale Supérieure des Télécommunications de Bretagne, Bretagne, France, where he was involved with developing millimeter-wave antennas. In 2007, he joined the Department of Electrical, Electronic and Computer Engineering, Heriot-Watt University, Edinburgh, U.K., as a Research Associate, where he was involved with developing multilayer integrated circuits and ultra-wide-band components. In 2011, he joined the School of Information Science and Engineering, Southeast University, Nanjing China as a professor. He holds 20 granted patents and has authored and coauthored over 150 referred journal and conference papers. His current research interests involve microwave and millimeter-wave systems, submillimeter-wave and terahertz components and passive circuits, including filters, antenna arrays, couplers and multiplexers.

Hao has served as the reviewer for many technique journals, including IEEE Trans. On MTT, IEEE Trans. On AP, IEEE AWPL and IEEE MWCL. He was the recipient of the Thousands of Young Talents presented by China government in 2011 and the High Level Innovative and Entrepreneurial Talent presented by Jiangsu Province, China in 2012.

Lei Qiao is a Professor of Beijing Institute of Control Engineering. His research interests involve operating system design and verification with a focus on OS architecture design, efficient OS scheduler design and formal verification, memory management design and formal verification.

A Qualitative Deep Learning Method for Inverse Scattering Problems

He Yang [1] **and Jun Liu** [2]

[1]Department of Mathematics, Augusta University, Augusta, GA 30912, USA
hyang1@augusta.edu

[2]Department of Mathematics and Statistics, Southern Illinois University Edwardsville, Edwardsville, IL 62026, USA
juliu@siue.edu

Abstract **–** In this paper, we propose a novel deep convolutional neural network (CNN) based qualitative learning method for solving the inverse scattering problem, which is notoriously difficult due to its highly nonlinearity and ill-posedness. The trained deep CNN accurately approximates the nonlinear mapping from the noisy far-field pattern (from measurements) to a disk that fits the location and size of the unknown scatterer. The used training data is derived from the simulated noisy-free far-field patterns of a large number of disks with different randomly generated centers and radii within the domain of interest. The reconstructed fitting disk is also very useful as a good initial guess for other established nonlinear optimization algorithms. Numerical results are presented to illustrate the promising reconstruction accuracy and efficiency of our proposed qualitative deep learning method.

Index Terms **–**convolutional neural network, deep learning, inverse acoustic scattering, qualitative method.

I. INTRODUCTION

Inverse scattering problems [1] arise in many fields of science and engineering, such as radar and sonar, biomedical imaging, and non-destructive testing. In the last few decades, many numerical algorithms have been developed for solving such nonlinear and ill-posed inverse problems, see, e.g., [2, 3]. In this paper, we propose a new deep learning based qualitative method.

Existing algorithms can be roughly categorized into two groups: (i) nonlinear optimization methods, and (ii) qualitative methods. The nonlinear optimization methods [4, 5] often need to solve a direct (forward) scattering problem at each iteration. Although such methods require less amount of data, they indeed require *a priori* knowledge of the boundary conditions of the unknown scatterer (e.g, sound-soft or not), which may not be available. Furthermore, if the initial guess is far away from the true solution, the optimization iterations may converge to a local minimum, leading to an inaccurate reconstruction of the true scatterer. On the other hand, the qualitative methods [6–9], including the linear sampling method (LSM) [6], the factorization method (FM) [10], and the direct sampling method (DSM) [3], have the advantage of not requiring much *a priori* information about the unknown scatterer. In addition, such qualitative methods were shown to be computationally faster than the nonlinear optimization methods and are highly parallelizable. However, it is well-known that both LSM and FM suffer from the severely ill-conditioned discretized far-field operator, which requires a costly Tikhonov regularization in order to achieve a robust approximation accuracy in the presence of noise in measured far-field data. To reduce the computational cost, an adaptive quadrature-based factorization method (AFM) was recently developed in [11, 12], which dramatically speeds up the standard FM while gives comparable reconstructions. Nevertheless, an effective implementation of the Tikhonov regularization relies on the knowledge of the unknown noise level. The recently developed DSM [3] and direct factorization method (DFM) [13] were shown to be capable of achieving similar reconstruction accuracy, without resorting to any such Tikhonov regularization processes. Therefore, such regularization-free DSM and DFM are more suitable to the real world applications.

All the above-discussed qualitative methods strive to reconstruct the accurate location and precise shape of the unknown scatterer, which sometimes may be unnecessary for some practical applications. In such situations, we merely need to find a rough estimation of the scatterer's location and size (support), which hopefully can be achieved with lower computational cost or even less amount of data. For example, the approach in [14] only approximately recovers a convex hull of obstacles by using limited aperture data. The range test method in [15] obtains a convex support of the scatterer as the intersection of many convex test domains. More recently, an interesting extended sampling method (ESM) was proposed in [16] and further improved in [17], where a fitting disk was identified to estimate the support (location and size) of the scatterer. In other words, the precise shape of unknown scatterer is not of primal interest anymore, but

Submitted On: November 17, 2019
Accepted On: January 10, 2020

its size (or support) is the reconstruction target.

In this paper, we propose a deep learning based qualitative method for solving the inverse scattering problems. Nowadays, most deep learning methods are based on the artificial neural networks, which are effective models for approximating certain functions. There are many types of neural networks (NNs), including the feedforward and recurrent NN. The feedforward NN is a network from the input layer to the output layer without any loops. Some widely used NNs, including the multilayer perceptron [18], the autoencoder [19], the convolutional NN [20] and the U-Net [21], belong to the category of feedforward NNs. The recurrent NNs, by contrast, can pass data forward and backward. For example, long short-term memory (LSTM) [22] is a type of recurrent NN. Since the pioneering work by Krizhevsky, Sutskever and Hinton [23], deep learning methods have been applied in various fields, including image recognition, medical imaging and language translation. Recently, deep learning approaches [24] have also been used to solve the inverse scattering problems. In particular, the authors in [25] proposed an U-net convolutional neural network to reconstruct the permittivities of dielectric scatters from the scattering data. In [26], the authors developed a convolutional neural network for the far-field subwavelength imaging. In [27], the authors proposed the so-called SwitchNet to reconstruct the scatterer field which is a mixture of Gaussians. Different from the aforementioned work, our present paper focuses on developing a *qualitative* method to approximate the location and size of the scatterer as a fitting disk, rather than its exact shape. Therefore, the training process of our proposed CNN is more efficient and the prediction is also robust with respect to noise. Moreover, our designed CNN utilizes three dropout layers which effectively prevent overfitting phenomena.

The remaining of the paper is organized as follows. In section II, we briefly review the standard inverse obstacle scattering problem. In section III, we describe our proposed deep convolutional neural network (CNN) for the inverse scattering problems. In section IV, we show some numerical results to demonstrate the performance of our proposed method. Finally, some concluding remarks are given in section V.

II. THE INVERSE OBSTACLE SCATTERING PROBLEM

Following [1], we briefly describe the standard inverse obstacle scattering problem. Let $D \subset \mathbb{R}^2$ be a bounded impenetrable sound-soft obstacle with a C^2 boundary ∂D. Let θ be an incident direction on the unit circle $\mathbb{S}$ and $\kappa > 0$ be the wave number (with wavelength $\lambda = 2\pi/\kappa$ meters). Given a time-harmonic incident plane wave field $u^i(x) = e^{i\kappa x\cdot\theta}$, its propagation in the presence of the obstacle D, which is situated in a homogeneous medium, will lead to a scattered wave field u^s. Then the obtained total field $u = u^i + u^s$ is the solution to the following scalar exterior Helmholtz equation:

$$\Delta u(x) + \kappa^2 u(x) = 0, \quad x \in \mathbb{R}^2\backslash\overline{D} \tag{1}$$

subject to the Dirichlet boundary condition (sound-soft)

$$u = 0, \quad \text{on} \quad \partial D \tag{2}$$

and the Sommerfeld radiation condition (here $|x|$ denotes the distance between x and the origin):

$$\lim_{|x|\to\infty} |x|^{\frac{1}{2}} \left(\frac{\partial u^s}{\partial |x|} - i\kappa u^s\right) = 0. \tag{3}$$

The above direct scattering problem (1-3) admits a unique solution $u \in C^2(\mathbb{R}^2\backslash\overline{D})\bigcap C^1(\mathbb{R}^2\backslash D)$. Moreover, the scattered field u^s has the asymptotic behavior:

$$u^s(x) = \frac{e^{i\kappa|x|}}{|x|^{1/2}} u^\infty(\hat{x},\theta) + O(|x|^{-3/2})$$

(as $|x| \to \infty$) uniformly in all directions, where $\hat{x} = x/|x|$ is the observation direction on the unit circle $\mathbb{S}$ and u^∞ is called the far-field pattern. Obviously, the measurable far-field pattern $u^\infty : \mathbb{S}\times\mathbb{S} \to \mathbb{C}$ depends nonlinearly on the obstacle's shape ∂D that is to be determined.

The standard inverse obstacle scattering problem is to recover the obstacle's shape ∂D from the measured noisy far-field pattern data $u^\infty(\hat{x},\theta)$ with a fixed $\kappa > 0$ for all incident directions $\theta \in \Gamma_s$ and observation directions $\hat{x} \in \Gamma_m$. In this paper, we assume full aperture data i.e. $\Gamma_s = [0, 2\pi]$ and $\Gamma_m = [0, 2\pi]$.

More precisely, we essentially need to invert the following nonlinear abstract operator equation:

$$\mathcal{F}(\partial D) = u^\infty(\hat{x},\theta), \quad \hat{x},\theta \in \mathbb{S},$$

where the forward operator $\mathcal{F}$ maps the boundary of the obstacle D to the corresponding far-field pattern for all pairs of directions $(\hat{x},\theta)$. This abstract operator equation turns out to be highly nonlinear and severely ill-posed, and it has been solved by Newton's method [4,28], with the Fréchet derivative of $\mathcal{F}$ being inverted using Tikhonov regularization at each iteration. Such a locally convergent nonlinear iterative method is costly in practical computations and its effectiveness highly depends on the initial guess, i.e., the *a priori* information, which may lead to incorrect approximations.

The main difficulty in the accurate reconstruction of ∂D lies in the nonlinearity and ill-posedness of $\mathcal{F}$, although ∂D is indeed uniquely determined by u^∞ on the unit disk. The inverse map $\mathcal{F}^{-1}$ from u^∞ to ∂D is not easy to compute numerically, but it may be easier to approximate if we simply estimate ∂D by a disk $B(z;r)$ with center $z = (x,y) \in [a,b]\times[c,d]$ and radius $r \in [r_{\min}, r_{\max}]$. Inspired by several recent works [25–27, 29–33] in this direction, we propose to qualitatively approximate $\mathcal{F}^{-1}$ by a convolutional neural network (CNN), denoted by $\mathcal{G}$, based on the simulated training data of randomly generated disks within a prescribed domain containing D. The trained CNN $\mathcal{G}$ approximately

maps the noisy far-field pattern data to a fitting disk (including its center location (x, y) and radius r), which is poised to estimate the support of the underlying unknown scatterer. The availability of a large amount of simulated training data is crucial to optimize such a robust qualitative CNN, so that it achieves a satisfactory approximation accuracy. Theoretically, one can also use any other shapes (e.g., ellipse) of interest to simulate the training data, but it will become computationally more expensive due to more degrees of freedom in parameterizing the targeting irregular shapes. The disk shape is the simplest since its far-field pattern is invariant with respect to rotation, and only 3 parameters (x, y, r) are sufficient to identify a disk.

III. A DEEP CONVOLUTIONAL NEURAL NETWORK

In this section, we introduce our deep convolutional neural network (CNN) for qualitatively solving the above inverse obstacle scattering problems. Generally speaking, a CNN can be regarded as the composition of a sequence of functions, with each function representing a layer that takes the output of the previous layer and computes the input for the next layer. For the classification tasks, for example in [34], the architecture of a CNN generally consists of convolutional layers, pooling layers, activation layers, dropout layers and a loss layer. For the tasks of regression, however, sometimes the pooling layer is not necessary in the CNN architecture [35].

In this work, we construct and train a deep convolutional neural network using the disk-shape scatterers and the corresponding far-field data matrices. All lengths are measured in meters (m). We first generate 5000 circles with their x- and y-coordinates randomly distributed between $a = c = 0.5$ and $b = d = 10$, and their radii are randomly distributed in $[r_{\min} = 0.5, r_{\max} = 5]$. For each circular obstacle, we further simulate the corresponding noisy far-field data matrix of size 32×32, representing 32 incident and observation directions. Since each far-field data matrix is a 32-by-32 complex matrix, it can be treated as a $32 \times 32 \times 2$ tensor, which is then used as the input of our CNN. The output of the CNN is a 3-by-1 vector representing the x- and y-coordinates as well as the radius of the corresponding circular obstacle. Next, we use the dataset (far-field data matrices) for the input of the deep CNN of size $32 \times 32 \times 2 \times 5000$, and their corresponding labels (ground truth centers and radii) of size $3 \times 1 \times 5000$ to train and test our designed CNN. It is worthwhile to emphasize that a much larger size of dataset can be easily simulated if a higher accuracy is pursued, which however takes longer training time. We remark that the architecture of our proposed convolutional neural network is quite different from those networks developed in [25–27, 30–33]. One special feature of our designed network architecture is that there are three dropout layers. Numerical simulations show that the network with these dropout layers leads to much better results than the network without dropout layers. This can prevent overfitting efficaciously so that the prediction are very accurate for both the training and test dataset. Our proposed CNN mainly serves as a proof of concept to demonstrate the feasibility of such a qualitative deep learning approach, which we believe has a lot more room for improvement in terms of different network architecture and better reconstruction accuracy.

The architecture of our deep convolutional neural network is depicted in Fig. 1, where the detailed configuration of each layer is summarized in Table 1. The output of the current layer is of the same size as the input of the next layer. The first layer of the network is a convolutional layer with 30 filters of size 5×5, stride size of 2×2, and the same size padding. The first layer is followed by a rectified linear unit (ReLU) layer. The third layer is a dropout layer which randomly selects the input neurons to zero according to 10% probability. Such a layer is used to prevent overfitting efficiently [23, 36]. The fourth to the sixth layers are the convolutional layer, ReLU layer and the dropout layer, respectively. The seventh to the ninth layers are arranged in the same pattern. The fourth layer, i.e., the convolutional layer, has 60 filters of size 3×3, with stride size of 3×3 and the same size padding. Another convolutional layer, i.e., the seventh layer, has 180 filters of size 3×3 with stride size of 2×2 and the same size padding. The sixth and ninth layers are both dropout layers which set the input neurons to zero according to 10% probability. The tenth layer is a fully connected layer which combines all the information from previous layers and predicts the radius and coordinates of the fitting disk. The output of this layer will be further used to compute the mean-square error between the predicted and the ground truth labels (3×1 vectors).

Mathematically, if we reshape each layer of neurons as a column vector, then our convolutional neural network $\mathcal{G}$ can be represented by a nonlinear mapping:

$$\mathcal{G}(v) := A_4 \,\mathrm{ReLU}(A_3 \,\mathrm{ReLU}(A_2 \,\mathrm{ReLU}(A_1 v))) + g,$$

where v is a 2048-by-1 vector representing the input far-field data, A_1, A_2 and A_3 are the sparse Toeplitz matrices due to the convolution operators, ReLU is the element-wise Rectified Linear Unit function, A_4 is a dense weight matrix and g is a bias vector. Both A_4 and g are from the last fully connected layer. The output $\mathcal{G}(v)$ is a 3×1 vector. Given m pairs of training data (v_i, w_i) for $i = 1, 2, \ldots, m$, where v_i is the far-field data and w_i is the corresponding ground truth label, the training process is to minimize the total mean-square error, i.e.,

$$\min_{A_k, g} \quad \frac{1}{m} \sum_{i=1}^{m} \|\mathcal{G}(v_i) - w_i\|_2^2. \tag{4}$$

In our simulations, about half million parameters (includ-

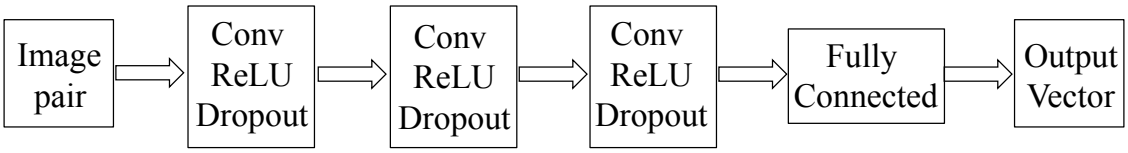

Fig. 1. Our proposed network architecture $\mathcal{G}$. The input image is of size $32 \times 32 \times 2$. There are three convolutional layers, three activation layers, three dropout layers, and one fully connected layer.

Table 1: Detail layers of our proposed deep convolutional neural network architecture $\mathcal{G}$

Layer	Type	Filter #	Filter Size	Stride Size	Input Size	Output Size
1	Conv	30	5×5	2×2	$32 \times 32 \times 2$	$32 \times 32 \times 30$
2	ReLU	-	-	-	$32 \times 32 \times 30$	$32 \times 32 \times 30$
3	Dropout	-	-	-	$32 \times 32 \times 30$	$32 \times 32 \times 30$
4	Conv	60	3×3	2×2	$32 \times 32 \times 30$	$32 \times 32 \times 60$
5	ReLU	-	-	-	$32 \times 32 \times 60$	$32 \times 32 \times 60$
6	Dropout	-	-	-	$32 \times 32 \times 60$	$32 \times 32 \times 60$
7	Conv	180	3×3	2×2	$32 \times 32 \times 60$	$32 \times 32 \times 180$
8	ReLU	-	-	-	$32 \times 32 \times 180$	$32 \times 32 \times 180$
9	Dropout	-	-	-	$32 \times 32 \times 180$	$32 \times 32 \times 180$
10	Fully Connected	-	-	-	$32 \times 32 \times 180$	3×1

ing $A_k (k = 1, 2, 3, 4)$ and g) of the CNN can be updated iteratively by the stochastic gradient descent (SGD) method (implemented in MATLAB Deep Learning Toolbox). Figure 2 shows the typical convergence history.

IV. NUMERICAL RESULTS

In this section, we provide several 2D inverse acoustic scattering examples from impenetrable and sound-soft obstacles to demonstrate the effectiveness of our proposed deep learning method. All simulations are implemented in MATLAB 2019a on a Dell Laptop with Intel(R) Core(TM) i7-7700HQ CPU@2.80GHz and 32GB RAM. The CPU time (in seconds) is estimated using timing functions `tic/toc`. To simulate the measurement noise, we added random noise to the simulated far-field data $F \in \mathbb{C}^{N \times N}$ according to:

$$F^{\delta} = F + \delta \|F\| \frac{S_1 + S_2 i}{\|S_1 + S_2 i\|},$$

where S_1 and S_2 are two $N \times N$ random matrices (with a standard normal distribution) generated by the MATLAB function `randn(N,N)`. Here the value of δ represents the level of noise based on relative error and the noise-free situation corresponds to the case with $\delta = 0\%$.

In our simulated training data, we choose the wave number $\kappa = 5$, the total number of incident and observation directions $N = 32$, and the noise level $\delta = 0\%$. As we have mentioned in the previous section, we first generate 5000 random circles of random radius between 0.5 and 5, and random x- and y-coordinates between 0.5 and 10. We then use these circles as the training scatterers, and generate the far-field data for each circle via the Nyström method [1]. We mention that numerical discretization errors are much smaller than the added noise. Our training dataset consists of $m = 4000$ far-field data matrices of size $32 \times 32 \times 2$, and 4000 corresponding labels of size 3×1. The remaining 1000 pairs are used as test dataset. We train our convolutional neural network using the training dataset and the SGD method with learning rate 0.01 and 1000 epochs. We use mini-batches of size 128 to speed up the computation time in each iteration. The training history of our convolutional neural network can be seen in Fig. 2. The blue curve is the base 10 logarithm of the mini-batch training loss, and the red curve the logarithm of the testing loss. Figure 2 indicates the convergence of the stochastic gradient descent method in the training procedure. We remark that different networks or learning rates may lead to different convergence rate.

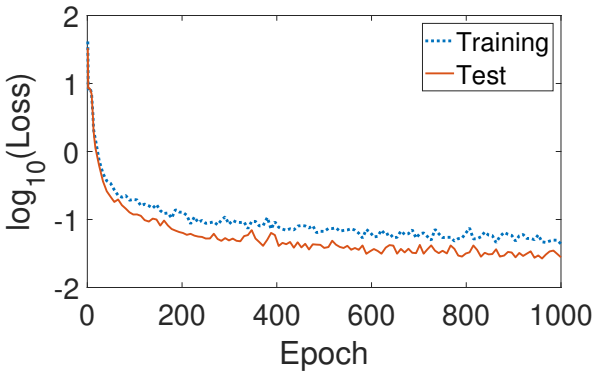

Fig. 2. Training history of our convolutional neural network. Horizontal axis: epoch number; vertical axis: logarithm (base 10) of the mini-batch loss.

Table 2: Mean square errors for the inverse scattering problem of circular scatterers with various random noise levels δ in the far-field data

Noise Level δ	Mean Square Error
0%	0.17249
10%	0.20229
20%	0.41218
30%	0.66666
40%	1.02110
50%	1.33220

Our results also show that the mean square errors of the training dataset and the test dataset are 0.13648 and 0.17249, respectively. Such convergence results indicate that our deep convolutional neural network model can generalize well from our training dataset to the unseen test dataset. A larger dataset would lead to better accuracy and it is also possible to use noisy far-field data as training dataset for better robustness.

We then investigate the performance of our deep neural network in reconstruction given far-field data with various noise levels. In Table 2, we present the mean square errors for the inverse scattering problem of 6000 circular scatterers (1000 scatterers for each test), with random noise levels $\delta = 0\%, 10\%, 20\%, 30\%, 40\%$ and 50% in the far-field data. The mean square errors are computed based on the prediction of our trained network, including the predicted radii, x- and y-coordinates of the centers. We observe that the mean square errors for $\delta = 0\%$ and 10% are quite similar. As the noise level goes up to 20%, the mean square error becomes twice as much as the error when $\delta = 10\%$ is used, but the roughly linear growth of error is still acceptable. When $\delta = 50\%$, the mean square error increases more dramatically due to the large amount of noise. Since we use circular objects with random locations and sizes, it is meaningful to check the relative errors of the predicted results. More specifically, (1) for $\delta = 0\%$, we find that 938 out of 1000 testing scatterers have the relative error of radius less than 0.1; 911 out of 1000 testing scatters have the relative error of the x-coordinate of the center less than 0.1; 937 out of 1000 testing scatterers have the relative error of the y-coordinate of the center less than 0.1. (2) For the dataset with 10% relative noise, 931 out of 1000 testing scatterers have the relative error of radius less than 0.1; 885 out of 1000 testing scatters have the relative error of the x-coordinate of the center less than 0.1; 890 out of 1000 testing scatterers have the relative error of y-coordinate of the center less than 0.1. (3) For $\delta = 20\%$, the numbers of testing scatterers that have relative error of radius, x- and y-coordinates to be less than 0.1 are 915, 718 and 745 out of 1000, respectively. These statistics indicate that our trained CNN can solve the inverse scattering problems of a circular object accurately in a high probability.

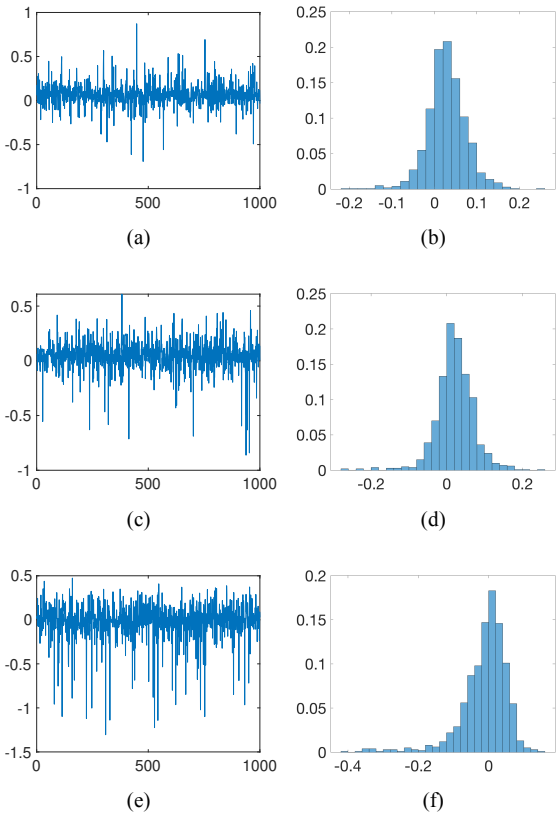

Fig. 3. The distribution of the prediction errors of the radii (left column) and the histogram of the relative errors (right column) with 3000 random far-field data under various noise levels: $\delta = 0\%$ (top row), 10% (middle row) and 20% (bottom row).

Moreover, among all three predicted parameters, the predicted radius is usually more accurate than the other parameters. This is due to the fact that the maximum of radii is smaller than that of x- and y-coordinates of the centers. In Fig. 3, we present the distribution of the prediction errors of the radii (in the left column) and the histogram of the relative errors (in the right column), where randomly perturbed far-field data with various noise levels are used. The prediction errors are roughly proportional to the added noise magnitude. We observe that the distributions of the relative errors in radius for $\delta = 0\%$ and 10% are quite similar, which means that our trained network is not sensitive to a small noise level.

Next, we investigate the performance of the proposed deep learning method for reconstructing randomly located scatterers with various shapes. In Figs. 4-6, we show the reconstructed fitting disks for obstacles in the shape of a circle, ellipse, rectangle, kite, peanut and triangle with $\delta = 0\%, 20\%$ and 40%, respectively. The center of mass for each object mostly lies in the reconstructed disk, although we do observe slightly increasing discrep-

ancy as the noise level becomes larger. For $\delta = 0\%$ and 20%, it is easy to see that the circular and triangular objects lead to the most accurate results. The reconstructed results for the obstacles in the shape of ellipse, kite and peanut for $\delta = 0$ and 20% are comparable. However, the reconstructed result for an object in the shape of a rectangle is worse when $\delta = 20\%$. For far-field data with $\delta = 40\%$, our trained network can still capture the unknown objects well except for the rectangular one.

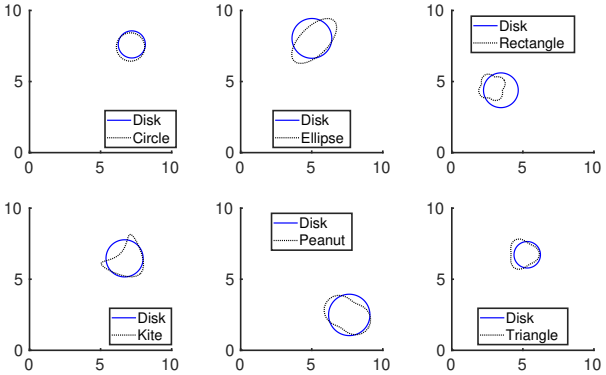

Fig. 4. The reconstructed fitting disks for randomly located different testing scatterers (noise level $\delta = 0\%$).

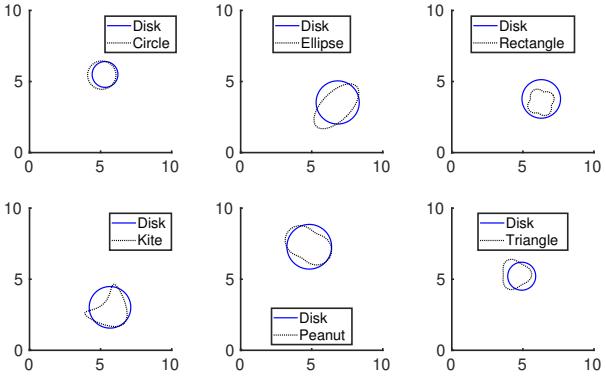

Fig. 5. The reconstructed fitting disks for randomly located different testing scatterers (noise level $\delta = 20\%$).

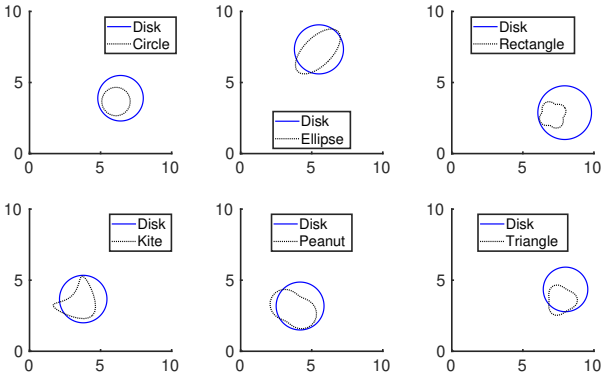

Fig. 6. The reconstructed fitting disks for randomly located different testing scatterers (noise level $\delta = 40\%$).

Figure 7 shows the reconstruction results for scatterers of various sizes. While most of the predicted disks are accurate, the rectangular-shape object was overestimated again. In particular, the radius of small scatterers (ellipse and peanut) is about 0.1, which is smaller than the minimal radius 0.5 used in the training dataset.

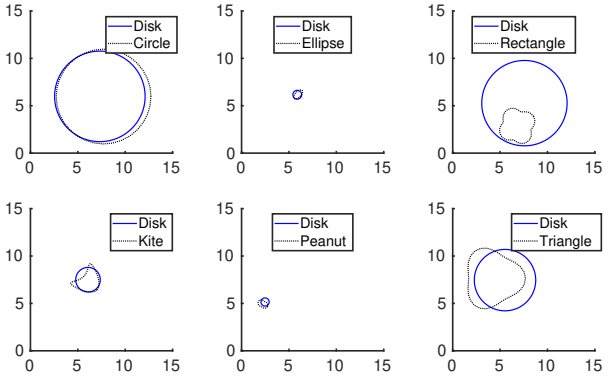

Fig. 7. The reconstructed fitting disks for randomly located scatterers of various sizes (noise level $\delta = 0\%$).

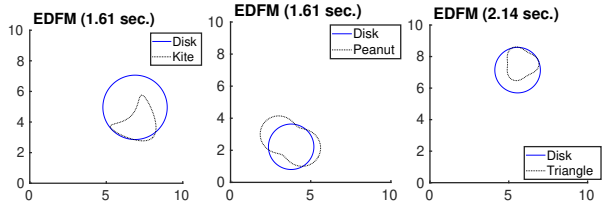

Fig. 8. The reconstructed fitting disks by EDFM [17] for randomly located scatterers (noise level $\delta = 40\%$). The EDFM is based on one incident direction at $\pi/2$ and 32 observation directions with a 500×500 sampling mesh.

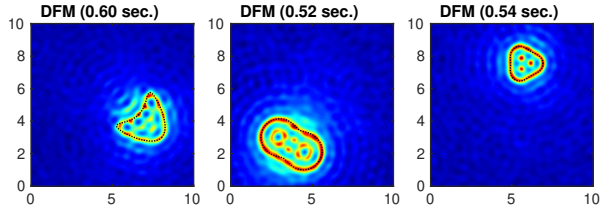

Fig. 9. The reconstructed profiles by DFM [13] for the same scatterers as in Fig. 7 (noise level $\delta = 40\%$). The DFM is based on 32 incident and observation directions with a 500×500 sampling mesh.

High computational efficiency is another remarkable advantage of our deep learning method, which of course relies on the expensive offline training that can be speed up by CPU/GPU parallel computing. Different from the extended sampling method [16] and the extended direct factorization method (EDFM) [17], where the radius is obtained with much more extra efforts after the center is chosen from a sampling process over the search domain, our deep learning method computes the radius and center simultaneously without any sampling procedure. With a pre-trained network, our deep learning method takes only *about 2 milliseconds* to estimate a fitting disk (using the

`predict` function provided by MATLAB).

As a comparison, Fig. 8 shows the corresponding results computed by the EDFM [17], where a similar fitting disk was estimated but with significantly higher CPU time. However, the EDFM can handle limited aperture data, which was not addressed in our deep learning model. In addition, Fig. 9 plots the constructed profiles by the highly efficient and vectorized DFM [13], where the same scatterers' shapes are qualitatively identified with more CPU time as well. Note the DFM gives much more detailed shape information that may not be necessary. In both EDFM and DFM, it would take much longer CPU time if using a finer sampling mesh in a larger domain.

Overall speaking, the trained CNN based solely on the circular-shape scatterers can handle the far-field data of the general shaped objects with various noise levels very well, where the non-circular shaped scatterers were never seen by the trained CNN. A possible explanation of the less satisfactory accuracy in reconstructing the rectangle scatterer is that its far-field pattern is vastly different from that of any nearby circular-shape scatterer, as illustrated in Fig. 10. Note that the far-field pattern of the kite is more similar to that of the circle, thus it leads to better reconstruction results. We would expect much improved reconstruction accuracy if the anticipated non-circular shapes were used in generating the training dataset. This is usually the case when tailored to a specific application where only certain shapes are of interest.

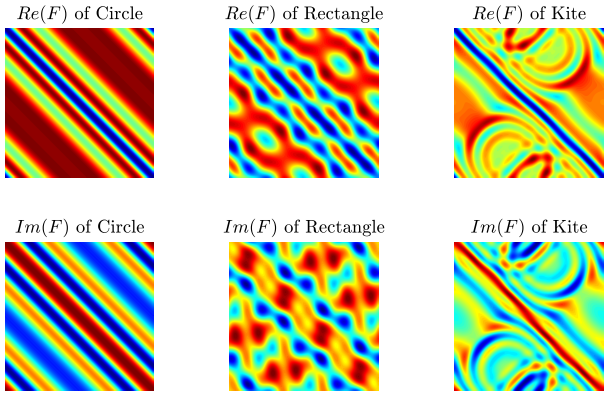

Fig. 10. The jet colormap of noise-free far-field data F of three different scatterers: Circle , Rectangle, and Kite.

V. CONCLUSION

In this paper, we propose a qualitative deep learning method for solving the inverse obstacle scattering problem. After constructing and training the deep convolutional neural network using the randomly generated disk-shape scatterers and the corresponding far-field data matrices, we can obtain a convolutional neural network which reliably maps the noisy far-field data to the center location and radius of the fitting disk that approximates the support of the unknown scatterer. The trained CNN has the advantage of solving the inverse scattering problem in much faster CPU time than other qualitative methods in literature. It takes only a few milliseconds (rather than a few seconds by EDFM and DFM) to estimate an accurate fitting disk with a PC laptop. Our numerical results show that our proposed deep CNN requires a small amount of training data to get very accurate predictions, and it performs very robust with noisy far-field data. The generalization of our proposed method on 2D problems (of finding a disk) to 3D problems (of finding a ball) is straightforward. It is possible to further improve the reconstruction accuracy by training the CNN with the dataset generated from other desired shapes (e.g., ellipse or airplanes). The application of our developed method to the inverse scattering problems with multiple obstacles or limited aperture data is currently undertaken.

REFERENCES

[1] D. Colton and R. Kress, *Inverse Acoustic and Electromagnetic Scattering Theory*, Springer New York, 2012.

[2] X. Liu and B. Zhang, "Recent progress on the factorization method for inverse acoustic scattering problems," *SCIENTIA SINICA Mathematica*, vol. 45, pp. 873–890, 2015.

[3] X. Liu, "A novel sampling method for multiple multiscale targets from scattering amplitudes at a fixed frequency," *Inverse Problems*, vol. 33, no. 8, p. 085011, 2017.

[4] A. Roger, "Newton-Kantorovitch algorithm applied to an electromagnetic inverse problem," *IEEE Transactions on Antennas and Propagation*, vol. 29, no. 2, pp. 232–238, 1981.

[5] G. Giorgi, M. Brignone, R. Aramini, and M. Piana, "Application of the Inhomogeneous Lippmann–Schwinger Equation to Inverse Scattering Problems," *SIAM Journal on Applied Mathematics*, vol. 73, no. 1, pp. 212–231, 2013.

[6] D. Colton, H. Haddar, and M. Piana, "The linear sampling method in inverse electromagnetic scattering theory," *Inverse Problems*, vol. 19, no. 6, pp. S105–S137, 2003.

[7] R. Potthast, "A survey on sampling and probe methods for inverse problems," *Inverse Problems*, vol. 22, no. 2, pp. R1–R47, 2006.

[8] T. Arens and A. Lechleiter, "The linear sampling method revisited," *Journal of Integral Equations and Applications*, vol. 21, no. 2, pp. 179–202, 2009.

[9] F. Cakoni and D. Colton, *A Qualitative Approach to Inverse Scattering Theory*, Springer US, 2013.

[10] A. Kirsch and N. Grinberg, *The Factorization Method for Inverse Problems*, OUP Oxford, 2008.

[11] K. H. Leem, J. Liu, and G. Pelekanos, "An adaptive quadrature-based factorization method for in-

verse acoustic scattering problems," *Inverse Problems in Science and Engineering*, vol. 27, no. 3, pp. 299–316, 2019.

[12] K. H. Leem, J. Liu, and G. Pelekanos, "Efficient Adaptive Qualitative Methods for 3D Inverse Scattering Problems," *ACES Journal*, vol. 33, no. 10, 2018.

[13] K. H. Leem, J. Liu, and G. Pelekanos, "Two direct factorization methods for inverse scattering problems," *Inverse Problems*, vol. 34, no. 12, p. 125004, 2018.

[14] M. Ikehata, E. Niemi, and S. Siltanen, "Inverse obstacle scattering with limited-aperture data," *Inverse Problems and Imaging*, vol. 6, no. 1, pp. 77–94, 2012.

[15] R. Potthast, J. Sylvester, and S. Kusiak, "A range test for determining scatterers with unknown physical properties," *Inverse Problems*, vol. 19, no. 3, pp. 533–547, 2003.

[16] J. Liu and J. Sun, "Extended sampling method in inverse scattering," *Inverse Problems*, vol. 34, no. 8, p. 085007, 2018.

[17] K. H. Leem, J. Liu, and G. Pelekanos, "An extended direct factorization method for inverse scattering with limited aperture data," *Inverse Problems in Science and Engineering*, p. to appear, 2019.

[18] F. Rosenblatt, *Principles of Neurodynamics: Perceptrons and the Theory of Brain Mechanisms*, Spartan Books, Washington DC, 1961.

[19] M. A. Kramer, "Nonlinear principal component analysis using autoassociative neural networks," *AIChE Journal*, vol. 37, no. 2, pp. 233–243, 1991.

[20] K. Fukushima, "Neocognitron: A self-organizing neural network model for a mechanism of pattern recognition unaffected by shift in position," *Biological Cybernetics*, vol. 36, no. 4, pp. 193–202, 1980.

[21] O. Ronneberger, P. Fischer, and T. Brox, "U-Net: Convolutional Networks for Biomedical Image Segmentation," *arXiv preprint*, vol. arXiv:1505.04597, 2015.

[22] S. Hochreiter and J. Schmidhuber, "Long short-term memory," *Neural Computation*, vol. 9, no. 8, pp. 1735–1780, 1997.

[23] A. Krizhevsky, I. Sutskever, and G. E. Hinton, "ImageNet classification with deep convolutional neural networks," *Communications of the ACM*, vol. 60, no. 6, pp. 84–90, 2017.

[24] H. Kabir, Y. Cao, Y. Cao, and Q. Zhang, "Advances of neural network modeling methods for RF/microwave applications," *ACES Journal*, vol. 25, no. 5, p. 423, 2010.

[25] Z. Wei and X. Chen, "Deep-learning schemes for full-wave nonlinear inverse scattering problems," *IEEE Transactions on Geoscience and Remote Sensing*, vol. 57, no. 4, pp. 1849–1860, 2019.

[26] H. Yao, M. Li, and L. Jiang, "Applying deep learning approach to the far-field subwavelength imaging based on near-field resonant metalens at microwave frequencies," *IEEE Access*, vol. 7, pp. 63801–63808, 2019.

[27] Y. Khoo and L. Ying, "SwitchNet: a neural network model for forward and inverse scattering problems," *SIAM Journal on Scientific Computing*, vol. 41, no. 5, pp. 3182–3201, 2019.

[28] R. D. Murch, D. G. H. Tan, and D. J. N. Wall, "Newton-Kantorovich method applied to two-dimensional inverse scattering for an exterior Helmholtz problem," *Inverse Problems*, vol. 4, no. 4, pp. 1117–1128, 1988.

[29] J. Adler and O. Öktem, "Solving ill-posed inverse problems using iterative deep neural networks," *Inverse Problems*, vol. 33, no. 12, p. 124007, 2017.

[30] L. Li, L. G. Wang, F. L. Teixeira, C. Liu, A. Nehorai, and T. J. Cui, "DeepNIS: Deep neural network for nonlinear electromagnetic inverse scattering," *IEEE Transactions on Antennas and Propagation*, vol. 67, no. 3, pp. 1819–1825, 2018.

[31] Y. Sanghvi, Y. N. G. B. Kalepu, and U. Khankhoje, "Embedding Deep Learning in Inverse Scattering Problems," *IEEE Transactions on Computational Imaging*, 2019.

[32] L. Li, L. G. Wang, D. O. Acero, and F. L. Teixeira, "Deep Convolutional Neural Network Approach for Solving Nonlinear Inverse Scattering Problems," in *2019 IEEE International Symposium on Antennas and Propagation and USNC-URSI Radio Science Meeting*, pp. 219–220, IEEE, 2019.

[33] Z. Wei and X. Chen, "Physics-Inspired Convolutional Neural Network for Solving Full-Wave Inverse Scattering Problems," *IEEE Transactions on Antennas and Propagation*, vol. 67, no. 9, pp. 6138–6148, 2019.

[34] H. Yang, H. Yu, and G. Wang, "Deep learning for the classification of lung nodules," *arXiv preprint*, vol. axXiv:1611.06651v2, 2017.

[35] H. Yang, W.-X. Cong, and G. Wang, "Deep learning for dual-energy X-ray computed tomography," *Proceedings of The 14th International Meeting on Fully Three-Dimensional Image Reconstruction in Radiology and Nuclear Medicine*, pp. 864–869, 2017.

[36] N. Srivastava, G. E. Hinton, A. Krizhevsky, I. Sutskever, and R. Salakhutdinov, "Dropout: a simple way to prevent neural networks from overfitting," *Journal of Machine Learning Research*, vol. 15, pp. 1929–1958, 2014.

Helmet Antenna Design Using Characteristic Mode Analysis

Naobumi Michishita and Hisashi Morishita

Department of Electrical and Electronic Engineering
National Defense Academy, Yokosuka, Kanagawa, 239-8686, Japan
naobumi@nda.ac.jp

Abstract ─ The helmet antenna is required to achieve hands-free operation for disaster prevention. The helmet antenna is not only low profile with a small configuration, but it also suppresses radiation toward the human head. This paper presents the characteristic mode analysis of the helmet, which is a hemispherical conductor shell to achieve the omnidirectional pattern in the horizontal plane. By deleting the weak part of the electric current on the hemispherical conductor shell, the shape of the folded dipole was obtained with a low resonant frequency. The folded dipole antenna with a slit-loaded copper ring structure with high radiation efficiency and a low SAR value was designed.

Index Terms ─ Characteristic mode analysis, folded dipole antenna, hemispherical shell, helmet antennas, omnidirectional pattern.

I. INTRODUCTION

For safety, a person must wear a helmet and use a transceiver in a one-hand operation. The helmet antenna is required to achieve hands-free operation. In the disaster radio systems operating at 150 MHz in Japan, the transceiver needs to be combined with the helmet for rescue operations. Helmet antennas are suitable for this purpose. In this case, the interaction between the antenna and the human body is essential [1], [2].

Helmet antennas have been investigated for various applications such as military, construction, and disaster prevention. The broadband [3] and omnidirectional radiation [4] are required for helmet antennas. In previous studies, the implementation of the antenna inside a helmet is also investigated. In various applications, the high-frequency antennas can be implemented efficiently in a helmet. However, it is challenging to implement low-frequency helmet antennas at 150 MHz in proximity to the human head.

For a radio system operated at a low frequency, the half-wavelength circular loop antenna [5] and the folded dipole antenna [6] have been proposed. The inverted-F antenna on a hemispherical ground plane has been proposed to enhance the antenna gain [7]. However, the inverted-F antenna has a narrow bandwidth. Since these antennas are arranged in proximity to the human head, the radiation efficiency is reduced, and the value of the specific absorption rate (SAR) increases. The installation of a conductor ring with the slit is effective [8] in reducing the unwanted radiation toward the human head.

The characteristics mode analysis (CMA) has been considered as the systematic design of the antenna shape [9], [10]. The design procedure using CMA has been adapted to the dual-mode antenna with orthogonal radiation patterns [11] and the ultra-wideband patch antenna [12]. However, to achieve the helmet antenna for low-frequency operation, low-profile and small antennas are required to be installed on a small platform. This paper presents the characteristic mode analysis of the helmet, which is a hemispherical conductor shell to achieve an omni-directional pattern in the horizontal plane.

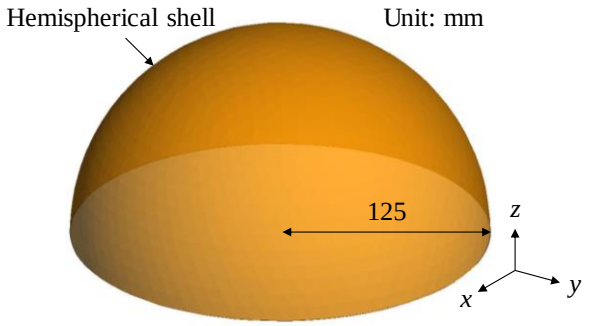

Fig. 1. Configuration of hemispherical conductor shell.

II. CHARACTERISTIC MODES ANALYSIS OF THE HEMISPHERICAL CONDUCTOR SHELL3

Figure 1 shows the simulation models of the hemispherical conductor shell with a radius of 125 mm. The antenna is assumed to be installed on the helmet formed from a dielectric material with ε_r = 3.0 and tanδ = 0.005. However, the characteristic modes are analyzed without the dielectric material, and by using Altair

Submitted On: August 20, 2019
Accepted On: February 23, 2020

FEKO Ver. 2019.0.1.

The modal significance [10] is defined as:

$$S_n = \left|\frac{1}{1+j\lambda_n}\right|. \quad (1)$$

Harrington and Mautz [9] obtained the eigenvalue equation as follows:

$$X(J_n) = \lambda_n R(J_n), \quad (2)$$

where λ_n are the eigenvalues, and J_n are eigenfunctions. R and X are the real and imaginary parts of the impedance matrix obtained from the moment method. Modes with a high modal significance are the current resonances of the structure. When the value of s_n is close to 1, the mode significantly contributes to radiation.

Figure 2 shows the modal significance characteristics of the hemispherical conductor shell. The resonant frequencies of J_1 and J_2 are over 600 MHz. The eigenvalue of J_1 becomes 0.02. Figure 3 shows the modal current distributions of J_1, J_2, J_3, and J_4. As shown in Figs. 3 (a) and (b), the current intensities become strong at the edge of the hemispherical shell. The resonant mode corresponds to a one-wavelength loop current. Furthermore, J_1 and J_2 are orthogonal to each other. Similarly, J_3 and J_4 are orthogonal to each other, as shown in Figs. 3 (c) and (d). In mode J_3, the edge current becomes strong. The current in the middle part of the shell becomes strong in the mode J_4.

Figure 4 shows the radiation patterns of each mode at 150 MHz. As shown in Figs. 4 (a) and (b), the radiation patterns of each polarization on the *xy* plane are shaped like the figure eight. The omnidirectional patterns of the horizontal and vertical polarization are obtained in mode J_3 and J_4, respectively. However, the resonance cannot be achieved easily because these modal significances are extremely low.

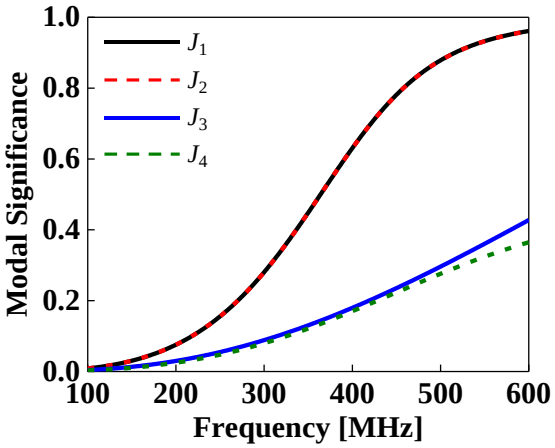

Fig. 2. Modal significance.

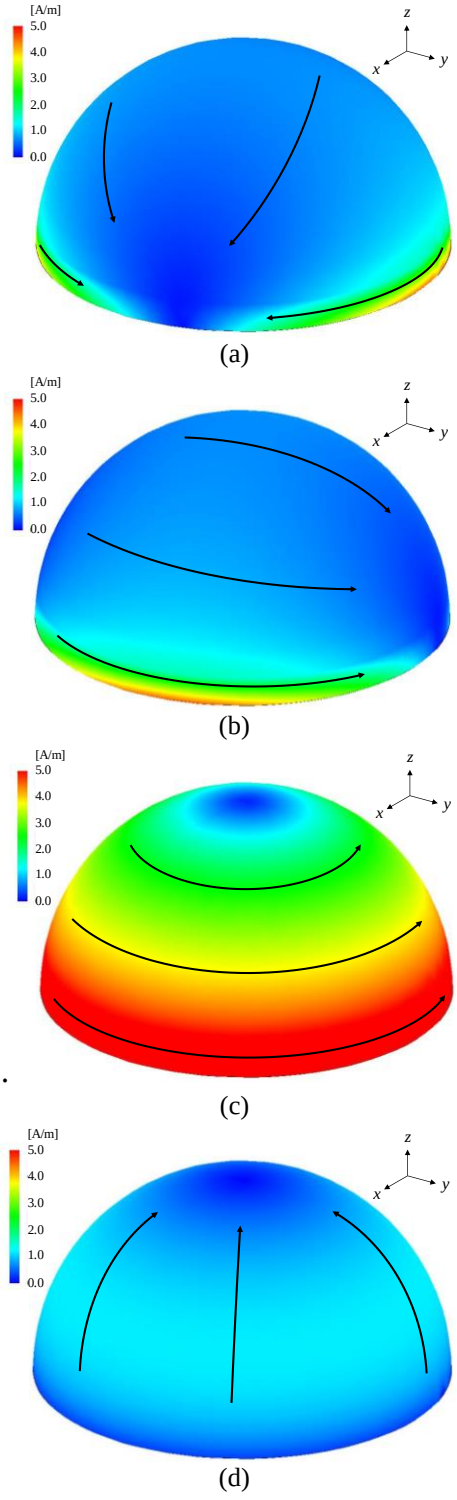

Fig. 3. Modal current distributions of: (a) J_1, (b) J_2, (c) J_3, and (d) J_4 on hemispherical shell.

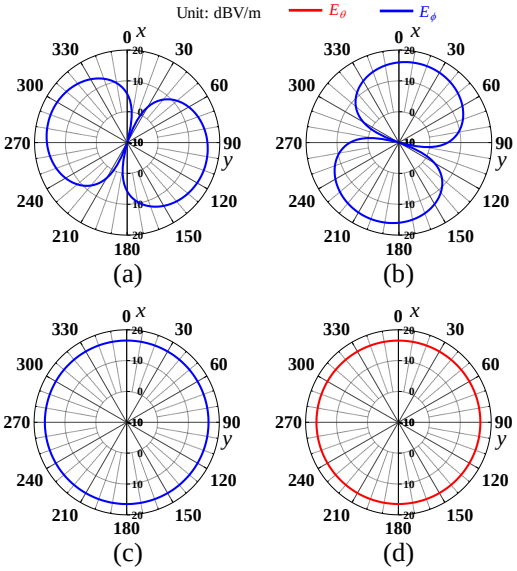

Fig. 4. Radiation patterns of: (a) J_1, (b) J_2, (c) J_3, and (d) J_4.

III. ANTENNA DESIGN BASED ON MODAL CURRENT DISTRIBUTIONS

Figure 5 shows the normalized modal current distribution of J_1. As shown in Fig. 5 (a), the strong electric current is distributed at the edge of the shell. The contour length of the edge of the shell corresponds to one wavelength loop.

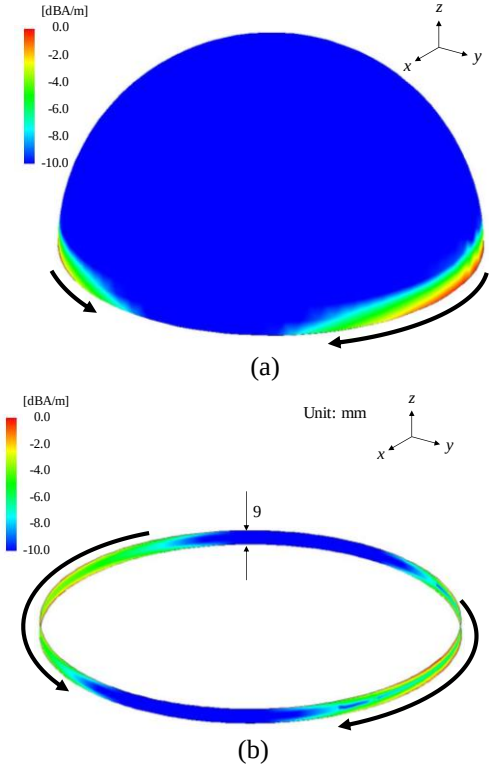

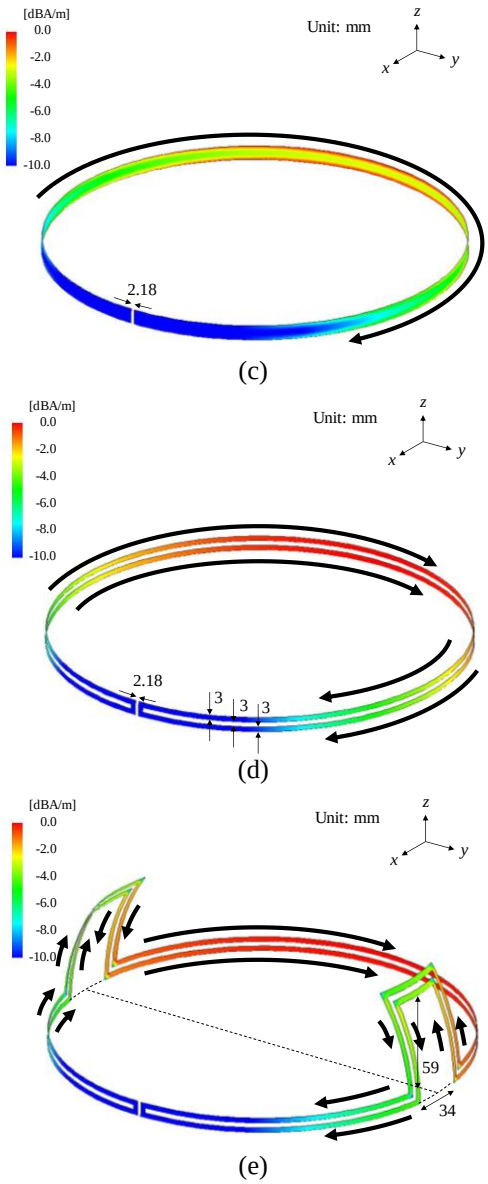

Fig. 5. Normalized modal current distributions of J_1 of: (a) model1, (b) model2, upper part of hemispherical shell is deleted, (c) model 3, slit is arranged, (d) model 4, middle part of conductor is deleted, and (e) model 5, crank structure is added.

Therefore, the upper part of the hemispherical shell is deleted as shown in Fig. 5 (b). The width of the conductor becomes 9 mm. The current flows widely on the conductor because of the narrow conductor.

To change the characteristic modes from the one-wavelength loop to the half-wavelength loop, the conductor is split, as shown in Fig. 5 (c). The slit with 2.18 mm width is arranged in the weak part of the electric current in the conductor in Fig. 5 (b). As a result, the electric current flows in one direction.

The current in the middle part of the conductor in Fig. 5 (c) becomes weak in comparison with that at the edge of the conductor. Therefore, the middle part of the conductor is deleted, as shown in Fig. 5 (d). The space between the two conductors is 3 mm. The current intensity of the two strips on the conductor increases. As a result, the configuration of the conductor takes the shape of a folded dipole.

Finally, two crank structures are added at the positions of the strong currents on the conductor in Fig. 5 (a) to adjust the resonant frequency, as shown in Fig. 5 (e).

IV. DESIGN RESULTS

Figure 6 shows the modal significance characteristics of each model, as shown in Fig. 5. The resonant frequency in model 2 becomes 408 MHz, and the resonant frequency of 173 MHz is confirmed by arranging the slit on the conductor in models 3 and 4. For the final design, the resonant frequency of 150 MHz can be achieved by installing the crank structures in model 5.

Figure 7 shows the radiation patterns on the *xy* plane of each model. In comparison with Fig. 4 (a), the radiation patterns of models 1 and 2 are almost the same, as shown in Fig. 7 (a). The radiation patterns with the slit on the conductor become omni-directional on *xy* plane as shown in Figs. 7 (b) and (c). The deviation in the *xy* plane is 4.5 dB in model 5 because of loading the crank structures.

The feed port is arranged at the center of the bottom conductor on the final configuration in Fig. 5 (e) to verify the validity of the characteristic mode analysis. Figure 8 shows the VSWR characteristics of the simulation and measurement. The measured result agrees with the simulated result. Therefore, the validity of the characteristic mode analysis is verified. Moreover, the antenna is attached to the dielectric material with ε_r = 3.0, $\tan\delta$ = 0.005, and a thickness of 2 mm. The resonant frequency shifts from 150 MHz to 136 MHz. Therefore, the dimension of the antenna should be adjusted during installation on the helmet.

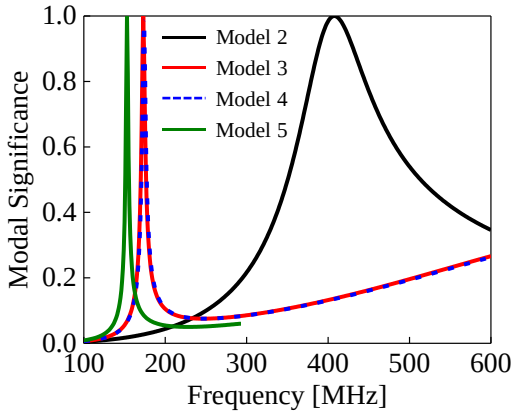

Fig. 6. Modal significance of J_1.

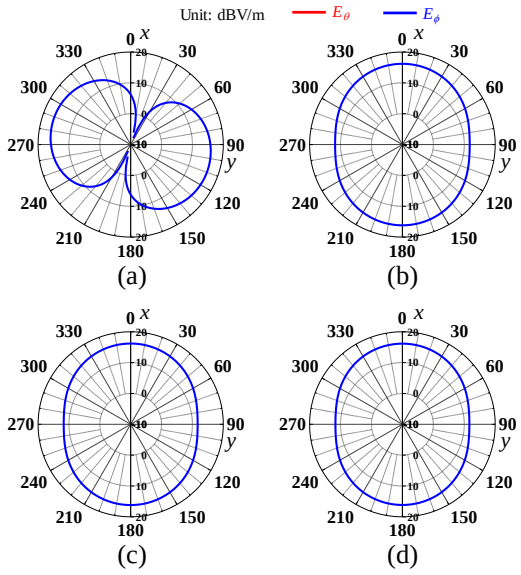

Fig. 7. Radiation patterns on *xy* plane of: (a) model 2, (b) model 3, (c) model 4, and (d) model 5.

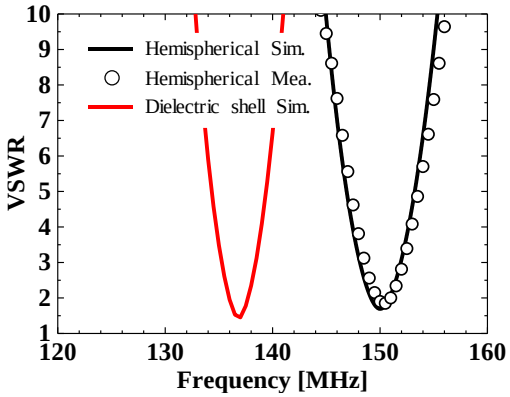

Fig. 8. VSWR characteristics.

V. FOLDED DIPOLE ANTENNA WITH SLIT-LOADED COPPER RING STRUCTURE

Figure 9 shows the simulation models of the folded dipole antenna with a human head with ε_r = 52.3 and a conductivity of 0.76 S/m. The antenna element is arranged on the hemispherical dielectric shell with ε_r = 3.0, $\tan\delta$ = 0.005, a radius of 125 mm, and a thickness of 2 mm. To achieve the impedance matching, the widths of the feed and non-fed arms of the dipole are 3 mm and 12 mm, respectively. Based on the previous results in [6], the additional conductor ring inside the helmet is effective for reducing the unwanted radiation towards the human head. Figure 9 (b) shows the slit-loaded copper ring structure to reduce the unwanted radiation toward the human head. The finite element method is employed for electromagnetic simulation.

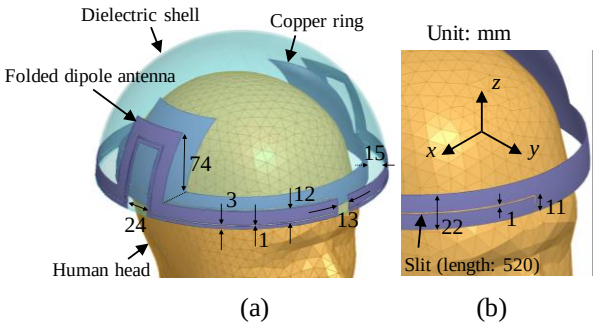

Fig. 9. (a) Configuration of folded dipole antenna with slit-loaded copper ring structure. (b) Detailed view.

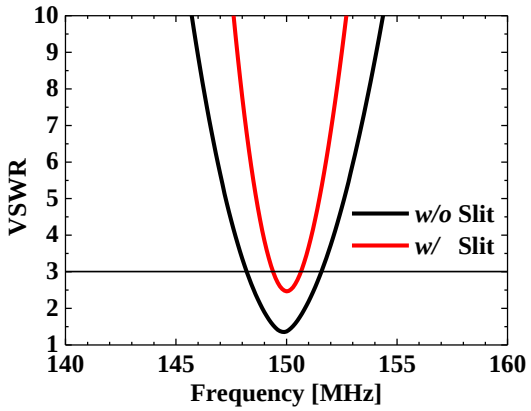

Fig. 10. VSWR characteristics.

Figure 10 shows the simulated VSWR characteristics. The relative bandwidth at VSWR = 3 becomes 2.1 % and 0.9 % with and without the slit, respectively. Figure 11 shows the radiation patterns. The radiation efficiency of 55 % can be achieved by loading the slit. As a result, the realized gain becomes −2.7 dBi. Figure 12 shows the simulated 10 g average local SAR distributions. The unwanted radiation toward the human head can be suppressed, and the maximum SAR value becomes 0.67 W/kg, which is lower than the specified value of 2 W/kg in the IEC 62209-1 standard.

VII. CONCLUSION

This paper presents the characteristic mode analysis of helmet antenna design. By deleting the weak part of the modal current on the hemispherical conductor shell, the shape of the folded dipole was obtained with a low resonant frequency of 150 MHz. The omnidirectional pattern can be achieved in the horizontal plane. A folded dipole antenna with slit-loaded copper ring structure, with a high radiation efficiency and a low SAR value, was designed.

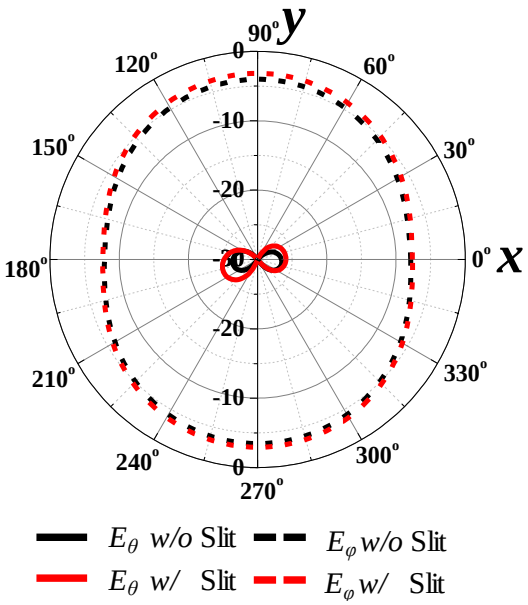

Fig. 11. Radiation patterns.

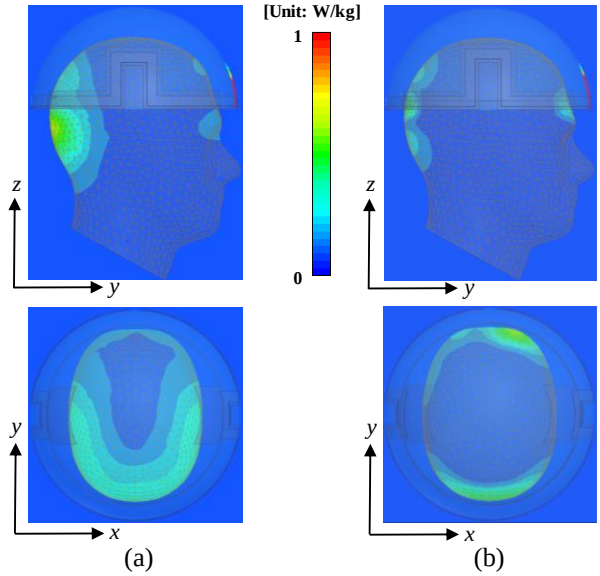

Fig. 12. 10 g average local SAR distributions: (a) without and (b) with slit.

ACKNOWLEDGMENT

This work was supported by JSPS KAKENHI Grant Number 15K06095.

REFERENCES

[1] H. King and J. Wong, “Effects of a human body on a dipole antenna at 450 and 900 MHz,” *IEEE Trans. Antennas Propag.*, vol. 25, no. 3, pp. 376-

379, 1977.

[2] H. R. Chuang, "Human operator coupling effects on radiation characteristics of a portable communication dipole antenna," *IEEE Trans. Antenna Propag.*, vol. 42, no. 4, pp. 556-560, Apr. 1994.

[3] J. Lebaric and A. T. Tan, "Ultra-wideband conformal helmet antenna," *Asia-Pacific Microw. Conf.*, Sydney, Australia, pp. 1477-1481, Dec. 2000.

[4] J. J. H. Wang, "Broadband omnidirectional helmet antennas," *IEEE AP-S Int. Symp.*, Albuquerque, NM, pp. 2129-2132, July 2006.

[5] J. Y. Park, H. K. Ryu, and J. M. Woo, "Helmet installed antenna using a half-wavelength circular loop antenna," *IEEE AP-S Int. Symp.*, Honolulu, HI, pp. 4176-4179, June 2007.

[6] T. Nakao, H. T. Nguyen, M. Nagatoshi, and H. Morishita, "Fundamental study on curved folded dipole antenna," *IEEE AP-S Int. Symp.*, Chicago, IL, pp. 1-2, July 2012.

[7] Y. Saita, T. Ito, N. Michishita, and H. Morishita, "Low frequency inverted-F antenna on hemispherical ground plane," *Int. Symp. Antennas Propag.*, Kaohsiung, Taiwan, pp. 183-184, Dec. 2014.

[8] N. Nishiyama, N. Michishita, and H. Morishita, "SAR reduction of helmet antenna composed of folded dipole with slit-loaded ring," *Int. Symp. Antennas Propag.*, Hobart, Australia, pp. 1-2, Nov. 2015.

[9] R. F. Harrington and J. R. Mautz, "The theory of characteristic modes for conducting bodies," *IEEE Trans. Antennas Propag.*, vol. 19, no. 5, pp. 622-628, Sept. 1971.

[10] M. Vogel, G. Gampala, D. Ludick, and C. J. Reddy, "Characteristic mode analysis: Putting physics back into simulation," *IEEE Antennas Propag. Mag.*, vol. 57, no. 2, pp. 307-317, Apr. 2015.

[11] A. Araghi and G. Dadashzadeh, "Detail-oriented design of a dual-mode antenna with orthogonal radiation patterns utilizing theory of characteristic modes," *ACES Journal*, vol. 28, no. 10, pp. 952-959, Oct. 2013.

[12] M. M. Elsewe and D. Chatterjee, "Ultra-wide bandwidth enhancement of single-layer single-feed patch antenna using the theory of characteristic modes," ACES Journal, vol.33, no.3, pp.363-366, March 2018.

Naobumi Michishita received the B.E., M.E. and D.E. degrees in Electrical and Computer Engineering from Yokohama National University, Yokohama, Japan, in 1999, 2001, and 2004, respectively. In 2004, he was a Research Associate at the Department of Electrical and Electronic Engineering, National Defense Academy, Kanagawa, Japan, where he is currently an Associate Professor. From 2006 to 2007, he was a Visiting Scholar at the University of California, Los Angeles. His current research interests include metamaterial antenna and electromagnetic analysis.

He is a member of the Institute of Electronics, Information and Communication Engineers (IEICE), Japan. He is also members of the Japan Society for Simulation Technology and the Institute of Electrical and Electronics Engineers (IEEE). He was the recipient of the Young Engineer Award presented by the IEEE Antennas and Propagation Society Japan Chapter and the IEICE, Japan (2004 and 2005). He received the Best Paper Award and the Best Tutorial Paper Award from the IEICE Communication Society in 2013 and 2014, respectively.

Hisashi Morishita received the B.S. degree in Electrical Engineering from National Defense Academy in 1980, the M.S. and Ph. D. degrees from University of Tsukuba in 1987 and 1990, respectively. From 1990 to 1992, he worked as a Research and Development Officer at Air Research and Development Command of Japan Air Self-Defense Force (JASDF). Since 1992, he has been with National Defense Academy and is currently a Professor in the Department of Electrical and Electronic Engineering. From 1996 to 1997, he was a Visiting Researcher at the Communication Research Laboratory, McMaster University, Canada. His research is concerned with mobile communication and small antennas. He is a fellow of IEICE and a senior member of IEEE.

Gain Enhancement of a Dual-Band Planar Slot Dipole using AMC Plane for WBAN and WLAN Applications

Fatin Nabilah Giman [1], Ping Jack Soh [1,5], Mohd Faizal Jamlos [2], Herwansyah Lago [3], Azremi Abdullah Al-Hadi [1], Sharul Kamal Abdul Rahim [4], Dominique Schreurs [5], Prayoot Akkaraekthalin [6], and Adalbert Beyer [7]

[1] Advanced Communication Engineering Centre (ACE), School of Computer and Communication Engineering
Universiti Malaysia Perlis (UniMAP), Pauh Putra, 02600, Arau, Perlis, Malaysia
pjsoh@unimap.edu.my

[2] Faculty of Mechanical Engineering, Universiti Malaysia Pahang, 26600 Pekan, Pahang, Malaysia

[3] Faculty of Engineering, Universiti Malaysia Sabah, 88400 Kota Kinabalu, Sabah, Malaysia

[4] Wireless Communication Center (WCC), Universiti Teknologi Malaysia, 81310 UTM Skudai, Johor, Malaysia

[5] ESAT-TELEMIC Research Division, KU Leuven, Kasteelpark Arenberg 10 Box 2444, 3001 Leuven, Belgium

[6] Department of Electrical and Computer Engineering, Faculty of Engineering
King Mongkut's University of Technology North Bangkok, (KMUTNB)
1518 Pracharat 1 Rd., Wongsawang, Bangsue, Bangkok, 10800 Thailand

[7] High Frequency Engineering (HFT), University Duisburg-Essen, Bismarckstrasse 81, 47057 Duisburg, Germany

Abstract ─ A dual band slot dipole antenna made from textile is proposed for Wireless Body Area Network and Wireless Local Area Network applications. The proposed antenna is integrated with an artificial magnetic conductor plane to mitigate backward radiation and reduce Specific Absorption Rate when operated on body. The artificial magnetic conductor plane is formed using a 3 x 3 array of unit cells, each consisting of a square patch integrated with diamond-shaped slot. The proposed antenna (denoted as Antenna B) is compared against another similar antenna (Antenna A) in free space and on-body, in flat condition (on chest) and under two bending axes (*x*- and *y*-axes) on the upper arm. Results indicate that Antenna B provided wider upper bandwidth to 766 MHz (in flat condition) and up to 875 MHz when bent. Besides that, higher gain of up to 5 dB with improved front-to-back ratio are also observed.

Index Terms ─ Antennas, artificial magnetic conductor, metamaterial, multiband antennas, wearable antennas.

I. INTRODUCTION

Wireless body area network (WBAN) and Wireless Local Area Network are two of the most widely researched applications globally. Their frequencies include the Industrial Scientific Medical (ISM) band (from 2.4 to 2.48 GHz), Ultra-Wide band (UWB) (from 3.1 to 10.76 GHz), Wireless Local Area Network (WLAN) (in the 2.4 and 5 GHz bands) [1]-[14]. In line with this development, wearable antenna made from flexible materials are also widely investigated due to its attractive features: low profile, flexible, inexpensive, lightweight, and most importantly, safe to be worn. However, when placed on body, an antenna with high back radiation or omnidirectional pattern such as dipole antenna [2] tends to increase the electromagnetic absorption in the human body due to its proximity during operation. This almost certainly results in high SAR value which potentially affect human body tissues. The American National Standards Institute (ANSI) and International Commission on Non-Ionizing radiation Protection (ICNIRP) regulated that the exposure for human tissues is limited to 1.6 W/kg averaged per 1g of tissue and 2 W/kg per 10 g of tissue, respectively.

One of the solutions to control the level of the back-radiation is either by selecting an antenna topology with a rear ground plane or to introduce a metallic plane to function as a reflector. However, conventional reflecting structure interferes antenna operation, and they are typically placed at an extended distance from the

Submitted On: September 30, 2018
Accepted On: July 1, 2019

radiator. Such setup, in turn, increases the height of the antenna structure and reduces its suitability to be worn on body due to increased thickness. Moreover, the gap of such structure is frequency-dependent, which requires the gap to be determined based on the lower frequency in the case of a multi-resonance antenna, which again increases the thickness. To overcome this, metasurfaces with dual-band behavior such as Electromagnetic Bandgap (EBG) or Artificial Magnetic Conductor (AMC) can be an ideal solution to balance between thickness and modifying radiation characteristics [3]-[10].

In this paper, a dual-band antenna and a dual-band AMC plane is proposed. The AMC plane is formed using an array of unit cell elements based on a square patch integrated with diamond-shaped slot to enable dual band operation. The optimized antenna (Antenna B) is compared with a previous work [1] (denoted as Antenna A) to assess its improvements in terms of bandwidth, gain and front-to-back ratio. The next section describes the antenna design and materials used, followed by the assessment of their performance in free space and on body. A comprehensive SAR investigation to validate the contribution of the AMC plane is presented prior to the concluding remarks.

II. TEXTILE MATERIALS AND ANTENNA SPECIFICATION

A. Antenna design

Two topologies of the proposed C-slotted dual band textile antenna are shown in Figs. 1 (a) and 1 (b). They operate in the 2.45 GHz (lower) and 5.8 GHz (upper) bands. The proposed antenna is integrated with an AMC layer between its substrate and ground. The previous antenna from [1] (denoted as Antenna A) shown in Fig. 1 (a) is compared with the proposed C-slotted dipole antenna with optimized AMC (denoted as Antenna B) and shown in Fig. 1 (b).

All antennas are designed using the same textile materials. Felt with a thickness of 3 mm is used as its substrate, while ShieldIt Super conductive textile with a thickness of 0.17 mm is used to form the patch, ground and AMC of the proposed antenna. The relative permittivity and loss tangent of the felt substrate is 1.44 and 0.044, respectively, whereas the conductivity of the ShieldIt Super is 1.18×10^5 S/m. To provide a fair comparison, the overall area of both antennas are limited to 90 x 90 mm^2 with the same thickness of 6.51 mm. Both antennas are built using five layers of textiles (see Fig. 1 (e)), as follows: a ground layer on the bottom-most layer, followed by two layers of substrate and a layer consisting of the AMC plane in between them. Finally, a patch layer is placed on the top. Their optimized dimensions are summarized in Table 1.

Table 1: Optimized parameters of the proposed antenna

Antenna/ Parameter Values (mm)	Antenna A (with AMC) [1]	Antenna/ Parameter Values (mm)	Antenna B (Optimized AMC)
L/W	90	*La/Wa*	90
L1	45	*Lb*	47
W1	55	*Wb*	62
A	10	*a*	9
B	30	*b*	34
C	22	*c*	26
D	4	*d*	4
E	16	*e*	21
F	2	*f*	2
-	-	*g*	12
-	-	*h*	2

In this work, the Finite Integration Technique (FIT) was used, which is a way of generalizing the FDTD method with weak link to the FEM method. The discretization of Maxwell's equations is done on a pair of dual discretization meshes. The degrees of freedom are corresponding to integral types: electrical voltages and magnetic fluxes on the first type of meshes, and magnetic voltages and electrical fluxes on the second type of meshes. The FIT technique can be used in a very wide frequency range from DC to THz, and for many types of meshes, and curved contours. This technique can be used advantageously and very efficiently for the calculation of multilayered structures, as the results of this work show. The numerical work was performed using CST Microwave Studio Suite, which incorporates this method.

B. AMC plane design

The 3 x 3 array of square patch unit cells integrated with diamond-shaped slots forms the AMC plane. This plane is implemented to reduce back radiation as shown in Figs. 1 (f) and 1 (g). The AMC is designed similar to [1] for a fair comparison and is further optimized to enable zero reflection phase at 2.45 and 5.8 GHz for Antenna B, as shown in Fig. 2. For the optimized AMC, a shorter current path is provided for the AMC to operate in the upper band (5.8 GHz). This resulted in a wider reflection phase bandwidth of 15.8% or 891 MHz (from 5.189 to 6.08 GHz), while the larger current path enables operation at the lower 2.45 GHz frequency. The phase reflection indicated operation with a bandwidth of 7.76% or 187 MHz (from 2.32 to 2.5 GHz). This indicated that the optimized AMC plane for Antenna B improved in terms of wider reflection phase bandwidth in the upper band.

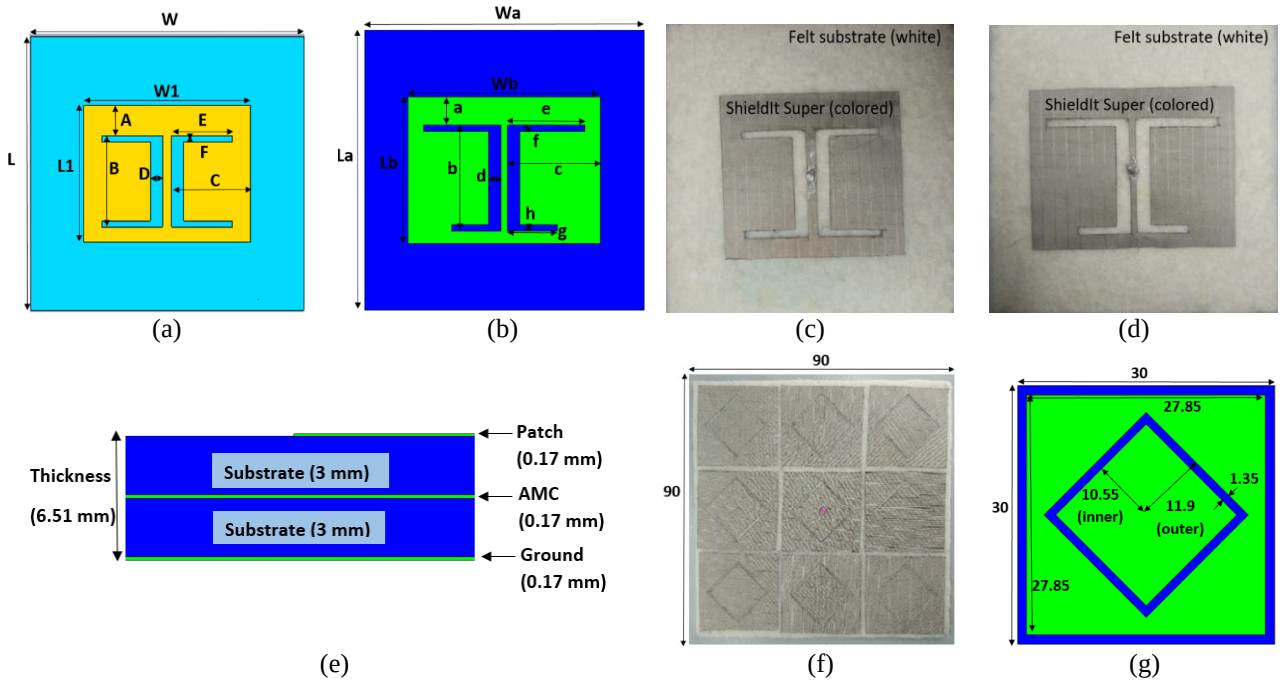

Fig. 1. Topology of the proposed antenna: (a) Antenna A (with AMC) [1], (b) Antenna B (with optimized AMC), (c) fabricated Antenna A, (d) fabricated Antenna B, (e) layer structure of the antenna, (f) fabricated AMC plane from [1], and (g) optimized AMC unit cell dimensions (in mm).

III. RESULTS AND DISCUSSIONS

A. Planar antenna in free space

The performance of both antennas (A and B) in free space are compared and summarized in Table 2. It shows that the simulated reflection coefficient (S_{11}) in free space planar condition for both antennas is below -15 dB and – 21 dB in the lower (2.45 GHz) and upper (5.8 GHz) band. The radiation pattern of both antennas in free space and planar condition is directional in the azimuth plane with a maximum directivity of 5.26 dBi (Antenna A) and 7.31 dBi (Antenna B) in the lower band, see Fig. 3. On the other hand, a maximum directivity of 10.7 dBi (for Antenna A) and 9.88 dBi (for Antenna B) is observed in the upper band. Table 2 shows that the realized gain in free space of flat for Antenna A produce a negative realized gain while Antenna B produce a positive realized gain. This indicates that the dissimilar slot length in the radiator and the integration of the optimized AMC plane contributed in improving the gain of Antenna B in the lower band from -2.47 dB to 2.38 dB, a significant increase of about 5 dB. Meanwhile, the realized gain in the upper band for Antenna B is higher than 6 dB. This is slightly lower than the realized gain for Antenna A in this band (which is about 7 dB) due to the marginal S_{11} at 5.8 GHz for Antenna B. Nonetheless, the simulated front-to-back ratio (FBR) of Antenna B in the flat condition is higher in both bands compared to Antenna A.

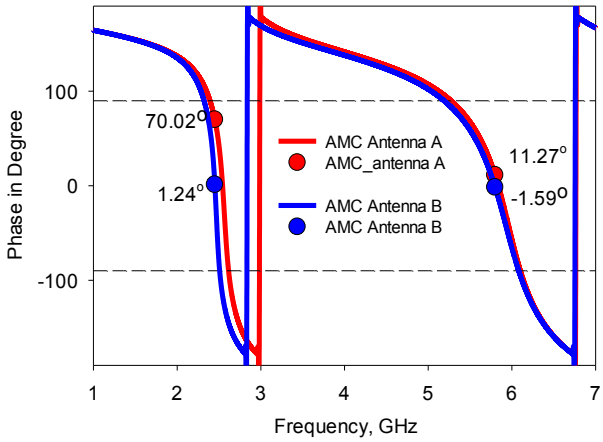

Fig. 2. Simulated reflection phase of the AMC plane for Antenna A [1] and B (proposed). The dotted lines represents the ±90° operating range of the AMC plane.

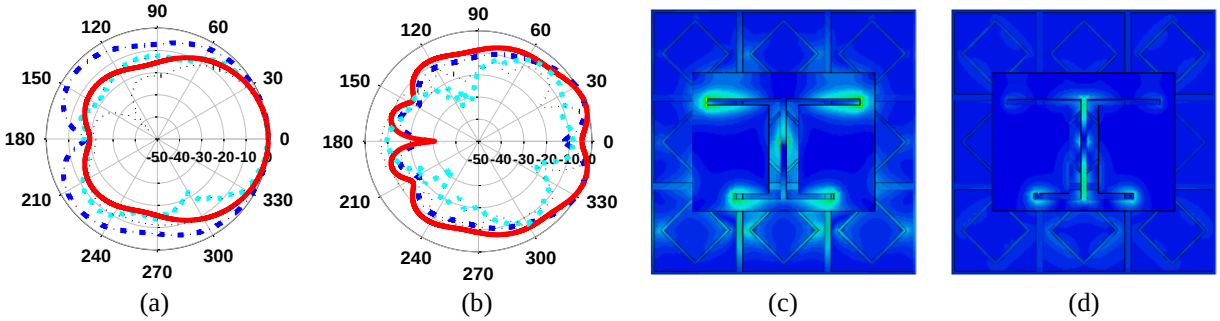

Fig. 3. Simulated and measured radiation pattern in planar free space condition at: (a) 2.45 GHz and (b) 5.8 GHz. Simulated surface currents distribution of Antenna B at: (c) 2.45 GHz and (d) 5.8 GHz. Legend: Dash dot (blue) line: simulated Antenna A, solid (red) line: simulated Antenna B, short dashed (cyan) line: measured Antenna A, dotted (black): measured Antenna B.

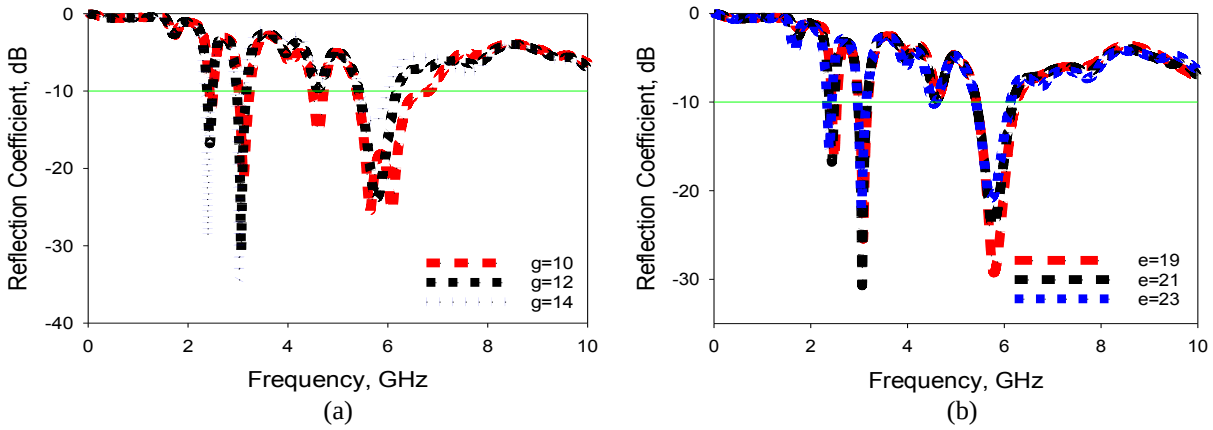

Fig. 4. Effects of the slot lengths on the antenna reflection coefficients: (a) *g* and (b) *e*.

The two arms of the slot dipoles are expected to provide tuning for the resonant frequency and impedance matching for the antenna structure, and are investigated. The slot lengths of the two arms are denoted as *g* and *e*, and their effects on the antenna performance are investigated. It can be summarized that the length of *g* highly determines the antenna's resonant frequency, whereas the length of *e* influences the impedance matching. More specifically, the resonant frequency can be shifted to the lower frequencies by increasing the length of *g*, as shown in Fig. 4 (a). Meanwhile, an improved impedance matching at the specific resonant frequency can be exhibited by decreasing the length of *e*, as shown in Fig. 4 (b). For that reason, the lengths of *g* and *e* are crucial parameters and must be accurately fabricated.

B. Assessment of antenna in free space under bending

As wearable antennas are designed to be worn on-body, there is always risks of them being operated when bent. To maintain operation in such situations, the proposed antennas are investigated further when bent in the *x*- and *y*-axes with a radius, *r* of 60 mm in free space, denoted as *X60* and *Y60*, respectively. Simulated and measured S_{11} of the antenna when bent at both axes are shown in Fig. 5. The maximum realized gains of Antenna B when bent at both axes are improved to 2.25 dB (*X60*) and 1.34 dB (*Y60*) in the lower band. In the upper band, its gains of 5.93 dB is observed under condition *X60* and 4.48 dB under condition *Y60*. On the contrary, Antenna A exhibited negative realized gains for all bending configurations. Besides that, Antenna B also improved in terms of FBR for both bending configurations. Its FBR are at least 9 dB in the lower band and 22 dB in the upper band. The measured radiation patterns of both antennas when bent in configurations *X60* and *Y60* are compared with planar free space in Fig. 6. Both bent antennas at both axes are directional in the azimuth plane with maximum directivities of at least 7 dBi and 9 dBi in the lower and upper bands, respectively.

Table 2: Performance summary of Antennas A and B in the planar and bent configurations

Antenna/Freq./Parameter	**Condition**	**A (with AMC)**		**B (with optimized AMC)**	
	Freq. (GHz)	**2.45**	**5.8**	**2.45**	**5.8**
S_{11} (dB)	*Flat (sim)*	-23.91	-22.55	-15.69	-24.55
	Flat (meas)	-5.75	-13.63	-16.41	-8.24
	Chest (meas)	-8.24	-25.51	-13.51	-8.30
	X60 (sim)	-25.18	-23.88	-10.69	-29.26
	X60 (meas)	-9.85	-21.68	-9.96	-7.12
	Y60 (sim)	-21.89	-27.22	-10.68	-34.68
	Y60 (meas)	-7.56	-21.68	-14.44	-8.09
Bandwidth (MHz)	*Flat (sim)*	123	714	109	766
	Flat (meas)	80	600	50	600
	Chest (meas)	100	870	105	475
	X60 (sim)	121	765	100	875
	X60 (meas)	50	900	55	550
	Y60 (sim)	124	800	104	850
	Y60 (meas)	75	750	80	570
Real. Gain (dB)	*Flat (sim)*	-2.47	7.17	2.38	6.53
	Flat (meas)	-2.2	9.32	5.89	7.21
	Chest (meas)	-2.87	5.54	3.21	6.99
	X60 (sim)	-1.33	5.96	2.25	5.93
	X60 (meas)	-8.78	5.1	3.96	5.2
	Y60 (sim)	-1.04	5.12	1.34	4.48
	Y60 (meas)	-2.66	-0.29	2.42	-2.54
Front to Back Ratio, FBR (dB)	*Flat (sim)*	2.74	22.62	17.35	18.8
	Flat (meas)	4.95	28.47	17.14	28.62
	Chest (meas)	6.42	5.54	22.83	22.07
	X60 (sim)	3.59	20.58	8.914	22.87
	X60 (meas)	16.0	16.46	20.89	21.33
	Y60 (sim)	3.76	16.53	10.415	16.71
	Y60 (meas)	7.19	14.50	23.76	4.69
Directivity, (dBi)	*Flat (sim)*	5.26	10.7	7.31	9.88
	X60 (sim)	5.7	8.41	7.81	8.98
	Y60 (sim)	6.25	9.21	6.5	7.57

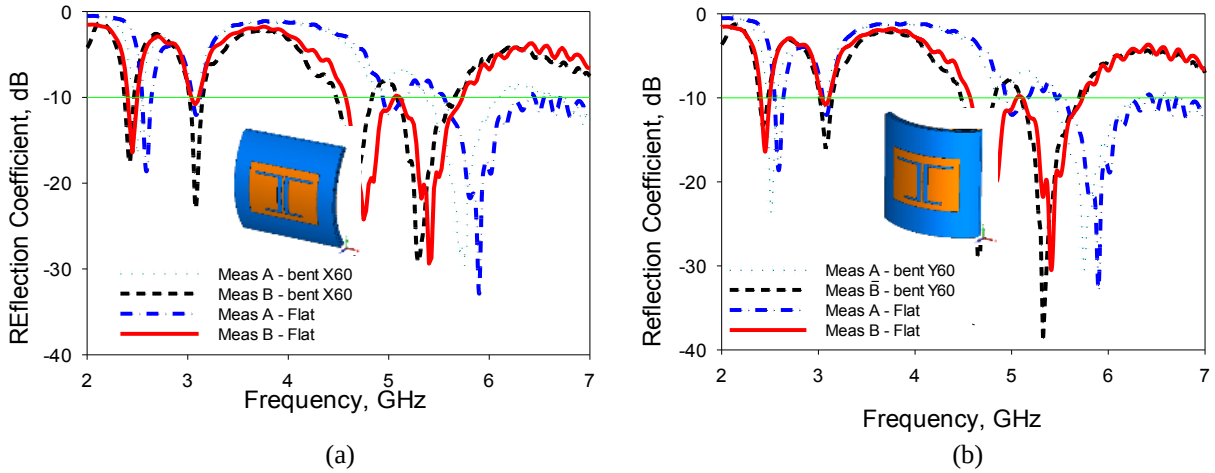

Fig. 5. Measured reflection coefficients of Antenna A and B in free space in planar condition (flat) and (a) under bending with *X60*; (b) under bending with *Y60*.

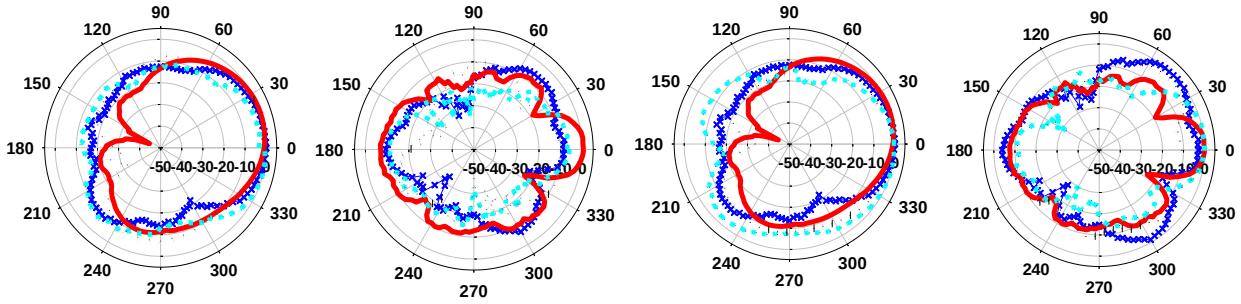

(a) (b) (c) (d)

Fig. 6. Normalized measured radiation patterns of Antennas A and B in planar (flat) and when bent with *X60* and *Y60* conditions in free space in the *xz*-plane at (a) 2.45 GHz (*X60*), (b) at 5.8 GHz (*X60*), (c) 2.45 GHz (*Y60*), and (d) 5.8 GHz (*Y60*). Legend: Crossed (blue) line: Antenna A flat, solid (red) line: Antenna B flat, short dash (cyan) line: Antenna A with *X60*/*Y60*, and dotted (black) line: Antenna B with *X60*/*Y60*.

C. Assessment of antenna placed on body in flat and under bending conditions

On body assessments were performed on a truncated detailed human body model (in simulations) with in three configurations: (1) in flat condition (on chest); (2) in *X60* condition on a truncated upper arm; and (3) in *Y60* condition on the same truncated upper arm. Simulations of the proposed structure on the dispersive tissues were performed using the finite time integral method using voxel resolutions of 2 x 2 x 2 mm^3. The chest and the upper arms contain mainly the skin, muscle and fat tissues, which properties are summarized in Table 3 [15]. Similarly, measurements were performed on a human volunteer on both locations and the three configurations when placed at 10 mm away from the body phantom. To evaluate the level of degradation contributed by the human body, the S_{11} for both antennas are first measured on-body in a flat condition on the chest as shown in Fig. 7. This is compared with its performance when simulated in planar form. Next, the antenna is further evaluated in terms of radiation patterns in an anechoic chamber, and measurements gathered are compared with simulations in Fig. 8.

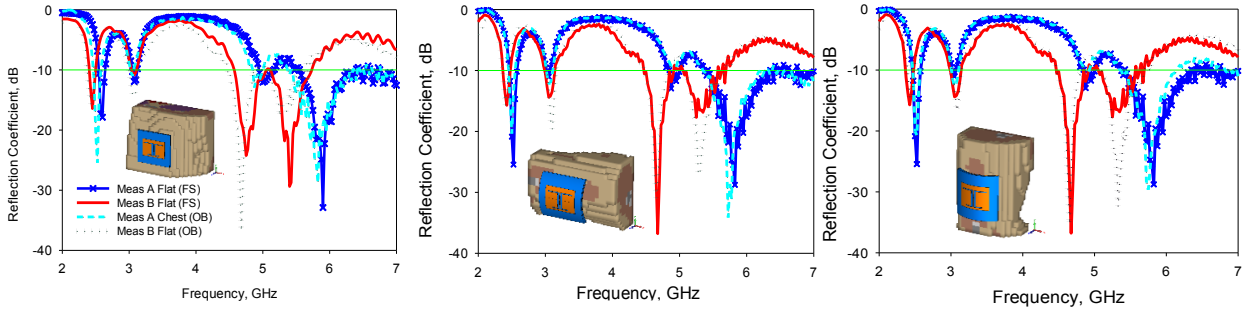

(a) (b) (c)

Fig. 7. Measured reflection coefficients of Antenna A and B when (a) placed on body (flat on chest and flat in free space), (b) bent with *X60* on the upper arm, and (c) bent with *Y60* on the upper arm. Legend: Crossed (blue) line: Antenna A flat on chest, solid (red) line: ant Antenna B flat on chest, short dashed (cyan) line: Antenna A in *X60 and* Y60 conditions and dotted (black) line: Antenna B in *X60 and Y60* conditions.

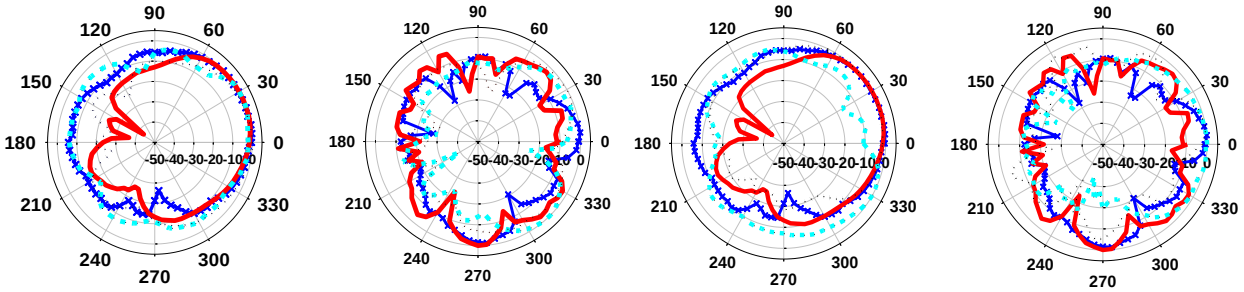

Fig. 8. Normalized measured radiation patterns for Antenna A and B when placed flat on chest and bent with *X60* and *Y60* on body: (a) at 2.45 GHz in the *xz*-plane (*X60*), (b) at 5.8 GHz in the *xz*-plane (*X60*), (c) at 2.45 GHz in the *xz*-plane (*X60*), (d) at 5.8 GHz in the *xz*-plane (*Y60*). Legend: Solid crossed (blue) line: Antenna A placed flat on chest, solid (red) line: Antenna B placed flat on chest, short dashed (cyan) line: Antenna A with *X60*/*Y60* on the upper arm, and dotted (black) line: Antenna B with *X60/Y60* on the upper arm.

Table 3: Summary of the tissue properties used in simulations

Tissue Type	**Blood**		**Muscle**		**Fat**	
Frequency (GHz)	2.45	5.8	2.45	5.8	2.45	5.8
ε	58.3	52.5	52.7	48.49	5.28	4.95
tanδ	0.32	0.38	0.24	0.32	0.15	0.18
Cond (S/m)	2.54	6.51	1.74	4.96	0.10	0.29

Finally, the antennas bent at the *x*- and *y*-axes are experimentally validated in terms of reflection coefficient. This is performed similarly as was done in simulations using a thin and hollow cylinder on a human volunteer. The measured results illustrated in Figs. 7 (b) and (c) indicated that there is minimal level of changes in the lower band despite bending the antenna structure at both *x*- and *y*-axes. Changes are mainly noticeable in the upper band, where the same antenna (either A or B) maintaining their behavior despite being bent at different axes. This indicates that the antenna is affected minimally when bent at either axis.

D. Specific Absorption Rate (SAR)

The SAR values for both proposed antenna is calculated using CST MWS by placing the antennas in proximity of a truncated human voxel model (either on the chest or upper arm). Similar to the previous investigation [17], the antennas are placed 10 mm away from these models. The SAR value is calculated based on the IEEE C95.1 standard averaged over 10 g of tissue volume and is regulated to be safe when lower than 2 W/kg.

SAR is a measure of power absorbed per unit mass, e.g., in the human body tissue. It is spatially averaged over the total mass of an exposed body or its parts, and it is calculated from the root-mean-square electric field strength, E (in volts per meter) inside the human body; the conductivity, σ (in Siemens per meter); and the mass density, ρ (in kilograms per cubic meter) of the biological tissue as follows:

$$SAR = \frac{\sigma \cdot E^2}{\rho}. \quad (1)$$

SAR is calculated by solving electromagnetic field interaction from different and adjacent meshes. In the case of the body tissues, their voxel properties were determined from MRI scans of different tissues. In this work, hexahedral meshes were used so that the constitutive parameters for each cell edge with irregular geometries and inhomogeneous dielectric composition can be calculated independently. Next, the simulator then solves the Maxwell's equations at each cell edge at discrete time steps, taking into consideration the three dimensional complex biological geometries, which involves a large amount of cells. In this work, SAR were calculated on the truncated chest and upper arm models with a total of about 20 million of hexahedral meshes per simulation. While meshes were generated automatically prior to simulations, at least 10 lines per wavelength with a mesh line ratio limit of 20 is set.

Table 4: Summary of the calculated SAR from both antennas

SAR Value	**Chest (W/kg)**		***X60* on the Upper Arm (W/kg)**		***Y60* on the Upper Arm (W/kg)**	
Freq (GHz)	2.45	5.8	2.45	5.8	2.45	5.8
Ant A	0.094	0.043	0.121	0.057	0.097	0.047
Ant B	0.082	0.052	0.122	0.061	0.089	0.059

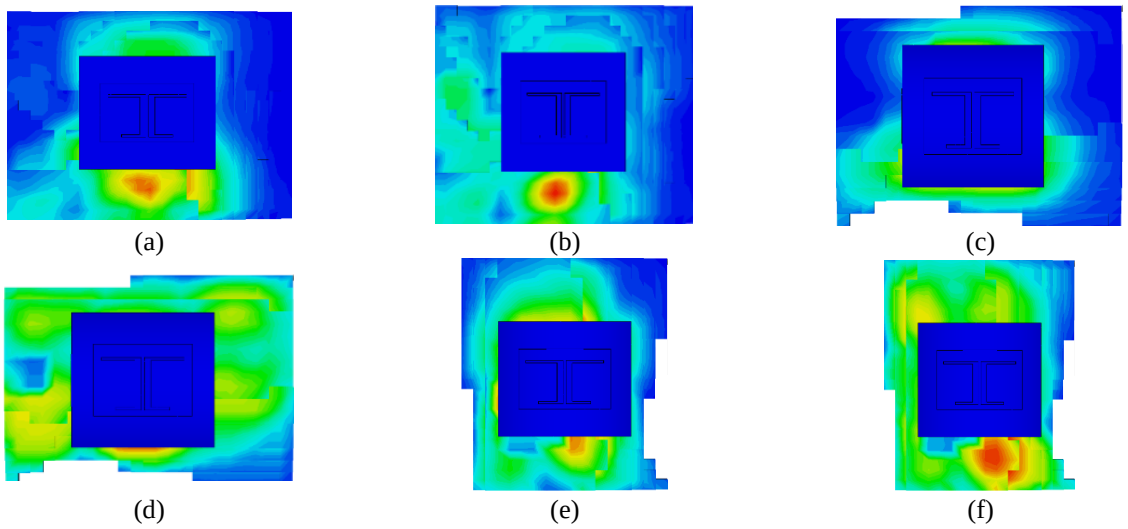

Fig. 9. Calculated SAR distribution for Antenna B when placed in planar and bent conditions at: (a) 2.45 GHz (flat), (b) 5.8 GHz (flat), (c) 2.45 GHz (with *X60*), (d) 5.8 GHz (with *X60*), (e) 2.45 GHz (with *Y60*), and (f) 5.8 GHz (with *Y60*).

Table 5: Comparison of the proposed antenna with recent literatures in terms of performance.

Ref. No.	Topology	Op. Bands (GHz)	10dB Frac. WBW (%)	Gain (dB)	10 dB BW Deviation on Body (GHz)	SAR (W/kg)
[2]	Planar dipole, fork shaped	2.4	12.7	4.9	0.3	1.98
		5.2	4.45	6.15	0.2	0.92
[3]	Planar slotted dipole	2.45	12.7	2.5	0.06	0.046
		5.2	18.9	0 to 4	0.2	0.023
[7]	Planar magneto-dielectric dipole	2.45	20	4.7	0.03	0.026
		5	31.5	3	0.05	0.044
[11]	Patch with metamaterial element	2.45	5.5	-3.5	0.02	0.012
		5.14	11.3	6.6	0.2	0.25
Ant B	Planar slotted dipole	2.45	4.11	5.9	0.05	0.082
		5.8	13.12	7.2	0.05	0.052

A summary of the SAR values calculated for both antennas is provided in Table 4. The calculated SAR distribution at 2.45 GHz and 5.8 GHz for Antenna B when placed in all three configurations (flat, *X60* and *Y60*) are shown in Fig. 9. Due to the use of the AMC plane, the SAR values for both antennas did not exceed 0.13 W/kg in all bands. It can be seen that SAR values for both antennas are similar when placed on all locations and for all configurations. It is also observed that the highest SAR is produced in the lower band when bent in *X60* condition for both antennas. The proposed antenna is compared with recent textile antennas operating in dual band mode and is summarized in Table 5. It can be observed that Antenna B provided comparable, if not better, balance in performance between bandwidth and gain, besides the reasonably low SAR when operated on body.

IV. CONCLUSIONS

A dual band slotted dipole antenna with AMC is proposed for operation in the in the 2.45 GHz and 5.8 GHz for WLAN and WBAN bands. To ensure a flexible, wearable and low profile structure, felt is used as its substrate and ShieldIt Super as its conductors. The proposed Antenna B is compared with a previous work denoted as Antenna A. It is observed that the integration of Antenna B with the optimized AMC produced wider bandwidths of 766 MHz (flat), 875 MHz (*X60*) and 850 MHz (*Y60*) in the upper band. In the lower band, both antennas produced similar narrow bandwidths of about 100 MHz. Despite this, Antenna B improved the realized gain and reduced backward radiation for all conditions relative to Antenna A. Maximum gains of 2.38 dB and 6.53 dB are observed in the lower and upper band, respectively, when assessed in a planar free space

condition. Higher directivities and gains are also observed for Antenna B in both bands. Finally, calculated SAR value using a detailed human body model for both antennas are below 0.13 W/kg indicating their safe operation in proximity of the human body in planar and bent conditions.

ACKNOWLEDGEMENTS

This work is supported in part by the Fundamental Research Grant Scheme (FRGS) (grant no 9003-00527), the MyBrain Scholarship, both from the Malaysian Ministry of Higher Education (MOHE); and the Thailand Research Fund though the TRF Senior Research Scholar Program under Grant RTA 6080008.

REFERENCES

[1] P. J. Soh, F. N. Giman, M. F. Jamlos, H. Lago, and A. A. Al-Hadi, "A C-slotted dual band textile antenna for WBAN applications," *IEEE URSI Asia-Pacific Radio Science Conference (URSI AP-RASC)*, Fajardo, Puerto Rico, pp. 1621-1624, June 2016.

[2] A. Afridi, S. Ullah, S. Khan, A. Ahmed, A. H. Khalil, and M. A. Tarar, "Design of dual band wearable antenna using metamaterials," *Journal of Microwave Power and Electromagnetic Energy*, vol. 47, no. 2, pp. 126-37, 2013.

[3] S. Yan, P. J. Soh, and G. A. E. Vandenbosch, "Low-profile dual-band textile antenna with artificial magnetic conductor plane," *IEEE Transactions on Antennas and Propagation*, vol. 62, no. 12, pp. 6487-90, 2014.

[4] H. Lago, J. P. Soh, M. F. Jamlos, et al., "Textile antenna integrated with compact AMC and parasitic elements for WLAN/WBAN applications," *Applied Physics A*, vol. 122, pp. 1059, 2016.

[5] Z. H. Jiang, D. E. Brocker, P. E. Sieber, and D. H. Werner, "A compact, low-profile metasurface-enabled antenna for wearable medical body-area network devices," *IEEE Transactions on Antennas and Propagation*, vol. 62, no. 8, pp. 4021-30, 2014.

[6] Y. H. Di, X. Y. Liu, and M. M. Tentzeris, "A conformable dual-band antenna equipped with AMC for WBAN applications," *IEEE Asia-Pacific Conference on Antennas and Propagation (APCAP)*, Harbin, China, pp. 388-391, July 2014.

[7] S. Yan, P. J. Soh, and G. A. E. Vandenbosch, "Wearable dual-band magneto-electric dipole antenna for WBAN/WLAN applications," *IEEE Transactions on Antennas and Propagation*, vol. 63. no. 9, pp. 4165-4169, 2015.

[8] Z. H. Jiang and D. H. Werner, "A metasurface-enabled low-profile wearable antenna," *IEEE Antennas and Propagation Society International Symposium (APSURSI)*, Memphis, USA, pp. 273-274, July 2014.

[9] S. Zhu and R. Langley, "Dual-band wearable textile antenna on an EBG substrate," *IEEE Transactions on Antennas and Propagation*, vol. 57, no. 4, pp. 926-35, 2009.

[10] A. Alermayeen and S. Noghanian, "AMC integrated textile monopole antenna for wearable applications," *ACES Journal*, vol. 31, no. 6, pp. 612-618, 2016.

[11] S. Yan, P. J. Soh, and G. A. E. Vandenbosch, "Compact all-textile dual-band antenna loaded with metamaterial-inspired structure," *IEEE Antennas and Wireless Propagation Letters*, vol. 14, pp. 1486-9, 2015.

[12] H. R. Khaleel, H. M. Al-Rizzo, and D. G. Rucker, "An AMC based antenna for telemedicine applications," *ACES Journal*, vol. 27, no. 2, pp. 59-66, 2012.

[13] R. C. Hadarig, M. E. De Cos, and F. Las-Heras, "Microstrip patch antenna bandwidth enhancement using AMC/EBG structures," *International Journal of Antennas and Propagation*, pp. 1-6, 2012.

[14] M. N. Pavan and N. Chattoraj, "Design and analysis of a frequency reconfigurable antenna using metasurface for wireless applications," *IEEE International Conference on Innovations in Information, Embedded and Communication Systems (ICIIECS)*, Coimbatore, India, pp. 1-5, Aug. 2015.

[15] V. Kumar and B. Gupta, "On-body measurements of SS-UWB patch antenna for WBAN applications," *AEU-International Journal of Electronics and Communications*, vol. 70, no. 5, pp. 668-675, 2016.

[16] S. Gabriel, R. W. Lau, and C. Gabriel, "The dielectric properties of biological tissues III: Parametric models for the dielectric spectrum of tissues," *Physics in Medicine and Biology*, vol. 41, no. 11, pp. 2271-93, 1996.

[17] P. J. Soh, G. A. E. Vandenbosch, F. H. Wee, et al., "Specific absorption rate (SAR) of textile antennas," *IEEE Antennas and Propagation Magazine*, vol. 57, no. 2, pp. 229-240, 2015.

Mutual Coupling Reduction of Dual-Band Uni-Planar MIMO System Using Neutralization Line Technique

Adham M. Saleh [1,2], Tariq A. Nagim [2], Raed A. Abd-Alhameed [1], James M. Noras [1], and Chan H. See [3]

[1] School of Electrical Engineering and Computer Science
University of Bradford, Bradford, BD7 1DP, UK
amssaleh@bradford.ac.uk, r.a.a.abd@bradford.ac.uk, j.m.noras@bradford.ac.uk

[2] College of Electronic Engineering
Ninevah University, Mosul, Iraq
tanalniemi@gmail.com

[3] School of Engineering and the Built Environment
Edinburgh Napier University, Edinburgh, EH14 1DJ
C.See@napier.ac.uk

Abstract ─ This paper presents a low–profile dual-band (2×2) MIMO antenna that works at 2.4GHz, 5.2GHz and 5.8GHz for wireless local area networks (WLAN) applications. A neutralization line technique for enhancing the isolation is used by introducing a strip line with a length of $\lambda_g/4$ at the isolation frequency (2.4GHz) between the radiating elements. The overall dimensions of the proposed antenna are 36×33.5×1.6 mm^3. The antenna is fabricated and tested to validate the simulation results. The practical results show fair agreements with the simulated outcomes. The antenna achieves impedance bandwidths from 2.15GHz to 2.52GHz and from 4.5GHZ to 6.45GHz for reflection coefficient |S11| < -10dB. On the other hand, the result of S21 for the two bands is better than -10dB and it has reached to -25dB around 2.4GHz and -35dB around 5.5GHz. The MIMO antenna performance characteristics are reported in terms of scattering parameters, envelope correlation coefficient (ECC), total active reflection coefficient (TARC), channel capacity loss (CCL), diversity gain (DG) and antenna radiation patterns. Analysis of these characteristics indicates that the design is appropriate for the WLAN.

Index Terms ─ MIMO antenna, mutual coupling, parasitic elements, WLAN.

I. INTRODUCTION

Recently, the wireless communications systems are expanded explosively to support the increasing demands of high transmission rate with high throughput for various fixed and mobile services. To fulfil these demands, the researchers and the manufacturers shifted from one antenna to multiple antenna systems. Multiple Input Multiple Output (MIMO) system can be considered as the backbone of the new wireless technologies due to its unique features of achieving higher data rates without consuming extra power in the multipath environment [1, 2]. One significant drawback associated with the MIMO system is the mutual coupling between the radiating elements inside the MIMO antenna structure. This means that some of the energy will be radiated from one element to the other one and vice versa. The main reason for this issue is the close placement of the multiple radiating elements inside the MIMO antenna structure. As a result, if the radiating elements are closer, the coupling between them will be stronger [3, 4].

Various techniques were developed in the last few years to enhance the isolation inside the MIMO antenna structure. Various antenna designs with different band classifications such as narrowband, wideband and dual/ triple band have used these approaches [5]. Methods reported include using parasitic elements between the antennas [6, 7], junctions and branches in the form of T-shape [8, 9], defected ground structures (DGS) [10, 11], stubs [11, 12], neutralization lines (NL) [13-17] and metamaterial resonators [18-25].

The neutralization line technique can be classified as one of the effective methods that are used to improve the isolation in MIMO antenna systems as illustrated in [13-17]. According to Chebihi *et al.* in [26], the main function of the NL is to pass the electromagnetic (EM) wave from one radiating element to the other one at a certain point inside the MIMO antenna structure via a metallic slit or lumped element. This EM wave should have an opposite coupling to reduce the main coupling in the antenna system at a specific frequency band [27].

Submitted On: August 16, 2019
Accepted On: December 15, 2019

The critical issue associated with this technique is the selection of the point. The position of the point inside the radiating structure should have low impedance and high current density [28]. Two parameters should be taken into account in the designing of NL; the first parameter is the length and the second one is the width. These parameters have a great effect on the results of the mutual coupling. Recently, the neutralization line technique was explained by several mobile phone companies. For example, Samsung [29] and LG Electronics [30] as a very effective mechanism for solving isolation problems in MIMO antenna systems. Several types of neutralization line structures are used in literature such as thin printed neutralization lines [31], pair of crossed neutralization lines [32], LC matching network and NL [33] and neutralization lines between ground planes [34].

In this paper, a low profile dual-band MIMO antenna is proposed to cover the WLAN bands (2.4/5.2/5.8GHz). The designed antenna basically consists of two uni-planar double T-shaped monopole antennas. A neutralization lines technique is used to connect the two radiating elements of the proposed MIMO antenna. The main aim of this paper is to optimize the NL positions and widths to validate the effectiveness of the NL on the isolation and the impedance bandwidth of the proposed antenna. The proposed antenna is fabricated to validate the simulation results. The antenna performance characteristics are reported in terms of scattering parameters, ECC, TARC, CCL, DG and antenna radiation patterns. Analysis of these characteristics indicates that the design is appropriate for WLAN applications.

II. ANTENNA DESIGN

In this design, a dual-band MIMO antenna with two double T-shaped radiating elements is modelled and simulated to fulfil the requirements of WLAN applications. FR4 with 1.6mm thickness, 4.3 relative permittivity, and 0.025 tangent loss is used as a substrate material for the proposed design of size 36×33.5×1.6 mm^3. The inter-element distance between the radiators is kept at $0.024\lambda_o$, which is equivalent to 3mm. on the other hand, the centre to centre separation is kept at 16.5mm. The antennas share the same ground plane in the bottom layer of the substrate. The ground plane is beveled to prevent proximity effects. Initially, a simple two double T-shaped radiating elements are modelled to work at dual frequency bands. The simple approach to design an antenna with a dual-band operation is by obtaining two elements with different lengths inside the antenna structure. So that, each element will resonate at the desired frequency by matching its length with a quarter of the wavelength of the operating frequency [35]. Therefore, the upper-frequency band is controlled by the shorter T-shaped arm while the lower frequency band is controlled by the longer T-shaped arm. Moreover, a neutralization line with a length of 16.5mm is constructed to connect the two radiating elements for isolation enhancement purposes. The length of the NL is equivalent to $\lambda_g/4$ at the isolation frequency (2.4GHz). The schematic structure of the proposed antenna is shown in Fig. 1 and all the optimized dimensions are summarized in Table 1.

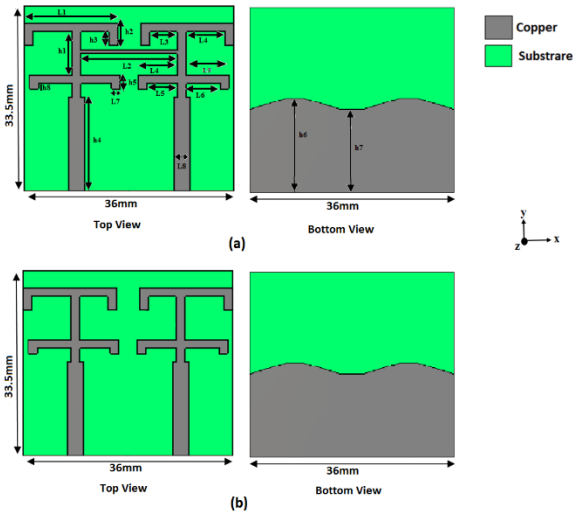

Fig. 1. The configuration of the proposed antenna: (a) antenna with NL, and (b) antenna without NL.

Table 1: MIMO antenna parameters values

Parameters	Value (mm)	Parameters	Value (mm)
h1	7.8	L1	16
h2	4	L2	16.5
h3	2.5	L3	4.75
h4	17	L4	6.75
h5	2.5	L5	5.25
h6	17	L6	5.75
h7	15	L7	1.5
h8	1	L8	2.6
		L9	7.25

The surface current distribution of the proposed antenna is used to analyse the contributions of the neutralization line properly. Two cases are studied at 2.4GHz, the first case is the proposed antenna with excluding neutralization line while the second case is the proposed antenna with including neutralization line. This study is performed by exciting port 1 and terminated port 2 with a matching load. Figure 2 demonstrates the surface current distribution with and without NL. It can be obviously seen that induced current in the feeding line port 2 is high in the case of the absence of the neutralization line. On the other hand, the existence of

the neutralization line will lead to introduce a new current path which generates an additional coupling to reduce the original coupling as shown in Fig. 2 (a) [36].

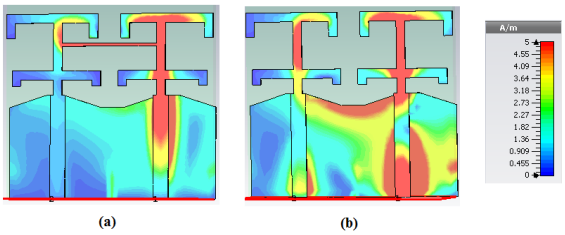

Fig. 2. Surface current distributions of the proposed MIMO antenna at 2.4GHz: (a) with NL and (b) without NL.

III. S-PARAMETERS OF THE PROPOSED ANTENNA WITH AND WITHOUT NL

The S-parameters of the antenna with and without the neutralization line are simulated to verify the effectiveness of the neutralization line (NL). Figure 3 shows the simulated result of the reflection coefficients S_{11}. It can be clearly observed that there is a shift to the right side (toward 2.4GHz) in the first band of operation and a reduction in the bandwidth of the same band. On the other hand, there is no effect on the second band after inserting the NL. Therefore, the same band is achieved.

The simulated coupling with and without NL is illustrated in Fig. 4. It can be clearly seen that the mutual coupling around 2.4GHz without NL is higher than -10dB. By inserting the neutralization line, the mutual coupling between the elements is decreased significantly in this band. The simulated isolation is nearly 27dB at 2.4GHz and 17dB at 5.5GHz as explained in Fig. 4.

IV. PARAMETRIC STUDY

To clarify the effects and obtain the optimized values of the proposed design, parametric studies based on the position and the width of the neutralization line were explained in Fig. 5 are carried out.

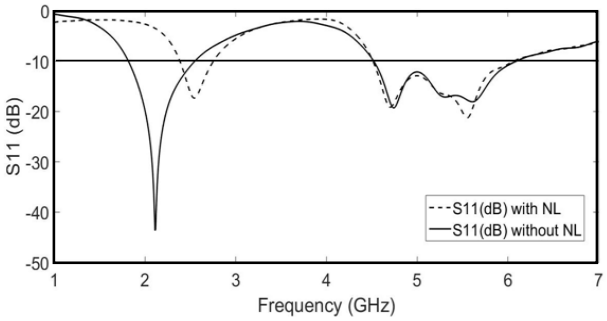

Fig. 3. Simulated reflection coefficients S_{11} with and without neutralization line for the proposed antenna.

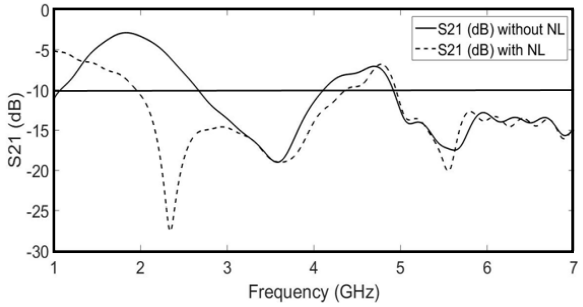

Fig. 4. Simulated transmission coefficients S_{21} with and without the neutralization line for the proposed antenna.

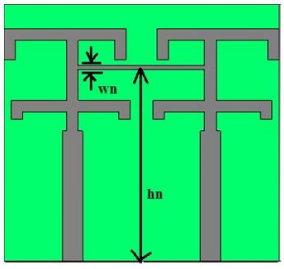

Fig. 5. Configuration of the proposed antenna for parametric study.

A. The effectiveness of the position of NL on the S-parameters

To validate the effectiveness of the position of the neutralization line, the simulated s-parameters of the antenna with different positions (hn) of the NL are investigated as shown in Fig. 6 and Fig. 7 respectively. Figure 6 shows that by raising the position of the NL, the first band is shifted toward 2.4GHz band while the beginning of the second band is shifted backward. On the other hand, raising the position of the NL leads to decrease the mutual coupling between the elements in the first band and there are no effects on the second band. Tables 2 and 3 are summarized the values for the two figures to clarify the results.

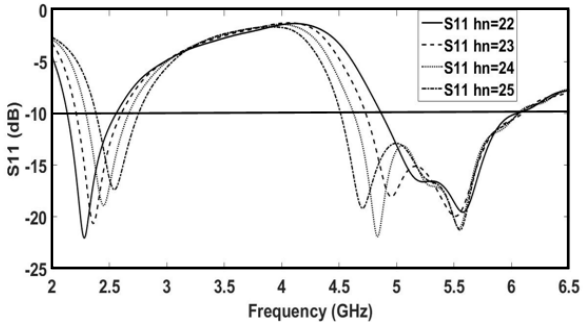

Fig. 6. The simulated reflection coefficient of the proposed antenna with different positions of NL.

Table 2: The effect of the position of NL on the reflection coefficients

	hn=22 mm	hn=23 mm	hn=24 mm	hn=25 mm
f=2.4 GHz	-11.1dB	-12.8dB	-16.7dB	-16.52dB
f=5.2 GHz	-16.58dB	-15.24dB	-15.8dB	-15.7dB
f=5.8 GHz	-13dB	-12.48dB	-12.29dB	-12.32dB

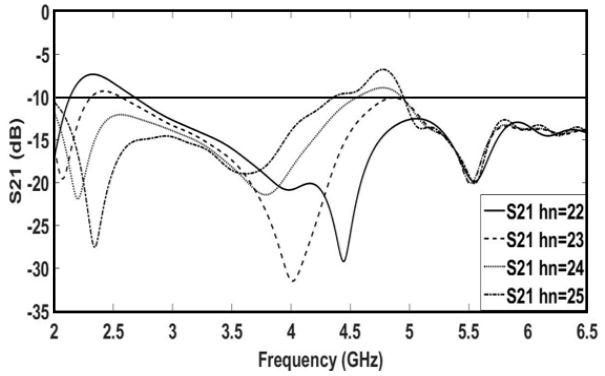

Fig. 7. Simulated transmission coefficient S21 of the third proposed antenna with different positions of NL.

Table 3: The effect of the position of NL on the transmission coefficients

	hn=22 mm	hn=23 mm	hn=24 mm	hn=25 mm
f=2.4 GHz	-8.3dB	-9.5dB	-12.2dB	-18.7dB
f=5.2 GHz	-13.19dB	-13.9dB	-13.99dB	-13.64dB
f=5.8 GHz	-13.76dB	-13.45dB	-13.28dB	-12.68dB

B. The effectiveness of the width of NL on the S-parameters of the proposed antenna

The width of the NL is changed form 0.25mm to 1mm. with 0.25mm steps. Figures 8 and 9 represent the reflection coefficients (S11) and the mutual coupling (S21) respectively. It can be clearly seen that by increasing the width of the NL, the reflection coefficients are decreased slightly and there are low effect on the two frequency bands. On the other hand, the mutual coupling values decrease by increasing the width of the NL at first band and there is a small effect on second band. The summarized values of the two figures are listed in Table 4 and Table 5 respectively.

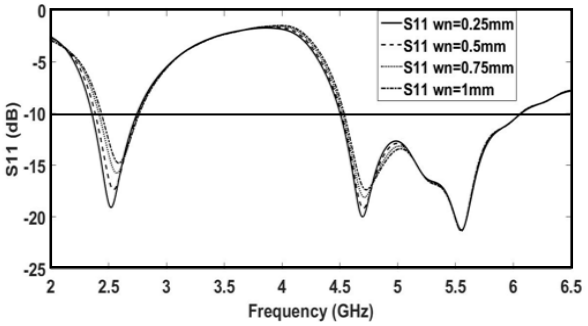

Fig. 8. Simulated reflection coefficient S11 of the third proposed antenna with different width of NL.

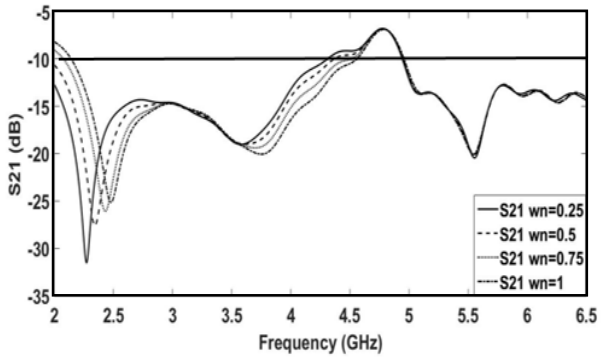

Fig. 9. Simulated transmission coefficient S21 of the third proposed antenna with different widths of NL.

Table 4: The effect of the width of NL on the reflection coefficients

	wn=0.25 mm	wn=0.5 mm	wn=0.75 mm	wn=1 mm
f=2.4 GHz	-18.7dB	-16.33dB	-13.9dB	-12.6dB
f=5.2 GHz	-15.7dB	-15.69dB	-15.6dB	-15.6dB
f=5.8 GHz	-12.32dB	-12.24dB	-12.1dB	-12.1dB

Table 5: The effect of the width of NL on the transmission coefficients

	wn=0.25 mm	wn=0.5 mm	wn=0.75 mm	wn=1 mm
f=2.4 GHz	-24 dB	-22.5 dB	-18.5dB	-16 dB
f=5.2 GHz	-13.7 dB	-13.66 dB	-13.68 dB	-13.7 dB
f=5.8 GHz	-12.8 dB	-12.7 dB	-12.7 dB	-12.7 dB

V. RESULTS AND DISCUSSION

To verify the simulated outcomes, the proposed

MIMO antenna is fabricated and tested. The prototype design of the proposed antenna is displayed in Fig. 10. The scattering parameters in terms of reflection coefficient (S_{11}) and transmission coefficient (S_{21}) were measured using vector network analyser (VNA) while the radiation patterns were measured facilities inside the anechoic chamber. Distinguishing features such as high isolation between the radiating elements, low values for envelope correlation coefficient and channel capacity loss, TARC value ≤ -10dB within the desired frequency band and omnidirectional radiation pattern, indicate the potential of proposed MIMO antenna. The designed antenna was prototyped using the same substrate and dimensions used in the simulation. The comparisons between the simulated and the measured results in terms of S-parameters are plotted in Fig. 11 and Fig. 12 respectively. It can be clearly seen that there is a reasonable agreement between results with some tolerance that can be attributed to reflections from the SMA connectors and the objects near the antenna during the tests. The measured impedance bandwidths of the antenna cover the operating frequency bands from 2.4 to 2.7GHz and from 4.4 GHz to 6.7GHz for the reflection coefficient |S11| ≤ -10dB. These achieved bandwidths fulfil the requirements of the WLAN applications. On the other hand, the result of S21 for the two bands is less than -10dB and it reaches to -30dB around 2.4 GHz and 5.5GHz.

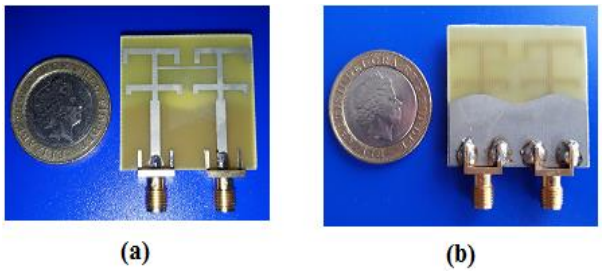

Fig. 10. The fabricated MIMO antenna design with N: (a) top view and (b) back view.

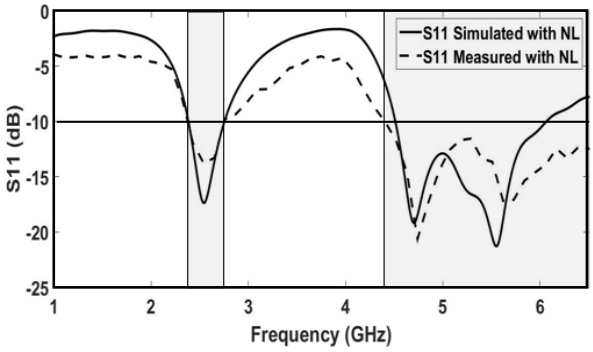

Fig. 11. Simulated and measured S11 of the proposed MIMO antenna with NL.

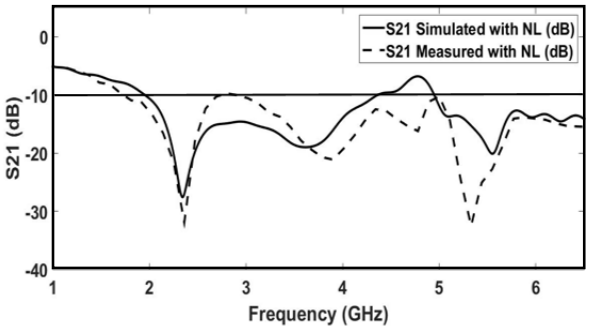

Fig. 12. Simulated and measured S21 of the proposed MIMO antenna with parasitic elements.

Generally, the envelope correlation coefficient (ECC) is a significant factor in MIMO antenna systems due to its ability to examine how much the radiating elements are independent and they rely on their individual performances. The evaluation of the ECC of a MIMO antenna could be obtained through two different approaches. The first method depends on the far-field radiation pattern of the antenna [1, 37] and the second method uses the S-parameters of the antenna [30]. The simulated and measured ECC of the proposed MIMO antenna were calculated using equation 1 [30] and the results are illustrated in Fig. 13. It can be clearly seen from Fig. 13 that the value of the ECC is less than 0.025 in two bands which is significantly less than the 0.3, the requirement for MIMO antenna applications [28]:

$$ECC = \frac{|S^*_{11}S_{12}+S^*_{21}S_{22}|}{(1-|S_{11}|^2-|S_{21}|^2)\,(1-|S_{22}|^2-|S_{12}|^2)}. \quad (1)$$

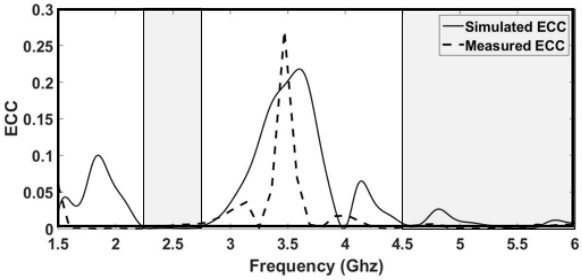

Fig. 13. Simulated and measured ECC of the proposed MIMO antenna with NL.

Basically, the channel capacity of the MIMO system could be improved by increasing the number of antennas. whilst the existence of the uncorrelated Rayleigh-fading may lead to a loss in the channel capacity. For two elements of MIMO systems, the channel capacity loss could be calculated by using the correlation matrix mentioned in [38]. The simplified form of channel capacity loss is listed below [39]:

$$C_{loss} = -log_2 \det(\varphi^R), \quad (2)$$

where φ^R is the correlation matrix receiving antenna:

$$\varphi^R = \begin{bmatrix} \rho_{11} & \rho_{12} \\ \rho_{21} & \rho_{22} \end{bmatrix},$$

$$\text{with } \rho_{ii} = \left(1 - \left(|S_{ii}|^2 + |S_{ij}|^2\right)\right),$$

$$\text{and } \rho_{ij} = -\left(S_{ii}^* S_{ij} + S_{ji}^* S_{jj}\right) \quad \text{i,j = 1 or 2.}$$

The computed and measured capacity loss of the proposed MIMO antenna is illustrated in Fig. 14. In this figure, the capacity loss is less than 1 bit/s/Hz for the two bands and there is a very good agreement between the calculated and measured results.

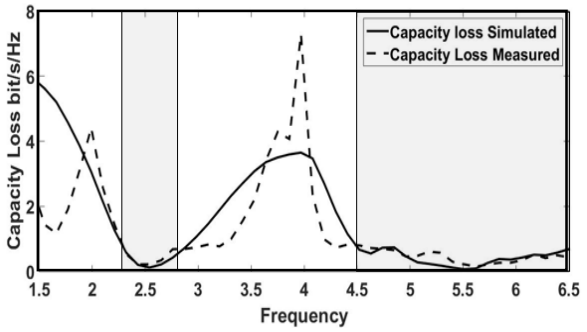

Fig. 14. Simulated and measured CCL of the proposed MIMO antenna with parasitic elements.

The total active reflection coefficient (TARC) is a considerable parameter in the MIMO antenna system which is used to properly characterize the bandwidth and efficiency of the system. TARC defines as the result of dividing the square root of the total reflected power to the square root of the total incident power [28]. Equation (3) uses to evaluate the TARC value in the two-port MIMO antenna system [14]:

$$\tau_a^t = \sqrt{\frac{\left(\left(|S_{11}+S_{12}e^{j\theta}|^2\right)+\left(|S_{21}+S_{22}e^{j\theta}|^2\right)\right)}{2}}. \qquad (3)$$

The computed TARC of the present design is explained in Fig. 15 and Fig. 16 respectively. Figure 15 is created using equation (3) to cover the phase range from 0 to 180 degrees with phase steps of 30 degrees. The average value of TARC is shown in Fig. 16. It can be clearly seen that the two bands appeared with a TARC value of less than -10dB.

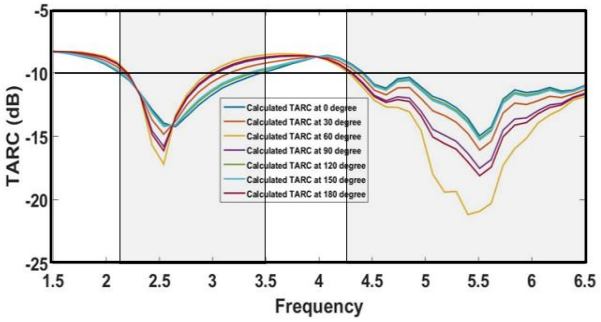

Fig. 15. Calculated TARC with a different phase of the proposed MIMO antenna with parasitic elements.

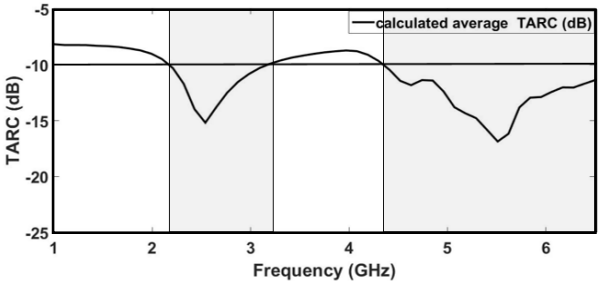

Fig. 16. The calculated average value of TARC for the proposed MIMO antenna with parasitic elements.

Diversity Gain (DG) is another important factor that affects the performance of a MIMO antenna system. This metric can be defined as the amount of improvement in the diversity antenna system compared to a single antenna system in one diversity channel [28]. In this paper, the DG can be calculated using the following equation [40]:

$$DG = 10\sqrt{1 - (ECC)^2}. \qquad (4)$$

Figure 17 represents the simulated DG of the proposed MIMO antenna. It can be clearly seen that the DSs values for the two frequency bands are very close to the ideal value of DG (DG=10dB).

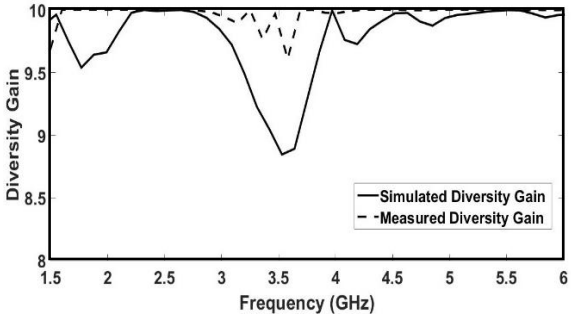

Fig. 17. The simulated and measured diversity gain of the proposed MIMO antenna.

Finally, the prototyped design of the proposed antenna is tested in terms of far-field radiation patterns at three different frequencies in the anechoic chamber of the University of Bradford. These patterns were measured in the two planes of XZ and YZ, in the case of exciting port 1 and terminating port 2. The elevation-over-azimuth positioner was used by synchronizing the elevation axis with the MIMO antenna's coordinate system at (θ = 0°). Therefore, cuts at constant ϕ will be generated by the azimuth drive. A broadband horn (EMCO type 3115) is used as a transmitting antenna and a 4m distance was kept between the transmitter and the antenna under test. The measurements have carried out by rotating the azimuth positioner from θ= -180 to 180 at increments of 5 degrees. The practical results are shown in Fig. 18 and they explain that at the three

frequencies, the far-field radiations achieve stable omnidirectional patterns. For further evaluation of the volumetric radiation patterns, the three-dimensional variation of the radiated field for the proposed antenna is calculated at three frequencies and are shown in Fig. 19. This figure gives more appreciation of the field shape as compared to that of the 2-D representations.

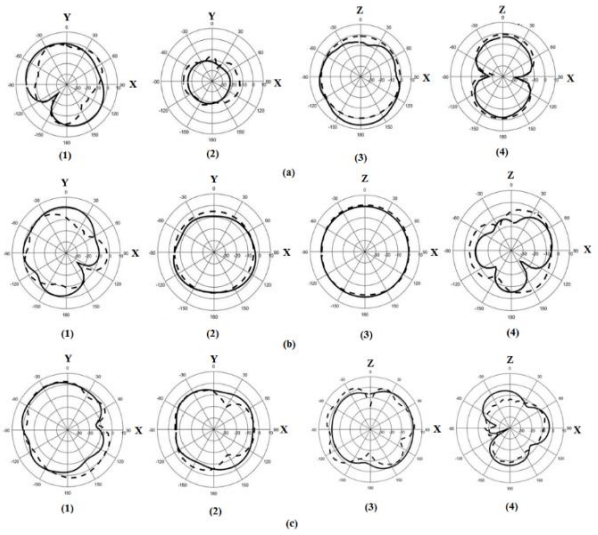

Fig. 18. Simulated and measured radiation patterns of the proposed antenna for two planes [(1 and 2) y-x plane and (3 and 4) z-x plane] at: (a) 2.4GHz, (b) 5.2GHz, and (c) 5.8GHz. Port 1 is excited and port 2 is terminated. "____" simulated results, "_ _ _" measured results, '1 and 3' co-polar components and "2 and 4" cross-polar components.

VI. COMPARISON WITH PUBLISHED WORKS

Furthermore, the proposed MIMO antenna is compared with several published data from other researchers. All the antennas in this comparison were used neutralization line as reduction technique in their antennas. This comparison is not comprehensive, but it has a fair representative for the state of the art of this technology. The comparison depends on the overall size of the antenna, the frequency of operation, the separation distance between the radiating elements, the isolation between the elements and the diversity performance in terms of ECC, CCL, TARC and DG. The summary of this comparison has listed in Table 6. It can be noticed that the dimensions of the proposed antenna are moderate between the other antennas. The isolation of the proposed antenna is shown to provide a good value compared to the distance between the radiating elements. Low-level correlation coefficient and minimum channel capacity loss compared with other designs have also been obtained. These features confirm that this design is a good candidate for the MIMO antenna design.

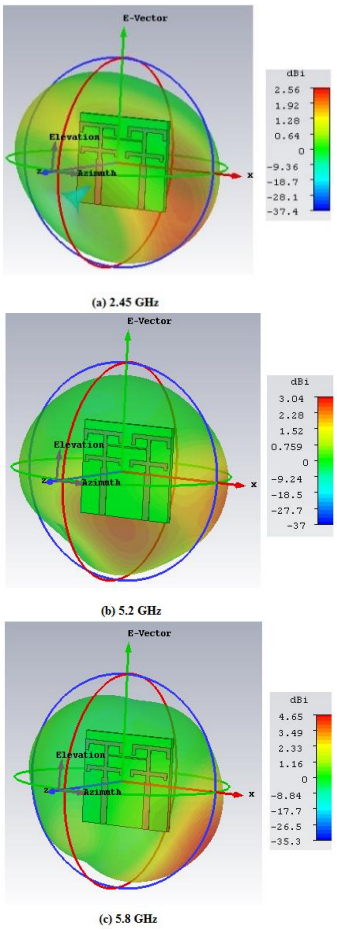

Fig. 19. The simulated 3-D pattern of the proposed MIMO antenna at: (a) 2.4GHz, (b) 5.2GHz, and (c) 5.8GHz.

Table 6: Comparison with other works

Ref. No.	41	42	43	44
Size (mm^3)	26.7x32.94 x1.6	60x7.5 x4.5	40x90 x0.79	35x16 x0.8
BW (GHz)	3.05-13.5	2.4–2.484 5.15–5.85	2.4-4.2	3.1-5
Separation distance	0.52mm	18mm	18.8mm	2.2mm
Isolation (dB)	≥10	Max 16, 23	≥16	Max 22
ECC	≤0.1	NA	≤0.06	NA
CCL (bps/s/Hz)	NA	NA	NA	NA
TARC≤-10dB	NA	NA	NA	NA
DG (dB)	NA	NA	NA	NA
Ref. No.	**45**	**46**	**47**	**This Antenna**
Size (mm^3)	120x60x0.8	80x60x0.8	65x30x1	36x33.5x1.6
BW (GHz)	0.76-0.82	1.67-2.76	2.38-2.51	2.42.7 4.4-6.7
Separation distance	10mm	10mm	14mm	3mm
Isolation (dB)	Max 11.5	≥15	Max 22	≥15
ECC	≤0.5	≤0.05	≤0.006	≤0.1
CCL (bps/s/Hz)	NA	NA	NA	≤0.05
TARC≤-10dB	NA	NA	Cover the band	Covers the two bands
DG (dB)	NA	≥9.98	NA	≥9.99

VII. CONCLUSION AND FUTURE WORK

A compact dual-band MIMO antenna operating at WLAN bands (2.4/5.2/5.8 GHz) has been designed. The schematic structure of this antenna consists of two double T-shaped radiating elements with a neutralization line to connect them. The optimum value of isolation has been obtained by optimizing the neutralization line in terms of width and position. The antenna has achieved bandwidths from 2.4GHz to 2.7GHz and from 4.4 to 6.7 for reflection coefficient $|S11| \leq$ -10dB. On the other hand, the results of S21 for the two bands are better than -15dB and it has reached to -30dB around 2.4GHz and 5.5GHz. The Envelope correlation coefficient has also been evaluated and found to be less than 0.01 in the two bands. Channel capacity loss is another parameter that has been calculated and presented. The obtained value of CCL is less than 0.5 bps/s/Hz in the two required bands. The simulated and measured average TARCs have been also illustrated. It has been observed that the two bands appeared with a TARC value of less than -10dB. Diversity gain is another important metric that has been studied in this work. The achieved value of DG is very close to the ideal value (10dB) over the two frequency bands. The simulated and measured radiation patterns were presented at three different frequencies and they showed nearly a stable omnidirectional behavior. These achievements indicate that the proposed antenna can be a good candidate to work within WLAN frequency band applications. Some differences have been noticed between the simulated and measured results which related to manufacturing and measurement tolerances. Finally, an interesting area of using a Genetic Algorithm (GA) to evaluate the effect of neutralization lines within the MIMO antenna structure can be used to extend this work in the future.

ACKNOLEDGEMENTS

Adham M. Saleh would like to thank the Higher Committee for Education Development in Iraq (HCED) for supporting this project financially and monitoring his Ph.D. progress. The authors would like to acknowledge Ninevah University and the University of Bradford for their massive support during this project.

REFERENCES

[1] R. G. Vaughan and J. B. Andersen, "Antenna diversity in mobile communications," *IEEE Transactions on Vehicular Technology*, vol. VT-36, pp. 147-172, Nov. 1987.

[2] G. J. Foschini and M. J. Gans, "On limits of wireless communications in a fading environment when using multiple antennas," *Wireless Pers. Commun.*, vol. 6, pp. 311-335, 1998.

[3] J. Leivo, "Improving the performance of strongly coupled antennas using a compensating transmission line network," *M.Sc. Thesis*, Gothenburg, Chalmers University of Technology, Sweden, 2009.

[4] S. R. Saunders and A. A. Zavala, *Antennas and Propagation for Wireless Communication Systems*, 2nd Ed., John Wiley & Sons Ltd, 2007.

[5] C. H. See, et al., *Compact Wideband Printed MIMO/Diversity Monopole Antenna for GSM/ UMTS and LTE Applications*. In: I. Elfergani, A. Hussaini, J. Rodriguez, R. Abd-Alhameed (eds), Antenna Fundamentals for Legacy Mobile Applications and Beyond. Springer, Cham, 2018.

[6] R. Addaci, A. Diallo, C. Luxey, P. Le Thuc, and R. Staraj, "Dual-band WLAN diversity antenna system with high port-to-port isolation," in *IEEE Antennas and Wireless Propagation Letters*, vol. 11, pp. 244-247, 2012.

[7] X. B. Sun and M. Y. Cao, "Low mutual coupling antenna array for WLAN application," in *Electronics Letters*, vol. 53, no. 6, pp. 368-370, 2017.

[8] X. L. Liu, Z. Wang, Y.-Z. Yin, and J. H. Wang, "Closely spaced dual band-notched UWB antenna for MIMO applications," *Progress In Electromagnetics Research C*, vol. 46, pp. 109-116, 2014.

[9] H. Qin and Y.-F. Liu, "Compact dual-band MIMO antenna with high port isolation for WLAN applications," *Progress In Electromagnetics Research C*, vol. 49, pp. 97-104, 2014.

[10] P. Sharmaa and T. Khanb, "A compact MIMO antenna with DGS structure," *International Journal of Current Engineering and Technology*, vol. 3, no. 3, pp. 780-782, 2013.

[11] W. N. N. W. Marzudi, et al., "Uni-planer MIMO antenna for WLAN and WiMAX wireless services," *International Journal of Computer and Information Technology*, vol. 8, no. 3, pp. 78-83, May 2019.

[12] H. Zhao, F. Zhang, C. Wang, and J. Liang, "A compact UWB diversity antenna," *International Journal of Antennas and Propagation*, vol. 2014, Article ID 805853, 6 pages, 2014.

[13] W. N. N. W. Marzudi, et al., *Two-Elements Crescent Shaped Printed Antenna for Wireless Applications*. In: H. Sulaiman, M. Othman, M. Othman, Y. Rahim, N. Pee (eds), Advanced Computer and Communication Engineering Technology. Lecture Notes in Electrical Engineering, vol. 315, Springer, Cham, 2015.

[14] S. Su, C. Lee, and F. Chang, "Printed MIMO-antenna system using neutralization-line technique for wireless USB-dongle applications," in *IEEE Transactions on Antennas and Propagation*, vol. 60, no. 2, pp. 456-463, Feb. 2012.

[15] Y. Wang and Z. Du, "A wideband printed dual-antenna with three neutralization lines for mobile terminals," in *IEEE Transactions on Antennas and Propagation*, vol. 62, no. 3, pp. 1495-1500, Mar. 2014.

[16] S. Zhang and G. F. Pedersen, "Mutual coupling reduction for UWB MIMO antennas with a

wideband neutralization line," in *IEEE Antennas and Wireless Propagation Letters*, vol. 15, pp. 166-169, 2016.

[17] A. M. Saleh, K. H. Sayidmarie, R. A. Abd-Alhameed, S. Jones, J. M. Noras, and P. S. Excell, "Compact tri-band MIMO antenna with high port isolation for WLAN and WiMAX applications," *2016 Loughborough Antennas & Propagation Conference (LAPC)*, Loughborough, pp. 1-4, 2016.

[18] R. Selvaraju, M. H. Jamaluddin, M. R. Kamarudin, J. Nasir, and M. H. Dahri, "Complementary split ring resonator for isolation enhancement in 5G communication antenna array," *Prog. Electromagn. Res.*, vol. 83, pp. 217-228, 2018.

[19] M. M. Bait-Suwailam, O. F. Siddiqui, and O. M. Ramahi, "Mutual coupling reduction between microstrip patch antennas using slotted-complementary split-ring resonators," in *IEEE Antennas and Wireless Propagation Letters*, vol. 9, pp. 876-878, 2010.

[20] Z. Qamar, L. Riaz, M. Chongcheawchamnan, S. A. Khan, and M. F. Shafique, "Slot combined complementary split-ring resonators for mutual coupling suppression in microstrip phased arrays," in *IET Microwaves, Antennas & Propagation*, vol. 8, no. 15, pp. 1261-1267, 9 12 2014.

[21] M. S. Sharawi, M. U. Khan, A. B. Numan, and D. N. Aloi, "A CSRR loaded MIMO antenna system for ISM band operation," in *IEEE Transactions on Antennas and Propagation*, vol. 61, no. 8, pp. 4265-4274, Aug. 2013.

[22] A. Ramachandran, S. Valiyaveettil Pushpakaran, M. Pezholil, and V. Kesavath, "A four-port MIMO antenna using soncentric square-ring patches loaded with CSRR for high isolation," in *IEEE Antennas and Wireless Propagation Letters*, vol. 15, pp. 1196-1199, 2016.

[23] M. S. Khan, A. Capobianco, S. M. Asif, D. E. Anagnostou, R. M. Shubair, and B. D. Braaten, "A compact CSRR-enabled UWB diversity antenna," in *IEEE Antennas and Wireless Propagation Letters*, vol. 16, pp. 808-812, 2017.

[24] W. T. Li, Y. Q. Hei, H. Subbaraman, X. W. Shi, and R. T. Chen, "Novel printed filtenna with dual notches and good out-of-band characteristics for UWB-MIMO applications," in *IEEE Microwave and Wireless Components Letters*, vol. 26, no. 10, pp. 765-767, Oct. 2016.

[25] D. A. Ketzaki and T. V. Yioultsis, "Metamaterial-based design of planar compact MIMO monopoles," in *IEEE Transactions on Antennas and Propagation*, vol. 61, no. 5, pp. 2758-2766, May 2013.

[26] M. G. N. Alsath, M. Kanagasabai, and B. Balasubramanian, "Implementation of slotted meander-line resonators for isolation enhancement in microstrip patch antenna arrays," *IEEE Antennas and Wireless Propagation Letters*, vol. 12, pp. 15-18, 2013.

[27] I. Nadeem and D. Choi, 'Study on mutual Coupling reduction technique for MIMO antennas," in *IEEE Access*, vol. 7, pp. 563-586, 2019.

[28] M. R. Sharawi, *Printed MIMO Antenna Engineering*. Norwood: Artech House, 2014.

[29] J. Byun, J.-H. Jo, and B. Lee, "Compact dual-band diversity antenna for mobile handset applications," *Microwave and Optical Technology Letters*, vol. 50, pp. 2600-2604, 2008.

[30] K. Chung and J. H. Yoon, "Integrated MIMO antenna with high isolation characteristic," *Electronics Letters*, vol. 43, pp. 199-201, 2007.

[31] S.-W. Su, C.-T. Lee, and F.-S. Chang, "Printed MIMO-antenna system using neutralization-line technique for wireless USB-dongle applications,"' *IEEE Transactions. Antennas Propagation*, vol. 60, no. 2, pp. 456-463, Feb. 2012.

[32] S. Wang and Z. Du, "Decoupled dual-antenna system using crossed neutralization lines for LTE/WWAN smartphone applications," in *IEEE Antennas and Wireless Propagation Letters*, vol. 14, pp. 523-526, 2015.

[33] Y. Ou, X. Cai, and K. Qian, "Two-element compact antennas decoupled with a simple neutralization line," *Prog. Electromagn. Res*., vol. 65, pp. 63-68, 2017.

[34] W. A. E. Ali and A. A. Ibrahim, "A compact double-sided MIMO antenna with an improved isolation for UWB applications," *AEU-Int. J. Electron. Commun*., vol. 82, pp. 7-13, Dec. 2017.

[35] S. Papantonis and E. Episkopou, "Compact dual-band printed 2.5-shaped monopole antenna for WLAN applications," *Progress In Electromagnetics Research C*, vol. 24, pp. 57-68, 2011.

[36] Y. Ban, Z. Chen, Z. Chen, K. Kang, and J. L. Li, "Decoupled hepta-band antenna array for WWAN/ LTE smartphone applications," in *IEEE Antennas and Wireless Propagation Letters*, vol. 13, pp. 999-1002, 2014.

[37] R. A. Bhatti, J. Choi, and S. Park, "Quad-band MIMO antenna array for portable wireless communications terminals," in*IEEE Antennas and Wireless Propagation Letters*, vol. 8, pp. 129-132, 2009.

[38] S. H. Chae, S. Oh, and S. Park, "Analysis of mutual coupling, correlations, and TARC in WiBro MIMO array antenna," in *IEEE Antennas and Wireless Propagation Letters*, vol. 6, pp. 122-125, 2007.

[39] C. H. See, R. A. Abd-Alhameed, Z. Z. Abidin, N. J. McEwan, and P. S. Excell, "Wideband printed MIMO/diversity monopole antenna for WiFi/ WiMAX applications," in I*EEE Transactions on Antennas and Propagation*, vol. 60, no. 4, pp. 2028-2035, Apr. 2012.

[40] A. Kumar, et al., "High isolation compact four-port MIMO antenna loaded with CSRR for multiband

applications,"*Frequenz*, 72.9-10, pp. 415-427, 2018. Retrieved 12 Aug. 2019, from doi:10.1515/freq-2017-0276.

[41] J. Banerjee, R. Ghatak, and A. Karmakar, "A compact planar UWB MIMO diversity antenna with Hilbert fractal neutralization line for isolation improvement and dual band notch characteristics," *2018 Emerging Trends in Electronic Devices and Computational Techniques (EDCT)*, Kolkata, pp. 1-6, 2018.

[42] C. Jui-Hung, et al., "Dual-band WLAN MIMO antenna with a decoupling element for full-metallic bottom cover tablet computer applications," *Microwave and Optical Technology Letters*, vol. 60, no. 5, pp. 1245-1251, 2018.

[43] E. Elkazmi, C. H. See, N. A. Jan, R. A. Abd-Alhameed, N. Ali, and N. J. McEwan, "Design of a wideband printed MIMO monopole antenna using neutralization lines technique," *Asia-Pacific Microwave Conference*, Sendai, Japan, pp. 983-985, 2014.

[44] S. Zhang and G. F. Pedersen, "Mutual coupling reduction for UWB MIMO antennas with a wideband neutralization line," in *IEEE Antennas and Wireless Propagation Letters*, vol. 15, pp. 166-169, 2016.

[45] A. Cihangir, F. Ferrero, G. Jacquemod, P. Brachat, and C. Luxey, "Neutralized coupling elements for MIMO operation in 4G mobile terminals," in *IEEE Antennas and Wireless Propagation Letters*, vol. 13, pp. 141-144, 2014.

[46] Y. Wang and Z. Du, "A wideband printed dual-antenna system with a novel neutralization line for mobile terminals," in *IEEE Antennas and Wireless Propagation Letters*, vol. 12, pp. 1428-1431, 2013.

[47] S. Su, C. Lee, and F. Chang, "Printed MIMO-antenna system using neutralization-line technique for wireless USB-dongle applications," in *IEEE Transactions on Antennas and Propagation*, vol. 60, no. 2, pp. 456-463, Feb. 2012.

Adham Maan Saleh was born in Mosul, Iraq, in 1984. He received the B.Sc. and M.Sc. degrees from Ninevah University, Iraq in 2006 and 2012, respectively, all in Communications Engineering. Currently, he is working toward the Ph.D. degree from the School of Engineering and Informatics, Bradford University, West Yorkshire, UK He was a Lecturer at Ninevah University since 2012. His current research interests include MIMO antenna design, defected ground structures (DGS), neutralization techniques for wireless and mobile systems, reflectarray antennas, and multiband antennas techniques.

Tariq A. Nagem was born in Mosul, Iraq, in 1984. He received the B.Sc. and M.Sc. degrees from Ninevah University, Iraq in 2006 and 2013, respectively, all in Communications Engineering. He was a Lecturer at Ninevah University since 2013. His current research interests include MIMO antenna design, filters design, ultra-wide band antennas (UWB) and multi-band antenna techniques.

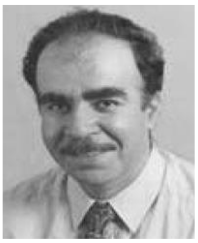

Raed A. Abd-Alhameed received the B.Sc. and M.Sc. degrees from Basrah University, Basrah, Iraq, in 1982 and 1985, respectively, and the Ph.D. degree from the University of Bradford, West Yorkshire, U.K., in 1997, all in Electrical Engineering. He is a Professor of electromagnetic and radio frequency engineering at the University of Bradford. He is the senior academic responsible for electromagnetics research in the Mobile and Satellite Communications Research Center, University of Bradford.

James M. Noras received the B.Sc. degree in Physics and the Ph.D. degree in Semiconductor Physics from St. Andrews University, Scotland, in 1973 and 1978, respectively, and the M.Sc. degree in Mathematics from the Open University, U.K., in 1995. He is a Senior Lecturer in the School of Engineering, Design and Technology at the University of Bradford, UK. He is the Director of five internationally franchised B.Eng. and M.Sc. courses in Electrical and Electronic Engineering has successfully supervised 18 Ph.D. students and is currently supervising the research of three Ph.D. students. His main research interests are now in digital system design and implementation, DSP and coding for communication systems, and localization algorithms for mobile systems.

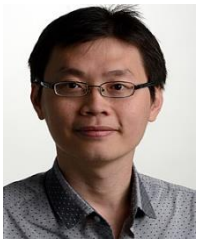

Chan H. See received a first-class B.Eng. Honours degree in Electronic, Telecommunication and Computer Engineering and a Ph.D. degree from the University of Bradford, UK. Since 2019, He has been appointed as Associate Professor within the School of Engineering and the Built Environment, Edinburgh Napier University. See is a

Chartered Engineer and Fellow of the Institution of Engineering and Technology (FIET) and Senior Member of Institute of Electrical and Electronics Engineers (SMIEEE). He has an NVQ level 4 in Management from the Chartered Management Institute.

A High-Gain Microstrip Patch Antenna Using Multiple Dielectric Superstrates for WLAN Applications

Niamat Hussain [1], Uktam Azimov [1], Minjoo Jeong [1], Seungyeop Rhee [2], Seung W. Lee [3], and Nam Kim [1*]

[1] Department of Computer and Communication Engineering
Chungbuk National University, Cheongju, 28644, Republic of Korea
* namkim@chungbuk.ac.kr

[2] Electronic Communication Engineering
Chonnam National University, Yeosu, 59626, Republic of Korea

[3] Korea Electric Power Research Institute, Daejeon, Republic of Korea

Abstract ─ This paper presents the design and characterization of a microstrip patch antenna with multiple superstrates for performance enhancement operating at the central frequency of 5.5 GHz for high-gain WLAN applications. The performance of the antenna in terms of reflection loss and the gain are investigated using multiple high dielectric constant superstrates of Taconic CER-10 (ε_r=10.2). Numerical results showed that the patch antenna has -10 dB impedance bandwidth of 2.54% which improves to 8.43% and 17.43% by employing a single and dual superstrate, respectively. The gain of the antenna increases from 6.1 dBi to 9.5 dBi using a single superstrate, which further enhances to 13.6 dBi by placing two optimized superstrates. Moreover, further increasing the number of superstrates did not significantly impact on the performance of the patch antenna. The final design of the antenna (patch antenna with two superstrates) is fabricated and measured. The measured results agree well with the simulated results. Due to the good impedance matching, high-gain and desired radiation patterns compared to the other superstrate antennas, this antenna is a good candidate for high-gain WLAN applications.

Index Terms ─ Fabry-Perot cavity antenna, gain enhancement, microstrip patch antenna, superstrate antenna, WLAN.

I. INTRODUCTION

The wireless communication revolution is bringing fundamental changes and updates to data networking, telecommunication, and is making integrated networks for future development. By freeing the user from the cord, personal communications networks, wireless local area networks, mobile radio networks, and cellular systems, harbor the promise of fully distributed wireless computing and communications, anywhere and anytime. Due to the development of information communication technology, the wireless network uses various frequency bands. The frequency bands are assigned based on the technology, purpose, network size, and requirements of the communication. For example, Wireless Local Area Networks (WLAN) bands work with maximum 250 m distance, with medium data rates and used in houses, small offices, factories or corporation areas.

On the other hand, WLAN is mainly used not only in industrial fields but also in every house, offices, and public places. Its usability and application range is expanding because it can be used conveniently regardless of location compared to a wired network. Being the key component of the communication systems, the design of the antennas having the desired characteristics has always been a challenge for the antenna engineers. Microstrip patch antennas offer advantages of low-cost, planar structure and easy design and have been studied thoroughly in the literature [1]. However, these antennas have low gain which limits the use of microstrip patch antennas in those applications which require high gain. These low gain antennas are not suitable for long-range communications and confined spaces like corridors, streets, tunnels, and highways. For the specific cases described above, high-gain and directional antennas with low back radiations are needed. Usually, microstrip antennas are coupled with extended hemispherical dielectric lenses to achieve high gain, especially at high frequencies [2, 3]. Lens-coupled antennas undergo the disadvantages of fabrication complexity and low radiation efficiencies [4]. On the other hand, Fabry-Perot cavities [5], and the metasurfaces/metamaterial [6-13] have also been used to increase the gain of antennas. However, the metasurfaces

Submitted On: October 4, 2019
Accepted On: November 15, 2019

unit cells need optimization of complex design having huge design parameters. One of the famous and easy methods to increase the gain is the use of superstrates, in which one or multiple dielectrics and printed superstrates are placed over an optimized distance from the patch or basic radiator [14-29]. These superstrate antennas are getting significant attention of researchers both in microwave and millimeter waves owing to its intrinsic advantages of low complexity, high-gain, and conformal deployment ability.

In this paper, we proposed a microstrip patch antenna with multiple dielectric superstrates to enhance performance, especially the broadside gain at 5.5 GHz for high-gain WLAN applications. The results show that the impedance bandwidth and gain of the patch antenna is increased using a single superstrate, which is further increased using two superstrates. All the antenna designs (patch antenna, a patch antenna with one superstrate, patch antenna with two superstrates, and patch antenna with three superstrates) are simulated using the finite integration time-domain commercial simulator CST Microwave Studio. A transient time-domain solver with a hexahedral mesh type with an accuracy level of -45 dB is used in the simulation setup. This solver enables the complete far-field characterization of the antennas at broadband frequencies at one simulation run. To ensure the accuracy of the numerical results, the maximum mesh type is set as one-twentieth of a free space wavelength at 5.5 GHz.

II. ANTENNA DESIGN

The geometry of the microstrip patch antenna is shown in Fig. 1. The antenna is consisting of a full ground plane and a microstrip patch, both of which are patterned on Taconic TLY5 (ε_r = 2.2, $tan\delta$ = 0.0009) due to its low loss tangent and stable dielectric constant values at high frequencies. The patch is fed by a 50-ohm microstrip feed line. The optimized parameters of the patch antenna are: A = 50 mm, h_p = 1.6 mm, p_x = 19 mm, p_y = 18 mm, g = 4.25 mm, L = 3 mm, ws = 1.5 mm, and Ls = 44 mm.

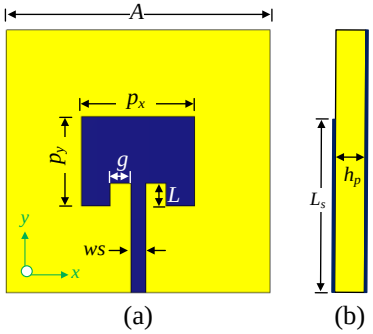

Fig. 1. Geometry of patch antenna: (a) front view and (b) side view.

The microstrip patch antenna is then coupled with a high dielectric constant superstrate to increase the broadside gain. Conventionally, an electrically thick superstrate is utilized to focus the radiated field in the broadside direction. Therefore, a planar slab of high dielectric Taconic substrate (ε_r = 10.2, $tan\delta$ = 0.0035) having a thickness of h_s = 1.6 mm is placed at an optimized distance of h_a = 4 mm from the antenna, as shown in Fig. 2. In this stage, only the parameters of the superstrate (h_a and h_s) are tuned for optimum performance, while all other parameters are kept unchanged.

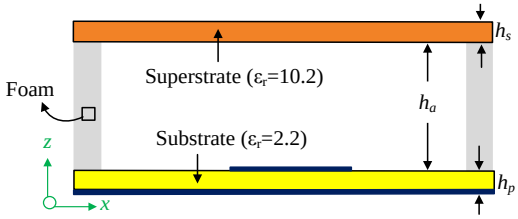

Fig. 2. Side view of the patch antenna with a single superstrate.

As the air gap is an important parameter in the design of such antennas. The antenna impedance and gain characteristics for the different values of superstrate height (h_a) from the patch antenna are shown in Fig. 3. The superstrate height greatly impacted on antenna performance. The gain and impedance of the antenna is improved when the superstrate height is increased from 2 mm to 4 mm, however, further increasing the height decreases the gain. Moreover, the impedance bandwidth is shifted to the higher frequencies for the increment in the air gap.

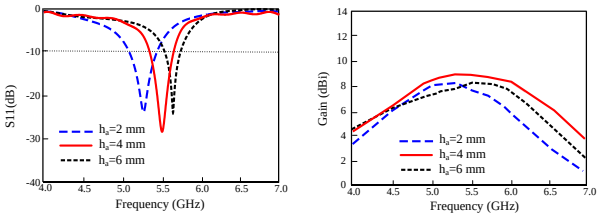

Fig. 3. Characteristics of patch antenna with single superstrate for different values of superstrate height (h_a): (a) $|S_{11}|$ and (b) broadside gain.

The patch antenna with single superstrate antenna is then modified by adding another identical superstrate for further gain enhancement to make the antenna suitable for high-gain WLAN applications, as shown in Fig. 4. A few antenna parameters are changed to reoptimized the antenna for two superstrates. The reoptimized parameters are: h_{s1} = 1.6 mm, h_a = 7 mm, and h_{a1} = 10 mm, while all other parameters remain the same.

The antenna characteristics in terms of $|S_{11}|$ and broadside gain of the antenna for the various separations (h_{a1}) between the two superstrates is shown in Fig. 5. A separation of h_{a1} = 12.5 mm gave the best results for the resonance at the desired frequency of 5.5 GHz with the high-gain and wide impedance bandwidth. Similarly, the antenna was optimized for three identical superstrates, where a third superstrate layer was placed on the antenna with two superstrates. The reoptimized parameters for this antenna configuration are as: h_{s2} = 1.6 mm, h_a = 6.5 mm, h_{a1} = 12, and h_{a2} = 7 mm (h_{s2} and h_{a2} is thickness and air separation of the third superstrate, respectively).

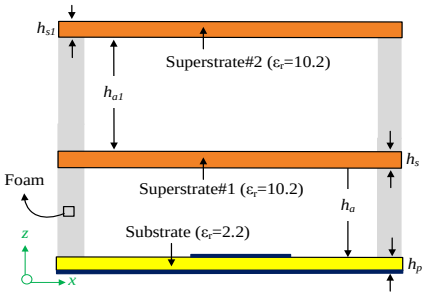

Fig. 4. Side view of the patch antenna with two superstrates.

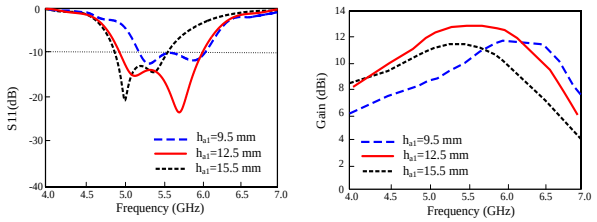

Fig. 5. Characteristics of patch antenna for the separation (h_{a1}) between two superstrates: (a) $|S_{11}|$ and (b) gain.

The antenna performance in terms of reflection loss and gain is compared for all cases of the patch antennas (a patch antenna with single superstrate, patch antenna with two superstrates, and patch antenna with three superstrates) is illustrated in Fig. 6. In summary, the overall performance especially impedance bandwidth and the gain of the patch antenna is improved using multiple superstrates. The antenna achieved the optimum performance for two superstrates. Further addition of the superstrates (three superstrates) did not improve the antenna performance. The detailed performance comparison of antennas for different superstrates is plotted in Table. 1. The antenna with two superstrates has a high-gain of 13.6 dBi and a wide impedance bandwidth from 4.8 - 6.1 GHz for $|S_{11}| < -10$dB covering the entire WLAN band. Compared to the patch antenna, the gain of the proposed antenna with two superstrates is increased 7.5 dBi, while impedance is increased almost four times.

The radiation patterns of the antenna at 5.5 GHz for three cases: antenna without substrate, antenna with one substrate, and antenna with two substrates are shown in Fig. 7. The radiation beam gets narrow with the addition of superstrates to increase the gain of the antenna. The half-power beamwidth of the patch antenna is around 70°, which decreases to 50° and 33° for the antenna with one superstrate and two superstrates, respectively.

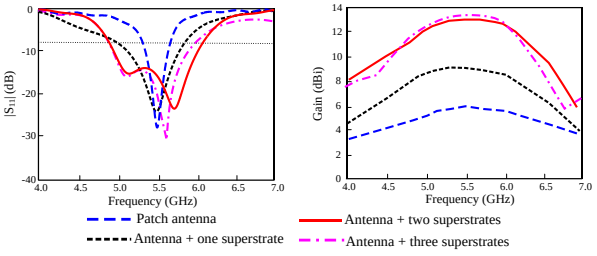

Fig. 6. The performance comparison for antennas with different configurations: (a) $|S_{11}|$ and (b) broadside gain.

Table 1: Performance comparison of antennas with different number of superstrates

Antenna Configuration	$\|S_{11}\|$ Bandwidth	Max. Gain (dBi)
Patch	5.43 - 5.57 GHz (2.54%)	6.1
Patch + one substrate	5.0 - 5.7 GHz (13%)	9.5
Patch + two substrates	4.8 - 6.1 GHz (23.8%)	13.6
Patch + three substrates	4.8 - 5.91 GHz (20.7%)	13.7

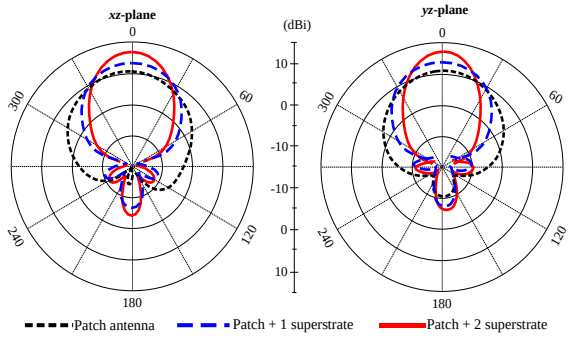

Fig. 7. Radiation patterns of the patch antenna for the different number of superstrates.

To explain the radiation mechanism of gain enhancement of the antennas using multiple superstrates, we computed the *E*-field of the antennas. The *E*-field for

each antenna configuration in *xz*-plane is plotted at the central frequency of 5.5 GHz as depicted in Fig. 8. The superstrate layer acts as a lens to focus the *E*-filed to increase its intensity in broadside direction, thus the gain of the patch antenna is increased for the increasing layers of superstrates. Meanwhile, the *E*-field is almost the same for the antennas with two and three superstrates. Therefore, the gain did not increase for three superstrates even though the superstrates layers were increased.

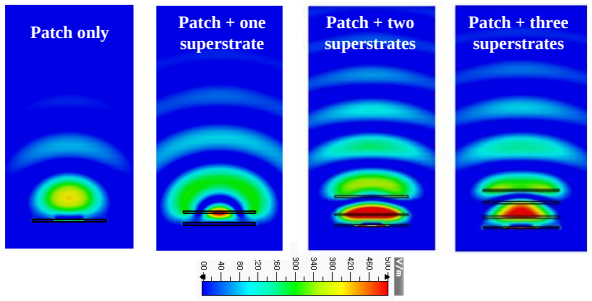

Fig. 8. *E*-filed of the antennas at *xz*-plane.

It is noted that in this study, we analyzed the performance of the patch antenna for the different numbers of superstrate layers, however, the size, thickness, and dielectric constant of the superstrate layers remained the same. The antenna with multiple superstrate layers, when the superstrate layers are different from each other would be the topic of a separate study in the near future.

III. MEASUREMENT RESULTS

The proposed antenna design that is the antenna with two superstrates is fabricated to obtain the measurement results. A fabricated prototype of the proposed antenna is shown in Fig. 9.

(a) (b) (c)

Fig. 9. Fabricated prototype of the proposed antenna: (a) Front view of the patch, (b) back view of the patch, and (c) side view of patch antenna with two superstrates.

The simulated and the measured impedance $|S_{11}|$ and gain characteristics of the proposed antenna are shown in Fig. 10. Simulation and measured results showed that the antenna has an improved 10 dB impedance bandwidth from 4.8 - 6.1 GHz (23.8%). In addition, the antenna achieved a higher gain of 13.6 dBi due to the enhanced beam collimation of multiple superstrates.

The measured and simulation radiation patterns of the antenna at 5.5 GHz at *xz*-plane (*E*-plane) and *yz*-plane (*H*-plane) are shown in Fig. 11. The antenna produced a symmetrical directional radiation pattern with low side and back lobe levels at both principal planes. The beam-width became narrow to increase gain and directivity. With the aforementioned features of wide bandwidth, high gain, and directive radiation patterns, the antenna is a good candidate for the high-gain WLAN applications at confined places including building corridors, tunnels, and streets.

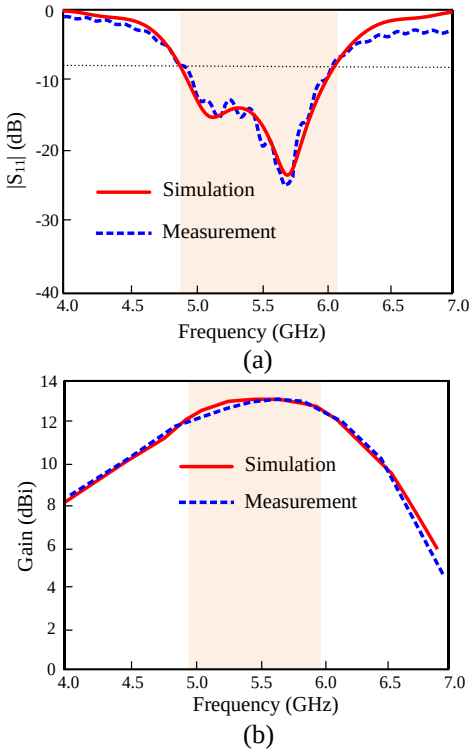

Fig. 10. Characteristics of patch antenna with two superstrates: (a) $|S_{11}|$ and (b) broadside gain.

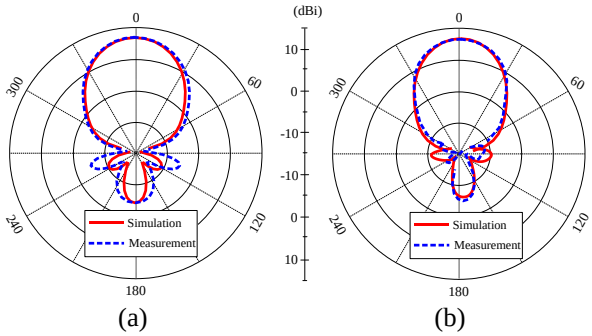

Fig. 11. The radiation pattern of the antenna with two superstrates: (a) *xz*-plane and (b) *yz*-plane.

Finally, the antenna performance is compared with the other superstrate antennas [18-25] in Table 2. In general, it can be concluded that the proposed antenna is offering wider bandwidth and high gain with the additional advantage of smaller size compared to most of the reference antennas, which verifies the worth of the proposed design. Among the reference antennas, only the designs presented in [19] and [21-22] has the advantages of smaller overall size, however, these antennas have narrow bandwidth and low-gain. Although the antenna with two printed superstrate [24] offers a high gain of 15 dBi, it has the disadvantages of complex superstrate design as well as high antenna profile and narrow bandwidth. Thus, the proposed antenna is offering the advantages of simple design, smaller size, wide-bandwidth, and high-gain.

Table 2: Performance comparison of the proposed antenna with other superstrate antennas

Ref. Antenna	Antenna Overall Size (λ_0^3)	$\lvert S_{11}\rvert$ BW (%)	Max. Gain (dBi)
[18]	5.28 × 5.28 × 0.6	5.28	11.95
[19]	0.67 × 0.5 × 0.53	3.14	10.3
[20]	2.06 × 2.06 × 0.83	3.0	12.8
[21]	0.88 × 0.88 × 0.07	15	8.4
[22]	0.67 × 0.67 × 0.14	3.14	7
[23]	1.6 × 1.2 × 0.8	3.7	12.86
[24]	2.5 × 2.5 × 1.44	8.2	15
[25]	1.93 × 1.93 × 0.61	2.7	6.8
Proposed	**0.91 × 0.91× 0.36**	**23.8**	**13.6**

IV. CONCLUSION

A patch antenna with multiple superstrates is designed at the central frequency of 5.5 GHz for WLAN applications. All antenna designs (patch antenna, a patch antenna with single superstrate, patch antenna with two superstrates, and patch antenna with three superstrates) are analyzed numerically to explain the design procedure and performance enhancement. Simulation and measured results confirm that the antenna performance (gain and $|S_{11}|$) is improved by coupling patch antenna with one superstrate which further improves using two superstrates. The antenna shows the optimum performance for the two superstrates, further increasing the number of superstrates did not increase the antenna performance. Owing to its wide bandwidth (23.8%) high-gain (13.6 dBi) and desired radiation patterns the proposed antenna (antenna with two superstrates) may find its usability in high-gain WLAN applications.

ACKNOWLEDGMENT

This work was supported by the ICT R&D Program of MSIT/IITP, Republic of Korea. [No. 2019-0-00102, A Study on Public Health and Safety in a Complex EMF Environment and was also supported by RRA of MSIT. [Development of Rapid Antenna Measurement Technique for Antennas with New Radio Technology].

REFERENCES

[1] K. F. Lee and K. M. Luk, *Microstrip Patch Antennas*, World Scientific, Singapore, 2010.

[2] L. Mall and R. B. Waterhouse, "Millimeter-wave proximity-coupled microstrip antenna on an extended hemispherical dielectric lens," *IEEE Trans. Antennas Propag*., vol. 49, no. 12, pp. 1769-1772, 2001.

[3] N. Hussain, T. K. Nguyen, H. Han, and I. Park, "Minimum lens size supporting the leaky-wave nature of slit dipole antenna at terahertz frequency," *Int. J. Antennas Propag*., vol. 2016, Article ID. 5826957, pp. 1-8, 2016.

[4] N. Hussain and I. Park "Optimization of a small lens for a leaky-wave slit dipole antenna at the terahertz band," In *2016 International Symposium on Antennas and Propagation (ISAP)*, Okinawa, Japan, pp. 782-783, 2016.

[5] N. Hussain, M. Jeong, J. Park, and N. Kim, "A broadband circularly polarized Fabry-Perot resonant antenna using a single-layered PRS for 5G MIMO applications," *IEEE Access*, vol. 7, pp. 42897-42907, 2019.

[6] A. H. Naqvi and S. Lim, "A beam-steering antenna with a fluidically programmable metasurface," *IEEE Trans. Antennas and Propag.*, vol. 67, no. 6, pp. 3704-3711, 2019.

[7] N. Hussain, U. Azimov, J. Park, S.-Y. Rhee, and N. Kim, "A microstrip patch antenna sandwiched between a ground plane and a metasurface for WiMAX applications," In *IEEE Asia Pacific Microwave Conference (APMC)*, Kyoto Japan, pp. 1016-1018, 2018.

[8] J. Park, M. Jeong, N. Hussain, S. Rhee, S. Park, and N. Kim, "A low- profile high- gain filtering antenna for fifth generation systems based on nonuniform metasurface," *Microw. Opt. Tech. Lett.*, vol. 61, no. 11, pp. 2513-2519, 2019.

[9] H. H. Tran, N. Hussain, and T. T. Le, "Single-layer low-profile wideband circularly polarized patch antenna surrounded by periodic metallic plates," *Int. J. RF Microw. Comput. Aided Eng*., e21969, 2019.

[10] N. Hussain and I. Park, "Performance of multiple-feed metasurface antennas with different numbers of patch cells and different substrate thicknesses," *Appl. Comput. Electromagn. Soc. J.*, vol. 33, no. 1, pp. 49-55, 2018.

[11] M. Veysi and A. Jafargholi, "Directivity and bandwidth enhancement of proximity-coupled microstrip antenna using metamaterial cover," *Appl. Comput. Electromagn Soc. J*., vol. 27, no. 11,

pp. 925-930, 2012.

[12] O. Amjad, S. W. Munir, S. T. Imeci, and A. Ö. Ercan, "Design and implementation of dual band microstrip patch antenna for WLAN energy harvesting system," *Appl. Comput. Electromagn. Soc. J.*, vol. 33, no. 7, pp. 746-751, 2018.

[13] N. Hussain, K. E. Kedze, and I. Park, "Performance of a planar leaky-wave slit antenna for different values of substrate thickness," *J. Electromagn. Eng. Sci.*, vol. 17, no. 4, pp. 202-207, 2017.

[14] A. Bhattacharya, B. Roy, S. K. Chowdhury, and A. K. Bhattacharjee, "A compact fractal monopole antenna with defected ground structure for wideband communication," *Appl. Comput. Electromagn. Soc. J.*, vol. 33, no. 3, pp. 347-350, 2018.

[15] P. K. T. Rajanna, K. Rudramuni, and K. Kandasamy, "A wideband circularly polarized slot antenna backed by a frequency selective surface," *J. Electromagn. Eng. Sci*., vol. 19, no. 3, pp. 166-171, 2019.

[16] R. K. Gupta and G. Kumar, "High-gain multilayered antenna for wireless applications," *Microw. Opt. Tech. Lett*., vol. 50, no. 7, pp. 152-154, 2005.

[17] S. M. Meriah, E. Cambiaggio, R. Staraj, and F. T. Bendimerad, "Gain enhancement for microstrip reflect array using superstrate layer," *Microw. Opt. Tech. Lett.*, vol. 46, no. 2, pp. 152-154, 2005.

[18] P. Jirasakulporn, S. Chaimool, and P. Akkaraekthalin, "Gain enhancement of microstrip antenna using square aperture superstrate," In *9th International Conference on Electrical Engineering/ Electronics, Computer, Telecommunications and Information Technology*, Phetchaburi, Thailand, pp. 1-4, 2012.

[19] B. Tütüncü and H. Torpi, "Omega-shaped metamaterial lens design for microstrip patch antenna performance optimization at 12 GHz," In *10th International Conference on Electrical and Electronics Engineering (ELECO)*, Bursa, pp. 987-990, 2017.

[20] D. Li, Z. Szabo, X. Qing, E. Li, and Z. N. Chen, "A high gain antenna with an optimized metamaterial inspired superstrate," *IEEE Trans. Antennas Propag.*, vol. 60, no. 12, pp. 6018-6023, 2012.

[21] K. L. Chung and S. Chaimool, "Diamagnetic metasurfaces for performance enhancement of microstrip patch antennas," *Proceedings of the 5th European Conference on Antennas and Propagation (EUCAP)*, Rome, Italy, pp. 48-52, 2011.

[22] Q. Cheng, X. Y. Zhou, B. Zhou, S. H. Xu, and T. J. Cui, "A superstrate for microstrip patch antennas," In *International Workshop on Metamaterials*, Nanjing, China, pp. 382-384, 2008.

[23] H. Errifi, A. Baghdad, A. Badri, and A. Sahel, "Directivity enhancement of aperture coupled microstrip patch antenna using two layers dielectric superstrate," *Proceedings of 2014 Mediterranean Microwave Symposium (MMS2014)*, Marrakech, pp. 1-4, 2014.

[24] M. Asaadi, I. Afifi, and A. Sebak, "High gain and wideband high dense dielectric patch antenna using FSS superstrate for millimeter-wave applications," *IEEE Access*, vol. 6, pp. 38243-38250, 2018.

[25] J. H. Kim, C. Ahn, and J. Bang, "Antenna gain enhancement using a holey superstrate," *IEEE Trans. Antennas Propag*., vol. 64, no. 3, pp. 1164-1167, Mar. 2016.

[26] L. Martin, E. M. Cruz, B. Froppier, and T. Razban, "New heterogeneous superstrate high gain antenna," In *9th European Conference on Antennas and Propagation* (*EuCAP*), Lisbon, pp. 1-5, 2015.

[27] S. K. Khamas and G. G. Cook, "Optimized design of a printed elliptical spiral antenna with a dielectric superstrate," *Appl. Comput. Electromagn Soc. J*., vol. 23, no. 4, pp. 345-351, 2008.

[28] M. J. Jeong, N. Hussain, J. W. Park, S. G. Park, S. Y. Rhee, and N. Kim, "Millimeter-wave microstrip patch antenna using vertically coupled split ring metaplate for gain enhancement," *Microw. Opt. Tech. Lett.*, vol. 61, no. 10, pp. 2360-2365, 2019.

[29] H. Xu, Z. Zhao, Y. Lv, C. Du, and X. Luo, "Metamaterial superstrate and electromagnetic band-gap substrate for high directive antenna," *Int. J. Infrared Milli. Waves*, vol. 29, no. 5, pp. 493-498, 2008.

Niamat Hussain got his B.S. degree in Electronics Engineering from Dawood University of Engineering and Technology, Karachi, Pakistan, in 2014 and did his M.S. in Electrical and Computer Engineering at Ajou University, Suwon, Korea. He is currently pursuing his Ph.D. in Information and Communication Engineering at Chungbuk National University, Chungju-si, Korea. He was bestowed with best paper award on 2017, for his presented paper at Korea Winter Conference. His research is mainly focused on lens-coupled antennas, metasurface antennas, metamaterial antennas, UWB antennas, mmWave antennas and terahertz antennas.

Uktam Azimov received his B.S. degree in Communication Engineering from Uzbekistan, in 2013. He is currently pursuing the M.S. degree in Information and Communication Engineering at Chungbuk National University, Chungju-si, Korea. His research interests include antenna design.

Minjoo Jeong received his B.S. degree in Electronics Engineering from Chosun University, in 2013 and M.S. degree in LED Fusion Engineering from Pukyong National University, Korea, in 2015. He is currently pursuing the Ph.D. degree in Information and Communication Engineering at Chungbuk National University, Chungju-si, Korea. His research interests include EMC, antenna design, and EMF.

Seungyeop Rhee received his Master's and a Ph.D. degrees from the Department of Electronics Engineering, Yonsei University, Korea in 1988 and 1993, respectively. He worked as a Professor at Yeosu National University, Korea from 1993 to 2006. Currently, he is a Professor at Dept. of Electronic Communication Engineering in Chonnam National University since 2006. His research is focused on antenna design and analysis, microwave circuit design, and wireless power transfer.

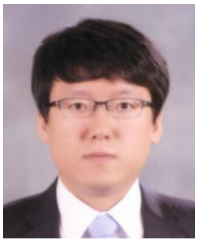

Seung Woo Lee received his Master's and Ph.D. degrees from the Department of Information and Communication Engineering, Chungbuk National University, Cheongju, Korea. Currently, he is a Senior Researcher at Korea Electric Power Research Institute, Daejeon, Republic of Korea. His research is focused on antenna design for the mobile phone applications, microwave circuit design, and wireless power transfer using metamaterials.

Nam Kim received the B.S., M.S., and Ph.D. degrees in Electronics Engineering from Yonsei University, Seoul, Korea, in 1981, 1983, and 1988, respectively. Kim is a Member of the International Advisory Committee for the World Health Organization project on EMF, the IEEE International Committee on Electromagnetic Safety, and the International Electro Technical Commission TC 106, and he was the President of the Bioelectromagnetics Society as well. He has been a Professor in the School of Information and Communication Engineering, Chungbuk National University, Cheongju, Korea, since 1989. His scientific interests are focused on optical information processing, the health effect of the EMF, wireless power transfer, and antennas for mobile communications.

A Tri-Band Frequency Reconfigurable Slot Antenna for Wireless Applications

Karam M. Younus and Khalil H. Sayidmarie

Department of Communication Engineering
College of Electronic Engineering, Ninevah University, Mosul, Iraq
karam.younus@uoninevah.edu.iq, kh.sayidmarie@gmail.com

Abstract ─ With the increase in wireless services, the demand for antennas that can operate at more than one frequency has increased. This work proposes a slot antenna whose frequency of operation can be configured into three bands of 2.4 GHz, 5 GHz, and 3.5 GHz for the Wireless-Area-Network (WLAN) and Worldwide Interoperability for Microwave Access (WiMAX) applications. The switching between the three bands is achieved by two PIN diodes properly placed between the two sides of the slot. The antenna consists of a rectangular slot etched on the ground plane, while on the other side of the substrate, there is a microstrip line to feed the slot with an open stub for matching. The tri-band frequency reconfigurable slot antenna has been studied, and its parameters optimized using computer simulation Technology (CST-MWS). Parametric study on the slot dimensions and the microstrip feeding is presented. For verification of the simulation results, the antenna is fabricated and measured. The simulated and measured parameters such as return loss, radiation pattern, and gain show excellent agreement for the three operation bands.

Index Terms ─ PIN diode, reconfigurable antenna, slot antenna, WLAN, WiMAX.

I. INTRODUCTION

The increasing development of wireless communications has led to diverse applications working at various bands for lower spectrum congestion. Thus, antennas that can operate at more than one frequency are desired. A single wide-band antenna may fulfill the requirement but on account of receiving more than one frequency band at the same time and consequently is prone to interference. A frequency reconfigurable antenna that can be switched from one band to another will be a better choice. Such antennas have received attention due to their selectivity for operation and attractive feature of using the spectrum. They can be easily integrated with switching and control circuits alongside providing a better reconfiguration. In addition to covering more than one application, frequency reconfigurable antennas are also governed by several factors such as; size, cost, and high data rate features. It is attractive to integrate more than one standard into a single wireless device, such as Worldwide Interoperability for Microwave Access (WiMAX) and Wireless-Area Network (WLAN) standards. Consequently, different multi-band antennas have been proposed, such as the dual-band monopole antenna for the WiMAX systems in [1], the multi-band planar inverted-F antenna (PIFA) for the wireless-wide-area-network (WWAN) system in [2], the multi-band patch antenna having varied polarization states in [3], and the dual-loop antenna for the 2.4/5.2/5.8 GHz bands in [4].

Various types of slot antennas have been designed for the WLAN, WiMAX, and ISM applications in the 2.4 GHz (802.11 b/g/h), 5 GHz (802.11 a/n), and 3.5 GHz (IEEE 802.16) operating bands. To achieve the above goals, slots of various shapes were used, leading to different bandwidth and gain characteristics [5-6]. The slot antenna, with the advantages of compact size, wide bandwidth, and easy integration with other devices, is a good candidate for the design of multi-band antennas.

In the past years, different designs of multi-band slot antennas have been proposed [7-16]. The dual-band characteristics of the slot antennas were generated by etching several narrow slots on the ground planes [7-8], or several stubs on the large slot as in [9-10]. The tri-band antennas in [11-12] and [13-14] were achieved using three folded slots etched on the ground planes or several stubs on the slots, respectively. In [15], a compact tri-band split-ring resonator (SRR) loaded slot antenna was proposed, which offers independent frequency tunability for operation at WLAN and WiMAX bands. In [16] the antenna is capable of being switched between single-band, dual-band or triple-band operation by incorporating three pairs of PIN diodes that are located within the dipole arms etched on the ground plane.

This work proposes a slot antenna whose frequency of operation can be configured into three bands for the WLAN and WiMAX applications. The switching between the three bands is achieved by two PIN diodes properly placed between the two sides of the slot. Section

Submitted On: November 16, 2019
Accepted On: December 15, 2019

II describes the proposed idea, while Section III presents the results of the parametric analysis and optimization. The obtained performance is compared with those of other published works in Section IV. Finally, the conclusions are listed in Section V.

II. DESIGN OF THE SLOT ANTENNA

The geometry of the proposed tri-band frequency-reconfigurable antenna is shown in Fig.1. The design consists of a rectangular slot of length *L* and width *W* etched on the ground plane, while on the other side of the substrate, there is a microstrip line to feed the slot. The feed length is L_4 while the microstrip line extends beyond the slot by *S*. This extension works as an open stub that can be used to match the microstrip line to the slot. The chosen substrate is FR-4 with thickness h=1.6 mm, relative permittivity $\varepsilon_r = 4.3$, and dielectric loss tangent of 0.025. The reconfigurability is achieved by properly inserting two PIN diodes along the slot. By switching these diodes between ON and OFF states, the antenna operation can be switched between the three bands (2.4 GHz, 3.5 GHz, and 5.3 GHz).

The radiating slot resonates at frequency *f* when its length *L* is equal to an integer (*N*) multiple of half the effective wavelength:

$$L = N \times \frac{\lambda_e}{2} = N \times \left(\frac{C}{2f \times \sqrt{\varepsilon_e}}\right). \quad (1)$$

Where *C* is the speed of light and ϵ_e is the effective permittivity inside the slot that is given by:

$$\varepsilon_e = \frac{\varepsilon_r+1}{2} + \frac{\varepsilon_r-1}{2}\left(\sqrt{1+\frac{12h}{w}}\right)^{-0.5}. \quad (2)$$

The performance of the proposed antenna was investigated using the Computer Simulation Technology (CST-MWS) software, which uses the Finite Integration Technique (FIT). This is a numerical simulation method for approximation-free solutions of Maxwell's equations in their integral form. The Time-Domain solver was used to obtain the results. Parametric studies and optimization using the built-in Trust Region Framework Algorithm which is a numerical optimization for solving nonlinear programming problems. The optimized parameters were the length and width of the microstrip feed line and the slot to obtain the dimensions that result in the best performance.

A. The effect of slot length

Slot antennas relay on Babinet's principle, which relates the radiated field and impedance of an aperture, of slot antenna to that of the field of a dipole antenna [17]. The slot length plays a significant role in the proposed design, as shown by (1) and (2). The length of the slot L for the operation at 2.4 GHz frequency was found to be 30.12 mm, and this initial value was then optimized. Figure 2 shows the variation of the reflection coefficient parameter (S_{11}) with frequency for various slot lengths, where it is seen that the resonance frequency increases when the slot length is decreased. The best value of the slot length for the 2.4 GHz WLAN operation is 34.55 mm.

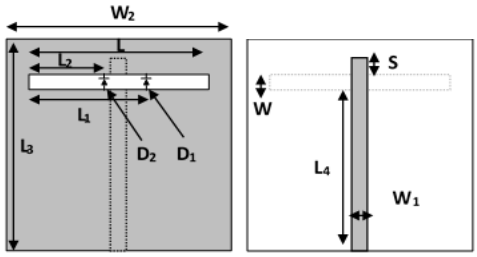

(a) (b)

Fig. 1. Configuration of the proposed antenna: (a) front view and (b) back view.

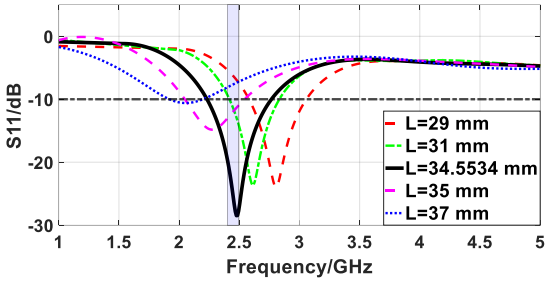

Fig. 2. S_{11}variation with frequency for various slot lengths *L*.

B. The effect of slot width

As regards the suitable width of the slot, there is no established design rule; thus, the parametric study is very beneficial in this respect. Figure 3 shows the effect of various slot widths, where it is clear that the resonant frequency decreases slightly by increasing the slot width. Larger bandwidth is also noticed for increasing the slot width. Therefore, if the slot width is to be increased, the slot length should be slightly decreased in order to keep the resonance frequency at 2.4 GHz.

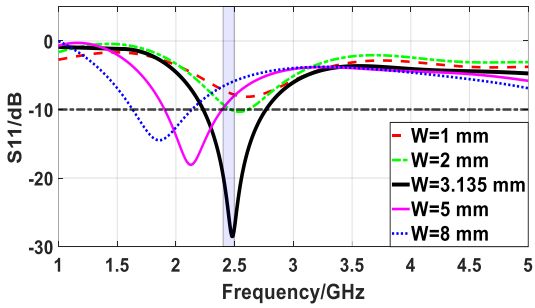

Fig. 3. S_{11} variation with frequency for various slot widths *W*, at *L*= 34.55 mm.

C. Effect of the Open Stub

In order to match the antenna feedline to the slot, a stub of length S has been added to the feed line. This open-ended stub adds a reactive impedance Z_s given by:

$$Z_s = -j \times Z_0 \times \cot(\beta S). \quad (3)$$

Where Z_o is the impedance of the feedline and $\beta = 2\pi/\lambda_e$. Figure 4 shows the effect of varying the stub length. Without the stub (S=0), proper matching (S_{11} < -10dB) cannot be achieved. Moreover, the resonance frequency decreases by increasing the stub length.

The parametric study shows that the slot length, width, and the stub length influence the design parameters, and the simulation with the CST is a useful tool to optimize the antenna dimensions. Table 1 shows the parameters of the designed antenna after the optimization.

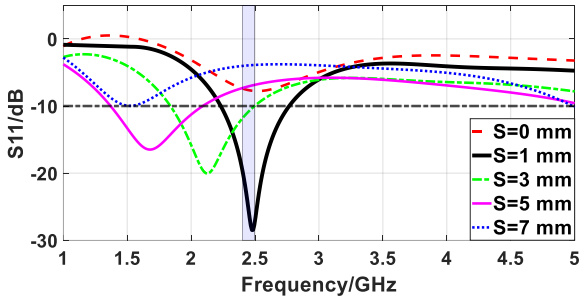

Fig. 4. S_{11} variation with frequency for various stub lengths S, at L= 34.55 mm.

Table 1: Parameters of the designed antennas, all dimensions are in millimeters

Parameter	Value
L	34.55
L_1	22.27
L_2	14.77
L_3	44
L_4	34
S	1
W	3.14
W_1	3.14
W_2	45

III. DESIGN OF THE FREQUENCY RECONFIGURABLE ANTENNA

The proposed antenna is wanted to operate at three bands by switching the two diodes D_1 and D_2 shown in Fig. 1. As mentioned in Section II, the slot was designed to resonate at 2.4 GHz by choosing its length according to (1) and (2). Then, by inserting a PIN diode across the slot edges, the slot can be divided into two adjacent slots when the diode is switched ON and thus short-circuiting the two sides of the slot. The positions of the two diodes can be chosen to change the length of the slot and thus excite resonance at the required frequency, as it is explained in the next section. Prototypes of the designed antenna were fabricated, as shown in Fig. 5. In the testing of the fabricated prototypes, the ON state of the PIN diode was realized by placing a shorting copper strip of width about 1.5 mm between the two sides of the slot.

(a) (b) (c)

Fig. 5. Photograph of the fabricated antennas: (a) resonate at 2.4GHz, (b) resonate at 3.5GHz, and (c) resonate at 5.3GHz.

A. Case-1, operation at 2.4 GHz

When the diodes D_1 and D_2 are in OFF state, the antenna resonates at 2.4 GHz, since the full length of the slot is radiating as shown in the previous section. Figure 6 shows the variation of the S_{11} with frequency for this case for both simulated and practical results, which indicate good agreement. It is clear that the antenna covers a bandwidth of about 290 MHz and has an S_{11} value of better than -23.87 dB along the 2.45 GHz WLAN band. Figure 7 shows the E-field distribution across the slot of the antenna at 2.4 GHz, where a peak is noticed at the center characterizing the ½ λ_e resonance. The radiation pattern of the fabricated prototype of the antenna was measured at 2.4 GHz and compared to that obtained from the simulation, as shown in Fig. 8. Figure 9 shows the variations of the calculated radiation efficiency and the total gain with frequency. The gain is about 4.5 dB, and the efficiency is better than 90% across the WLAN band.

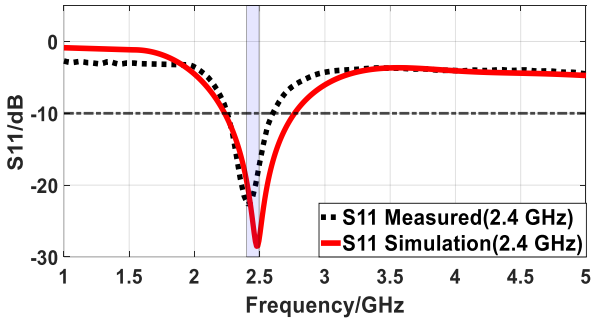

Fig. 6. Simulated and measured S_{11} variation with frequency when the diodes D_1 and D_2 are in the OFF state.

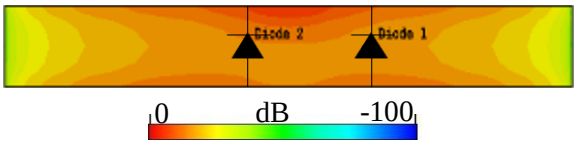

Fig. 7. Simulated E-field at 2.4 GHz (zooming on the slot), the diodes D_1 and D_2 are in the OFF state.

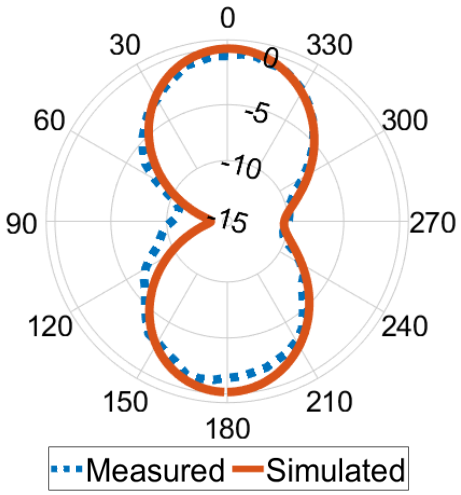

Fig. 8. Normalized simulated and measured radiation patterns of the antenna at 2.4GHz, both diodes D1 and D2 are in the OFF state.

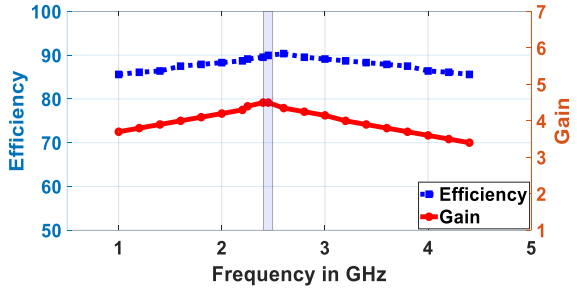

Fig. 9. Antenna gain and efficiency when the diodes D_1 and D_2 are in the OFF state.

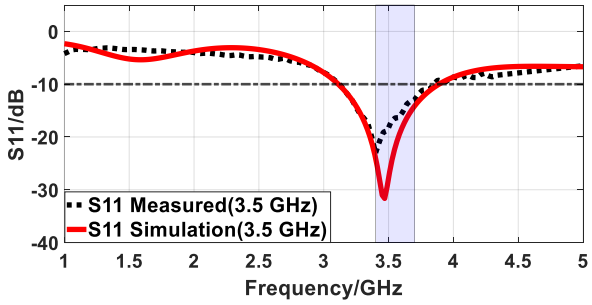

Fig. 10. Simulated and measured S_{11} variation with frequency, when the diode D_1 is ON, and D_2 is OFF state.

B. Case-2, operation at 3.5 GHz

To achieve operation at the frequency of 3.5 GHz, the slot length is reduced by switching the diode D_1 to ON state while keeping the diode D_2 in the OFF state. Thus, the position of the diode D_1 is found, such that the left part of the slot has a length $L_1 = 0.5\lambda_{e2}$ at the frequency of 3.5 GHz. According to (1) and (2), the length L_1 is found to be 22.275 mm. In this case, the right part of the slot will have a length of 12.275 mm, and it may resonate at 6.3 GHz. Figure 10 shows the variation of the simulated and measured S_{11} with frequency. It is clear that the antenna operates at the WiMAX band of 3.5 GHz with a bandwidth of about 310 MHz and an S_{11} value of better than -15 dB. Figure 11 shows the E-field distribution in the slot of the antenna at 3.5 GHz, where it is seen the $\frac{1}{2}\lambda_e$ distribution is across the left part of the slot. The field at the right side of the slot exhibits small values indicating no resonance. Figure 12 illustrates the normalized simulated and measured radiation patterns of the antenna at 3.5 GHz, where good agreement between the two results is evident. Figure 13 shows the variation of the radiation efficiency and the total gain with frequency. The gain is better than 4.5 dB, and the efficiency is about to 86% across the WiMAX band. The maximum value of the gain is almost equal to that obtained at 2.45 GHz since in the two cases the slot length is 0.5 λ_e, while the efficiency is slightly smaller probably due to the loss in the shorting strip and the increased loss in the substrate at the higher frequency of 3.5 GHz.

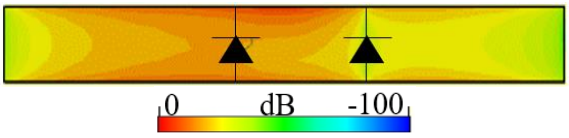

Fig. 11. Simulated normalized E-field at 3.5 GHz (zooming on the slot), the diode D_1 is ON, while D_2 is OFF state.

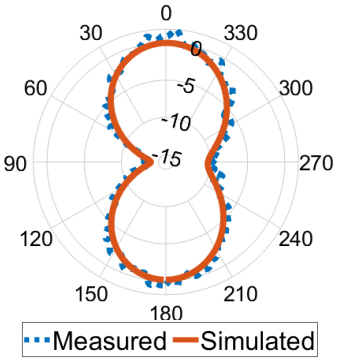

Fig. 12. Normalized simulated and measured radiation patterns of the antenna at 3.5GHz, the diode D_1 is ON, while D_2 is OFF state.

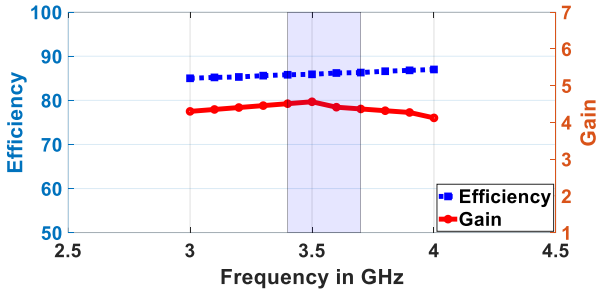

Fig. 13. Antenna gain and efficiency when the diode D_1 is ON and diode D_2 is OFF.

C. Case-3, operation at 5.3 GHz

To realize the operation at 5.3 GHz, there should be a slot of smaller length compared to the two former cases. When both of the diodes D_1 and D_2 are switched ON, then the slot will be divided into three parts. If the part at the left is to resonate, then it should have a length of $L_2 = ½ \lambda_e$ at the frequency of 5.3 GHz. According to (1) and (2), L_2 was found to be 14.775 mm. Again, the ON states of the two diodes were realized by placing two strips between the two sides of the slot. Figure 14 shows the S_{11} parameter for this case for both simulated and practical results, where the condition of (S11 < -10dB) is insured across a bandwidth of more than 2000 MHz. The measured results are few dB's higher than the simulated ones, but still, it is lower than -10B across the wanted band. Figure 15 shows the E-field distributions in the slot of the antenna at 5.3 GHz. The field intensity at the left part is highest, and its distribution resembles a half-sinusoid variation. This confirms that the left part of the slot is resonating at 5.3 GHz. The field along the two copper strips is minimal, showing the short-circuit action of the strips. The normalized simulated and measured radiation patterns of the antenna at 5.3 GHz are compared in Fig. 16. Figure 17 shows the radiation efficiency and the total gain in the 5.3 GHz band.

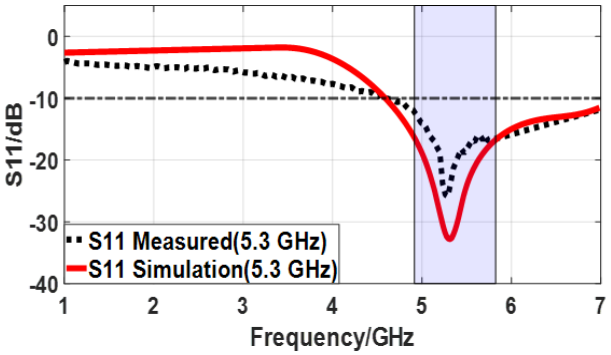

Fig. 14. Simulated and measured S_{11} variation with frequency when both diodes D1 and D2 are in ON state.

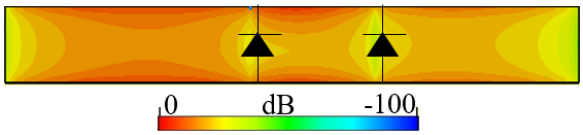

Fig. 15. Simulated E-field distribution in the slot (zooming on the slot), the diodes D_1 and D_2 are ON.

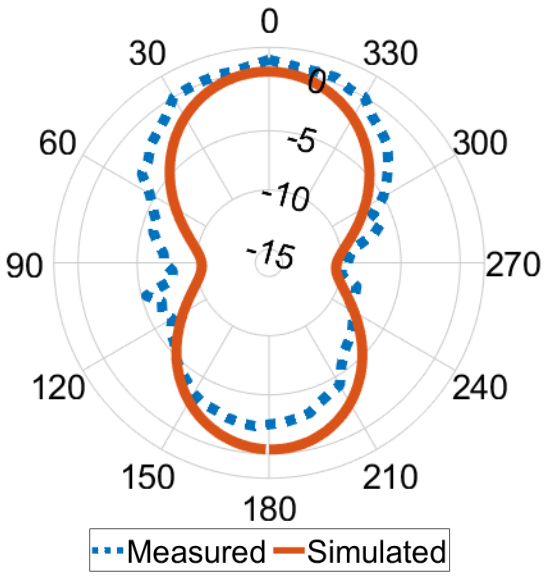

Fig. 16. Normalized simulated and measured radiation patterns of the antenna at 5.3 GHz and both diodes are in the ON state.

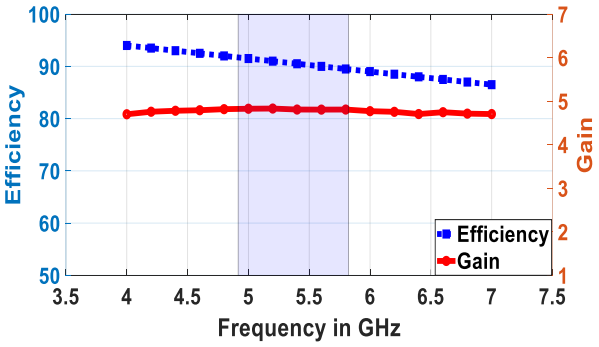

Fig. 17. Antenna gain and efficiency when the diodes D_1 and D_2=ON.

IV. COMPARISON OF OBTAINED RESULTS WITH THOSE OF PUBLISHED WORKS

The performance of the proposed antenna is compared with other tri-band antennas that were published for WiMAX and WLAN applications, as

shown in Table 2. The comparison comprised antenna size, operation frequencies, and gain. The proposed antenna matches the frequency bands of those presented in [6], [18-21]. The table shows that, in general, the larger gain is related to the larger size of the antenna in terms of the effective wavelength. However, the proposed antenna has a higher gain than most of the shown antennas, while its size smaller than those of [6, 22, 25]. The size of the proposed antenna is basically occupied by the ground plane. The antennas in [24, 25] cover a frequency range extending to 0.9 GHz and 1.5 GHz, where it is easier to keep the characteristics of the antenna, yet they offer lower gain compared to the proposed antenna. One important characteristic of the proposed antenna is its capability to switch its operation among the three bands, where only those in [21-23] are reconfigurable.

V. CONCLUSION

A Tri-Band frequency reconfigurable slot antenna for wireless WLAN and WiMAX applications has been demonstrated. The design consists of a rectangular slot etched on the ground plane, while on the back of the substrate, a microstrip line feeds the slot. Two diodes are placed at proper positions along the slot to achieve reconfigurability by switching them into ON and OFF states. The antenna can be switched to operate at any one of three bands of 2.4, 3.5 and 5.3 GHz. The relation between the band frequency and the position of the diode is derived. A prototype of the proposed antenna was fabricated and measured. The S_{11}, radiation patterns, efficiency, and gain results are obtained for both simulation and the prototype. The simulated and measured parameters show excellent agreement for the three operation bands, thus verifying the design rules.

Table 2: Comparison of the performance of the proposed antenna with other designs

Reference	Dimensions in (mm)	Dimensions in (λ_o) at the Lower Band	Substrate (ε_r)	Operation Frequencies (GHz)	Gain (dB)
6	40×45×0.8	0.46x0.52×0.001	2.55	3.5/4.1/5/6.4/6.8	4.3/4.3/4.4/5.5/5.3
18	26×20×1.6	0.2×0.16×0.012	4.4	2.4/3.5/5.8	2.24/2.8/2.6
19	35×30×1.6	0.29×0.25×0.013	4.4	2.5/3.5/5.5	3.86/3.52/4.32
20	25×22×1.6	0.2×0.183×0.013	4.4	2.5/3.5/5.8	1.98/3.15/2.68
21	40×40×1.6	0.32×0.32×0.012	4.4	2.4/3.5/5.3	2.4/3.3/3.2
22	80×80×1	0.64×0.64×0.008	4.4	2.4/3.5/5.8	2.33/3.14/2.89
23	58×40×1.2	0.42×0.29×0.001	4.4	2.2/ 2.4/3.8	4.2/3.7/4.7
24	100×65×1.6	0.3×0.195×0.004	4.4	0.9/1.8/2.6	0.25/0.6/3.28
25	120×60×1.6	0.6×0.3×0.008	4.4	1.5/2.4/5.8	0.16/2.62/2.04
This work	45×44×1.6	0.36×0.35×0.013	4.3	2.4/3.5/5.3	4.5/4.4/4.7

REFERENCES

[1] X. L. Sun, S. W. Cheung, and T. I. Yuk, "Dual-band monopole antenna with frequency tunable feature for WiMAX applications," *IEEE Antennas Wireless Propag. Lett.*, vol. 12, pp. 100-103, 2013.

[2] C. H. Chang and K. L. Wong, "Printed λ/8-PIFA for penta-band WWAN operation in the mobile phone," *IEEE Trans. Antennas Propag.*, vol. 57, no. 5, pp. 1373-1381, May 2009.

[3] Y. D. Dong, H. Toyao, and T. Itoh, "Design and characterization of miniaturized patch antennas loaded with complementary split-ring resonators," *IEEE Trans. Antennas Propag.*, vol. 60, no. 2, pp. 772-785, Feb. 2012.

[4] S. W. Su, "High-gain dual-loop antennas for MIMO access points in the 2.4/5.2/5.8 GHz bands," *IEEE Trans. Antennas Propag.*, vol. 58, no. 7, pp. 2412-2419, July 2010.

[5] A. A. Eldek, A. Z. Elsherbeni, C. E. Smith, and K. Lee, "Wideband planar slot antennas," *ACES Journal*, vol. 9, no. 1, 2004.

[6] N. H. Gad and M. Vidmar, "Design of a microstrip-fed printed-slot antenna using defected ground structures for multiband applications," *ACES Journal*, vol. 33, no. 8, pp. 854-860, Aug. 2018.

[7] K. L. Wong and L. C. Lee, "Multiband printed monopole slot antenna for WWAN operation in the laptop computer," *IEEE Trans. Antennas Propag.*, vol. 57, no. 2, pp. 324-330, Feb. 2009.

[8] Y. Cao, B. Yuan, and G. F. Wang, "A compact multiband open-ended slot antenna for mobile handsets," *IEEE Antennas Wireless Propag. Lett.*, vol. 10, pp. 911-914, 2011.

[9] Y. C. Lu and Y. C. Lin, "A mode-based design method for dual-band and self-duplexing antennas using double T-stubs loaded aperture," *IEEE Trans. Antennas Propag.*, vol. 60, no. 12, pp. 5596-5603, Dec. 2012.

[10] M. J. Chiang, S. Wang, and C. C. Hsu, "Compact multifrequency slot antenna design incorporating embedded arc-strip," *IEEE Antennas Wireless Propag. Lett.*, vol. 11, pp. 834-837, 2012.

[11] A. P. Spaghetti, M. Azarmanesh, and R. Zaker, "A novel switchable single and multifrequency triple-slot antenna for 2.4-GHz Bluetooth, 3.5-GHz WiMax, and 5.8-GHz WLAN," *IEEE Antennas*

Wireless Propag. Lett., vol. 9, pp. 534-537, 2010.

[12] J. H. Lu and B. J. Huang, "Planar compact slot antenna with multi-band operation for IEEE 802.16m application," *IEEE Trans. Antennas Propag.*, vol. 61, no. 3, pp. 1411-1414, Mar. 2013.

[13] L. Dang, Z. Y. Lei, Y. J. Xie, G. L. Ning, and J. Fan, "A compact microstrip slot triple-band antenna for WLAN/WiMAX applications," *IEEE Antennas Wireless Propag. Lett.*, vol. 9, pp. 1178-1181, 2010.

[14] W. Hu, Y. Z. Yin, P. Fei, and X. Yang, "Compact triband square-slot antenna with symmetrical L-strips for WLAN/WiMAX applications," *IEEE Antennas Wireless Propag. Lett.*, vol. 10, pp. 462-465, 2011.

[15] P. M. Paul, K. Kandasamy, and M. S. Sharawi, "A tri-band SRR loaded half slot antenna with wideband properties," *2018 IEEE Radio and Antenna Days of the Indian Ocean* (*RADIO*), Grand Port, pp. 1-2, 2018.

[16] I. H. Idris, M. R. Hamid, M. H. Jamaluddin, M. K. A. Rahim, J. R. Kelly, and H. A. Majid, "Single-, dual- and triple-band frequency reconfigurable Antenna," *Radioengineering*, vol. 23, no. 3, pp. 805-811, 2014.

[17] C. Chulvanich, J. Nakasuwan, N. Songthanapitak, N. Anantrasirichai, and T. Wakabayashi, "Design narrow slot antenna for dual frequency," *PIERS Online*, vol. 3, no. 7, pp. 1024-1028, 2007.

[18] L. Li, X. Zhang, X. Yin, and L. Zhou, "A compact triple-band printed monopole antenna for WLAN/ WiMAX applications," in *IEEE Antennas and Wireless Propagation Letters*, vol. 15, pp. 1853-1855, 2016.

[19] L. Dang, Z. Y. Lei, Y. J. Xie, G. L. Ning, and J. Fan, "A compact microstrip slot triple-band antenna for WLAN/WiMAX applications," in *IEEE Antennas and Wireless Propagation Letters*, vol. 9, pp. 1178-1181, 2010.

[20] T. Ali and R. C. Biradar, "A compact multiband antenna using λ/4 rectangular stub loaded with metamaterial for IEEE 802.11N and IEEE 802.16E," *Microwave and Optical Technology Letters*, vol. 59, pp.1000-1006, 2017.

[21] A. P. Saghati, M. Azarmanesh, and R. Zaker, "A novel switchable single- and multifrequency triple-slot antenna for 2.4-GHz Bluetooth, 3.5-GHz WiMax, and 5.8-GHz WLAN," in *IEEE Antennas and Wireless Propagation Letters*, vol. 9, pp. 534-537, 2010.

[22] H. Boudaghi, M. Azarmanesh, and M. Mehranpour, "A frequency-reconfigurable monopole antenna using switchable slotted ground structure," in *IEEE Antennas and Wireless Propagation Letters*, vol. 11, pp. 655-658, 2012.

[23] Y. Pan, Y. Ma, Z. Hou, and Y. Zeng, "A compact antenna with frequency and pattern reconfigurable characteristics," *Microwave and Optical Technology Letters*, vol. 57, no. 11, pp. 2467-71, Aug. 2015.

[24] J.-S. Sun, H.-S. Fang, P.-Y. Lin, and C.-S. Chuang, "Triple-band MIMO antenna for mobile wireless applications," *IEEE Antennas Wirel. Propag Lett.*, vol. 15, pp. 500-503, 2015.

[25] R. Zhang, H.-H. Kim, and H. Kim, "Triple-band ground radiation antenna for GPS, WiFi 2.4 and 5 GHz band application," *Electron Lett.*, vol. 51, no. 25, pp. 2082-4, 2015.

Karam M. Younus was born in Mosul, Iraq, in 1986. He received the B.Sc. degree in Communication Engineering from the University of Mosul, Iraq, in 2010, and an M.Sc. degree in Communication Engineering, University of Bradford, U.K., in 2015. He is currently an Assistant-Lecturer at the Communication Engineering Department, College of Electronics Engineering, Ninevah University. His research interest includes beam steering, reconfigurable antennas, and antenna design.

Khalil H. Sayidmarie received a B.Sc. degree in Electronic & Communication Eng. from Mosul University, Iraq, in 1976, and Ph.D. degree in Antennas & Propagation from Sheffield University/U.K. in 1981. Then he joined the College of Engineering at Mosul University in 1983 and was promoted to full professor in 1992. He worked as the head of the Electrical Engineering department for 9 years. Sayidmarie served as Prof. of Communication Engineering at the College of Engineering/University of Amman/Jordan from Oct. 2006 to Sept. 2009, and as the Dean of that college from Sept. 2008 to Sept. 2009. He is Prof of Communication Engineering at the college of Electronic Engineering/ Ninevah University since July 2002. His research interests cover antennas, propagation, and microwaves, and he has published more than 120 papers in international journals and conferences.

A Novel Omnidirectional Circularly Polarized Pagoda Antenna with Four Shorting Pins for UAV Applications

Zheyu Li, Yongzhong Zhu*, Yu Shen, Xiaoyu Liu, and Guohao Peng

School of Information Engineering
Engineering University of PAP, Xi'an, Shanxi, 710086, P. R. China
lzyewe@163.com, *bsbs1980@sina.com, 348511372@qq.com, lxywjgd@163.com, 302662481@qq.com

Abstract ─ A novel omnidirectional circularly polarized (CP) pagoda antenna with four shorting pins is presented. In this structure, four curved branches are utilized to generate horizontal polarization, while coaxial cable and four shorting pins produce vertical polarization. Omnidirectional CP radiation is achieved by combining the radiation from the branches and the shorting pins. The curved branches loaded with shorting pins reduce the size of the antenna and the antenna is loaded with the lower substrate with two coupling patches to improve the bandwidth. The novel pagoda antenna is fabricated and measured. Its final dimensions are $0.42\lambda_0*0.42\lambda_0*0.33\lambda_0$ (λ_0 is the free-space wavelength at operating frequency). The impedance bandwidth (S_{11}≤-10dB) is 0.53GHz and the axial ratio (AR) bandwidth (AR≤3dB) is 0.95GHz, which can be used for unmanned aerial vehicles' diagram transmission in China.

Index Terms ─ Circularly Polarized (CP), coupling patch, curved branch, omnidirectional antenna, shorting pin.

I. INTRODUCTION

Omnidirectional circularly polarized (CP) antennas have attracted more and more attention from experts and scholars due to they widely used in wireless communication, remote sensing and telemetry and satellite communication systems. Omnidirectional antenna can radiate electromagnetic wave in any direction in a plane, which is suitable for multipoint simultaneous communication and communication in uncertain position during movement. The CP antennas can accept arbitrary polarized wave, reduce multipath interference, and have high polarization isolation. Having both advantages of omnidirectional antenna and CP antenna, omnidirectional CP antenna can meet the requirements of accurate signal transmission of unmanned aerial vehicle (UAV) systems and be used as its image transmission antenna, which can effectively reduce the signal blind area and polarization interference.

In recent years, many methods of realizing omnidirectional CP antennas have been proposed, which can be roughly classified into three categories. The first method is circular polarized method of omnidirectional antenna that a circular polarizer is loaded outside the omnidirectional antenna. In [1], the omnidirectional CP antenna is realized by using the parallelepiped medium element with high dielectric constant to embrace around the coaxial probe. In [2], the inner conductor is fed, while the spiral groove is opened on the outer cylinder conductor. The second method is element combination [3-6], which uses the combination of CP antenna elements to achieve omnidirectivity. In [3], circular open rings loaded with parasitic rings are used as CP antenna elements, and they are combined around cylinder to attain omnidirectivity. In [4], a rectangular ring is used as a CP antenna element.

However, omnidirectional CP antennas realized by these two methods are generally large in size and have high profile, which is difficult to install on small and lightweight UAVs. In order to reduce the size and profile, a third method is proposed, which combines the antenna that generates the vertical polarized wave with the antenna that generates the horizontal polarized wave [7-15]. In [7], a broadband omnidirectional CP antenna was proposed, in which two sets of dipoles were used to generate omnidirectional CP waves. In [8], capacitive feeding is used to widen the bandwidth of the antenna. The antenna's profile is greatly reduced, but the radius is still large. In [9], planar sector-shaped endfire elements are used to realize omnidirectional circular polarization of the antenna, which further reduces the antenna profile. V-shaped slot on the same principle was used in omnidirectional CP antenna [10], which also makes the size of the antenna even smaller. The profile and radius of this kind of antenna are small, but the bandwidth is too narrow to meet the actual needs.

Based on the comparison with the antenna mentioned above, this paper proposes an omnidirectional CP antenna suitable for UAV image transmission system. The antenna's size is relatively small and has an adequate

Submitted On: December 9, 2019
Accepted On: February 23, 2020

bandwidth to ensure the transmission of information. Coaxial cable and four shorting pins are used to generate vertical polarized waves, while four curved branches are used to generate horizontal polarized waves. The structure of curved branches loaded with shorting pins are used to reduce the size of the antenna, and the dielectric substrates at the bottom with two ring patches are coupled to extend the bandwidth. Finally, the antenna's size is $0.42\lambda_0$*$0.42\lambda_0$*$0.33\lambda_0$. The impedance bandwidth of the antenna (S_{11}≤-10dB) ranges from 5.56GHz to 6.09GHz, and the axial ratio (AR) bandwidth (AR≤3dB) is from 5.07GHz to 6.02GHz, effectively covering UAVs' diagram transmission frequency in China at 5.8GHz. The configuration, principles, simulation used by Ansoft high-frequency structure simulator (HFSS) and results of the antenna are described in detail in the following sections.

II. ANTENNA CONFIGURATION

Figure 1 shows the configuration of omnidirectional CP pagoda antenna. It consists of three dielectric substrates with a thickness of 1mm, a radiant patch, a reference ground, four shorting pins and four ring patches. The radiation patch and ground plane are located on the upper surface of the upper substrates and the middle substrates respectively, the material of which is FR-4 with the permittivity of 4.4 and the loss tangent of 0.002. The radiation patch and ground plane each contains four curved branches in opposite direction connected by shorting pins at the end, which are commonly used to reduce the size of antenna. The coaxial cable is in direct contact with the radiation patch for feeding. The inner conductor of coaxial cable and shorting pins are both made of copper.

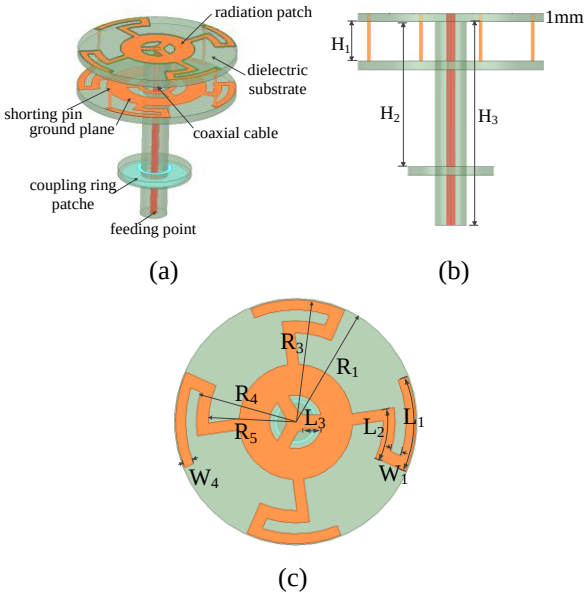

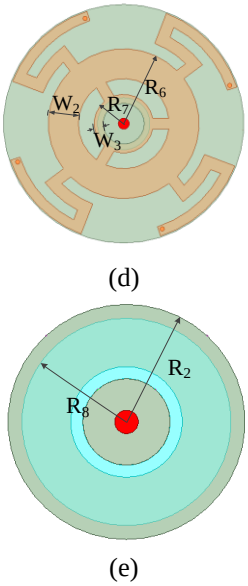

Fig. 1. Geometrical configuration of the proposed antenna. (a) Perspective view, (b) side view, (c) top view of the upper substrates, (d) top view of the middle substrates, and (e) top view of the lower substrates.

The curved branches loaded with shorting pin reduce the size of the antenna, but the bandwidth is relatively narrow. In order to improve the bandwidth for better practicability, the antenna is loaded with the lower substrate with two ring patches on the upper surface and the lower surface respectively. The lower substrate with two ring patches acts as a choking coil, similar to a metal sleeve. Because it can be coupled with the radiation patch to enhance the radiation intensity, the lower substrate broadens both impedance bandwidth and AR bandwidth. The parameters of the antenna are listed as follows: R_1=11mm, R_2=5.1mm, R_3=10.9mm, R_4=9mm, R_5=8mm, R_6=6.9mm, R_7=2.7mm, R_8=4.5mm, W_1=1mm, W_2=2.75mm, W_3=0.82mm, W_4=0.9mm, L_1=8.74mm, L_2=5mm, L_3=3mm, H_1=4.65mm, H_2=17.09mm, H_3=24mm.

III. PRINCIPLE AND METHODOLOGY

For omnidirectional CP pagoda antenna is understand clearly, working principle and parameters analysis of the proposed antenna are discussed in this section.

A. Omnidirectional CP property

CP waves are composed of two orthogonal linearly polarized waves with a phase difference of 90°. According to the duality principle, the electric field ($\vec{E}$) in the far field generated by the magnetic currents on the pagoda antenna can be expressed as:

$$\vec{E} = \hat{\theta}E_\theta + \hat{\phi}E_\phi. \quad (1)$$

It is found that when there are more branches,

omnidirectivity of the antenna is better, as shown in Fig. 2. And the operating frequency is reduced as the increase in the number of branches, which has the function of miniaturization, as shown in Fig. 3. However, considering the size of the antenna, four branches are finally chosen. The four branch elements are arranged in sequence and fed by coaxial cables, forming a clockwise current loop. The end of each branch element is connected to the ground plane by a shorting pin, that form a current path. According to the boundary condition, the clockwise current loop generates a vertical down magnetic pole ($\vec{J} = \vec{n} \times \vec{H}$), which forms a horizontal polarization component, the E_φ field. The radius of the current loop is R_1. The far field of the current loop E_φ can be expressed as [16]:

$$E_\varphi = \frac{[I]R_1\omega\mu_0}{2r} J_1(\beta R_1 \sin\theta)\hat{\varphi}. \quad (2)$$

Where $[I]$ represents the magnitude of current on the loop, ω is the operating frequency, μ_0 is the free-space permeability, J_1 is Bessel's first order function, β is the propagation parameter of space and r is the distance between the antenna and the measuring point.

Vertical polarized waves are generated by coaxial cable and four shorting pins, which act as electrodes. What is more, the vertical polarized waves produced by the electrodes are omnidirectional. The height of the shorting pin can be seen as H_1. Its far field E_θ can be expressed as [16]:

$$E_\theta = j\frac{[I]H\omega\mu_0}{4\pi r} \sin\theta\ \hat{\theta}. \quad (3)$$

Based on (2) and (3), it is noted that as long as the current $[I]$ through coaxial cable, curved branch and shorting pin is uniform, there will be a 90° phase difference between the vertical polarized component and the horizontal polarized component. The CP radiation pattern will be generated when the magnitude of E_θ and E_ϕ are adjusted to be equal. As shown in the Fig. 4, it can be found that the current passing through does not change its direction in one time. Therefore, two polarization components exist 90° phase difference to each other in the far field. Due to the compact structure of the antenna, two polarization components have the same amplitude and orthogonal to each other in space at the same time. Finally, the omnidirectional CP pagoda antenna is realized in theory.

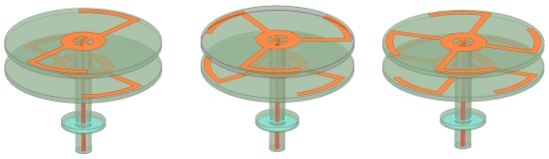

Fig. 2. Three improved prototypes of the proposed antenna.

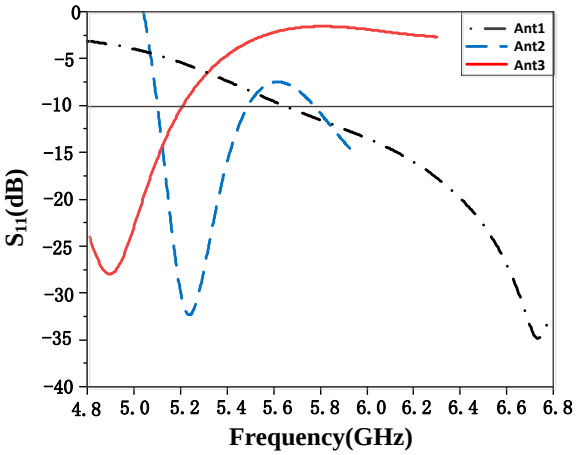

Fig. 3. Simulated $|S_{11}|$ of Ant 1, Ant 2 and Ant 3.

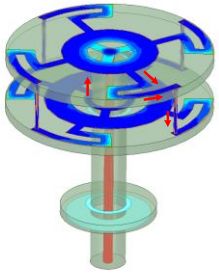

Fig. 4. Current distribution of the proposed antenna at 5.8GHz.

B. Parametric study and analysis

Curved branch can change the path of current, effectively reducing the size of the antenna. The length of the branches is approximately determined by:

$$\frac{R_6\pi}{4} + L_2 + \frac{W_4}{2} + R_5 = \lambda. \quad (4)$$

Where λ is the operating wavelength. As shown in Fig. 5, the radius of the curved branch is much smaller than that of the straight branch by adjusting the width of the branches when the current passes through the same length.

The shorting pin at the end of the branch not only supports the upper and middle dielectric substrates, but also miniaturizes the antenna. The two ends of the radiation patch are open, and there must be zero potential points in the standing wave. Loading shorting pin at zero potential points, the original state of standing wave will be made from open circuit to short circuit state, equivalent to make $\lambda/2$ to $\lambda/4$ harmonic resonance. The antenna size (R) can be approximately calculated by [17]:

$$R = \frac{\lambda}{4} = \frac{c}{4\times\sqrt{\varepsilon_{eq}}\times f}, \quad (5)$$

$$\varepsilon_{eq} = \frac{H_1+H_2}{\frac{H_1}{\varepsilon_r}+\frac{H_2}{\varepsilon_{air}}}. \quad (6)$$

Where c is the speed of light in vacuum, and ε_{eq} is the equivalent dielectric constant of multilayered substrate. Figure 6 compares the S parameters of antenna with shorting pin and without shorting pin. As can be seen from Fig. 6, the impedance characteristic of the antenna with shorting pin is obviously better than that without shorting pin, and the resonant frequency of antenna reduces, thus achieving the miniaturization. Therefore, the antenna size is reduced due to the curved branch loaded with shorting pin.

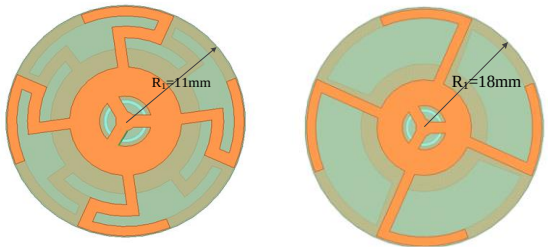

(a) (b)

Fig. 5. Radius of (a) curved branch and (b) straight branch.

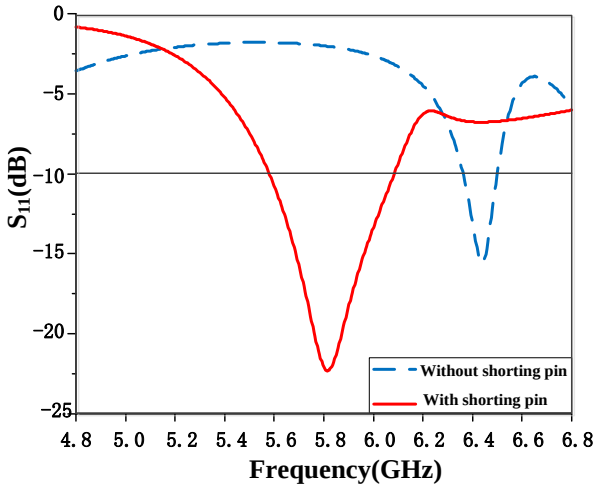

Fig. 6. Simulated $|S_{11}|$ of the proposed antenna with and without shorting pins.

The lower substrate with two coupling patches can adjust the resonance point and enlarge the bandwidth of the antenna. Figure 7 shows the comparison of S parameters and AR bandwidth of antennas with and without the coupling patches. It can be seen that the impedance bandwidth and AR bandwidth of the antenna both increase after the coupling patches loaded.

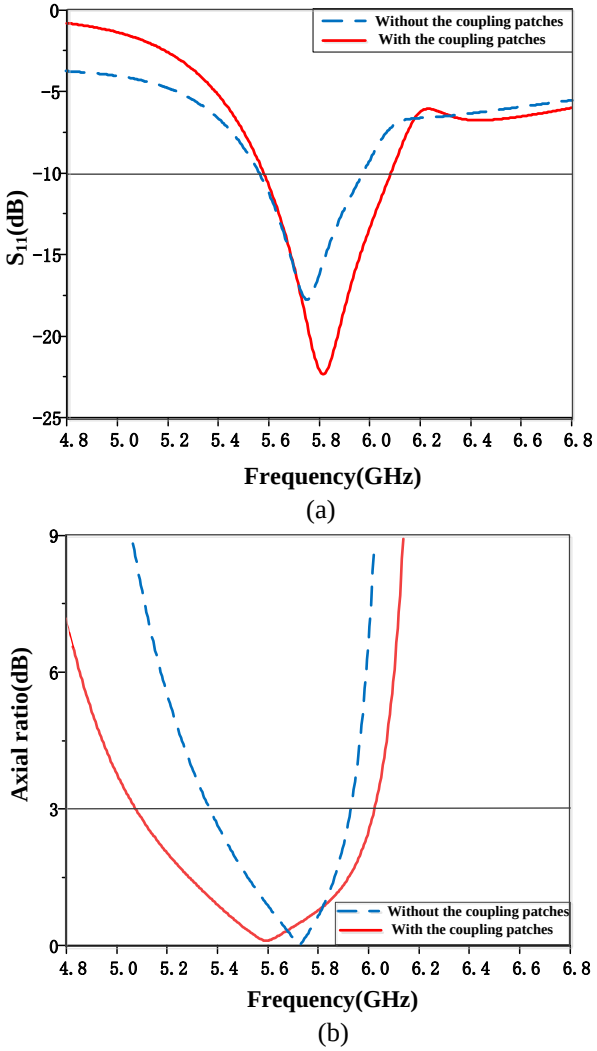

(a)

(b)

Fig. 7. Simulated (a) $|S_{11}|$ and (b) AR of the proposed antenna with and without coupling patches.

The coupling strength is affected by two factors [18], one is the distance between the upper substrate and the middle substrate H_1, the other is curved branch arc width of the radiation patch W_4. Figure 8 shows the influence of the distance H_1 on the operating frequency of the antenna. It can be seen from Fig. 8 (a) that when the distance H_1 decreases, the resonant frequency of the antenna increases, while Fig. 8 (b) shows that AR points shift towards higher frequency. Figure 9 shows the effect of the width W_4. Figure 9 (a) shows that when W_4 decreases, the S-parameter curves of the antenna decrease while Fig. 9 (b) shows that the AR values have no obvious changes.

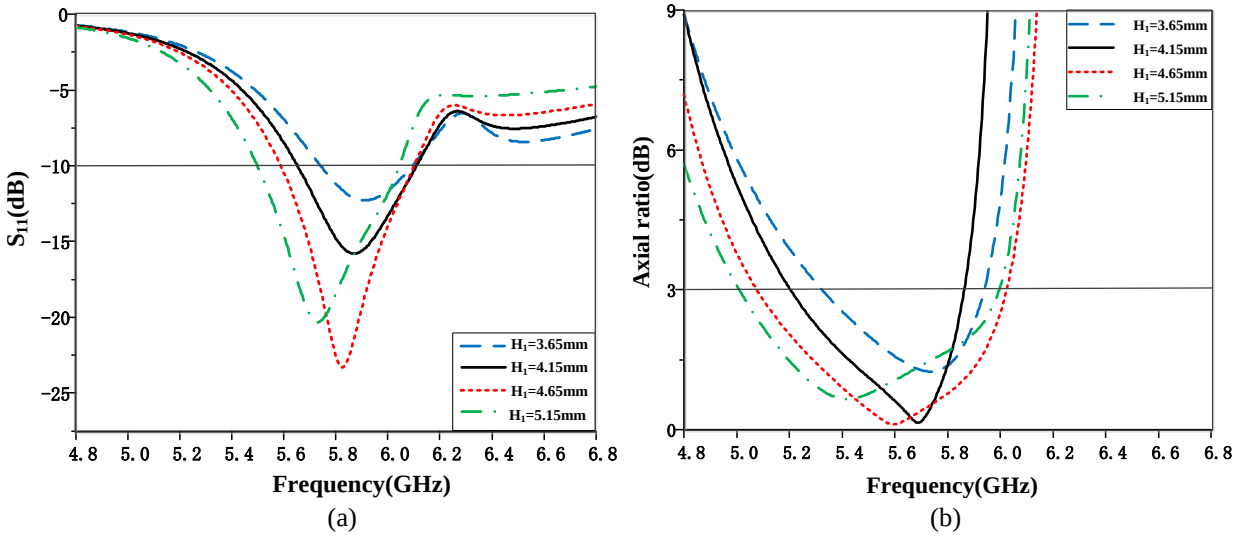

(a) (b)

Fig. 8. Simulated (a) $|S_{11}|$ and (b) AR of the proposed antenna with different H_1.

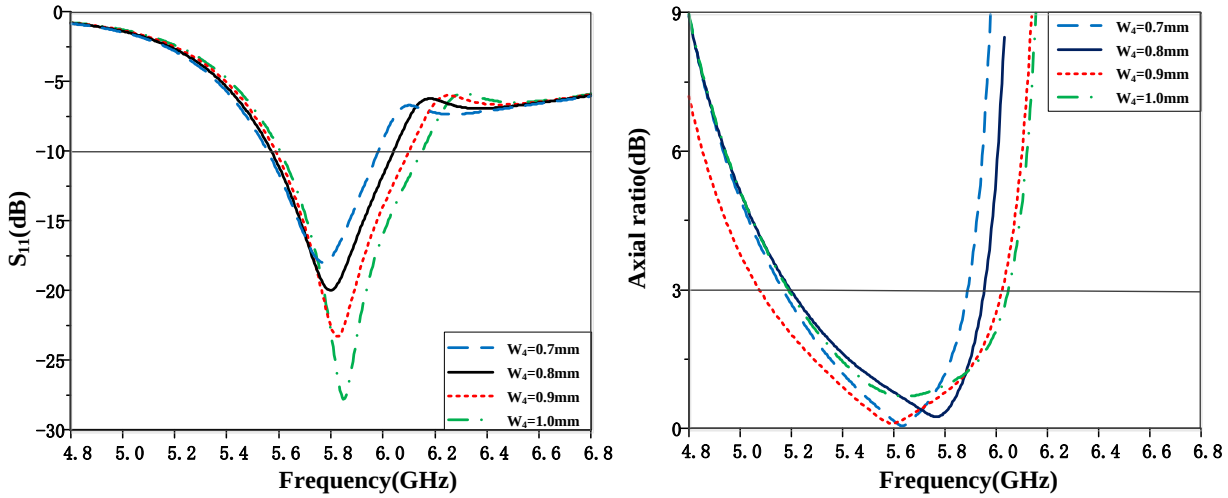

(a) (b)

Fig. 9. Simulated (a) $|S_{11}|$ and (b) AR of the proposed antenna with different W_4.

IV. EXPERIMENTAL RESULTS

In order to validate the proposed method, the antenna is fabricated, as shown in the Fig. 10. The antenna weighs only 4 grams, which makes it more suitable for UAVs diagram transmission because it's light enough. The measurements were implemented by an Agilent E8363B network analyzer and a far-field system in anechoic chamber.

Simulated and measured S parameters of antenna are shown in Fig. 11 (a). It can be seen that the measured S parameters agree with the simulated values well. The measured bandwidth of the antenna (S_{11}≤-10dB) is 0.64GHz, from 5.56GHz to 6.21GHz, equivalent to 11% at 5.8GHz. Figure 11 (b) shows simulated and measured AR bandwidth of antenna. The AR bandwidth (AR≤3dB) is 0.9GHz, from 5.10GHz to 6.00GHz, equivalent to 15.5%. It can be found that the overlapped bandwidth of Impedance and AR from 5.56GHz to 6.00GHz covers the UAVs diagram transmission frequency of 5.8GHz in China.

Fig. 10. Photograph of the fabricated antenna.

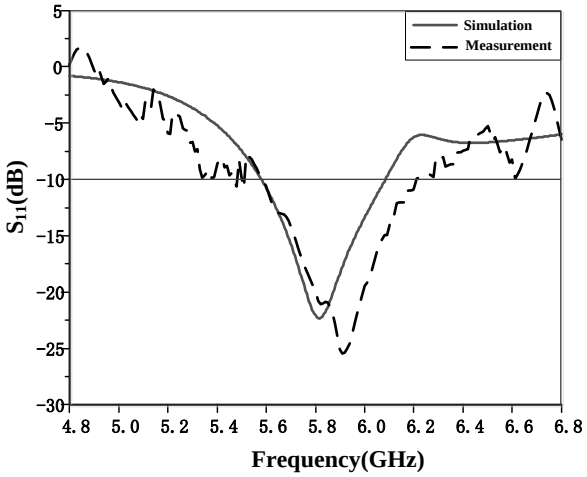

(a)

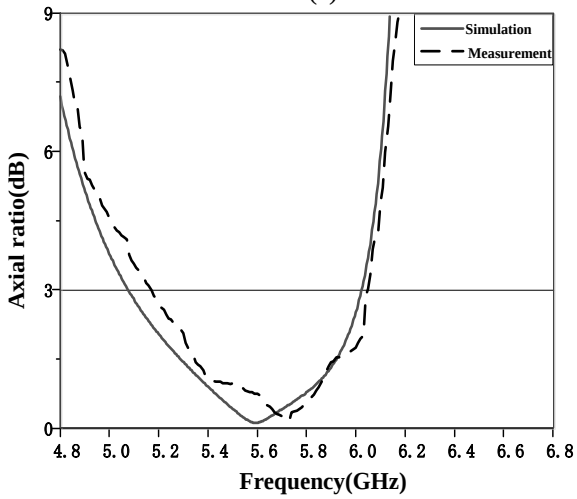

(b)

Fig. 11. Simulated and measured (a) $|S_{11}|$ and (b) AR of the fabricated prototype.

Figure 12 shows simulated and measured AR of the antenna in the azimuth plane ($\theta = 90^\circ$) at 5.8GHz. It can be seen that there are some small differences between the simulated and measured values due to fabrication errors. From the figure, when it is simulated, the ARs fluctuate within 1dB. The measured ARs are slightly higher than the calculated results in all directions, but they are all less than 3dB in the plane, the ripple of which is 0.7dB. Both the simulated and measured values meet the requirement of circular polarization, which indicates that the antenna has good CP characteristics at 5.8GHz.

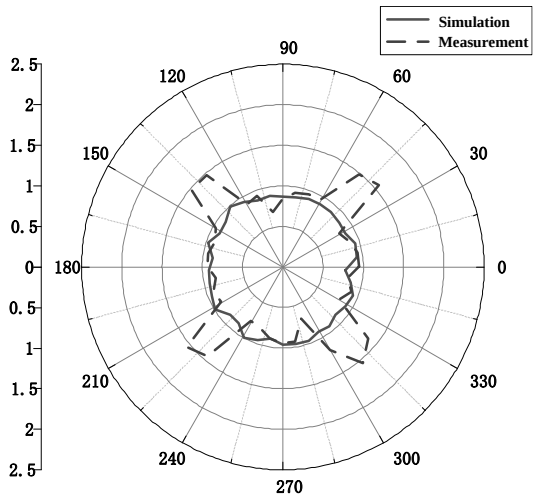

Fig. 12. Simulated and measured AR of the CP antenna in the azimuth plane ($\theta = 90^\circ$).

The simulated LHCP gain at 5.8 GHz is 1.12 dBic. Figure 13 shows the measured and calculated radiation patterns of the proposed antenna at 5.8 GHz in the azimuth (xy plane) and elevation (xz plane) planes, respectively. In xy plane, both the simulated and measured values of left-hand circularly polarized (LHCP) fluctuate around 1dB, while the simulated and measured values of right-hand circularly polarized (RHCP) are less than -15dB. In xz plane, it also can be seen that the results of the simulated and measured agree well with each other, and the level differences between the RHCP and LHCP are more than 15dB, that indicates the antenna is LHCP and has good omnidirectivity.

In order to show the advantage of the antenna, Table 1 compares the omnidirectional CP pagoda antenna with existing antennas in bandwidth and dimensions, from which the overall advantage of the novel pagoda antenna can be seen. Compared with the existing antenna, the overall size of novel pagoda antenna proposed is more advantageous. For the same size, the bandwidth is wider than that of the compared antenna.

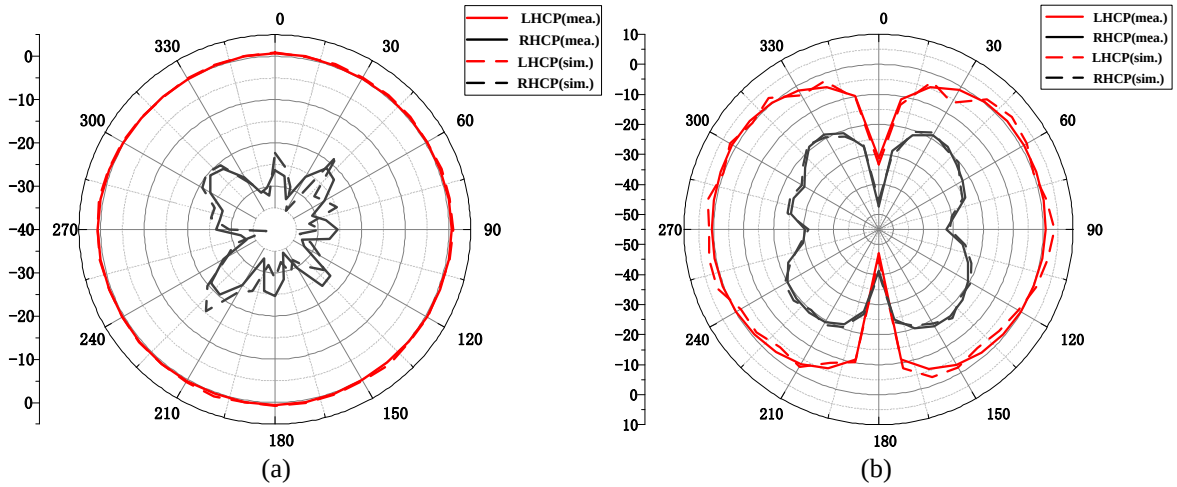

Fig. 13. Simulated and measured radiation patterns in (a) azimuth (xy plane) and (b) elevation (xz plane) planes at 5.8GHz.

Table 1: Performance comparison of reported omnidirectional CP antennas with existing antenna

Ref.	**Dimensions (λ_0)**	**Imp. Bandwidth (%)**	**3dB AR Bandwidth (%)**	**Usable Bandwidth (%)**
[7]	$1.63\lambda_0\times1.63\lambda_0\times0.28\lambda_0$	21.60	25.3	21.60
[9]	$0.62\lambda_0\times0.62\lambda_0\times0.029\lambda_0$	3.97	-	3.97
[10]	$0.52\lambda_0\times0.52\lambda_0\times0.026\lambda_0$	3.50	-	3.50
[15]	$0.24\lambda_0\times0.24\lambda_0\times0.12\lambda_0$	3.90	7.5	3.90
This work	$0.42\lambda_0\times0.42\lambda_0\times0.33\lambda_0$	9.00	16.4	9.00

V. CONCLUSION

A novel omnidirectional RHCP antenna is presented in this letter. The novel pagoda antenna loaded with the shorting pin and the lower substrate with two coupling patches achieves miniaturization in size with adequate bandwidth. The principle and experiment of the antenna are discussed in detail above. Finally, the impedance bandwidth of novel pagoda antenna is 0.53GHz, AR bandwidth is 0.95GHz and usable bandwidth is 0.53GHz, which can cover the UAVs diagram transmission frequency of 5.8GHz in China. With the final dimensions of $0.42\lambda_0$*$0.42\lambda_0$*$0.33\lambda_0$, the antenna has advantages compared with the existing antennas. At the same time, it can be found that the AR bandwidth of the antenna is wider than the impedance bandwidth, which provides a potential for the following research. Impedance bandwidth can be further broadened to achieve miniaturized broadband omnidirectional CP pagoda antenna.

ACKNOWLEDGMENT

This work was supported by the National Natural Science Foundation of China (No. 61771490), Shaanxi Natural Science Foundation Project (No. 2018JM6055), the Basic Research Program of ENGG University of the Chinese People Armed Police Force (No. WJY201606) and Research team project (KYTD201803).

REFERENCES

[1] Y. M. Pan and K. W. Leung, "Wideband circularly polarized dielectric bird-nest antenna with conical radiation pattern," *IEEE Trans. Antennas Propag.*, vol. 61, no. 2, pp. 563-570, 2013.

[2] G. Zheng and B. Sun, "High-gain normal-mode omnidirectional circularly polarized antenna," *IEEE Antennas and Wireless Propagation Letters*, vol. 17, no. 6, pp. 1104-1108, June 2018.

[3] Y. Fan, X. Y. Liu, and R. Li, "A broadband circularly polarized omnidirectional antenna with circular open-loops," *2016 IEEE International Conference on Computational Electromagnetics (ICCEM)*, Guangzhou, pp. 200-201, 2016.

[4] X. Quan, R. Li, and M. M. Tentzeris, "A broadband omnidirectional circularly polarized antenna," *IEEE Transactions on Antennas and Propagation*, vol. 61, no. 5, pp. 2363-2370, May 2013.

[5] Y. Fan, X. L. Quan, Y. Pan, Y. H. Cui, and R. L. Li, "Wideband omnidirectional circularly polarized

antenna based on tilted dipoles," *IEEE Trans. Antennas Propag.*, vol. 63, no. 12, pp. 5961-5966, Dec. 2015.

[6] C. Y. Liu and Q. X. Chu, "Omnidirectional circularly polarized antenna based on crossed dipoles," *2016 IEEE International Conference on Microwave and Millimeter Wave Technology (ICMMT)*, Beijing, pp. 731-733, 2016.

[7] L. Yang, N. W. Liu, Z. Y. Zhang, et al., "A novel single feed omnidirectional circularly polarized antenna with wide AR bandwidth," *Progress In Electromagnetics Research C*, vol. 51, pp. 35-43, 2014.

[8] J. Su and F. Zhang, "Capacitive probe fed broadband circularly polarized omnidirectional Antenna," *2018 Cross Strait Quad-Regional Radio Science and Wireless Technology Conference (CSQRWC)*, Xuzhou, pp. 1-1, 2018.

[9] Q. X. Chu, Y. Mao, and X. R. Li, "A low-profile omnidirectional circularly polarized antenna using planar sector-shaped endfire elements," *IEEE Transactions on Antennas & Propagation*:1-1.

[10] C. Guo, R. Yang, and W. Zhang, "Compact omnidirectional circularly polarized antenna loaded with complementary V-shaped slits," *IEEE Antennas and Wireless Propagation Letters*, vol. 17, no. 9, pp. 1593-1597, Sept. 2018.

[11] Q. Nie, Z. Zhang, and G. Fu, "A compact omnidirectional circularly polarized antenna for 5G communication system," *2018 International Conference on Microwave and Millimeter Wave Technology (ICMMT)*, Chengdu, pp. 1-2, 2018.

[12] H. H. Tran, N. Nguyen-Trong, and H. C. Park, "A compact wideband omnidirectional circularly polarized antenna using TM_{01} mode with capacitive feeding," *IEEE Antennas and Wireless Propagation Letters*, vol. 18, no. 1, pp. 19-23, Jan. 2019.

[13] Y. Cai, S. Gao, Y. Yin, W. Li, and Q. Luo, "Compact-size low-profile wideband circularly polarized omnidirectional patch antenna with reconfigurable polarizations," *IEEE Transactions on Antennas and Propagation*, vol. 64, no. 5, pp. 2016-2021, May 2016.

[14] J. Li, Y. Huang, and G. Wen, "Design of a compact tri-band omnidirectional circularly polarized antenna," *2018 IEEE International Symposium on Antennas and Propagation & USNC/URSI National Radio Science Meeting*, Boston, MA, pp. 121-122, 2018.

[15] C. Y. Liu and Q. X. Chu, "A compact omni-directional circularly polarized antenna," *European Conference on Antennas and Propagation (Eu CAP 2018), IET*, 1-2, 2018.

[16] D. Wu, X. Chen, L. Yang, et al., "Compact and low-profile omnidirectional circularly polarized antenna with four coupling arcs for UAV applications," *IEEE Antennas and Wireless Propagation Letters*, pp. (99):1-1, 2017.

[17] J. Liu, Q. Xue, H. Wong, H. W. Lai, and Y. Long, "Design and analysis of a low-profile and broadband microstrip monopolar patch antenna," *IEEE Transactions on Antennas and Propagation*, vol. 61, no. 1, pp. 11-18, Jan. 2013.

[18] Y. Z. Zhu, D. Su, W. Xie, et al., "Design of a novel miniaturized Vivaldi antenna with loading resistance for ultra wideband (UWB) applications," *Applied Computational Electromagnetics Society Journal*, vol. 32, no. 10, 2017.

Zheyu Li was born in Hubei, China. She received the B.S. degree in Communication Engineering from Engineering University of People's Armed Police in 2018, and she is now studying for a master's degree at Engineering University of People'sArmed Police. Her research interests are mainly in microwave antennas.

Yongzhong Zhu was born in Anhui, China. He received the B.S. degree in Communication Engineering from Engineering University of People's Armed Police, the M.S. degree in Military Communication from Engineering University of People's Armed Police, and the Ph.D. degree in Electronic Science and Technology from Xidian University, in 2002, 2005 and 2008, respectively. From 2009 to 2011, he was a Postdoctoral Fellow with Northwestern Polytechnical University. Since 2012, he has been an Associate Professor of microwave engineering with Engineering University of People's Armed Police. His research interests are in microwave antennas and devices, wireless communications and information systems.

Shen Yu was born in Shanxi, China. She received the Bachelor degree in Military Communication from Engineering University of People's Armed Police in 2006 and the M.S degree in Military Communication from Engineering University of People's Armed Police in 2009. Since 2019, she has been an Associate Professor of Command Information System of Engineering University of People's Armed Police. Her research interests are in command information system.

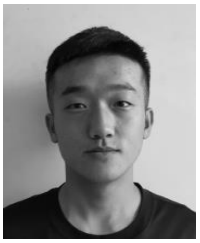

Xiaoyu Liu was born in Inner Mongolia, China. He received the B.S. degree in Communication Engineering from Engineering University of People' s Armed Police in 2018, and he is now studying for a master's degree at Engineering University of People' s Armed Police. His research interests are mainly in microwave antennas.

Guohao Peng was born in Sichuan, China. He received the B.S. degree in Electronic and Information Engineering from Wuhan University of Science and Technology in 2018,and he is now studying for a master's degree at Engineering University of People' s Armed Police. His research interests are mainly in microwave antennas.

A High-Efficient Wideband Transmitarray Antenna with Vias

Yongliang Zhang[*1,2], Xiuzhu Lv[2], Lina Liu[2], Yaxin Yi[2], and Zhao Wu[3]

[1] College of Transportation
Inner Mongolia University, Hohhot, 010021, China
namar@imu.edu.cn

[2] College of Electronic Information Engineering
Inner Mongolia University, Hohhot, 010021, China
31856006@mail.imu.edu.cn, lnliu1207@163.com, m18804709243@163.com

[3] College of Physics and Telecommunication Engineering
Yulin Normal University, Yulin, 537006, China
kianty@163.com

Abstract ─ This paper presents a high-efficient wideband transmitarray antenna with vias. The transmitarray element consists of two layers of Jerusalem cross patches and four metal vias. Two Jerusalem cross patches are printed on both sides of the substrate and are connected by four symmetrical metal vias. The metal vias can improve the coupling strength between the two patches. By adjusting the size of the patch and the position of the metal vias, the transmission phase of the element is greater than 360º. Then, an transmitarray antenna consists of the proposed elements is designed, manufactured, and measured. The experiment results show that the maximum gain of the transmitarray antenna is 25.7dB, and the corresponding aperture efficiency is 46.6%. The measured 1-dB gain bandwidth is 14.9% (8.7GHz-10.1GHz).

Index Terms ─ High-efficient, transmitarray antenna, wideband.

I. INTRODUCTION

In recent years, planar array antenna has attracted more and more attention due to its light weight and easy installation. The planar array antenna includes the reflectarray antenna (RA) and the transmitarray antenna (TA). Compared with the RA [1-3], the feed horn of the TA and the transmitted wave are not on the same side, so it has higher aperture efficiency and lower side lobe. However, the bandwidth of the TA is narrow.

In order to improve the broadband characteristics of TA, scholars have proposed a variety of methods [4-12]. In [4], a four layers TA using double split-ring slot is presented. The 1-dB gain bandwidth of the TA is 7.4% and the aperture efficiency is 55%. [5] presents a four layer TA using a double square ring as the element. It has 7.5% 1-dB gain bandwidth. [6] using triple-layer spiral-dipole to realize the 360º transmission phase, but the transmission amplitude of the TA element is less than -4dB. In [7], a triple-layer TA without substrate is proposed. The proposed TA realized 15.5% 1-dB bandwidth and 55% efficiency. In [8], a novel TA element based on bandpass filter is designed. The TA element consists of two triple-layer frequency selective surfaces. Experimental results that the TA has 16% 1-dB gain bandwidth and 60% aperture efficiency. Other studies on transimitarray antenna is proposed in [9-12]. [13-17] are metasurface application on antenna array and MIMO antennas. From the above report, in order to improve the bandwidth of the TA, it is necessary to use the multi-layer patch to realize the 360º transmission phase and desired transmission amplitude. That will results to higher processing costs and increased installation complexity.

In this paper, a double-layer high-efficient wideband transmitarray antenna is present. The transmitarray element consists of two layers of Jerusalem cross patches and four metal vias. The metal vias are used to improve the internal coupling of the TA element. The structure of the article is as follows: Section I is the introduction of transmitarray antenna. Section Ⅱ is the design and simulation of the TA element. To verify the validity of the proposed element, a transmitarray antenna is designed and measured. The transmitarray prototype and measurement results are given in Section III. Section IV is the summary of the whole design.

II. DOUBLE-LAYER TRANSMITARRAY ANTENNA ELEMENT DESIGN

A. Element structure

Figure 1 is a plane geometric model of the proposed

Submitted On: December 8, 2019
Accepted On: December 31, 2019

TA element. The purpose of the TA element design is to realize the transmission phase of 360° with the least number of patch layers. The TA element consists of two Jerusalem cross patches. The dielectric constant of the substrate is 2.2 and the tangent of loss angle is 0.0009. Four symmetrical metal vias are used to connect the two-layer of patch. The metal vias are made of copper. Two layers of patches are printed on both sides of the substrate. The role of the metal vias are improve the internal coupling of the TA element.

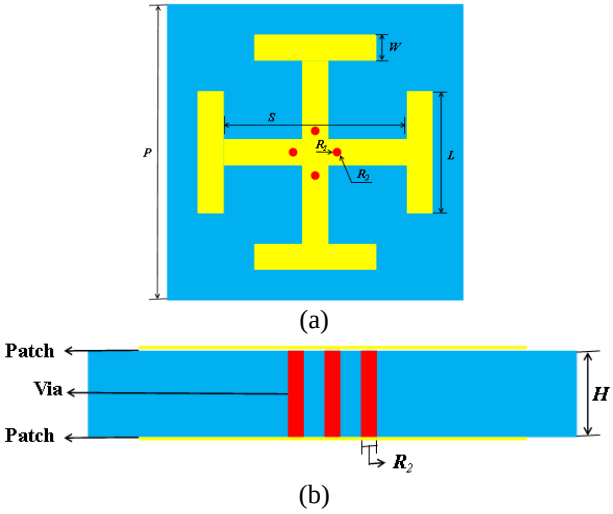

Fig. 1. Geometric model of the TA element: (a) vertical view and (b) lateral view.

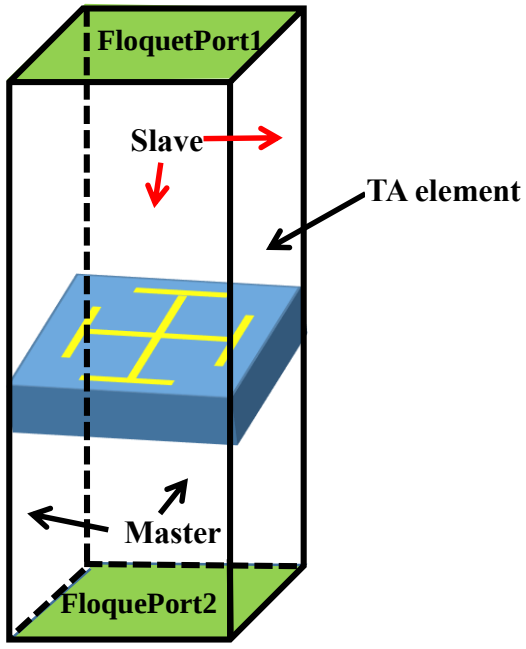

Fig. 2. The TA element simulation settings.

Table 1: Design parameters of the TA element

Parameter	Value
P	17mm
W	1.5mm
L	2~9mm
S	L+3.5mm
R_1	1.55mm
R_2	0.6mm
H	4mm

Ansoft HFSS is used to simulate and optimize the proposed element. In order to simulate the electromagnetic characteristics of elements in infinite period arrangement, the master-slave boundary is adopted. Because of transmitarray antenna needs to consider both transmission and phase shift characteristics, two Floquet-port excitations need to be set, as shown in Fig. 2. Figure 3 is the transmission characteristics of TA element with different structure parameters. As shown in (a), the thicker the substrate, the better the linearity of the phase shift curve. But the increase in the substrate thickness will lead to the reduction of the radiation efficiency of the TA. Therefore, the substrate thickness is 4mm. In order to avoid the generation of grating lobe, the TA element period is generally greater than 0.5λ. As shown in (b), when *P*=17mm (0.53λ), the phase shift curve is the most linear. It is can be seen from (c) and (e) that, the size and position of the metal vias have little effect on the linearity of the phase shift curve. In (d) and (f), it can be concluded that the size and position of the metal vias have a great influence on the transmission performance of the TA element. After a series of parameter optimization, the geometric dimensions of the element are shown in table 1.

B. Element transmission characteristic

The transmission amplitude and transmission phase versus L of the proposed TA element is shown in Fig. 4. As shown in this figure, the transmission phase of the element is greater than 360°. Within the range of 360° phase shift, the transmission amplitude of the element is always greater than -3.5dB. By adjusting the size of the TA element, the phase shift curve is parallel in a wide frequency band, which widens the frequency band width of the transmission array antenna. The transmission phase curves of the TA element at different frequencies are shown in Fig. 5. It can be seen from the figure that the transmission phase curves of different frequencies are approximately parallel. Therefore, the designed TA element has broadband characteristics. In order to observe the aperture efficiency of the TA element, the current distribution on the surface of the element is shown in the Fig. 6. As can be seen from the figure, the element surface current distribution is relatively uniform, so the TA has high efficiency. In addition, the current at

the element edge is weak, which can reduce the coupling between the TA elements and improve the gain of the TA.

Since most of the TA elements are irradiated by oblique incident electromagnetic waves, the oblique incident characteristics of the element must be considered when designing the element. θ and φ are the angles of the incident wave with Z-axis and X-axis, respectively. Figure 7 shows the transmission amplitude and phase of the TA element at different incident angles. As shown in this figure, within the range of 15°, the transmission phase of the cell is always greater than 360°, and the corresponding transmission phase is greater than -3.5dB.

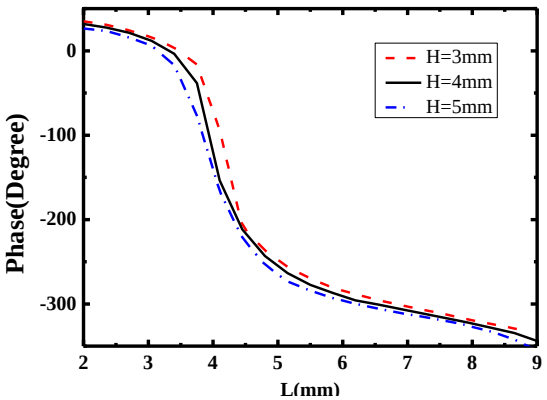

(a)

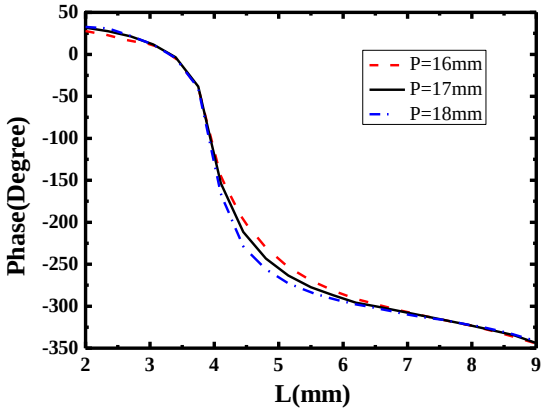

(b)

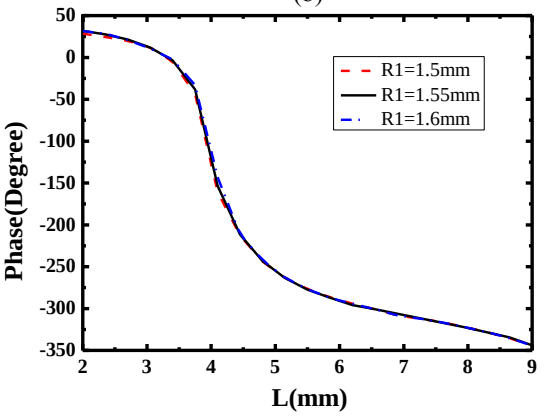

(c)

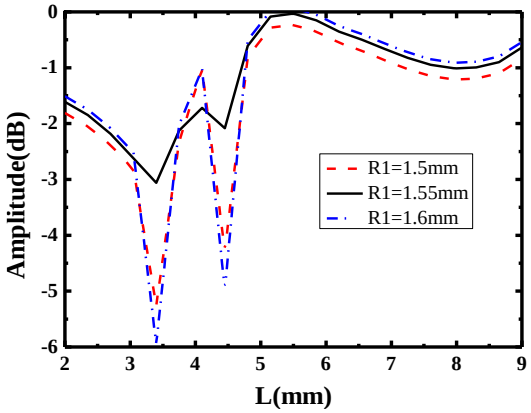

(d)

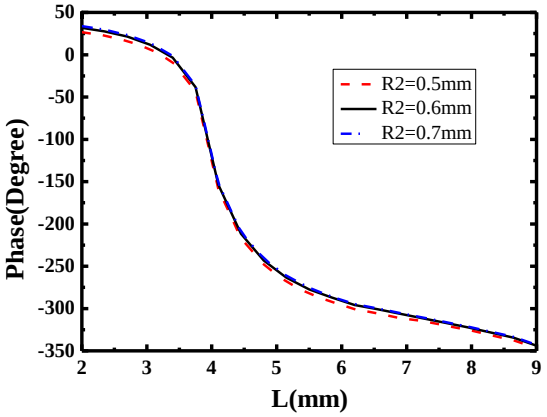

(e)

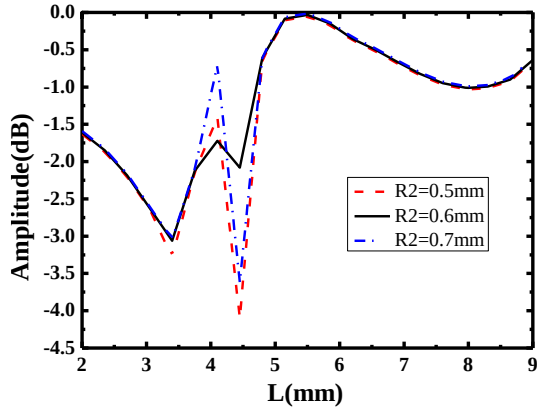

(f)

Fig. 3. The transmission characteristics of TA element with different structure parameters (9.5 GHz), (a) transmission phase of different substrate thickness (P=17mm, R_1=1.55mm, R_2=0.6mm), (b) transmission phase of different element periods (H=4mm, R_1=1.55mm, R_2=0.6mm), (c) transmission phase of different metal vias location (H=4mm, P=17mm, R_2=0.6mm), (d) transmission amplitude of different vias location (H=4mm, P=17mm, R_2=0.6mm), (e) transmission phase of different vias size (H=4mm, P=17mm, R_1=1.55mm), and (f) transmission amplitude of different vias size (H=4mm, P=17mm, R_1=1.55mm).

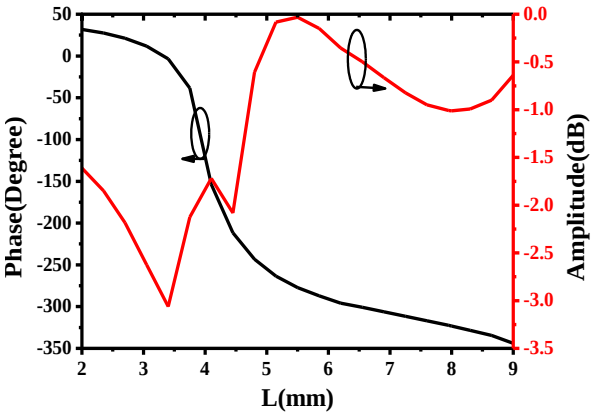

Fig. 4. Transmission characteristics of the TA element versus L.

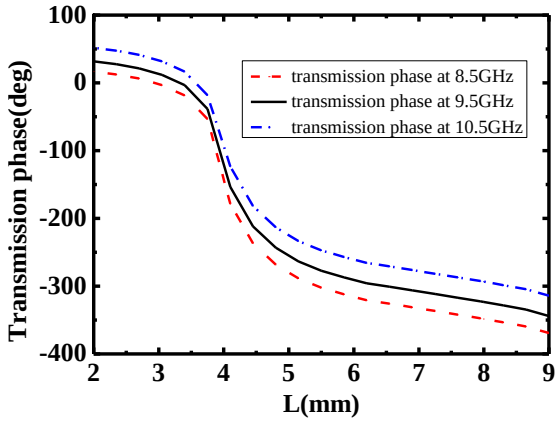

Fig. 5. Transmission phase of the TA element at different frequencies.

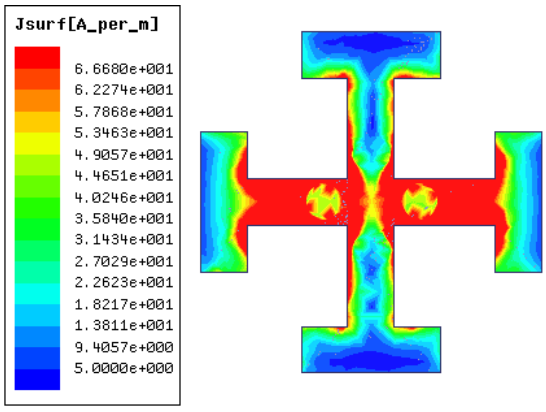

Fig. 6. The current distribution of the TA element.

C. Metal vias

Four vertical metal vias are placed symmetrically between the Jerusalem cross patches, they create a strong coupling between the two patches. The four metal vias can be used as an additional coupling structure, which can reduce the number of patch layers of the TA element. The decrease of the number of patch layers will result in the decrease of transmission amplitude and phase. Currently, no TA element with only two layers of patches can achieve 360°'s transmission phase and desired transmission amplitude [18].

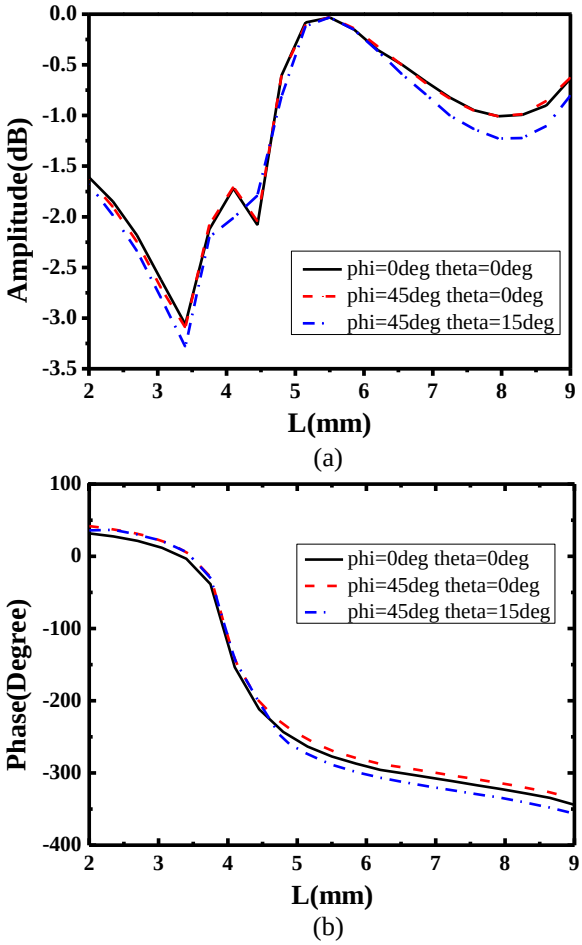

Fig. 7. Transmission characteristics of the TA element at different incident angles: (a) transmission amplitude, and (b) transmission phase.

Figure 8 is the transmission characteristic curve of the TA element without metal vias. It is obvious from the figure that the transmission amplitude is very small and the transmission phase is less than 360°. This is because the coupling between the upper and lower Jerusalem cross patches is weak. Therefore, it can be concluded that the introduction of metal vias can reduce the number of patch layers and improve the transmission performance of the TA element.

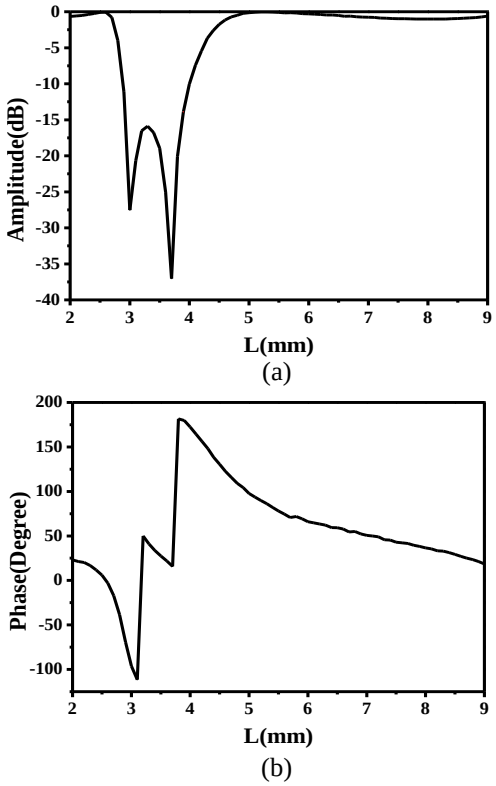

Fig. 8. Transmission characteristic of the TA element without metal vias: (a) transmission amplitude, and (b) transmission phase.

III. DOUBLE-LAYER TRANSMITARRAY ANTENNA DESIGN AND MEASUREMENT

A. Design of the TA

To verify the validity of the proposed TA element, a transmitarray antenna working at 9.5GHz is designed. The transmitarray antenna consists of 15×15 TA elements and the dimension size is 255mm×255mm×4mm. The focal length is 400mm and the corresponding focal diameter ratio is 1.57. Focal length is the distance from the feed to the transmitarray. Once the position of the feed is determined, the compensation phase of the TA element can be calculated by formula [19]. Figure 9 is the compensated phase distribution diagram of the transmitarray. The value of L corresponding to the compensation phase can be obtained from Fig. 4. As the value of L is obtained, the size of each TA element in the transmitarray can be determined. The feed of this design is a wideband pyramidal horn. The aperture dimension of the pyramidal horn is 187mm×60mm. The operating frequency of the horn is 8GHz-11GHz and its gain at 9.5GHz is 16dB.

B. Experimental results

The TA prototype was measured in a microwave anechoic chamber at Xidian University. The test system is shown in the Fig. 10, Tx is the transmitting horn and Rx is the receiving horn. The polarization modes of Tx and Rx are vertical polarization, the center of Tx, Rx and TA is aligned, which can ensure the effectiveness of the test system. The distance from Tx, Rx and TA to the ground is 1.5 meters, the distance between Rx and TA is 3 meters. The simulated and measured normalized radiation patterns at 9.5GHz is shown in Fig. 11. In Fig. 11 (a), the sidelobe level and the cross-polarization of the E-plane radiation pattern is 17dB and 37dB, respectively. In Fig. 11 (b), the sidelobe level and the cross-polarization of the H-plane radiation pattern is 16dB and 36dB, respectively. The simulated and measured gain versus frequency is shown in Fig. 12. The measured maximum is 25.7dB at 9.5GHz and the corresponding aperture efficiency is 46.6%. The measured 1-dB gain bandwidth is 14.9%. The measured maximum gain is 0.33dB lower than the simulated maximum gain. There are two main reason: 1. There is an error in the size of the patch during processing, which will result in an error between the theoretical phase compensation value and the actual phase compensation value, resulting in an increase in sidelobe and a decrease in gain. 2. The phase center of the horn is not stable.

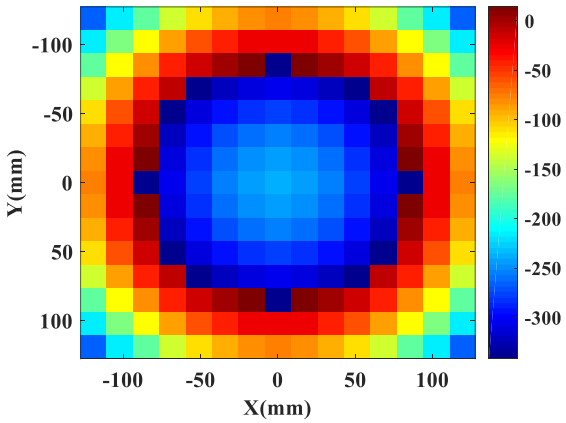

Fig. 9. Transmission phase distribution.

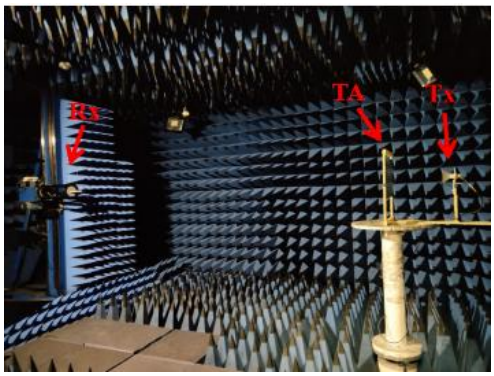

Fig. 10. The test system in microwave anechoic.

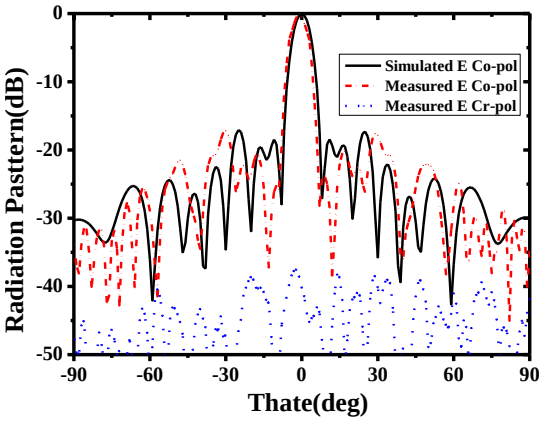

(a)

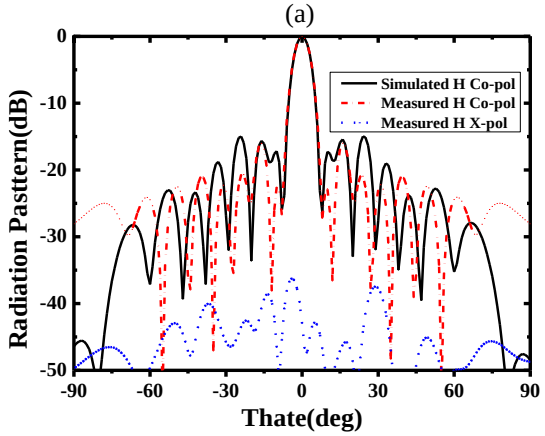

(b)

Fig. 11. The simulated and measured normalized radiation patterns at 9.5GHz: (a) E-plane and (b) H-plane.

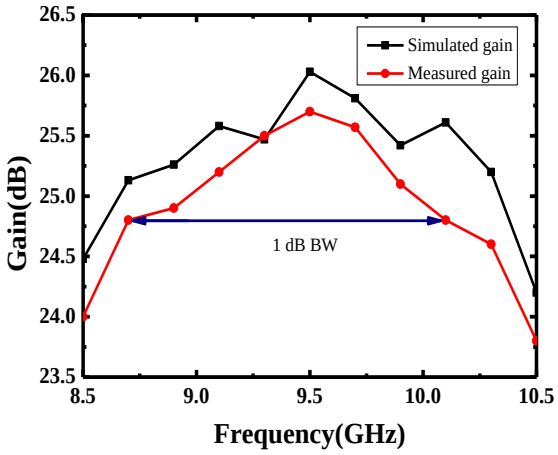

Fig. 12. The simulated and measured gain versus frequency.

Table 2 shows the performance comparison between the proposed antenna and other antennas. It can be concluded from the table that the proposed TA has the advantages of high efficient and broadband with only two layers of patches compared to the published antenna in [4], [12], [20-21].

Table 2: The comparison between the proposed TA and other published TA

Ref.	Freq. (GHz)	Numbers of Layers	Gain (dB)	Aperture Efficiency (%)	1dB gain Bandwidth (%)
[4]	12.5	4	18.9	20.9	9.6
[12]	13.58	3	23.9	55	7.4
[20]	6.1	3	20.1	27	8.3
[21]	10	3	21.9	36	4
This work	9.5	2	25.7	46.6	14.9

IV. CONCLUSION

In this paper, a double-layer high-efficient wideband transmitaray antenna with vias is designed and measured. The designed transmitarray element consists of two-layer Jerusalem cross patche and four metal vias. The introduction of metal vias could effectively improve the transmission performance of the element. After a series of design and simulation, a transmitarray antenna consisting of 255-element is fabricated and measured. The measurement and simulation results are basically consistent. The measured maximum gain is 25.7dB at 9.5GHz and the corresponding aperture efficiency is 46.6%. The 1-dB gain bandwidth of the transmitarray antenna is 14.9% (8.7GHz-10.1GHz). Since the designed element has only two-layers patch, the complexity of the design can be simplified and the production cost can be reduced.

ACKNOWLEDGMENT

The author would like to thank Prof. Long Li and Mingyang Chang of Xidian University for providing the measurement results in this paper. This work was supported by the National Natural Science Foundation of China (NSFC) under Project No. 61761032, Nature Science Foundation of Inner Mongolia under Contract No. 2019MS06006, Natural Science Foundation Youth Fund Project in Guangxi of China under No. 2018GXNSFBA281124 and China Scholarship Fund.

REFERENCES

[1] Q. Wang, Z. H. Shao, Y. Jian Cheng, and P. K. Li, "Broadband low-cost reflectarray using modified double-square loop loaded by spiral stubs," *IEEE Trans. Antennas Propag.*, vol. 63, no. 9, pp. 4224-4229, Sep. 2015.

[2] X. Xia and Q. wu, "Wideband millimeter-wave microstrip reflectarray using dual-resonance unit cells," *IEEE Antennas Wireless Propag. Lett.*, vol. 16, pp. 4-7, 2017.

[3] Q. Gao and J. Wang, "A multiresonant element for

bandwidth enhancement of circularly polarized reflectarray antennas," *IEEE Antennas Wireless Propag. Lett.*, vol. 17, no. 5, pp. 727-730, May 2018.

[4] G. Liu, H. Wang, J. Jiang, F. Xue, and M. Yi, "A high-efficiency transmitarray antenna using double split ring slot elements," in *IEEE Antennas and Wireless Propagation Letters*, vol. 14, pp. 1415-1418, 2015.

[5] C. G. M. Ryan, M. R. Chaharmir, J. Shaker, J. R. Bray, Y. M. M. Antar, and A. Ittipiboon, "A wideband transmitarray using dual-resonant double square rings," in *IEEE Transactions on Antennas and Propagation*, vol. 58, no. 5, pp. 1486-1493, May 2010.

[6] A. H. Abdelrahman, A. Z. Elsherbeni, and F. Yang, "High-gain and broadband transmitarray antenna using triple-layer spiral dipole elements," in *IEEE Antennas and Wireless Propagation Letters*, vol. 13, pp. 1288-1291, 2014.

[7] C. Tian, Y. Jiao, G. Zhao, and H. Wang, "A wideband transmitarray using triple-layer elements combined with cross slots and double square rings," in *IEEE Antennas and Wireless Propagation Letters*, vol. 16, pp. 1561-1564, 2017.

[8] Q. Luo, S. Gao, M. Sobhy, and X. Yang, "Wideband transmitarray with reduced profile," in *IEEE Antennas and Wireless Propagation Letters*, vol. 17, no. 3, pp. 450-453, Mar. 2018.

[9] B. Rahmati and H. R. Hassani, "High-efficient wideband slot transmitarray antenna," *IEEE Trans. Antennas Propag.*, vol. 63, no. 11, pp. 5149-5155, Nov. 2015.

[10] W. An, S. H. Xu, F. Yang, and M. K. Li, "A double-layer transmitarray antenna using Malta crosses with vias," *IEEE Trans. Antennas Propag.*, vol. 64, no. 3, pp. 1120-1125, Mar. 2016.

[11] K. Pham, et al., "Design of wideband dual linearly polarized transmitarray antennas," *IEEE Trans. Antennas Propag.*, vol. 64, no. 5, pp. 2022-2026, May 2016.

[12] J. F. Yu, L. Chen, J. Yang, and X.W. Shi, "Design of a transmitarray using split diagonal cross elements with limited phase range," *IEEE Antennas Wireless Propag. Lett.*, vol. 15, pp. 1514-1517, 2016.

[13] F. Liu, J. Guo, L. Zhao, G. Huang, Y. Li, and Y. Yin, "Dual-band metasurface-based decoupling method for two closely packed dual-band antennas," in *IEEE Transactions on Antennas and Propagation*.

[14] J. Guo, F. Liu, L. Zhao, Y. Yin, G. Huang, and Y. Li, "Meta-surface antenna array decoupling designs for two linear polarized antennas coupled in H-plane and E-plane," in *IEEE Access*, vol. 7, pp. 100442-100452, 2019.

[15] S. Luo, Y. Li, Y. Xia, and L. Zhang, "A low mutual coupling antenna array with gain enhancement using metamaterial loading and neutralization line structure," in *Applied Computational Electromagnetics Society Journal*, vol. 34, no. 3, pp. 411-418, 2019.

[16] K. Yu, Y. Li, and X. Liu, "Mutual coupling reduction of a MIMO antenna array using 3-D novel meta-material structures," in *Applied Computational Electromagnetics Society Journal*, vol. 33, pp. 758-763, 2018.

[17] T. Jiang, T. Jiao, and Y. Li, "A low mutual coupling MIMO antenna using periodic multi-layered electromagnetic band gap structures," in *Applied Computational Electromagnetics Society Journal*, vol. 33, pp. 305-311, 2018.

[18] X. Yi, T. Su, B. Wu, J. Chen, L. Yang, and X. Li, "A double-layer highly efficient and wideband transmitarray antenna," in *IEEE Access*, vol. 7, pp. 23285-23290, 2019.

[19] A. Clemente and L. Dussopt, "Wideabnd 400-element eletronically reconfigurable trasmitarray in X band," *IEEE Trans. Antennas Propag.*, vol. 61, no. 10, pp. 5017-5026, Nov. 2013.

[20] X. Zhong, L. Chen, Y. Shi, and X. Shi, "Design of multiple-polarization transmitarray antenna using rectangle ring slot elements," in *IEEE Antennas and Wireless Propagation Letters*, vol. 15, pp. 1803-1806, 2016.

[21] C. Tian, Y. Jiao, and G. Zhao, "Circularly polarized transmitarray antenna using low-profile dual-linearly polarized elements," in *IEEE Antennas and Wireless Propagation Letters*, vol. 16, pp. 465-468, 2017.

Yongliang Zhang received the B.S. and Ph.D. degrees from Xidian University, Xi'an, China, in 2009 and 2014, respectively. He is currently with College of Transportation Inner Mongolia University, Hohhot, China. His research interests include passive microwave/ millimeter wave device, filtering antenna, smart antennas, reconfigurable antennas, and frequency selective surfaces, electromagnetic compatibility, metasurface based antenna.

Xiuzhu Lv received bachelor degree in Communication Engineering from Inner Mongolia University of Science and Technology, Baotou, China, in 2018. From 2018, she pursued her Master degree in Inner Mongolia University. Her research interest are transmitarray antenna and frequency selective surface.

Lina Liu received bachelor degree in Electronic Information Engineering from Southwest Minzu University, Chengdu, China, in 2019. From 2019, she pursued her Master degree in Inner Mongolia University. Her research interests is series-fed micro-strip antenna array.

Yaxin Yi received bachelor degree in Electronic Information Engineering from Dalian University, Dalian, China, from 2014 to 2018. From 2019, she pursed her Master degree in Inner Mongolia University. Her research interests is reconfigurable transmitarray.

Zhao Wu (M'19) was born in Guangxi, China, in 1987. He received the B.E. Degree in Electronic and Information Engineering and Ph.D. degree in Electromagnetic Fields and Microwave Technology from Xidian University, Xi'an, China, in 2011 and 2016, respectively. From October 2016 to March 2017, he was with Huawei Technologies Co Ltd. Since April 2017, he has been working with College of Physics and Telecommunication Engineering as a Lecturer, Yulin Normal University. His research interests include metamaterials, novel antennas, reconfigurable antenna design and applications.

Design of a Dielectric-loaded Wide Beam Quad-ridged Horn Antenna

Yaqing Yu [1], Wen Jiang [1], Lv Qin [2], and Shuxi Gong [1]

[1] National Key Laboratory of Antennas and Microwave Technology
Xidian University, Xi'an, 710071, China
yuyaqing27@163.com, jw13@vip.qq.com, shxgong@xidian.edu.cn

[2] The 39th Research Institute of China Electronics Technology Group Corporation
Xi'an, 710071, China
1759803286@qq.com

Abstract ─ A quad-ridged horn antenna with dielectric loading covering the 0.6 GHz to 4 GHz band is proposed. Through the comprehensive design of differential feeding, a quad-ridged flare and loaded dielectrics, the feed antenna can be used to match a reflector with a large illumination angle of approximately 150 degrees. In the working band, the reflection coefficient is less than -8 dB, the isolation is larger than 40 dB, and its cross-polarization discrimination is larger than 31 dB for both polarizations. To verify the simulations, a prototype is fabricated and measured, and the measurements are in good agreement with the simulations. A reflector with a diameter of 33 meters and a focal diameter ratio of 0.33 is adopted to analyze the in-dish performance of the feed. The simulated results show that an average efficiency of 55.16% is realized and that the problem of the efficiency decrease caused by beamwidth narrowing at high frequencies is solved.

Index Terms ─ Dielectric loading, differential feed, quad-ridged horn, reflector antenna.

I. INTRODUCTION

Radio astronomy uses radio telescopes to study the phenomena of the universe. The performance of the antenna, the signal-receiving component of a radio telescope system, will dramatically influence the performance of the whole system.

Antennas on radio telescopes can be generally divided into two kinds: the single reflector antenna and the synthetic aperture antenna. The former is usually a large aperture reflector antenna, which mainly relies on structural technology and has the advantage of an easy replacement of the feed. The latter uses a reflector antenna or an array antenna as a unit to form the synthetic aperture radio telescope, which mainly relies on the numerical processing of a large amount of observation data. For example, the Effelsberg 100-m radio telescope, the Five-hundred-meter Aperture Spherical Telescope (FAST), the Shang Hai Astronomy Observatory (SHAO) 65-m radio telescope and the Parkes 64-m radio telescope all adopt the single reflector antenna system. Meanwhile, the Very Large Array (VLA), the Australia Telescope Compact Array (ATCA) and the Australian Square Kilometer Array Pathfinder (ASKAP) employ the synthetic aperture system. However, they are usually unable to meet the hardware requirements for a synthetic aperture radio telescope at this stage. For instance, the computation ability required by SKA is expected to be satisfied in one or two decades. Therefore, radio telescopes currently rely mainly on the single reflector antennas for observation.

For the best feed of the reflector antenna, the characteristics across the working band should be as follows: 1) dual-polarized operation, 2) good match, 3) high isolation, 4) low cross-polarization level, and 5) a nearly constant beamwidth.

Specifically, there are several kinds of feed for radio telescopes, such as a horn antenna, a phased array antenna, a log-periodic antenna and an eleven feed. In these feeds, the phased array has a flexible beam scanning capability, but its structure and feeding network are often complex, and the working bandwidth is usually not wide enough to cover a several octave band, such as the phased array feed used in the ASKAP [1, 2] and FAST [3, 4]. The log-periodic antenna used in ATA [5] and its deformation-eleven feed [6, 7] all have the problems of being difficult to match at low frequencies, to refrigerate and lacking structural robustness. Horn antennas are widely used as feeds for radio telescopes with the merits of a stable structure and easy regulation of electrical performance, such as the feed for the Goddard Geophysical and Astronomical Observatory (GGAO) 12-m radio telescope in the US, [8], the Parkes 64-m radio telescope in Australia [9] and the Effelsberg 100-m radio telescope in Germany [10, 11].

The 110-m Qi Tai Telescope (QTT), which is under construction in northwest China. It covers the 150 MHz

Submitted On: June 28, 2019
Accepted On: February 23, 2020

to 110 GHz observation band, and will soon become the largest fully steerable radio telescope in the world. The most difficult design of its feed group is the one covering the 0.6-4 GHz band, and needs to illuminates the main reflector with a diameter of 110 meters and a focal diameter ratio of 0.33 to receive the pulsar signal [8]. Combined with the previous discussion, the horn antenna is chosen as the feed for this band.

Typically, the horn antenna can be divided into the single-mode smooth-walled horn, the hybrid mode horn, the ridged horn or the lens horn. The single-mode smooth-walled horn has the simplest and most reliable structure [12]. However, due to the single-mode limitation, it has a relatively narrow working bandwidth of approximately 20% with inconsistent E and H planes in the radiation pattern. To solve the latter problem, the hybrid-mode horn antenna is presented, which can excite a certain proportion of the TM_{11} mode for a conical horn or the TE_{12}/TM_{12} mode for a pyramid horn to compensate for the asymmetry of the dominant mode on the pattern. The hybrid horn can be divided into smooth-walled multisection [13], corrugated [14], dielectric-loaded [15] and metasurface-loaded [16] types. However, the hybrid-mode technology can only broaden the working bandwidth to approximately 2.2 octaves, which is far from the required 6.7 octaves. In addition, the inconsistent beamwidths of the horn antenna in the high and the low frequencies are not instrumental in the high efficiency illumination of the reflector. A lens horn antenn modifies the field distribution on the antenna aperture by loading the dielectric [17] or metasurface [18] to enhance the gain of the main radiation direction. Although the lens loading technology does not help broaden the working bandwidth of the horn antenna, it is a good solution for solving the beamwidth inconsistency problem for high and low frequencies.

Through the capacitive loading of the ridge, the cutoff frequency of the dominant mode for a ridged horn is lowered, and then the working band is expanded. To meet the requirements of a dual-polarized operation, a quad-ridged horn antenna should be adopted. However, the traditional quad-ridged horn antenna suffers from the efficiency decreasing at high frequencies due to the inherent narrowing of the beamwidths [8]. To solve this problem, dielectric loading technology is applied to the design of a quad-ridged horn antenna. However, the gain can only be enhanced across the whole band when a ball-like [19] or cone-like [20] lens is loaded onto the aperture, without narrowing the beamwidth difference between high and low frequencies. By loading a three-layered spear-like dielectric, a nearly constant-beam feed with a 12 dB beamwidth of approximately 100 degrees in 6 octaves is realized [9]. Since the illumination angle of the QTT's main reflector needs to reach approximately 150 degrees, obviously, none of the above feeds meet the requirement. A single-layered cylindrical dielectric is loaded to achieve a 150-degree illumination of a 100-m reflector [21]. However, the feed is failed to generate sufficient hybrid-mode of HE_{11} to reduce the beamwidth difference between E and H planes of the radiation patterns.

In this paper, a quad-ridged horn antenna based on dielectric loading is proposed, covering the 0.6 GHz to 4GHz band. By applying differential feeding, the special ridge and dielectric loading technology, the feed can realize the characteristics of a nearly constant beamwidth, a low cross-polarization level and a high isolation in nearly 7 octaves. To match the QTT's 110-m reflector, the horn antenna's 12 dB beamwidth reaches nearly 150 degrees in most in-band frequencies. The corresponding phase of the electric field in the angular domain is maintained within ±20 degrees. To verify the design, a prototype is fabricated and measured, and the results are compared with the simulations.

The remainder of the paper is arranged as follows. Section II mainly describes the structure and design procedure of the antenna. In Section III, a prototype is fabricated and measured to verify the proposed design. The in-dish performance of the antenna combined with the reflector is determined in Section IV. Finally, a brief summary is given in Section V.

II. ANTENNA DESIGN

This section mainly describes the structure introduction, the beam control mechanism and the design process of the proposed antenna.

A. Structure introduction

The horn antenna, including the differential feeding structure, the loaded dielectrics and the quad-ridged flare part, is shown in Fig. 1 and is explained below.

The differential feeding structure consists of four differential feeding coaxial cables and the coaxial cable to the quad-ridged waveguide transition, which can suppress the higher order modes, especially the pattern deterioration mode of TE_{21L} [22]. In addition, compared with the traditional criss-crossed side feeding structure, the bottom differential feeding technology provides a fully asymmetry, which brings the working characteristics of the antenna's two polarizations closer.

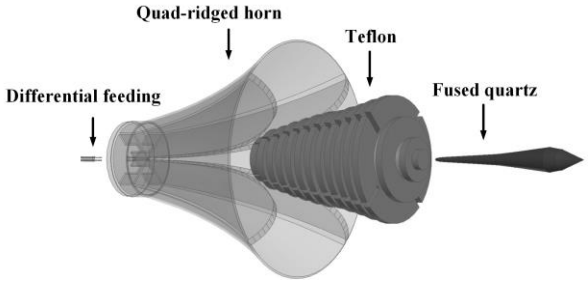

Fig. 1. The structural sketch of the horn antenna.

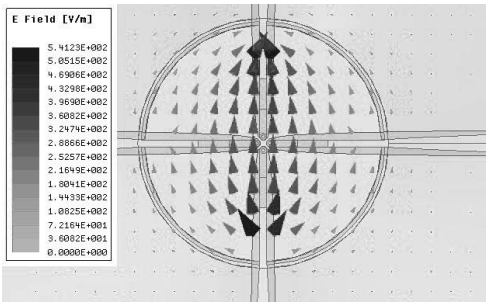

Fig. 2. The sectional electric field distribution of the horn antenna excited by differential feeding.

As for the cross-polarization, due to the fully axisymmetric structure, the electric field vectors orthogonal components excited on each side of the stimulated double ridge pair are equal in magnitude but opposite in phase, shown in Fig. 2. When the out-of-phase components of the two groups are closer in magnitude, the superposition and cancellation of the components formed in the far-field will be more thorough [23]. As a result, the symmetry of the structure can ensure the high cross polarization discrimination of the feed at the same time.

The dielectric part is composed of Teflon and fused quartz. The fused quartz has a spear-like shape with a dielectric constant of 3.82, which is outlined by multiple lines. The Teflon has a dielectric constant of 2.1 and consists of two parts: the inner part is solid except the hollow space reserved for the fused quartz; the outer part is cut with grooves to realize a lower equivalent permittivity. To mount on the quad-ridged horn, the parts of the Teflon is cut out the space for the four ridges. These dielectrics are set along the central axis of the quad-ridged horn, whose bottoms are located at the beginning of the taper section of the horn.

The outline of the special ridge of the quad-ridged horn is formed by several straight lines, two exponential lines and one arc. The detailed design of these parts will be discussed in part C.

B. Beam control mechanism

If the reflector feed has a constant beamwidth characteristic within the working bandwidth, it will help to improve the efficiency of the reflector antenna. To achieve the characteristics above, we can adopt the following ideas for a dielectric-loaded quad-ridged horn antenna.

As for medium and low frequencies, the radiation pattern is mainly determined by the structural parameters. Of all the parameters describing the quad-ridge horn geometry, the ridges and sidewall play the most critical roles in determining the performance of the horn [8].

For high frequencies, the field distribution is mainly concentrated between the two corresponding ridges when a polarization is stimulated. Considering that the dielectric rod antenna can control the radiation pattern by adjusting the dielectric shape [24], the dielectric rod can also be used to broaden the high frequencies' beamwidth when the dielectric constant of each layer changes in the gradient form. The composite antenna working in high frequencies can be seen as a dielectric rod antenna excited by the quad-ridged waveguide. At the same time, it has the quad-ridged flare around the rod to regulate and suppress the fields of some high-order modes. From another perspective, it can also be understood as a quad-ridged horn antenna that regulates the aperture field distribution by dielectric loading. As a result, the narrowing problem of the radiation pattern at high frequencies can be effectively solved by dielectric loading.

The beamwidth characteristic of the feed should match the f/D ratio of the reflector. For traditional conical or pyramidal feed horns, the commonly adopted illumination level of the feed is -10 dBi. However, for modern high-efficiency hybrid-mode feed horns, the feed factor of G/T will reach a maximum when illumination level of the feed is approximately -16 dB [25]. Since the distance between the feed and each point of the reflector is not the same, there exists spatial diffusion attenuation between the center and the edge of the reflector. Therefore, to form the best illumination, the spatial diffusion attenuation needs to be considered. For instance, for a reflector with an f/D ratio of 0.33, the best illumination angle is approximately ±74 degrees, and the spatial diffusion attenuation at the edge is approximately 3.8 dB [26]. As a result, the illumination level of the designed feed should be -12.2 dBi. Two illumination cases for the traditional and designed feeds are shown in Fig. 3.

C. Design process

First, we aim to design a quad-ridged horn antenna without dielectric loading. We divide the design into two parts: the transition from coaxial cables to a quad-ridged waveguide and the quad-ridged horn.

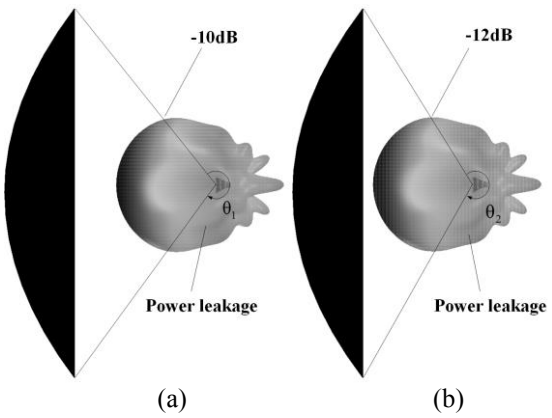

Fig. 3. The schematic diagrams of illumination level comparison for the feed: (a) the case for traditional feed, and (b) the case for designed feed.

The antenna is differentially fed by four coaxial connectors in the bottom, with each pair stimulating a polarization. Since the start frequency of our design is 0.6 GHz, the cutoff frequency of the quad-ridged waveguide should be 0.48 GHz to guarantee an allowance of 25%. According to the normalized cutoff wavenumbers of the circular quad-ridged waveguide [27], the ratio of the ridge spacing to the circular waveguide diameter should be as small as possible to obtain the widest bandwidth. When the ratio is close to 0, the cutoff frequency can be reduced to approximately one half of the circular hollow waveguide. Therefore, the diameter of the quad-ridged waveguide should be designed as the cutoff wavelength of the circular hollow waveguide at 0.96 GHz. The simplified equation for the cutoff frequency of the TE_{11} mode in a hollow circular waveguide can be expressed as follows [28],

$$f_c = \frac{c}{4\pi}\frac{p'_{11}}{a}, \tag{1}$$

where c is the speed of light in free space, a is the diameter of the circular waveguide and p'_{11} is the first zero of the derivative of the first-order Bessel function.

From (1), we can get that the cutoff wavelength of the TE_{11} mode at 0.96 GHz is approximately 183.2 mm. Therefore, the theoretical diameter of the quad-ridged waveguide should be larger than 91.6 mm. All four ridges are chamfered to achieve a smaller ridge spacing. A concave structure at the bottom of the ridge is adopted to adjust the broadband matching characteristics from the coaxial cable to the quad-ridged waveguide [9].

The detailed structural parameters of the transition are shown in Fig. 4. With the help of the full-wave simulation software ANSYS HFSS 15, the transition is optimized to work in the 0.6 GHz to 4 GHz band, as shown in Fig. 5.

The far-field characteristics are mainly determined by the quad-ridged horn. For the target performance of a 12 dB beamwidth of 150 degrees, the maximum gain of the antenna at medium frequencies should be controlled to approximately 9 dBi. As mentioned in part B, we analyze different ridges and sidewalls, with the diagram of controlling parameters of the four ridges depicted in Fig. 6. The inner special ridge curve is composed of an exponential line and a tangent arc, where the exponential part can be expressed as follows:

$$y_{inner} = \frac{d}{2}e^{\ln\left(\frac{a_2-2b_1h_2}{d}\right)\cdot\frac{z}{h_2}} + b_1 z, \tag{2}$$

where d is the spacing of the ridged waveguide, a_2 is the aperture diameter of the horn, h_2 is the height controlling parameter of the exponential curve, and b_1 is the linear part controlling parameter of the exponential curve.

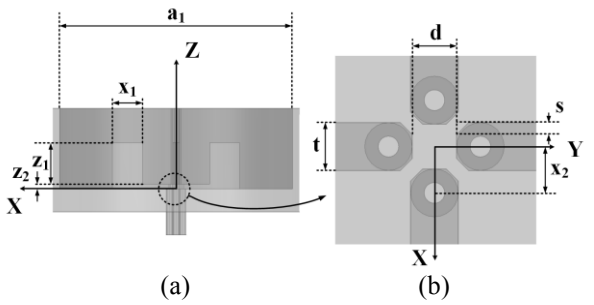

Fig. 4. Structural parameters of the transition. The optimized parameters are (unit: mm): a_1=52.5, x_1=13.1, x_2=1.5, z_1=17.9, z_2=2.1, d=2.8, t=3, s=0.75: (a) side view, and (b) top view of the dotted part.

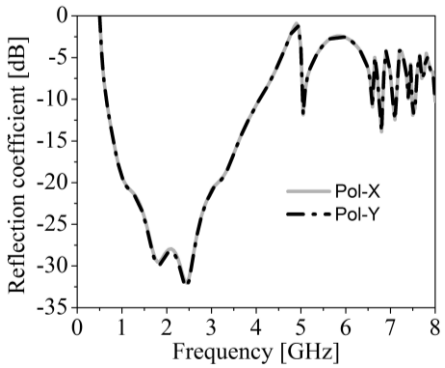

Fig. 5. The reflection coefficients for two polarizations of the transition.

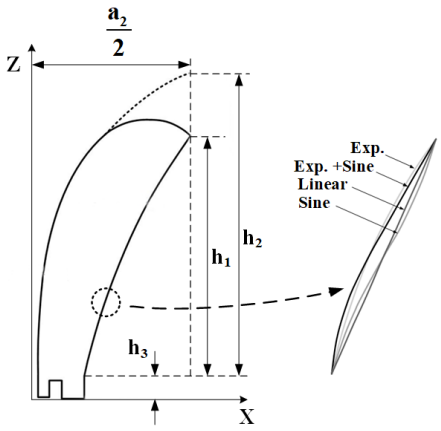

Fig. 6. Profile sketch of the ridge and the side wall.

The curve of side wall can be expressed as follows:

$$y_{outer} = \frac{a_1}{2}e^{\ln\left(\frac{a_2-2b_2h_1}{a_1}\right)\cdot\frac{z}{h_1}} + b_2 z, \tag{3}$$

where a is the diameter of the quad-ridged waveguide, h_1 is the height controlling parameter of the exponential curve, and b_2 is the linear part controlling parameter of the exponential curve.

Different from a traditional exponential ridge, the special ridge has a more compact size and a lighter weight. This structure can also improve the high frequency pattern deterioration problem to some extent [29].

By controlling the parametrics b_1 and h_2, we can adjust the distance variation speed of each pair of ridges when d and a_2 are fixed. As is known, the ridge and sidewall mainly affect the beamwidth in the middle-frequency band (1 GHz to 1.7 GHz), while the beamwidth in the high-frequency band (1.7 GHz to 4 GHz) can be controlled by the dielectrics mentioned below [9]. Therefore, we aim to determine a set of parameters that can guarantee a good in-band reflection and make the antenna's gain close to 9 dBi in the middle-frequency band. Since the ridge curve has been discussed in reference [8], here, we compare the linear, exponential, sinusoids and exponential combined sinusoids types. Some contrast simulations are given in Fig. 7, such as comparisons of different b_1, h_2 and sidewall types.

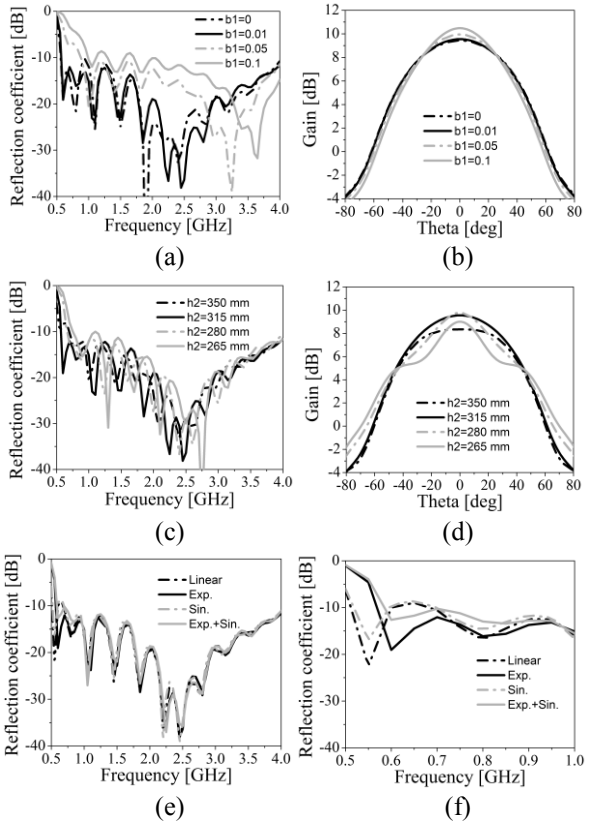

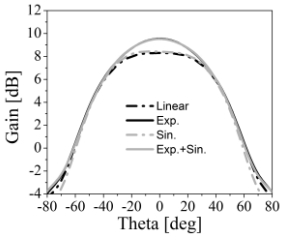

(g)

Fig. 7. Contrast simulations of the ridges and sidewall: (a) reflection coefficient with different b_1,.(b) radiation pattern at 1.5GHz with different b_1 when X-pol. is stimulated, (c) reflection coefficient with different h_2, (d) radiation pattern at 1.5 GHz with different h_2 when X-pol. is stimulated, (e) reflection coefficient with different side wall type, (f) detailed reflection coefficient with different sidewall types, and (g) radiation pattern at 1.5 GHz with different sidewall type when X-pol. is stimulated.

From Fig. 7 we can see that by selecting reasonable parameters, the performance of the reflection and far-field characteristics can satisfy the requirements.

As a result, b_1=0.01, h_2=335mm and an exponential curve with a linear part of b_2=0.01 for the sidewall are chosen to achieve good in-band matching and close to 9 dBi gain characteristics.

The quad-ridged horn is depicted in Fig. 8, and its electrical characteristics are shown in Fig. 9. The antenna working from 0.6 GHz to 4 GHz has a good reflection performance less than -10 dB, a polarization isolation larger than 60 dB and a cross-polarization level less than -40 dB. However, from Figs. 9. (e) and (f) we can determine that the beamwidths at low and high frequencies are quite different, and the latter are too narrow, which do not match with the main reflector of the QTT.

Fig. 8. Modelling of the quad-ridged horn.

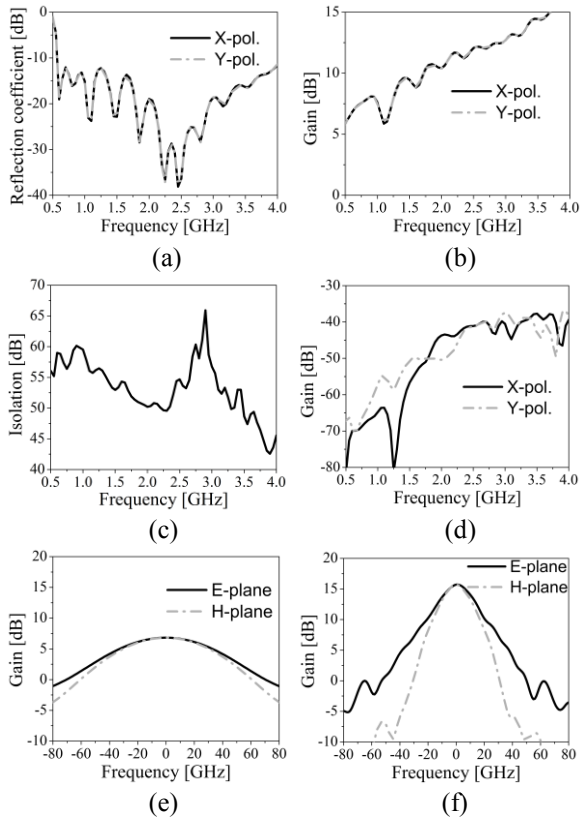

Fig. 9. Simulation of the quad-ridged horn: (a) reflection coefficient, (b) gain in the Z-axis direction, (c) isolation of two polarizations, (d) cross-polarization level in the Z-axis direction, (e) radiation pattern at 0.6GHz when X-pol. is stimulated, and (f) radiation pattern at 4GHz when X-pol. is stimulated.

As mentioned in part B, here, we conduct some work about the dielectric loading. First, we study the case of single-layered dielectric loading, as depicted in Fig. 10. The dielectric adopts a fused quartz with a dielectric constant of 3.82, which is composed of two cones.

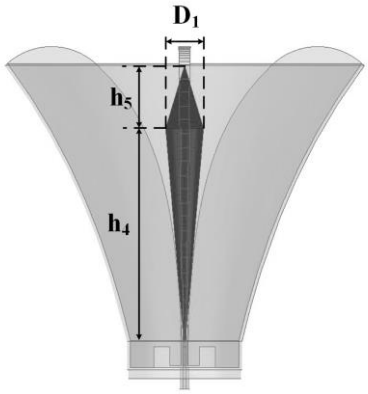

Fig. 10. The sectional view of the single-layered case.

Through the parameter study of the single-layered dielectric, we can see that the shape change of the dielectric can affect the radiation characteristics, as shown in Fig. 11. However, the load of single-layered dielectric is not sufficient to cover all the high frequencies.

Then, the second layer of dielectric is added, which applies the PTFE with a dielectric constant of 2.1, as depicted in Fig. 12. Similar to the above, we study the shape parameters of the second layer when the parameters of the inner dielectric are set as: D_1=36 mm, h_4=200 mm and h_5=60 mm. From the comparison results in Fig. 13, we pick out a group of parameters that has a relative stable gain across the band. The specific parameters are as follows: D_2=30 mm, D_3=130 mm, h_6=220 mm and h_7=52 mm.

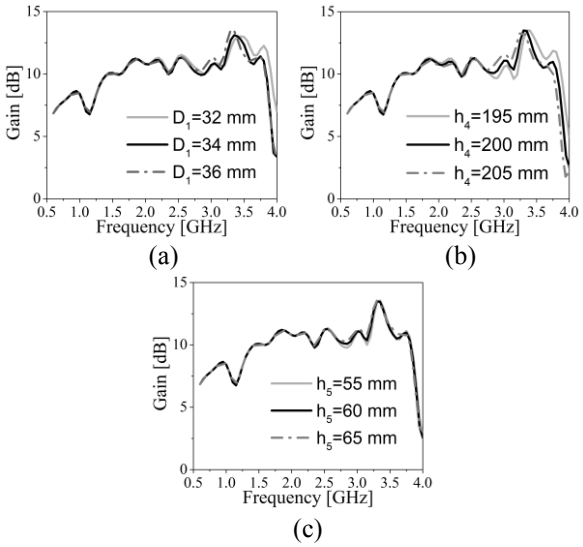

Fig. 11. Gain variation curves in main radiation direction: (a) study of D_1 when h_4=200 mm and h_5=60 mm are fixed, (b) study of h_4 when D_1=36 mm and h_5=60 mm are fixed, and (c) study of h_5 when D_1=36 mm and h_4=200 mm are fixed.

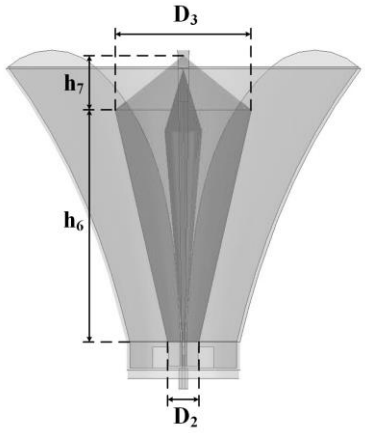

Fig. 12. The sectional view of the double-layered case.

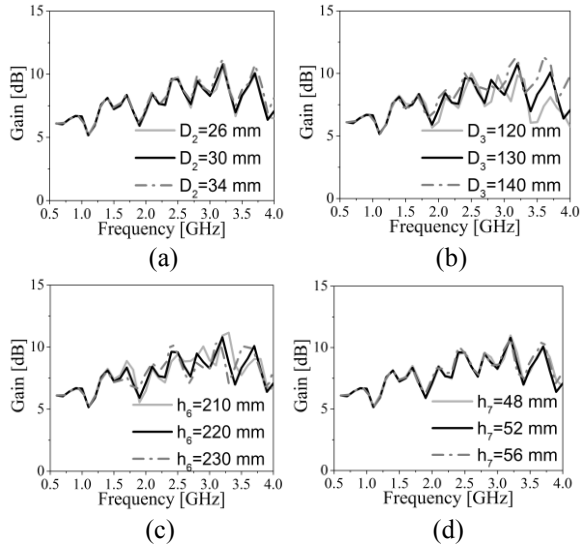

Fig. 13. Gain variation curves in main radiation direction: (a) D_3=130 mm, h_6=220 mm and h_7=52 mm are fixed, (b) D_2=30 mm, h_6=220 mm and h_7=52 mm are fixed, (c) D_2=30 mm, D_3=130 mm and h_7=52 mm are fixed, and (d) D_2=30 mm, D_3=130 mm and h_6=220 mm are fixed.

However, in the form of double-layered dielectric loading, the gain in the main radiation direction cannot be adjusted to 9 dBi for most high frequencies. Therefore, based on this double-layered design, the third layer is added to optimize the radiation characteristics. To achieve a lower equivalent dielectric constant, the dielectric of the PTFE cut with grooves is adopted. With the help of ANSYS HFSS 15, the final dielectric design is optimized, as shown in Fig. 14. The performance of the dielectric-loaded horn antenna will be presented in the next section.

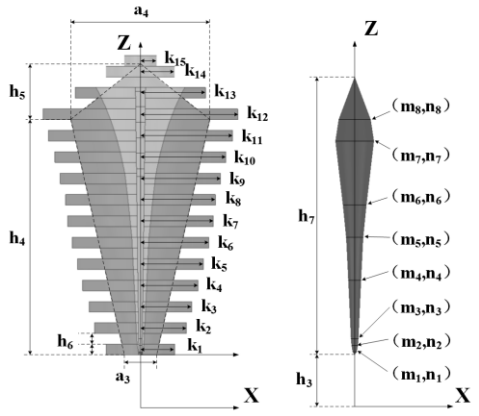

Fig. 14. The sectional view of the optimized dielectrics. The optimized parameters are (unit: mm): h_3=25, h_4=220, h_5=52, h_6=10, h_7=260, a_3=30, a_4=130, k_1=32, k_2=43, k_3=48, k_4=54, k_5=59, k_6=64, k_7=68, k_8=70, k_9=75, k_{10}=80, k_{11}=86, k_{12}=91, k_{13}=61, k_{14}=32, k_{15}=15, m_1=2, n_1=28, m_2=3, n_2=34, m_3=3.5, n_3=40, m_4=6, n_4=95, m_5=8, n_5=135, m_6=11, n_6=165, m_7=18, n_7=225, m_8=15, n_8=245.

To further analyze the effect of dielectric loading, the electric field distributions in the diagonal plane of the antenna before and after loading the dielectrics are given in Fig. 15. It can be seen from the comparison that the electric field distributions of the latter are more identical. To confirm this, the antenna aperture electric field distributions of the latter are depicted in Fig. 16.

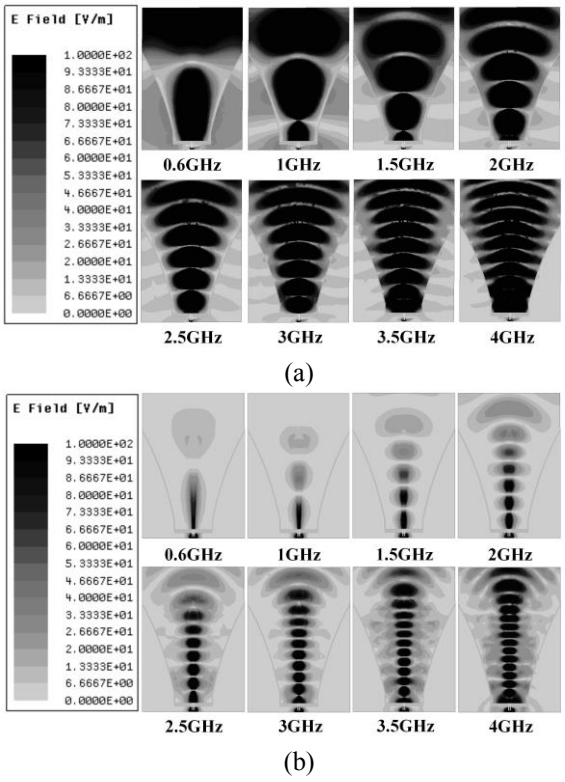

Fig. 15. Electric field distributions of the antenna in the diagonal plane: (a) quad-ridged horn without dielectric loading, and (b) quad-ridged horn with dielectric loading.

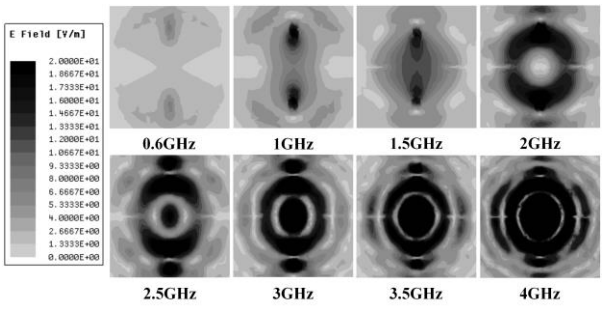

Fig. 16. Aperture electric field distributions of the antenna.

To verify the simulation, a prototype is fabricated. The reflection coefficient and the radiation pattern characteristics are measured and compared with the simulation.

III. MODELING AND EXPERIMENTAL RESULTS

The electrical characteristics of the proposed dielectric-loaded quad-ridged horn antenna are analyzed by using ANSYS HFSS 15. A prototype of the feed antenna is manufactured and tested, as shown in Fig. 17. The metal parts including the ridges, the flared horn and the back cavity are fabricated with CNC milling technology. For the dielectrics, the cylinders are first made by casting molding technology, and then CNC milling technology is utilized to obtain the designed shape. To facilitate the test, we use a transmission line balun to differentially feed the antenna.

The simulated and measured results are demonstrated in Fig. 18. The proposed antenna possesses a reflection coefficient of less than -8 dB across the working band of 0.6 GHz to 4 GHz, and less than -10 dB for most frequencies, as shown in Fig. 18 (a). The isolation is larger than 40 dB, and its cross-polarization discrimination is larger than 31 dB for both polarizations, as shown in Fig. 18 (b) and Fig. 18 (c). From (c), we can also see that the gains in medium and high frequency ranges are highly suppressed to approximately 9 dBi. Due to the symmetry structure and differential feeding technology, the isolation and cross-polarization level are both very low.

From (d), the 12 dB beamwidth of E and H plane are close to each other at most frequencies, with an average difference of 33 degrees. To verify the simulated beamwidths of the feed, figure (f) to (h) give the radiation pattern comparisons of 0.6 GHz, 2.5 GHz and 4 GHz. From the results, we can see that the simulations are in good agreement with the measurements.

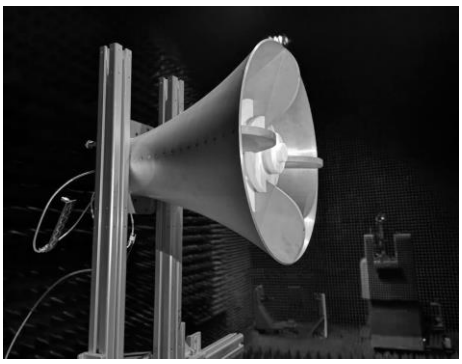

Fig. 17 The antenna under testing in a microwave anechoic chamber.

As seen with the beamwidth, the phase consistency of the wavefront is a very important parameter for the reflector feed. The simulated equal phase angle (defined as the angular range of the phase fluctuation being less than ±20 degrees) of the radiated electric field is depicted in Fig. 18 (e), when the observation point is located on the Z axis and 250 mm above the antenna bottom. The simulated distance from the antenna bottom to the phase center is also depicted in (e), which shows it to be stable to 240±20 mm across the 1.7-4.2 GHz band.

The differences between the simulations and measurements are mainly caused by the reflection and phase imbalance brought from the balun, machine errors and test errors. For example, we find that when the balun is connected with a long transmission line, some resonances will be produced, which will affect the reflection and phase characteristics.

To further verify the performance of the feed in the reflector system, the in-dish simulation of the reflector antenna is carried out in the next section.

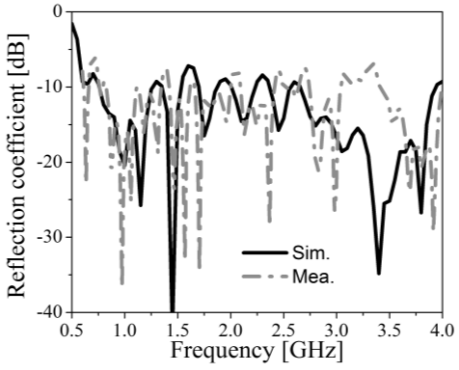

(a)

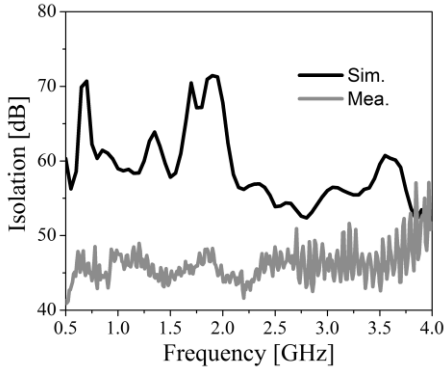

(b)

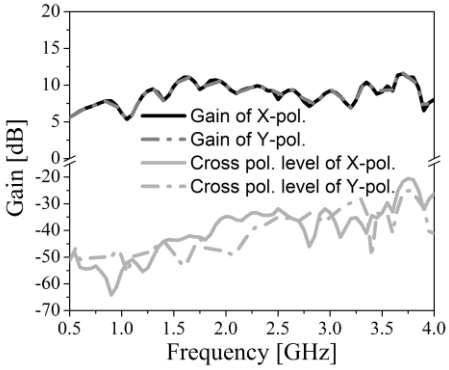

(c)

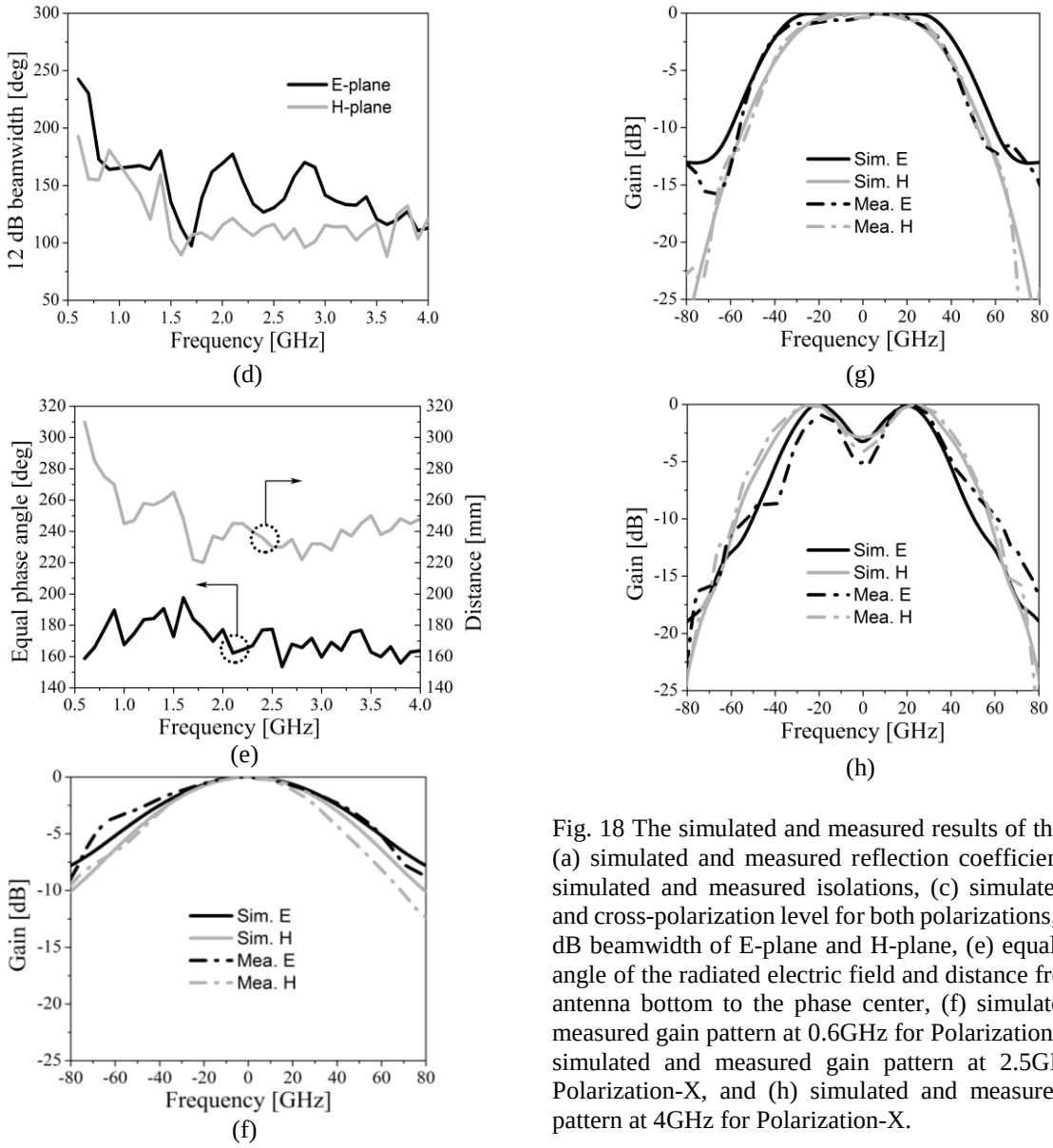

Fig. 18 The simulated and measured results of the feed: (a) simulated and measured reflection coefficients, (b) simulated and measured isolations, (c) simulated gain and cross-polarization level for both polarizations, (d) 12 dB beamwidth of E-plane and H-plane, (e) equal phase angle of the radiated electric field and distance from the antenna bottom to the phase center, (f) simulated and measured gain pattern at 0.6GHz for Polarization-X, (g) simulated and measured gain pattern at 2.5GHz for Polarization-X, and (h) simulated and measured gain pattern at 4GHz for Polarization-X.

Table 1: The comparison between other dielectric loaded quad-ridged horn antennas

Ref.	Reflection/ dB	Band/ GHz	Isolation/ dB	XPD/ dB	f/D of Matched Reflector	Avg. Aperture Efficiency	Avg. Diff. between E and H Plane/deg
[9]	<-15	0.7-4.2	>45	>28	0.41	65%	N/A
[19]	<-7	5-15	>45	>28	N/A	N/A	N/A
[21]	<-7	1.5-15.5	>40	>15	0.3	50%	~51
This work	<-8	0.6-4	>40	>31	0.33	55%	33

XPD: cross-polarization discrimination; f/D: focal diameter ratio; Avg.: average; Diff.: difference

IV. IN-DISH SIMULATION WITH REFLECTOR

The feedforward mode is adopted for the feed to illuminate the main reflector of the QTT in the 0.6 GHz to 4 GHz band. With the help of the HFSS-IE function, we can analyze the in-dish performance of the feed. However, due to the limitation of computational resource, here we can only calculate the performance of the feed on a scaled 33-m parabolic reflector with the same focal diameter ratio of 0.33. In this simulation, the

phase center of the feed, which is 250 mm above the antenna bottom, is put at the focus of the 33-m reflector. The main radiation direction of the antenna is aligned with the center point of the reflector, as illustrated in Fig. 19. Then, we can determine the efficiency of the reflector antenna by processing the theoretical gain and simulated gain. The aperture efficiency of the reflector antenna is shown in Fig. 20, and the theoretical gain can be expressed as the following formula:

$$Gain = 10\log(\frac{4\pi A\eta}{\lambda^2}),$$

where A represents the aperture area of the antenna, λ denotes the working wavelength, η represents the efficiency and η=1 when calculating the theoretical gain.

From the results, we can see that the efficiency of the antenna can be maintained at 46%-67% in the working frequency band. An average efficiency of 55.16% can make the reflector antenna work normally.

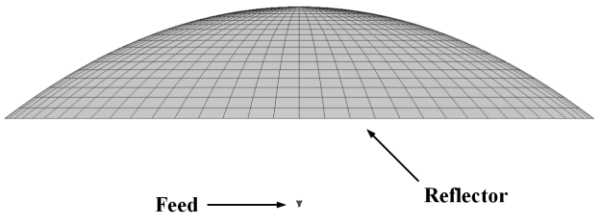

Fig. 19 Diagram of the reflector antenna.

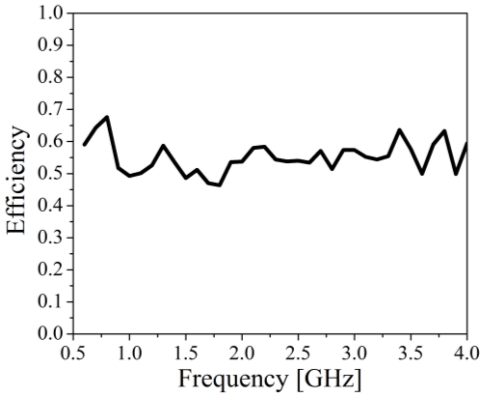

Fig. 20 The efficiency of the reflector antenna.

V. CONCLUSION

A dielectric-loaded quad-ridged horn antenna was proposed for operation in the 0.6 GHz to 4 GHz. The design procedure of the quad-ridged horn antenna and loaded dielectrics were presented to realize a nearly constant beamwidth characteristic in middle and high frequencies. Then, to verify the performance, the feed was fabricated and measured. The simulations and measurements were in good agreement. In the end, the in-dish simulation of the feed was performed to verify the efficiency of reflector antenna. The results showed that the antenna can be a feed candidate of the QTT's main reflector for the pulsar observation band.

ACKNOWLEDGMENT

This work was supported by National Basic Research Program of China-973 program 2015CB857100.

REFERENCES

[1] D. R. DeBoer, *et al.*, "Australian SKA pathfinder: A high-dynamic range wide-field of view survey telescope," *Proceedings of the IEEE*, vol. 97, no. 8, pp. 1507-1521, July 2009.

[2] A. Chippendale, *et al.*, "Phased array feed testing for astronomy with ASKAP," *2010 IEEE International Symposium on Phased Array Systems and Technology*, Waltham, MA, USA, pp. 648-652, Oct. 2010.

[3] D. Li and Z. C. Pan, "The five-hundred-meter aperture spherical radio telescope project," *Radio Science*, vol. 51, no. 7, pp. 1060-1064, Dec. 2016.

[4] Y. Wu, K. F. Warnick, and C. J. Jin, "Design study of an L-band phased array feed for wide-field surveys and vibration compensation on FAST," *IEEE Transactions on Antennas and Propagation*, vol. 61, no. 6, pp. 3026-3033, Mar. 2013.

[5] D. R. DeBoer and D. C. J. Bock, "The Allen telescope array: Splitting the aperture," *IEEE Microwave Magazine*, vol. 5, no. 2, pp. 46-53, June 2004.

[6] J. Yang, *et al.*, "Cryogenic 2–13 GHz eleven feed for reflector antennas in future wideband radio telescopes," *IEEE Transactions on Antennas and Propagation*, vol. 59, no. 6, pp. 1918-1934, Mar. 2011.

[7] J. Yang, *et al.*, "A compact dual-polarized 4-port eleven feed with high sensitivity for reflectors over 0.35–1.05 GHz," *IEEE Transactions on Antennas and Propagation*, vol. 63, no. 12, pp. 5955-5960, Oct. 2015.

[8] A. Akgiray, *et al.*, "Circular quadruple-ridged flared horn achieving near-constant beamwidth over multioctave bandwidth design and measurements," *IEEE Transactions on Antennas and Propagation*, vol. 61, no. 3, pp. 1099-1108, Mar. 2013.

[9] A. Dunning, *et al.*, "An ultra-wideband dielectrically loaded quad-ridged feed horn for radio astronomy," *2015 IEEE-APS Topical Conference on Antennas and Propagation in Wireless Communications (APWC)*, Turin, Italy, pp. 787-790, Oct. 2015.

[10] W. HeB and B. Liesenkotter, "A dual mode horn feed for deep space telemetry reception by the Effelsberg radio telescope," *1973 3rd European Microwave Conference*, Brussels, Belgium, Sept. 1973.

[11] J. Flygare, M. Pantaleev, and S. Olvhammar, "BRAND: Ultra-wideband feed development for

the European VLBI network — A dielectrically loaded decade bandwidth quad-ridge flared horn," *12th European Conference on Antennas and Propagation (EuCAP 2018)*, London, UK, Apr. 2018.

[12] K. T. Selvan, *et al.*, "Accurate design method for pyramidal horns of any desired gain and aperture phase error," *IEEE Antennas and Wireless Propagation Letters*, vol. 7, pp. 31-32, Feb. 2008.

[13] D. A. Monto, *et al.*, "High-performance smooth-walled horn antennas for THz frequency range: Design and evaluation," *IEEE Transactions on Terahertz Science and Technology*, vol. 9, no. 6, pp. 587-597, Sept. 2019.

[14] S. S. Roy, *et al.*, "Design of a compact multielement monopulse feed for ground-station satellite tracking applications," *IEEE Antennas and Wireless Propagation Letters*, vol. 18, no. 9, pp. 1721-1725, July 2019.

[15] S. Zhang, D. Cadman, and J. Y. C. Vardaxoglou, "Additively manufactured profiled conical horn antenna with dielectric loading," *IEEE Antennas and Wireless Propagation Letters*, vol. 17, no. 11, pp. 2128-2132, Sept. 2018.

[16] Q. Wu, *et al.*, "A Ku-band dual polarization hybrid-mode horn antenna enabled by printed-circuit-board metasurfaces," *IEEE Transactions on Antennas and Propagation*, vol. 61, no. 3, pp. 1089-1098, Nov. 2012.

[17] G. B. Wu, *et al.*, "High-gain circularly polarized lens antenna for terahertz applications," *IEEE Antennas and Wireless Propagation Letters*, vol. 18, no. 5, pp. 921-925, Mar. 2019.

[18] K. T. Liu, Y. H. Ge, and C. X. Lin, "A compact wideband high-gain metasurface-lens-corrected conical horn antenna," *IEEE Antennas and Wireless Propagation Letters*, vol. 18, no. 3, pp. 457-461, Jan. 2019.

[19] Y. Li, Z. Y. Zhang, and G. Fu, "A design of quad-ridged horn antenna with dielectric loading," *2014 XXXIth URSI General Assembly and Scientific Symposium (URSI GASS)*, Beijing, China, Oct. 2014.

[20] R. J. Bauerle, *et al.*, "The use of a dielectric lens to improve the efficiency of a dual-polarized quad-ridge horn from 5 to 15 GHz," *IEEE Transactions on Antennas and Propagation*, vol. 57, no. 6, pp. 1822-1825, June 2009.

[21] J. Flygare and M. Pantaleev, "Dielectrically loaded quad-ridge flared horn for beamwidth control over decade bandwidth—optimization, manufacture, and measurement," *IEEE Transactions on Antennas and Propagation*, vol. 68, no. 1, pp. 207-216, Sept. 2019.

[22] T. S. Beukman, *et al.*, "A quadraxial feed for ultra-wide bandwidth quadruple-ridged flared horn antennas," *The 8th European Conference on Antennas and Propagation (EuCAP 2014)*, The Hague, Netherland, pp. 3312-3316, Sept. 2014.

[23] Q. Xue, S. W. Liao, and J. H. Xu, "A differentially-driven dual-polarized magneto-electric dipole antenna," *IEEE Transactions on Antennas and Propagation*, vol. 61, no. 1, pp. 425-430, Jan. 2013.

[24] C. W. Liu and C. C. Chen, "A UWB three-layer dielectric rod antenna with constant gain, pattern and phase center," *IEEE Transactions on Antennas and Propagation*, vol. 60, no. 10, pp. 4500-4508, Oct. 2012.

[25] G. L. James and B. MacA. Thomas, "Comparison of G/T between dual-reflector and primary-focus antennas," *Electronics Letters*, vol. 16, no. 8, pp. 286-288, Apr. 1980.

[26] J. L. Volakis, *Antenna Engineering Handbook*, 4nd ed., McGraw-Hill, New York, 2007.

[27] W. M. Sun and C. A. Balanis, "Analysis and design of quadruple-ridged waveguides," *IEEE Transactions on Antennas and Propagation*, vol. 42, no. 12, pp. 2201-2207, Dec. 1994.

[28] N. Marcuvitz, *Waveguide Handbook*, ser. MIT Radiation Laboratory. Lexington, MA: Boston Technical, 1964.

[29] B. Jacobs, J. W. Odendaal, and J. Joubert, "An improved design for a 1–18 GHz double-ridged guide horn antenna," *IEEE Transactions on Antennas and Propagation*, vol. 60, no. 9, pp. 4110-4118, July 2012.

Yaqing Yu was born in Zhejiang Province, China, in October 1990. He received the B.S. degree in Electromagnetic Field and Wireless Technology from Xidian University, Xi'an, China, in 2009. He is currently studying for a doctor's degree in Electromagnetic Field and Microwave Technology from Xidian University. His research interests include wideband antennas, wide beam antennas and antenna feeding structures.

Wen Jiang was born in Shandong Province, China, in November 1985. He received the B.S. and Ph.D. degrees from Xidian University, Xi'an, China, in 2008 and 2012, respectively. He is the Vice Director of the National Key Laboratory of Science and Technology on

Antennas and Microwaves, Xidian University, where he is currently an Associate Professor. His current research interests include electromagnetic scattering and stealth technology, antenna theory and engineering, and electromagnetic measurement theory and technology.

Lv Qin was born in Guangxi Province, China, in 1979. He received his bachelor's degree in Computer Communications from the College of Electronic Information, Sichuan University. He is currently a Senior Engineer at the 39th Research Institute of China Electronics Technology Group Corporation. He has presided over or participated in many 863 and 973 National Key R&D projects about the design of feed systems, such as high-power measurement radar, TT&C antenna and radio telescope antenna. His current research interests include the design of horn antenna, feed antenna and core components of the feed.

Shuxi Gong was born in Hebei Province, China, in March 1957. He received the B.S. and M.S. degrees from Xidian University, Xi'an, China, in 1982 and 1984, respectively, and the Ph.D. degree from Xi'an Jiaotong University, Xi'an, in 1988. He was the Director of the National Key Laboratory of Science and Technology on Antennas and Microwaves, Xidian University, where he is currently a Full Professor. He has authored or coauthored over 200 refereed journal papers. He has also authored Principles of Generalized Eigenfunction Expansions in Electromagnetic Theory (Xi'an: Xidian Univ. Press, 2010), Prediction and Reduction of Antenna Radar Cross Section (Xi'an: Xidian Univ. Press, 2010), and Antennas for Mobile Communication Systems (Beijing: Electronics Industry Press, 2011). His current research interests include antenna theory and technology, prediction and control of antenna radar cross section (RCS), and RCS calculation of complex targets.

Wearable Textile Fabric Based 3D Metamaterials Absorber in X-Band

E. Delihasanlar and A. H. Yuzer

Department of Electrical-Electronics Engineering
Karabuk University, Karabuk, 78050, Turkey
edizdelihasanlar@karabuk.edu.tr, hayrettinyuzer@karabuk.edu.tr

Abstract ─ In this paper, a new wearable (flexible) textile fabric-based 3D metamaterials absorber (MMA) structure is proposed. The proposed MMA was created from three layers; weft-knitted fabric, silicone, and plain weave fabric and then, it was simulated in Computer Simulation Technology (CST). It was obtained maximum absorption power (99.66%) at 9.38 GHz, and the average absorption power of 81-95% was obtained in the frequency range of 8 to 12 GHz depending on the incident angle in the simulation. The effect of the wearable textile structure on absorption was investigated. When compared with other materials, it can be said that the proposed MMA is broadband, incident angle independent, TE and TM polarization-independent, flexible, breathable, wearable, ease of fabrication, practical, low weight, and cost advantage. With this designed the textile fabric-based MMA, it can be obtained both low reflection coefficients and low transmission coefficients at broadband X-band frequencies. This provides a good solution for the cloaking of radar systems.

Index Terms ─ 3D metamaterial, cloaking, plain weave, textile, wearable absorber, weft-knitted.

I. INTRODUCTION

Metamaterials, which is not found in nature, is an artificial material having extraordinary features. The material has negative dielectric permeability (ε) and negative magnetic permeability (μ) in the special frequency range. Metamaterials can be adapted to the desired range in the electromagnetic spectrum according to the application areas. It has a wide potential application in many areas such as electromagnetic cloaking [1-2], superlens [3-4], sensing [5], absorber [6-9], the antenna [10-17], etc. [18-20].

Metamaterial periodic resonator shapes are on the order of a wavelength of incident electromagnetic waves. When the EM wave arrives at the metamaterial structure, the periodic resonator will generate a surface current that causes electrical resonance. The periodic resonator layer and the conductive layer will generate reverse current to the surface current. This will cause magnetic resonance. If the electrical and magnetic resonance are obtained at the same bandwidth, the perfect absorber is obtained [21-22]. The transmission and reflection coefficients depend on the MMA. If the intrinsic impedance of the medium and MMA are matched, the incident wave will not be reflected and will be absorbed perfectly as dielectric losses. Typically, MMA is fabricated on rigid [21, 23] and flexible [6] materials depending on the application. Recent studies have been focused on flexible MMA that can be easily integrated application. Many materials have been used to get flexible MMA designs, for example polydimethysiloxane [24], polymer [25-26], polymide [27-31], silicone [32], polypropylene [33], composite [34], and textile [3, 35-39]. The advantage of the textile, compared to other materials is flexibility, breathability, wearable, ease of fabrication, practicability, low weight and cost. In the literature, there are many works on textile-based MMA applications. In these works, periodic shapes were made by using sticking techniques on textiles. It was created by using the screen-printing [22], inkjet printing [24, 40], lithographic processes [25], and stamping [26] techniques. It is not found an application at which 3D textile geometry was used for designing textile-based MMA.

In this study, a 3D textile fabric-based MMA was designated for the X-band frequency range (8-12 GHz) in the CST simulation. The MMA consists of the periodic resonator shapes, a conductive layer, and a dielectric substrate. The weft-knitted fabric and plain weave fabric was used as periodic resonator shapes and the conductive layer, respectively. The 3D periodic resonator shapes were obtained by forming copper in the half-loop of weft-knitted fabric. Details of the usage of plain weave fabric structure as a conductive layer are given in the [41]. The flexible 1.6 mm thick silicone dielectric layer was used to combine the periodic resonator shapes with the conductive layer to improve the absorption performance. The simulation measurements were performed in the range of 8-12 GHz (X-Band), where many communication systems operate. The incident angle and the polarization effect were investigated. 99.66% of the highest absorption was observed at TM polarization with 0° incident angle at

Submitted On: October 14, 2019
Accepted On: January 2, 2020

9.38 GHz. The average absorption power of MMA is swinging between 81% to 95% depending on the incident angle. Moreover, the effect of the wearable textile structure on absorption was investigated by using the scaling method in the CST simulation program. The major difference of the designed material from the previously published studies is that it is not only the 3D wearable textile structure but also it provides high absorption in wideband and is independent of incident angle and polarization [35-39]. Designed MMA can be used in commercial, communication and military defense application.

The outline of this study is as follows. It was introduced the theory, preparation, and simulation of textile-based MMA in Section II. Next, the incident angle effect, the polarization effect, the scaling effect on the absorption power of the designed MMA were given in Section III. Finally, it was described how to use MMA of results and was drawn future works in Section IV.

II. MATERIALS AND METHODS

Materials complex permittivity and complex permeability properties depend on the frequency. When a perfect absorbent is wanted to design, the imaginary parts of dielectric materials are also very important because they add extra dielectric loss. If the intrinsic impedance of the medium and materials impedance can be matched, incident electromagnetic waves will not be reflected. Many researchers have been working intensively on impedance matching and dielectric loss with MMA.

MMA structures consist of three layers, which are periodic resonator shapes, a conductive layer, and a dielectric substrate. The periodic resonator shape resonates with the incident electromagnetic waves as its size is smaller than the wavelength of the incident electromagnetic waves. The periodic resonator shape and conductive layer were adapted to the textile structure to form the MMA structure. To create 3D periodic resonator shapes, a weft-knitted fabric structure having a wide range of the loop was used. Since the loop of plain weave fabric is very smaller than the measured wavelength, it behaves like a conductive surface. The silicone material was used to form a flexible structure. It keeps the two fabrics fixed and create a high dielectric loss.

The absorption power of materials can be calculated from the reflection coefficient and the transmission coefficients of the medium. Total reflection coefficients and transmission coefficients can be explained by using the multiple reflections theory [42]. The first interface medium reflects part of the incident electromagnetic wave and transmits the other part of the incident electromagnetic waves. The end interface reflects and transmits a portion of the waves transmitted from the first interface. This event continues until the wave disappears in the lossy medium. Illustration and mathematical representation of this phenomenon are given in Fig. 1. The total reflections coefficient, S_{11}, is written as a function of frequency as given in (1):

$$\Gamma_1(\omega) = \rho_1 + \sum_{n=1}^{\infty} \tau_1 \tau_1' (\rho_1')^{n-1} \rho_2^n e^{-j\omega nT},$$
$$R(\omega) = \Gamma_1(\omega)^2 = |S_{11}|^2, \quad (1)$$

where $R(\omega)$ represents the reflection coefficient.

The total transmission coefficients, S_{21}, are written as a function as given in (2):

$$T(\omega) = \sum_{n=1}^{\infty} \tau_1 \tau_2 (\rho_1')^n \rho_2^n e^{-j\omega nT} e^{-j\omega T/2},$$
$$T(\omega) = |S_{21}|^2 . \quad (2)$$

The absorption power of materials is calculated by using the equation given in (3):

$$A(\omega) = 1 - T(\omega) - R(\omega) = 1 - |S_{11}|^2 - |S_{21}|^2. \quad (3)$$

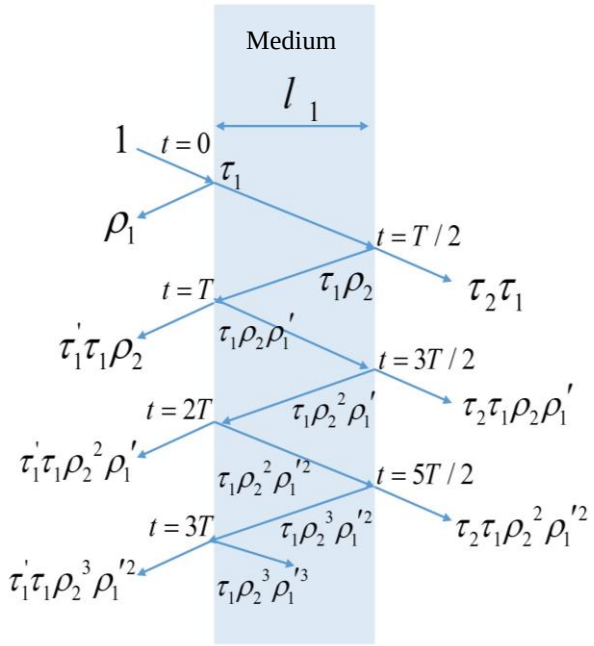

Fig. 1. Multiple reflections theory.

A. Material properties of the knitted and woven fabrics

Weft-knitted fabric is one of the basic knitting fabric structures. Wales and course density construct its horizontal pattern and vertical pattern, respectively [43].

Plain weave fabric has the simplest structure among woven fabrics. It consists of the weft and warp yarns woven together that are knitted one after another. When the cotton yarn is taken from the conductive yarn that forms the fabric, the only metal mesh will leave. Hence, the physical structure of the composite plain weave fabric is similar to metal mesh. Many analytical solutions have been derived from this type of structure [44]. The weft-knitted and plain weave fabrics properties are given in Table 1.

Table 1: Fabric properties

	Copper Content (%)	Yarn (nm)	Knitting Density		Weaving Density	
			Wales (1/10 cm)	Courses (Loops/ cm)	Warp (Tread/ cm)	Weft (Tread/ cm)
Weft-Knitted	5.5	7.06	50	3	-	-
Plain Weave	11	7.06	-	-	10	10

B. Metamaterials based textile design

The weft-knitted and the plain weave fabric structures are designed by using computer-aided design software (AutoCAD). The designed half-loop periodic copper structure was applied to the drawn geometry of weft-knitted fabric. Then it was included in the entire loop structure. The plain weave fabric structure was created as full copper. In the designs, the yarn thickness was as 50 µm and the dielectric constant of the textile yarn was neglected. The designed textile fabrics were imported into the CST program for simulation.

The designed 3D half-loop periodic copper weft-knitted structure is shown in Fig. 2. The designed copper plain weave fabric structure is presented in Fig. 3. Silicone was used as the dielectric substrate. The thickness of the material was 1.6 mm. The silicone material properties in the CST program were given in Table 2.

Table 2: Silicone properties

Epsilon (ε)	11.9
Mue (µ)	1
Electrical Conductivity	0.00025 S/m
Material Density (Rho)	2330 Kg/m3
Thermal Conductivity	148 W/K/m
Heat Capacity	0.7 kj/K/kg

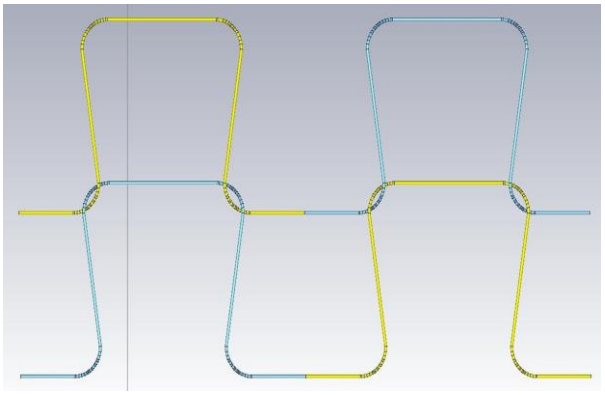

Fig. 2. Weft-knitted fabric with half loop copper structure.

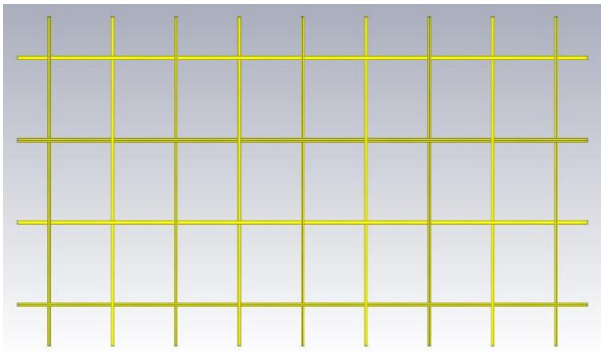

Fig. 3. The copper plain weave fabric structure.

One-unit 3D half-loop periodic copper weft-knitted fabric structure dimensions were given in Fig. 4 (a). The 3D side view was given in Fig. 4 (b). One-unit copper plain weave fabric structure dimensions were given in Fig. 4 (c). The 3D side view was given in Fig. 4 (d).

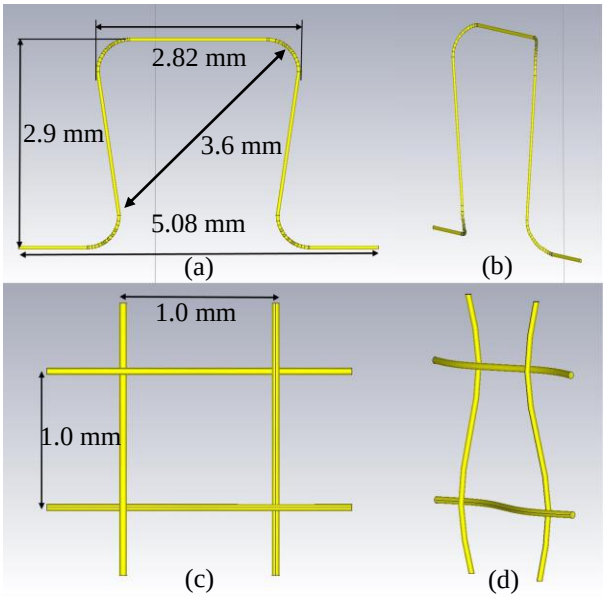

Fig. 4. (a) One-unit half-loop copper weft-knitted fabric dimension, (b) one-unit half-loop copper weft-knitted fabric side view, (c) one-unit copper plain weave fabric structure dimension, and (d) one-unit copper plain weave fabric side view.

C. Simulation setup

The MMA was formed by combining weft-knitted fabric, silicone and plain weave fabric. It is given in Fig. 5. Front view of the weft-knitted fabric (a), side view of the weft-knitted fabric (b), rear view of the plain weave fabric(c), and side view of the plain weave fabric (d). The total thickness of the textile-based MMA is 2.23 mm. The weft-knitted fabric, silicone, and plain woven

fabric thicknesses are 0.38 mm, 1.6 mm, and 0.25 mm, respectively.

The 2-port waveguide measurement system was created in the CST simulation program to investigate the absorption power of MMA at 8-12 GHz frequency range. A full mesh cell MMA is simulated in the CST program by using the finite-difference time-domain (FDTD) method. The full mesh cell MMA size was defined as 10×10 cm. The defined physical properties of the surrounding space were selected as "normal". Boundary conditions were selected according to the polarization mode (TE, TM). The waveguide simulation setup is shown in Fig. 6. The MMA was rotated on the axis by the specified angle to investigate the incidence angle dependence.

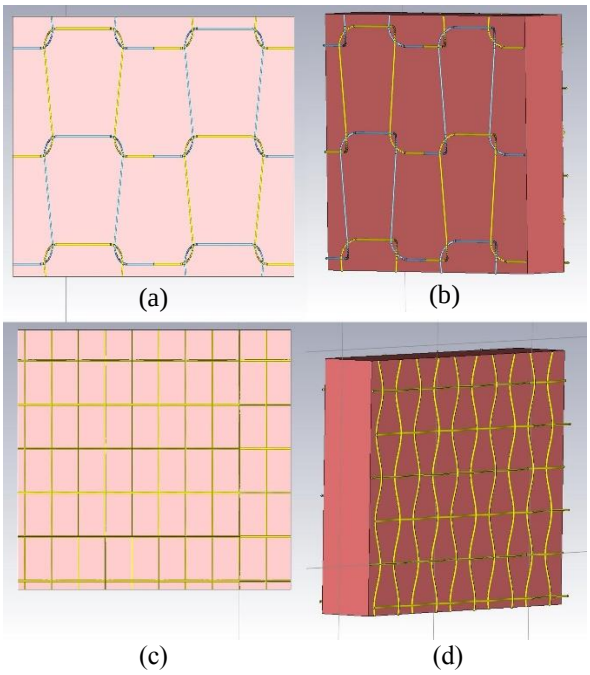

Fig. 5. (a) Front view of the weft-knitted fabric, (b) side view of the weft-knitted fabric, (c) rear view of the plain weave fabric, and (d) side view of the plain weave fabric.

III. RESULTS AND DISCUSSION

The absorption power of materials was calculated by using S parameters. Polarizations (TM and TE) and incident angles (-20° to 20°) effects on absorption are investigated in the measurements. Besides, the absorption power of MMA was investigated by forming an MMA structure with a just dielectric substrate (silicone) without copper to reveal the MMA structure effect. The effect of silicone on the absorption power of MMA without copper is also given in Fig. 7 and Fig. 8.

Figure 7 shows the result of the absorption power of MMA at TM polarization within the 8-12 GHz frequency range and gives the effect of incident angles on absorption. The maximum and average absorption power of MMA are also given on the same figure.

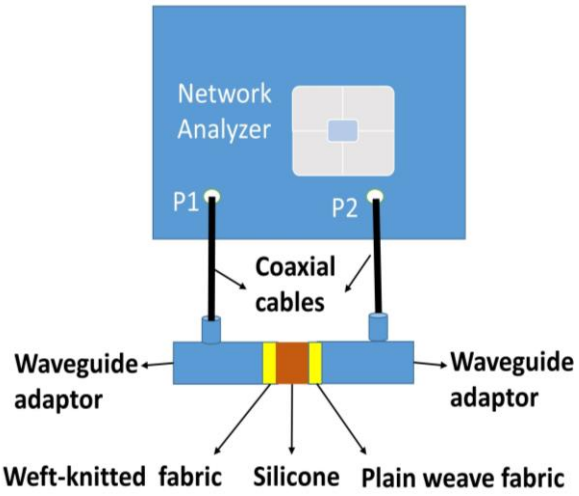

Fig. 6. Waveguide simulation setup.

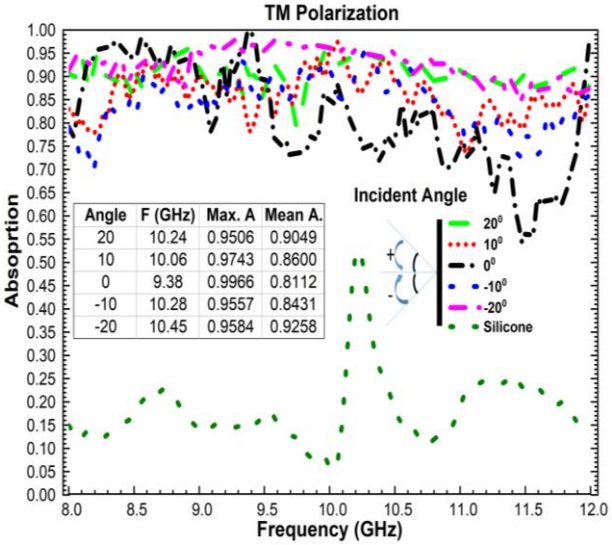

Fig. 7. Absorption power at TM polarization.

Figure 8 shows the result of the absorption power of MMA at TE polarization within the 8-12 GHz frequency range and gives the effect of incident angles on absorption. The maximum and average absorption power of MMA are also given on the same figure.

Ideally, a perfect absorber should have very low transmission coefficients and a reflection coefficient. The maximum absorption power (99.66%) was obtained at TM polarization with 0° incident angle at 9.38 GHz. As the angle increases, the cross-sectional area of the periodic shape becomes smaller. This causes the maximum absorption power of MMA occurred at a higher frequency. The average absorption power of

MMA is swinging between 81% to 95% depending on the incident angle. The designed MMA achieved high absorption power in wideband. It can be said that the absorption power of MMA is almost independent of incident angle and polarization.

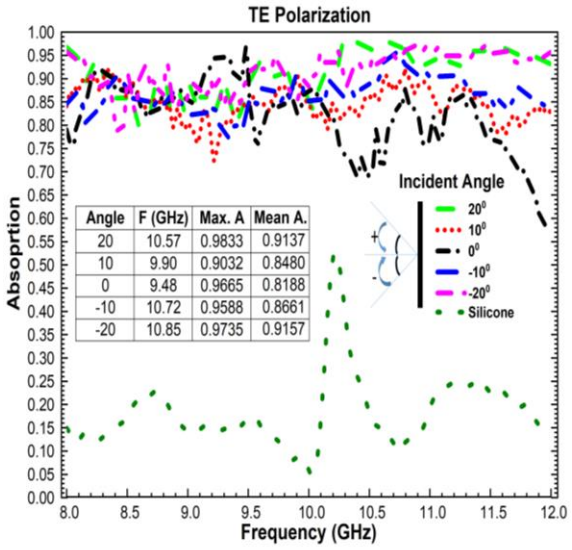

Fig. 8. Absorption power at TE polarization.

Other simulations were performed to investigate the effect of flatness, flexibility, compression, and folding of the structure in the CST program. In these situations, the textile loop size is changing. Thus, the dimension of the textile structure was scaled to investigate the effect of these situations on absorption. The whole textile-based MMA structure was scaled by -10%, -5%, 0%, 5%, and 10% at TE polarization with +20˚ incident angle and simulations were performed. The maximum absorption resonance frequency is shifted, and the average amount of absorption is gradually increased. The results are given in Fig. 9.

IV. CONCLUSION

The textile-based MMA design operating at the X-band was demonstrated in the CST simulation program. The absorption power of MMA was calculated by using the transmission coefficient and the reflection coefficient. The maximum absorption power (99.66%) was obtained at TM polarization with 0˚ incident angle at 9.38 GHz. The average absorption power of MMA is swinging between 81% to 95% at 8-12 GHz frequency band depending on the incident angle. It was found that the angle of the incident and the polarization type of electromagnetic waves did not affect the absorption power of MMA. Initially, it was aimed to design the MMA absorbing at 8-12 GHz. In the incident angles simulation results, absorption was as expected at 8-11 GHz. However, the same performance could not be achieved at high frequencies (11 GHz < f < 12 GHz) for normal incidence. When the angle of incidence was increased, the cross-sectional area would be decreased, therefore better results were obtained for angular incidence. The proposed MMA was scaled to investigate the effect of wearable textile structure on absorption, too. As a result of scaling, the maximum absorption frequency is shifted, and the average absorption is a bit increased. It was found that wearability did not have a remarkable effect on absorption.

The optimum production process is under process. When the best production technique is determined, MMA will be produced. The proposed MMA can be used to prevent the detection of soldiers and military equipment from radar. Also, this proposed MMA can be used as an anechoic chamber for X-band applications.

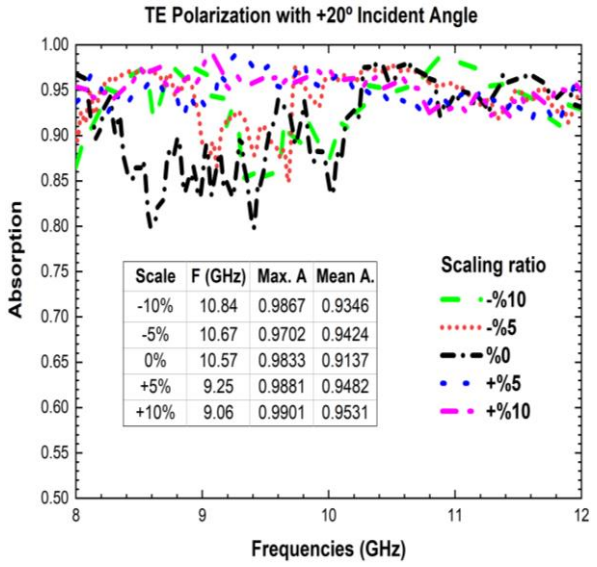

Fig. 9. The scaling effect results.

REFERENCES

[1] B. Greinke, M. Candotti, A. Alomainy, and C. Parini, "Parameters extraction of three-dimensional structures for graded textile cloaking materials," *2013 Loughbrgh. Antennas Propag. Conf. LAPC 2013*, pp. 84-87, Nov. 2013.

[2] T. Zhang, *et al.*, "Tunable plasmon induced transparency in a metallodielectric grating coupled with graphene metamaterials," *J. Light. Technol.*, vol. 35, no. 23, pp. 5142-5149, 2017.

[3] M. Esen, I. Ilhan, M. Karaaslan, E. Unal, F. Dincer, and C. Sabah, "Electromagnetic absorbance properties of a textile material coated using filtered arc-physical vapor deposition method," *J. Ind. Text.*, vol. 45, no. 2, pp. 298-309, 2015.

[4] Y. Tao, E. Yang, and G. Wang, "Left-handed metamaterial lens applicator with built-in cooling feature for superficial tumor hyperthermia," *Appl.*

Comput. Electromagn. Soc. J., vol. 32, no. 11, pp. 1029-1034, 2017.

[5] M. Bakır, M. Karaaslan, F. Karadag, S. Dalgac, E. Ünal, and O. Akgöl, "Metamaterial sensor for transformer oil, and microfluidics," *Appl. Comput. Electromagn. Soc. J.*, vol. 34, no. 5, pp. 799-806, 2019.

[6] H. Wakatsuchi, D. F. Sievenpiper, and C. Christopoulos, "Designing flexible and versatile metamaterial absorbers," *IEEE Electromagn. Compat. Mag.*, vol. 5, no. 2, pp. 76-82, 2016.

[7] X. Lu, J. Chen, Y. Huang, Z. Wu, and A. Zhang, "Design of ultra-wideband and transparent absorber based on resistive films," *Appl. Comput. Electromagn. Soc. J.*, vol. 34, no. 5, pp. 765-770, 2019.

[8] Y. Ozturk and A. E. Yilmaz, "Multiband and perfect absorber with circular fishnet metamaterial and its variations," *Appl. Comput. Electromagn. Soc. J.*, vol. 31, no. 12, pp. 1445-1451, 2016.

[9] P. Zhou, Q. Huang, L. Ji, and X. Shi, "Design of a thin broadband metamaterial absorber based on resistance frequency selective surface," *Appl. Comput. Electromagn. Soc. J.*, vol. 37, no. 10, pp. 1494-1499, 2019.

[10] S. I. Rosaline and S. Raghavan, "Metamaterial-inspired split ring monopole antenna for WLAN applications," *Appl. Comput. Electromagn. Soc. J.*, vol. 33, no. 2, pp. 188-191, 2018.

[11] K. Yu, Y. Li, and X. Liu, "Mutual coupling reduction of a MIMO antenna array using 3-D novel meta-material structures," *Appl. Comput. Electromagn. Soc. J.*, vol. 33, no. 7, pp. 758-763, 2018.

[12] M. F. Finch and B. A. Lail, "A subwavelength perfect absorbing metamaterial patch array coupled with a molecular resonance," *Appl. Comput. Electromagn. Soc. J.*, vol. 33, no. 2, pp. 196-199, 2018.

[13] M. Valayil and K. Chamberlin, "Enhancement of parameters of slotted waveguide antennas using metamaterials," *Appl. Comput. Electromagn. Soc. J.*, vol. 34, no. 2, pp. 272-279, 2019.

[14] S. Luo, Y. Li, Y. Xia, and L. Zhang, "A low mutual coupling antenna array with gain enhancement using metamaterial loading and neutralization line structure," *Appl. Comput. Electromagn. Soc. J.*, vol. 34, no. 3, pp. 411-418, 2019.

[15] S. Luo, Y. Li, Y. Xia, G. Yang, L. Sun, and L. Zhao, "Mutual coupling reduction of a dual-band antenna array using dual-frequency metamaterial structure," *Appl. Comput. Electromagn. Soc. J.*, vol. 34, no. 3, pp. 403-410, 2019.

[16] H. R. Vani, M. A. Goutham, and Paramesha, "Gain enhancement of microstrip patch antenna using metamaterial superstrate," *Appl. Comput. Electromagn. Soc. J.*, vol. 34, no. 5, pp. 823-826, 2019.

[17] A. Mersani, O. Lotfi, and J.-M. Ribero, "Design of a textile antenna with artificial magnetic conductor for wearable applications," *Microw. Opt. Technol. Lett.*, vol. 60, no. 6, pp. 1343-1349, Jun. 2018.

[18] S. Can and A. E. Yilmaz, "Radar cross section reduction of a plate with textile-based single negative metamaterial," *2016 10th Eur. Conf. Antennas Propagation, EuCAP 2016*, pp. 1-4, 2016.

[19] M. A. A. Abessolo, Y. Diallo, A. Jaoujal, A. E. Moussaoui, and N. Aknin, "Stop-band filter using a new metamaterial complementary split triangle resonators (CSTRs)," *Appl. Comput. Electromagn. Soc. J.*, vol. 28, no. 4, pp. 353-358, 2013.

[20] M. E. Jalil, N. A. Samsuri, M. K. A. Rahim, and R. Dewan, "Compact chipless RFID metamaterial based structure using textile material," *2015 International Symposium on Antennas and Propagation (ISAP)*, pp. 5-8, 2015.

[21] S. Lai, Y. Wu, X. Zhu, W. Gu, and W. Wu, "An optically transparent ultrabroadband microwave absorber," *IEEE Photonics J.*, vol. 9, no. 6, pp. 1-10, Dec. 2017.

[22] M. Ghebrebrhan, *et al.*, "Textile frequency selective surface," *IEEE Microw. Wirel. Components Lett.*, vol. 27, no. 11, pp. 989-991, 2017.

[23] Y. Zhang, J. Duan, B. Zhang, W. Zhang, and W. Wang, "A flexible metamaterial absorber with four bands and two resonators," *J. Alloys Compd.*, vol. 705, pp. 262-268, 2017.

[24] K. Ling, K. Kim, and S. Lim, "Flexible liquid metal-filled metamaterial absorber on polydimethyl-siloxane (PDMS)," *Opt. Express*, vol. 23, no. 16, pp. 21375, 2015.

[25] R. Yahiaoui, S. Tan, L. Cong, R. Singh, F. Yan, and W. Zhang, "Multispectral terahertz sensing with highly flexible ultrathin metamaterial absorber," *J. Appl. Phys.*, vol. 118, no. 8, 2015.

[26] H. K. Kim, K. Ling, K. Kim, and S. Lim, "Flexible inkjet-printed metamaterial absorber for coating a cylindrical object," *Opt. Express*, vol. 23, no. 5, pp. 5898, 2015.

[27] H.-M. Lee, "A broadband flexible metamaterial absorber based on double resonance," *Prog. Electromagn. Res. Lett.*, vol. 46, pp. 73-78, Mar. 2014.

[28] M. Nasr, *et al.*, "Narrowband metamaterial absorber for terahertz secure labeling," *J. Infrared, Millimeter, Terahertz Waves*, vol. 38, no. 9, pp. 1120-1129, 2017.

[29] X. Kong, J. Xu, J. jun Mo, and S. Liu, "Broadband and conformal metamaterial absorber," *Front. Optoelectron.*, vol. 10, no. 2, pp. 124-131, 2017.

[30] X. Yan, L.-J. Liang, X. Ding, and J.-Q. Yao, "Solid analyte and aqueous solutions sensing based on a flexible terahertz dual-band metamaterial

absorber," *Opt. Eng.*, vol. 56, no. 2, pp. 027104, 2017.
[31] J. H. Kim, *et al.*, "Investigation of robust flexible conformal THz perfect metamaterial absorber," *Appl. Phys. A Mater. Sci. Process.*, vol. 122, no. 4, pp. 1-7, 2016.
[32] Y. He, *et al.*, "Optically-controlled metamaterial absorber based on hybrid structure," *Opt. Commun.*, vol. 356, pp. 595-598, 2015.
[33] M. Michalak, R. Brazis, V. Kazakevicius, J. Bilska, and I. Krucinska, "Novel approach to textile design for barriers against electromagnetic radiation," *Int. J. Mater. Prod. Technol.*, vol. 36, no. 1/2/3/4, pp. 166, 2010.
[34] P. Pa, M. S. Mirotznik, R. McCauley, S. Yarlagadda, and K. Duncan, "Integrating meta-materials within a structural composite using additive manufacturing methods," *IEEE Antennas Propag. Soc. AP-S Int. Symp.*, pp. 0-1, 2012.
[35] S. Can, A. E. Yilmaz, and E. Karakaya, "Conformai dual-band frequency selective surface on textile: design, prototyping and expriment," *2017 Usn. Radio Sci. Meet.* (*Joint with AP-S Symp. Usn. 2017*), pp. 17-18, 2017.
[36] C. Huppé, *et al.*, "Woven metamaterials with an electromagnetic phase-advance for selective shielding," *IOP Conf. Ser. Mater. Sci. Eng.*, vol. 254, no. 3, 2017.
[37] D. Lee and S. Lim, "Wearable metamaterial absorber using screen printed chanel logo," *Int. Symp. Antennas Propag.*, pp. 928-929, 2016.
[38] J. Tak and J. Choi, "A wearable metamaterial microwave absorber," *IEEE Antennas Wirel. Propag. Lett.*, vol. 16, pp. 784-787, 2017.
[39] G. A. Cavalcante, A. G. D'Assunção, and A. G. D'Assunção, "An iterative full-wave method for designing bandstop frequency selective surfaces on textile substrates," *Microw. Opt. Technol. Lett.*, vol. 56, no. 2, pp. 383-388, Feb. 2014.
[40] H. İbili, B. Karaosmanoğlu, and Ö. Ergül, "Demonstration of negative refractive index with low-cost inkjet-printed microwave metamaterials," *Microw. Opt. Technol. Lett.*, vol. 60, no. 1, pp. 187-191, 2018.
[41] R. Abdulla, E. Delihasanlar, F. G. Kizilcay Abdulla, and A. H. Yuzer, "Electromagnetic shielding characterization of conductive knitted fabrics," *Prog. Electromagn. Res. M*, vol. 56, pp. 33-41, Jan. 2017.
[42] S. J. Orfanidis, *Electromagnetic Waves and Antennas*, Rutgers University New Brunswick, NJ, 2002.
[43] T. S. Nutting and G. A. V. Leaf, "5-A generalized geometry of weft-knitted fabrics," *J. Text. Inst. Trans.*, vol. 55, no. 1, pp. T45-T53, Jan. 1964.
[44] T. M. McBride and J. Chen, "Unit-cell geometry in plain-weave fabrics during shear deformations," *Compos. Sci. Technol.*, vol. 57, no. 3, pp. 345-351, 1997.

Ediz Delihasanlar received an Electronics and Communication Engineering degree from the Suleyman Demirel University and a Master's degree from Karabuk University, Turkey. He is a Research Assistant of Electrical-Electronics Engineering at the Karabuk University. His current research interests include meta-materials, applied electromagnetic, wave propagations, and dielectric constant.

Ahmet Hayrettin Yuzer received his B.Sc. and M.Sc. degrees in Electrical and Electronics Engineering from Inonu University, Malatya, Turkey, in 1995 and 2002, respectively and his Ph.D. degree in Electrical and Electronics Engineering in 2011 from Middle East Technical University (METU), Ankara, Turkey. He worked as a Research Assistant from 1999 to 2002 at Inonu University and from 2002 to 2011 at METU. He was at the Intelligent RF Radio Laboratory (iRadio Lab), University of Calgary, Calgary, Canada, as a visiting Ph.D. student from Sept. 2010 to Mar. 2011. Since 2011, he has been an Assistant Professor with the Department of Electrical and Electronics Engineering at Karabuk University, Karabuk, Turkey. His current scientific research includes amplifier modeling, measurement, linearization, and active and passive microwave components. Yuzer has been given a URSI 2008 Student Paper Contest award.

An Analytic Method of Determining a Critical Cable Spacing for Acceptable Crosstalk

Pei Xiao, Wan-Wei Ran, and Ping-An Du*

School of Mechanical and Electrical Engineering
University of Electronic Science and Technology of China, Chengdu 611731, China
xiaopei_uestc@sina.cn, rww4gz@163.com, dupingan@uestc.edu.cn*

Abstract ─ Some wiring rules have been used to prevent crosstalk in industrial application, but the technical rationale is not clear. This paper aims at proposing an analytic method of determining a critical cable spacing for acceptable crosstalk. First of all, we derive a calculation function of crosstalk with cable spacing. Then, we discuss about the crosstalk characteristics according to the crosstalk function and its curve. On this basis, we define the critical cable spacing via a critical point on the curve and explain physical meaning of the critical point by use of the fringe field around the victim cable. After that, we analyze the influence of wiring parameters on the critical cable spacing. Finally, we conduct an experiment to validate the proposed method of the critical cable spacing.

Index Terms ─ Critical cable spacing, critical point, crosstalk, wiring parameters.

I. INTRODUCTION

Crosstalk interference is a phenomenon affecting signals propagated in cables and has a close relationship with cable spacing. The aggressor cable may produce induced degradation or failures on the adjacent victim cable due to the coupling of fringe electric field, which may arouse overall electromagnetic compatibility problem of the whole electronic system [1-4]. Some rules have been used for guiding wiring of adjacent cables to prevent crosstalk [5-7], but the technical rationale is not clear. Thus, analytic determination of critical cable spacing is an important issue in industrial application.

Previous work mainly concentrated on the methods of evaluating crosstalk [8-10]. Numerical simulation has been widely adopted to obtain the coupled crosstalk, but it requires a reliable model of cable harness [11-13]. Compared with numerical simulation in calculating induced interference on the victim cable, analytic technique performs better computing efficiency and consumes less computation resources. As twisted pair cable is generally applied to transmit information from a piece of equipment to another, many works have been published on modeling of predicting the coupling problem on twisted cables [14-16]. For the discontinuities such as via, bends and changes in geometry of a multiconductor transmission lines (MTLs) system, some researchers apply the scalar and vector potentials associated with boundary conditions to obtain non-uniform transmission line equation and crosstalk for conductors [17-18]. Some others used the cascaded transmission line theory to deal with crosstalk calculation of conductors with bends and varying size [19-20]. Recently measurement-based modeling techniques are presented to determine the crosstalk parameters of cables [21-22], which helps to give a worst-case estimation of crosstalk.

A simple and efficient way of controlling crosstalk is to keep the cables farther apart, but the question is how far apart enough, seldom analytic work about cable spacing rules are studied so far. Hence, this paper proposed an analytic method to deal with the determination of critical cable spacing for acceptable crosstalk so that an effective way of wiring can be formed. Firstly, we derived an analytic calculation formula of crosstalk with cable spacing, which contains the determination of parasitic capacitive and inductive and solution of coupled crosstalk equations. Then, we discussed about the crosstalk characteristics according to the crosstalk function and its curve. On this basis, we defined the critical cable spacing via a critical point on the curve and explained physical meaning of the critical point by use of the fringe field around the victim cable, in addition, analyzed the influence of wiring parameters on the critical cable spacing. Finally, we conducted an experiment to validate the proposed calculation method of the critical cable spacing. This work can provide an analytic way of wiring rules.

II. DERIVATION OF THE FUNCTION OF CROSSTALK WITH CABLE SPACING

A. Derivation of crosstalk calculation

A transmission line model is often used to describe the crosstalk phenomenon between two parallel cables, as illustrated in Fig. 1, where the aggressor and victim

Submitted On: January 16, 2019
Accepted On: January 3, 2020

cables are placed over a perfectly conducting ground plane and excited by voltage sources, Z represents terminal loads on both cables, L_{ji} and C_{ji} $(j=1,2)$ are the per unit length self-inductance and self-capacitance, L_i and C_i the mutual inductance and capacitance. The crosstalk problem arises from the sum of mutual capacitive and inductive coupling noise propagating in the length direction along the victim cable.

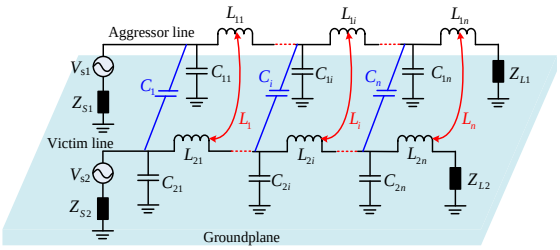

Fig. 1. Schematic for crosstalk coupling of two conductors.

The calculation formula of inductance matrix $\hat{L}$ can be written as [19]:

$$\hat{L}=\begin{bmatrix} \frac{\mu_0}{2\pi}\ln\left(\frac{2h_A}{r_A}\right) & \frac{\mu_0}{4\pi}\ln\left(1+\frac{4h_Ah_B}{S^2}\right) \\ \frac{\mu_0}{4\pi}\ln\left(1+\frac{4h_Ah_B}{S^2}\right) & \frac{\mu_0}{2\pi}\ln\left(\frac{2h_B}{r_B}\right) \end{bmatrix}, \tag{1}$$

where S is the spacing between two cables, r_A and r_B the radius of two cable, Δr_A and Δr_B the dielectric thickness, h_A and h_B the height to the ground, μ_0 the permeability for free space.

The calculation formula of capacitance matrix $\hat{C}$ can be given as [19]:

$$\hat{C}=\begin{bmatrix} a_{11} & a_{12} \\ a_{21} & a_{22} \end{bmatrix}^{-1}, \tag{2}$$

where a_{11}, a_{12}, a_{21} and a_{22} are defined by:

$$\begin{cases} a_{11}=\dfrac{1}{2\pi\varepsilon_0}\left(\dfrac{1}{\varepsilon_r}\ln\dfrac{1}{r_A}+\varepsilon_e\ln\dfrac{1}{r_A+\Delta r_A}-\ln\dfrac{1}{2h_A}\right) \\ a_{12}=a_{21}=\dfrac{1}{4\pi\varepsilon_0}\ln\left(1+\dfrac{4h_Ah_B}{S^2}\right) \\ a_{22}=\dfrac{1}{2\pi\varepsilon_0}\left(\dfrac{1}{\varepsilon_r}\ln\dfrac{1}{r_B}+\varepsilon_e\ln\dfrac{1}{r_B+\Delta r_B}-\ln\dfrac{1}{2h_B}\right) \end{cases}, \tag{3}$$

where ε_0 is the permittivity for free space, ε_r the relative dielectric constant and $\varepsilon_e=(\varepsilon_r-1)/\varepsilon_r$.

According to the multi-conductor transmission lines theory, the induced voltage and current along the cables in frequency domain can be written as:

$$\frac{\mathrm{d}^2\hat{V}(z)}{\mathrm{d}z^2}=\hat{Z}\hat{Y}\hat{V}(z), \tag{4}$$

$$\frac{\mathrm{d}^2\hat{I}(z)}{\mathrm{d}z}=\hat{Y}\hat{Z}\hat{I}(z), \tag{5}$$

where $\hat{V}(z)$ and $\hat{I}(z)$ are the voltage and current matrix, $\hat{Z}=j\omega\hat{L}$ and $\hat{Y}=j\omega\hat{C}$ the impedance and admittance matrix.

To solve the coupled (4) and (5), a decoupling approach is applied to obtain $\hat{V}(z)$ and $\hat{I}(z)$. Thus, the key problem is how to find the transformational matrix $\hat{T}_V$ and $\hat{T}_I$ which satisfy:

$$\hat{V}=\hat{T}_V\hat{V}_m, \tag{6}$$

$$\hat{I}=\hat{T}_I\hat{I}_m, \tag{7}$$

where $\hat{V}_m$ and $\hat{I}_m$ are diagonal matrix and denote mode voltage and current propagating along the cables. $\hat{T}_V$ and $\hat{T}_I$ transform the off-diagonal matrix $\hat{Z}\hat{Y}$ and $\hat{Y}\hat{Z}$ to the diagonal matrix $\hat{\gamma}$ which satisfy $\hat{T}_V^{-1}\hat{Z}\hat{Y}\hat{T}_V=\hat{T}_I^{-1}\hat{Y}\hat{Z}\hat{T}_I=\hat{\gamma}^2$.

Then, we can obtain the decoupled voltage and current equations as follows:

$$\frac{\mathrm{d}^2V_m(z)}{\mathrm{d}z^2}=\hat{\gamma}^2\hat{V}_m(z), \tag{8}$$

$$\frac{\mathrm{d}^2\hat{I}_m(z)}{\mathrm{d}z^2}=\hat{\gamma}^2\hat{I}_m(z). \tag{9}$$

Consequently, the solution of mode voltage $\hat{V}_m$ and current $\hat{I}_m$ at position z along the cables can be written as:

$$\hat{V}_m(z)=\hat{e}^{-\gamma z}\hat{V}_m^{+}+\hat{e}^{\gamma z}\hat{V}_m^{-}, \tag{10}$$

$$\hat{I}_m(z)=\hat{e}^{-\gamma z}\hat{I}_m^{+}-\hat{e}^{\gamma z}\hat{I}_m^{-}, \tag{11}$$

where $\hat{V}_m^{+}$ and $\hat{I}_m^{+}$ are the forward transmission mode voltage and current, while $\hat{V}_m^{-}$ and $\hat{I}_m^{-}$ the backward transmission mode voltage and current matrix. Transmission coefficient matrix $\hat{e}^{\pm\gamma z}$ equals to:

$$\hat{e}^{\pm\gamma z}=\begin{bmatrix} e^{\pm\gamma_1 z} & 0 \\ 0 & e^{\pm\gamma_2 z} \end{bmatrix}. \tag{12}$$

According to the calculation results of mode voltage

$\hat{V}_m$ and mode current $\hat{I}_m$, we obtain the crosstalk voltage and current:

$$\hat{I}(z) = \hat{T}_I \left(e^{-\gamma z} \hat{I}_m^+ - e^{\gamma z} \hat{I}_m^- \right), \tag{13}$$

$$\hat{V}(z) = \hat{Y}^{-1} \hat{T}_I \hat{\gamma} \left(e^{-\gamma z} \hat{I}_m^+ + e^{\gamma z} \hat{I}_m^- \right). \tag{14}$$

Assuming the conductors only contain voltage source excitation on both terminals, (13) and (14) satisfy:

$$\hat{V}(0) = \hat{V}_S - \hat{Z}_S \hat{I}(0), \tag{15}$$

$$\hat{V}(L) = \hat{V}_L + \hat{Z}_L \hat{I}(L), \tag{16}$$

where $\hat{V}(0)$ and $\hat{V}(L)$ represent the terminal voltage, $\hat{I}(0)$ and $\hat{I}(L)$ the terminal current.

Inserting (13) and (14) at z=0 into (15), we obtain:

$$\hat{Y}^{-1} \hat{T}_I \hat{\gamma} (\hat{I}_m^+ + \hat{I}_m^-) = \hat{V}_S - \hat{Z}_S \hat{T}_I (\hat{I}_m^+ - \hat{I}_m^-). \tag{17}$$

Inserting (13) and (14) at z=L into (16), we obtain:

$$\hat{Y}^{-1} \hat{T}_I \hat{\gamma} (\hat{e}^{-\gamma L} \hat{I}_m^+ + \hat{e}^{\gamma L} \hat{I}_m^-) = \hat{V}_L + \hat{Z}_L \hat{T}_I (\hat{e}^{-\gamma L} \hat{I}_m^+ - \hat{e}^{\gamma L} \hat{I}_m^-). \tag{18}$$

(17) and (18) can be written as a matrix equation:

$$\begin{bmatrix} \hat{Y}^{-1} \hat{T}_I \hat{\gamma} + \hat{Z}_S \hat{T}_I & \hat{Y}^{-1} \hat{T}_I \hat{\gamma} - \hat{Z}_S \hat{T}_I \\ \left(\hat{Y}^{-1} \hat{T}_I \hat{\gamma} - \hat{Z}_L \hat{T}_I \right) \hat{e}^{-\gamma L} & \left(\hat{Y}^{-1} \hat{T}_I \hat{\gamma} + \hat{Z}_L \hat{T}_I \right) \hat{e}^{-\gamma L} \end{bmatrix} \begin{bmatrix} \hat{I}_m^+ \\ \hat{I}_m^- \end{bmatrix} = \begin{bmatrix} \hat{V}_S \\ \hat{V}_L \end{bmatrix}. \tag{19}$$

Through this matrix equation, we can obtain $\hat{I}_m^+$ and $\hat{I}_m^-$. Substituting the calculated results of $\hat{I}_m^+$ and $\hat{I}_m^-$ into (13) and (14), we can obtain the crosstalk $\hat{I}(z)$ and $\hat{V}(z)$ along the victim cable, which is used for the derivation of critical cable spacing.

B. Definition of the function of crosstalk with cable spacing

Define matrix $\hat{M}$:

$$\hat{M} = \begin{bmatrix} \hat{Y}^{-1} \hat{T}_I \hat{\gamma} + \hat{Z}_S \hat{T}_I & \hat{Y}^{-1} \hat{T}_I \hat{\gamma} - \hat{Z}_S \hat{T}_I \\ \left(\hat{Y}^{-1} \hat{T}_I \hat{\gamma} - \hat{Z}_L \hat{T}_I \right) \hat{e}^{-\gamma L} & \left(\hat{Y}^{-1} \hat{T}_I \hat{\gamma} + \hat{Z}_L \hat{T}_I \right) \hat{e}^{-\gamma L} \end{bmatrix}^{-1} = \begin{bmatrix} \hat{A} & \hat{B} \\ \hat{C} & \hat{D} \end{bmatrix}, \tag{20}$$

where matrix A, B, C and D are all the function of cable spacing S. Letting,

$\hat{A} = f_1(S)$, $\hat{B} = f_2(S)$, $\hat{C} = f_3(S)$ and $\hat{D} = f_4(S)$, then,

$$\hat{I}_m^+ = f_1(S) \hat{V}_S + f_2(S) \hat{V}_L, \tag{21}$$

$$\hat{I}_m^- = f_3(S) \hat{V}_S + f_4(S) \hat{V}_L. \tag{22}$$

Inserting (21) and (22) into (13) and (14) respectively, the calculation formula of $\hat{I}(z,S)$ and $\hat{V}(z,S)$ at position z with cable spacing of S can be modified as:

$$\hat{I}(z,S) = \hat{T}_I \left[\hat{e}^{-\gamma z} \left(f_1(S) \hat{V}_S + f_2(S) \hat{V}_L \right) - \hat{e}^{\gamma z} \left(f_3(S) \hat{V}_S + f_4(S) \hat{V}_L \right) \right], \tag{23}$$

$$\hat{V}(z,S) = \hat{Y}^{-1} \hat{T}_I \hat{\gamma} \left[\hat{e}^{-\gamma z} \left(f_1(S) \hat{V}_S + f_2(S) \hat{V}_L \right) + \hat{e}^{\gamma z} \left(f_3(S) \hat{V}_S + f_4(S) \hat{V}_L \right) \right]. \tag{24}$$

Through (23) and (24), we can analyze the influence of cable spacing on crosstalk voltage and current.

C. Numerical validation of crosstalk calculation

To validate the addressed analytic calculation of crosstalk between adjacent cables, a two copper cables model is constructed, as illustrated in Fig. 2. The two cables have a core radius of 0.7 mm, a dielectric insulation layer thickness of 0.7 mm, a height of 10 mm to the ground, and a spacing of 25 mm. The aggressor cable is excited by a 1 V voltage over frequency (0,500MHz), and all terminal impedance are 50Ω.

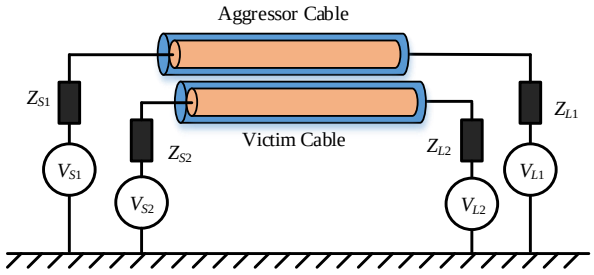

Fig. 2. Voltage source excitation on the cables' terminals.

In this paper, a full-analysis commercial software CST based on transmission line matrix (TLM) technique is utilized to provide a numerical validation. By using 2D(TL) modeling technique, the equivalent circuit of cable model is obtained and then the crosstalk is calculated by using AC combine results solver. The solid curves in Figs. 3 (a) and (b) respectively show the calculation results of induced voltage on the near and far end of the victim cable by the analytic method, while the dotted curves demonstrate the results from CST simulation.

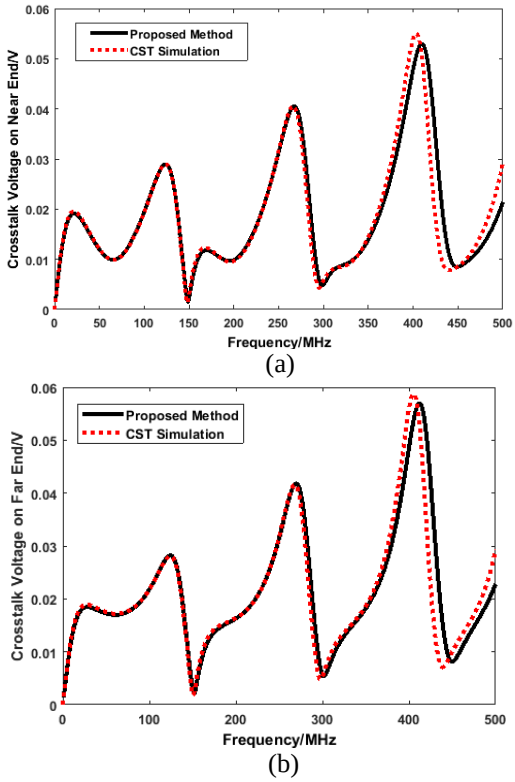

Fig. 3. Comparison results of crosstalk voltage on victim cable: (a) near end; (b) far end.

A good agreement between the analytic and simulation results establishes the validation of crosstalk calculation formula. A little difference between two curves can be seen at higher frequency, which may be caused by the error during the analytic calculation of capacitance at higher frequency due to dielectric insulation layer.

III. DISCUSSION

A. Definition of critical cable spacing

According to (24), we can draw out the curve of near crosstalk voltage $\hat{V}(z,S)$ with cable spacing S by changing S from 25 mm to 180 mm at frequency 276MHz, as illustrated in Fig. 4 (a). The curve shows that crosstalk voltage decreases with the increased S, especially decreases very sharply at the beginning but begins to flatten when S reaches a certain value which we define as the critical point. As illustrated in Fig. 4 (b), the variation of crosstalk at different frequency point is consistent with the cable spacing. So, the choice for frequency 274 MHz in our method is unintentional and the proposed method can be extended to other frequency points.

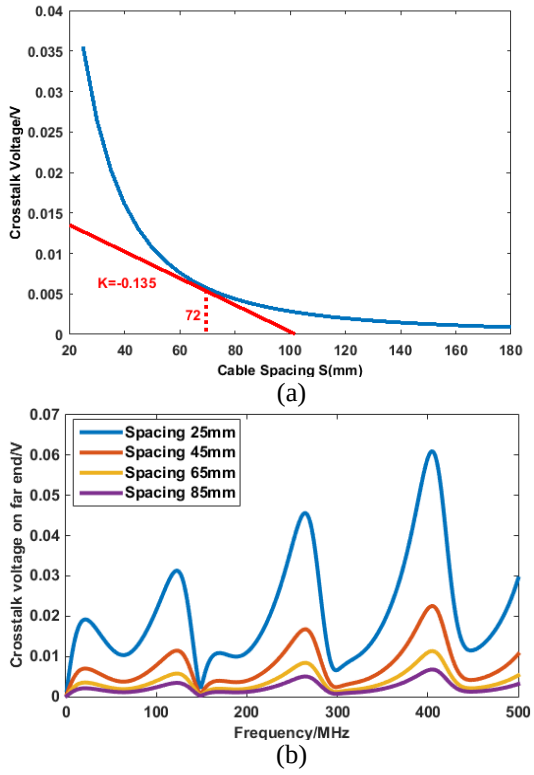

Fig. 4. Crosstalk: (a) crosstalk voltage with cable spacing from 20 mm to 180 mm; (b) crosstalk voltage at different cable spacing.

Since the derivative reflects the change rate of a function with an independent variable, taking the derivation of the crosstalk voltage function (24) to variable S, we obtain:

$$K = \frac{\mathrm{d}\left(\hat{V}(z,S)\right)}{\mathrm{d}S}. \tag{25}$$

The function K describes the change rate of crosstalk voltage with S. Here, we define S_0 at the critical point in Fig. 4 as the critical cable spacing. Therefore, S_0 satisfy that the change rate of crosstalk begins to reduce slowly enough when $S > S_0$. The determination of S_0 refer to the difference value of K between evenly spaced adjacent points. The choice of value for K is based on the trend of the slope between evenly spaced adjacent points. When the slope difference change little, we take the intermediate value to be K at the critical point. For example, a series of derivative value K at S of (25, 35, 45, 55, 65, 75, 85, 95) mm correspond to (-2.60, -1.02, -0.50, -0.29, -0.18, -0.12, -0.09, -0.06) respectively. The calculated results denote a little

difference of K starting from the range (-0.18, -0.12). Taking the intermediate value to be K at the critical point, namely K = -0.135, the corresponding S_0 = 72mm, as illustrated in Fig. 3. Thus, the analytic calculation process of S_0 can be summarized as the following steps:

a) Definition of the function of crosstalk with cable spacing;

b) Determination of the value of K at the critical point according to its derivative;

c) Calculation of S_0 by substituting K to the derivative function.

B. Physical interpretation of critical cable spacing

If ignoring the field reflection effect of victim cable, the fringe E-field generated by a dipole $I(z)$dz at position z along the aggressor cable in Cartesian coordinate can be defined by:

$$\begin{cases} dE_x = e_x\left\{-j\dfrac{I(z)dz}{4\pi\omega\varepsilon_0}\dfrac{e^{-jkr}}{r^2}\sin\theta\cos\theta\cos\varphi[3jk-rk^2+\dfrac{3}{r}]\right\} \\ dE_y = e_y\left\{-j\dfrac{I(z)dz}{4\pi\omega\varepsilon_0}\dfrac{e^{-jkr}}{r^2}\sin\theta\cos\theta\sin\varphi[3jk-rk^2+\dfrac{3}{r}]\right\} \\ dE_z = e_z\left\{j\dfrac{I(z)dz}{4\pi\omega\varepsilon_0}\dfrac{e^{-jkr}}{r^2}[(jk-rk^2+\dfrac{1}{r})\sin^2\theta-(2jk+\dfrac{2}{r})\cos^2\theta]\right\} \end{cases}, \quad (26)$$

where $k=\omega\sqrt{\mu_0\varepsilon_0}$ is propagation constant, ω angular frequency, r radiation distance, θ and φ the radiation angles of the fringe fields.

Then, the E-field generated by the aggressor cable can be obtained by adding up the sum of the contribution from each dipole to the field components, that is:

$$E = e_x\int_0^l dE_x + e_y\int_0^l dE_y + e_z\int_0^l dE_z \,. \quad (27)$$

Figure 5 gives the mechanism of E-field coupling to conductor. The victim conductor is illuminated by a uniform plane-wave field characterized by strength of electric field vector E and arbitrary incidence (θ, ψ) and polarization η angles, as shown in the following figure. The coupling crosstalk V_{cp} can be written as [23]:

$$V_{cp} = 2Eh\left\{F\frac{\gamma_0 e^{-\hat{\gamma}_0 L}-\gamma_0\cosh(\gamma_0 L)+\hat{\gamma}_0\sinh(\gamma_0 L)}{\gamma_0\sinh(\gamma_0 L)}-G\right\}, \quad (28)$$

where

$$F=\frac{\cos\theta(\cos\psi\cos\theta\cos\eta+\sin\psi\sin\eta)}{1-\sin^2\theta\cos^2\psi}, \quad (29)$$

$$G=\sin\theta\cos\eta\,, \quad (30)$$

$$\hat{\gamma}_0=\gamma_0\sin\theta\cos\psi\,. \quad (31)$$

From (27)-(31), we can know that the induced crosstalk is related to the incident E-field. For crosstalk problem between two conductors, the fringe coupling E-field is generated by the aggressor cable. Therefore, we can explain the influence of cable spacing on the fringe fields around the victim cable. The detailed interpretation can be founded in the reference [23].

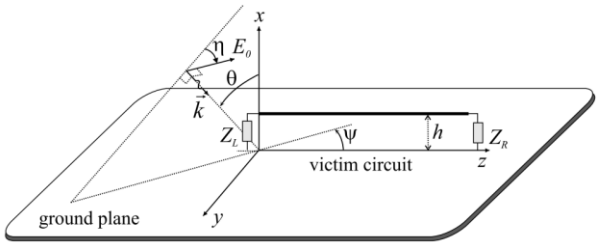

Fig. 5. Principle drawing of the victim circuit illuminated by a uniform plane-wave EM field: definition of wave angles [23].

Figure 6 shows the relationship between E-field and radiation distance r from 25 mm to 180 mm at frequency 420MHz. From Fig. 6, we can see that the radiated E-field reduces quickly at the beginning of the curve, then begins to flatten when spacing reaches a value. This change rule is consistent with that of crosstalk. As crosstalk voltage is induced by the fringe E-fields, Fig. 5 gives a reasonable interpretation of determination of the critical cable spacing.

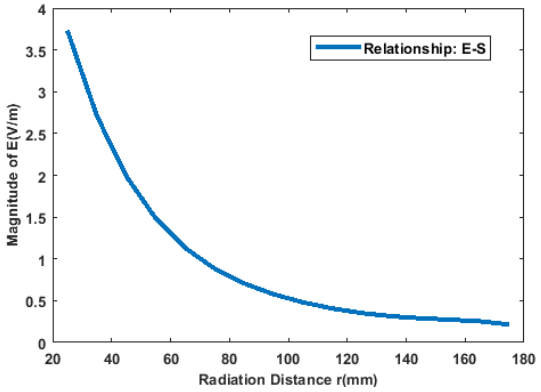

Fig. 6. Relationship between radiation distance r and E-field radiated from the aggressor cable.

From the crosstalk curve in Fig. 4 and E-field curve in Fig. 6, we can see that the basic trend of the two curves is the same. However, it should be noted that the change rate of E-field with distance is not strictly the same as that of crosstalk, especially at low frequencies. This may be caused by the magnetic field.

C. Influence of wiring parameters on critical cable spacing

According to the derivation of crosstalk calculation, the critical cable spacing is related to wiring parameters. Figure 7 (a) and Fig. 7 (b) show the influence of cable

length and height to the ground on critical cable spacing, which are calculated at the resonance frequency 276MHz. The two figures indicate obviously that the longer of the cable or the higher to the ground, the greater the critical cable spacing. This phenomenon can be explained by the coupled fringe E-field, that is, the longer of the cable and the higher to the ground, the more fringe E-field coupled and the greater voltage induced.

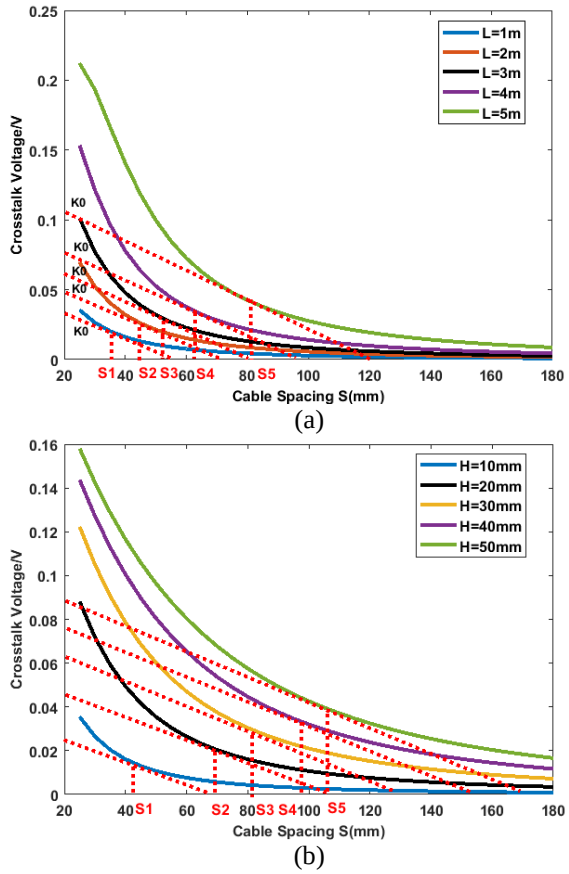

Fig. 7. Influence of wiring parameters on critical cable spacing: (a) cable length; (b) cable height to the ground.

IV. EXPERIMENTAL VALIDATION OF CRITICAL CABLE SPACING

To validate the analytic calculation of the critical cable spacing, we test the crosstalk of two cables based on S_{21} parameter measurement in a well-controlled test setup. Define the incident voltage U_0 and reflected voltage U_1, equals to:

$$S_{21} = \frac{U_1}{U_0}. \tag{32}$$

Therefore, we can measure the S_{21} of a two cables system to obtain the crosstalk on the victim cable by injecting a voltage U_0 into the aggressor cable.

The diagram of the measurement system is shown in Fig. 8, where a Keysight FieldFox Analyzers N9913A (it can be used as Vector Network Analyzer and Spectrum Analyzer and its test frequency band ranges from 30 kHz to 4 GHz) is adopted to measure S_{21} on the near end of the victim wire, and the tested cable has a core radius of 0.7 mm, a dielectric insulation layer of 0.7 mm and 300 mm long and 10 mm high above a ground reference which is a finite metallic plane with a length of 1m and width of 0.5 m. Two cables are connected to the analyzer through SMA connectors. The impedance of matching resistor at each terminal of the cable is 50 Ω .

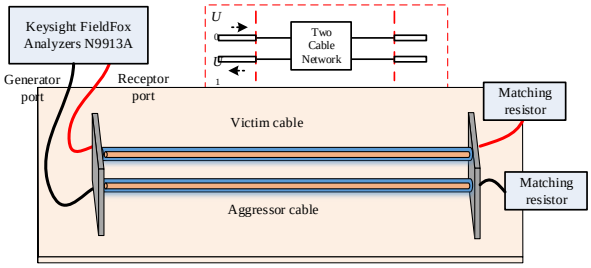

Fig 8. Principle diagram of S_{21} parameter test.

The experimental test picture is illustrated in Fig. 9. Measurements were performed over (30KHz, 200MHz) by moving the aggressor cable from 25mm to 145mm with a distance interval of 20mm and recording S_{21} of each step.

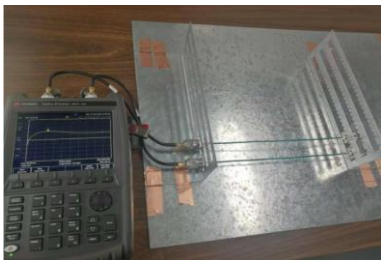

Fig. 9. Experimental test picture of S_{21}.

Figure 10 (a) gives the measurement results of S_{21} at different cable spacing. Figure 10 (b) is the fitted curve of S_{21} with cable spacing at the first resonance frequency 35 MHz, which demonstrates the relationship between S_{21} and cable spacing. Figure 10 denotes that the greater the cable spacing, the slower the change rate of S_{21}. The fitted function of the relationship between S_{21} and cable spacing are written as:

$$F = \alpha S^b + \beta, \tag{33}$$

where the coefficient α = 86.12, β = -44.93, b = -0.3746.

By taking the derivative of F to S and making the derived function be the critical derivative K_0, we can obtain the corresponding critical cable spacing S_0. For

example, inserting K_0 = -0.135 into the derivative of F, the calculation result of critical cable spacing S_0 is 54 mm. A little difference of the S_0 exists between measurement and analytic results at K_0 = -0.135, which is caused by the experimental cable model due to the inevitable bending in the wiring process. But the trend of the measurement curve in Fig. 10 establishes the validation of proposed calculation method of critical cable spacing.

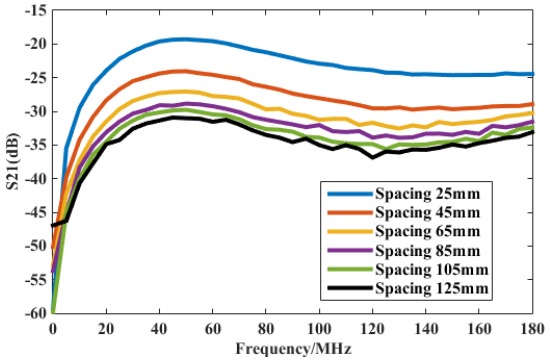

(a)

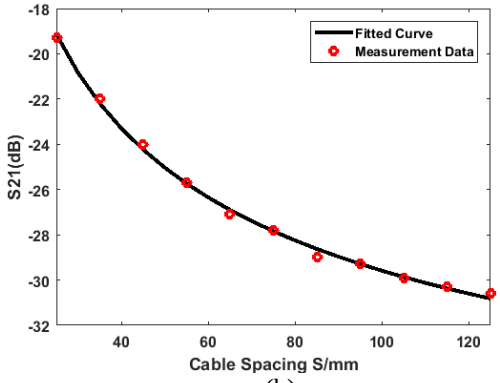

(b)

Fig. 10. Experimental measurement of S_{21}: (a) S_{21} at different cable spacing, and (b) the measurement data of S_{21} and its fitted curve at resonance frequency 35MHz.

V. CONCLUSION

To deal with the relationship between crosstalk and cable spacing, this paper proposed an analytic method of determining the critical cable spacing for acceptable crosstalk. First of all, a calculation function of crosstalk with cable spacing was derived, which gave more insight in crosstalk with cable spacing. Then, the crosstalk characteristic was discussed according to the crosstalk function and its curve. On this basis, the critical cable spacing was defined via a critical point on the curve and a physical explanation of the critical point was given by use of the fringe E-field around the victim cable, in addition, wiring parameters of cable length and height was studied to analyze the influence on critical cable spacing. Finally, an experiment based on S_{21} parameter measurement in a well-controlled test setup was carried out to validate the proposed calculation method of the critical cable spacing.

From the analytic process of critical cable spacing, it can be expected that the universality of crosstalk versus separation curve can be applied for more complex cases such as multi-wire and shielded cables. The difference is the way of calculating crosstalk, but the law of crosstalk varying with the spacing is in a similar way. This work contributed to wiring rules of cables in industrial application.

ACKNOWLEDGMENT

This project is supported by the National Natural Science Foundation of China (Grant No. 51675086).

REFERENCES

[1] S. Sun, G. Liu, J. L. Drewniak, et al., "Hand-assembled cable bundle modeling for crosstalk and common-mode radiation prediction," [J]. *IEEE Transactions on Electromagnetic Compatibility*, vol. 49, no. 3, pp. 708-718, 2007.

[2] J. Wang, "Leaky coaxial cable with circular polarization property," [J]. *IEEE Transactions on Antennas & Propagation*, vol. 59, no. 2, pp. 682-685, 2011.

[3] H. K. Dong and H. J. Eom, "Radiation of a leaky coaxial cable with narrow transverse slots," [J]. *IEEE Transactions on Antennas & Propagation*, vol. 55, no. 1, pp. 107-110, 2007.

[4] B. L. Nie, P. A. Du, Y. T. Yu, et al., "Study of the shielding properties of enclosures with apertures at higher frequencies using the transmission-line modeling method," [J]. *IEEE Transactions on Electromagnetic Compatibility*, vol. 53, no. 1, pp. 73-81, 2011.

[5] EN 50174-1, Integrated Standards for Telecommunications cabling installation. [S]. 2018.

[6] IEC 61000-5-2, Electromagnetic Compatiblity (EMC)-Part 5: Installation and mitigation guidelines-Section 2: Earthing and Cabling. [S]. 1997.

[7] IET. IET wiring regulations (BS 7671:2008 incorporating amendment number 3:2015). [S]. 2015.

[8] M. Sung, W. Ryu, H. Kim, et al., "An efficient crosstalk parameter extraction method for high-speed interconnection lines," [J]. *IEEE Transactions on Advanced Packaging*, vol. 23, no. 2, pp. 148-155, 2000.

[9] A. Palczyńska, A. Wymysłowski, T. Bieniek, et al., "Crosstalk phenomena analysis using electromagnetic wave propagation by experimental an numerical simulation methods," [C]. *International Conference on Thermal, Mechanical and Mulit-Physics Simulation and Experiments in Micro-electronics and Microsystems. IEEE*, 2014:1-10.

[10] L. Ding, D. Blaauw, and P. Mazumder, "Accurate

crosstalk noise modeling for early signal integrity analysis," [J]. *IEEE Transactions on Computer-Aided Design of Integrated Circuits and Systems*, vol. 22, no. 5, pp. 627-634, 2003.

[11] Y. Massoud and J. White, "Simulation and modeling of the effect of substrate conductivity on coupling inductance and circuit crosstalk," [J]. *Very Large Scale Integration Systems IEEE Transactions on*, vol. 10, no. 3, pp. 286-291, 2002.

[12] P. Lafata and P. Jares, "Analysis of simulation methods for far-end crosstalk cancellation," [J]. *Radioengineering*, vol. 20, no. 1, pp. 143-150, 2011.

[13] Z. Li, L. L. Liu, J. Yan, et al., "An efficient simplification scheme for modeling crosstalk of complex cable bundles above an orthogonal ground plane," [J]. *IEEE Transactions on Electromagnetic Compatibility*, vol. 55, no. 5, pp. 975-978, 2013.

[14] C. Jullien, P. Besnier, M. Dunand, et al., "Advanced modeling of crosstalk between an unshielded twisted pair cable and an unshielded wire above a ground plane," [J]. *IEEE Transactions on Electromagnetic Compatibility*, vol. 55, no. 1, pp. 183-194, 2013.

[15] G. Spadacini, F Grassi, F. Marliani, et al., "Transmission-line model for field-to-wire coupling in bundles of twisted-wire pairs above ground," [J]. *IEEE Transactions on Electromagnetic Compatibility*, vol. 56, no. 6, pp. 1682-1690, 2014.

[16] P. Kirawanich, J. R. Wilson, N. E. Islam, et al., "Minimizing crosstalks in unshielded twisted-pair cables by using electromagnetic topology techniques," [J]. *IEEE Transactions on Electromagnetic Compatibility*, vol. 63, pp. 125-140, 2006.

[17] C. Ye, E. Li, and Y. S. Gan, "Crosstalk for curvilinear conductors by utilising a nonuniform transmission line approach," [C]. *Electrical Performance of Electronic Packaging. IEEE*, pp. 189-192, 2001.

[18] R. Nevels and J. A. Miller, "Simple equation for analysis of nonuniform transmission lines," [J]. *IEEE Transactions on Microwave Theory & Techniques*, vol. 49, no. 4, pp. 721-724, 2002.

[19] C. R. Paul, Analysis of Multiconductor Transmission Lines. Wiley, pp. 45-54, 1994.

[20] A. Shoory, M. Rubinstein, A. Rubinstein, et al., "Application of the cascaded transmission line theory of Paul and McKnight to the evaluation of NEXT and FEXT in twisted wire pair bundles," [J]. *IEEE Transactions on Electromagnetic Compatibility*, vol. 55, no. 4, pp. 648-656, 2013.

[21] G. Li, G. Hess, R. Hoeckele, et al., "Measurement-based modeling and worst-case estimation of crosstalk inside an aircraft cable connector," [J]. *IEEE Transactions on Electromagnetic Compatibility*, vol. 57, no. 4, pp. 827-835, 2015.

[22] F. Loete, Q. Zhang, and M. Sorine, "Experimental validation of the inverse scattering method for distributed characteristic impedance estimation," [J]. *IEEE Transactions on Antennas & Propagation*, vol. 63, no. 6, pp. 2532-2538, 2015.

[23] F. Grassi, H. Abdollahi, G. Spadacini, et al., "Radiated immunity test involving crosstalk and enforcing equivalence with field-to-wire coupling," [J]. *IEEE Transactions on Electromagnetic Compatibility*, vol. 58, no. 1, pp. 1-9, 2015.

Pei Xiao was born in Shaoyang, Hunan province, China, in 1989. He received the bachelor and Ph.D. degrees in Mechanical Engineering from UESTC, Chengdu, China, in 2013 and 2019 respectively. He is currently a Postdoctoral Research Fellow in Research Center for Antennas and EMC, Hunan University.

His research interests are numerical computation, theoretical electromagnetic analysis including the EMT method, and EMC/EMI in Multi-conductor transmission line, power electronic device and electric vehicle.

Wan-Wei Ruan was born in Yiwu, Zhejiang province, China, in 1994. She received the B.E. from Huazhong Agricultural University in 2016.

She is currently a master student of UESTC. Her research interest is numerical methods of electromagnetic radiation and crosstalk.

Ping-An Du received the M.S. and Ph.D. degrees in Mechanical Engineering from Chongqing University, Chongqing, China, in 1989 and 1992, respectively.

He is currently a Full Professor of Mechanical Engineering at the University of Electronic Science and Technology of China, Chengdu, China. His research interests include numerical simulation in EMI, vibration, temperature, and so on.